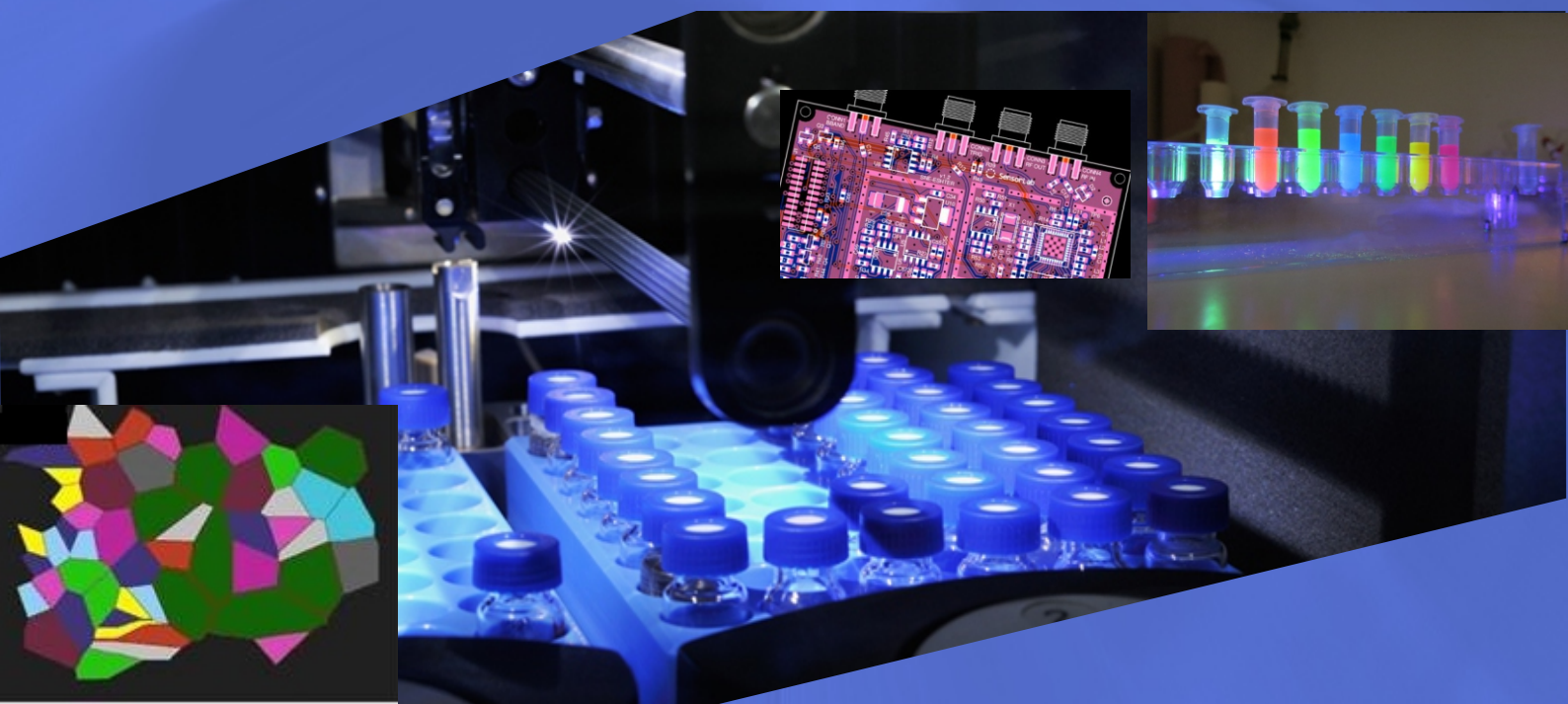




**MEDNARODNA
PODIPLOMSKA ŠOLA
JOŽEFA STEFANA**

**8. ŠTUDENTSKA KONFERENCA
MEDNARODNE PODIPLOMSKE ŠOLE
JOŽEFA STEFANA
Zbornik - 1. del**

**8th JOŽEF STEFAN
INTERNATIONAL POSTGRADUATE SCHOOL
STUDENTS' CONFERENCE
Proceedings - Part 1**



31.5 - 1.6. 2016, Ljubljana

Zbornik 8. Študentske konference Mednarodne podiplomske šole Jožefa Stefana
(Proceedings of the 8th Jožef Stefan International Postgraduate School Students' Conference)

Uredniki / Editors:

Majda Pavlin
Janja Vidmar
Ana Kroflič
Johanna Amalia Robinson
Klemen Bregar
Aleksander Matavž

Založnik / Publisher:

Mednarodna podiplomska šola Jožefa Stefana, Ljubljana

Dosegljivo na / Attainable at:

http://ipssc.mps.si/2016/Proceedings8_IPSSC_2016_Part1.pdf

Ljubljana, maj 2016

Konferenco organizira Študentski Svet Mednarodne podiplomske šole Jožefa Štefana
(The Conference is organized by Jožef Stefan International Postgraduate School - IPS Student Council)

CIP - Kataložni zapis o publikaciji
Narodna in univerzitetna knjižnica, Ljubljana

5/6(082)(0.034.2)
378.046-021.68:001.891(497.4)(082)(0.034.2)

MEDNARODNA podiplomska šola Jožefa Stefana. Študentska konferenca (8 ; 2016 ; Ljubljana)
Zbornik [Elektronski vir]: 1. del = Proceedings part 1/ 8. študentska konferenca Mednarodne podiplomske šole Jožefa Stefana = 8th Jožef Stefan International Postgraduate School Students' Conference, 31. maj in 1. junij 2016, Ljubljana, Slovenija ; [organizira študentski svet Mednarodne podiplomske šole Jožefa Stefana = organized by Jožef Stefan International Postgraduate School - IPS Student Council] ; uredili, edited by Majda Pavlin ... [et al.]. - El. knjiga. - Ljubljana : Mednarodna podiplomska šola Jožefa Stefana, 2016

Način dostopa (URL): http://ipssc.mps.si/2016/Proceedings8_IPSSC_2016_Part1.pdf

ISBN 978-961-94034-0-2 (pdf)

1. Pavlin, Majda, 1988- 2. Mednarodna podiplomska šola Jožefa Stefana (Ljubljana)
284835328

**8. ŠTUDENTSKA KONFERENČA
MEDNARODNE PODIPLOMSKE ŠOLE
JOŽEFA STEFANA**

Zbornik – 1. del

***8th JOŽEF STEFAN INTERNATIONAL
POSTGRADUATE SCHOOL STUDENTS'
CONFERENCE***

Proceedings – part 1

Uredili / Edited by

Majda Pavlin, Janja Vidmar, Ana Kroflič, Johanna Amalia Robinson, Klemen
Bregar in Aleksander Matavž

31. maj in 1. junij 2016, Ljubljana, Slovenija

Organizacijski odbor / Organising Committee

Majda Pavlin

Janja Vidmar

Ana Kroflič

Johanna Amalia Robinson

Klemen Bregar

Maja Somrak

Aleksander Matavž

Andraž Bradeško

Barbara Breznik

Redakcijski odbor / Technical Review Committee

prof. dr. Ester Heath	doc. dr. Boštjan Jančar
prof. dr. Nives Ogrinc	doc. dr. Maja Ponikvar-Svet
prof. dr. Janez Ščančar	prof. dr. Aleš Švigelj
doc. dr. Zdenka Šlejkovec	doc. dr. Tomaž Javornik
prof. dr. Janja Vaupotič	prof. dr. Marko Bohanec
prof. dr. Borut Smodiš	doc. dr. Leon Žlajpah
doc. dr. Gašper Tavčar	doc. dr. Damir Vrančič
prof. dr. Stojan Stavber	prof. dr. Bogdan Filipič
doc. dr. Miha Čekada	prof. dr. Marko Debeljak
prof. dr. Spomenka Kobe	prof. dr. Nada Lavrač

Končna komisija za oceno prispevkov in predstavitev / Final commission for the evaluation of contributions and presentations

prof. dr. Radmila Milačič (predsednik komisije / commission head)

prof. dr. Milena Horvat (ECO professor)

prof. dr. Boris Žemva (ECO/NANO professor)

prof. dr. Barbara Malič (NANO professor)

doc. dr. Tomaž Klobučar (ICT professor)

Majda Pavlin (predstavnica študentov / student representative)

Beseda predsednika MPŠ: prof. dr. Vito Turk



Mednarodna podiplomska šola Jožefa Stefana (MPŠ) se je kljub svoji mladosti hitro uveljavila in postala odmevna ne le doma, pač pa tudi v tujini. Na področju vseh treh usmeritev se vpisujete praviloma odlični mladi podiplomski študentje iz Slovenije, pa tudi mnogi iz tujine. Z vašimi dosežki v času doktorskega študija (nekateri tudi

magistrskega študija) dokazujete, da ste se opremili s kvalitetnim znanjem, ki so vam ga dali oz. omogočili kvalitetni mentorji in somentorji ter ostali raziskovalci. Ob tem je ključnega pomena odlična infrastruktura, ki vam je na voljo. Pri tem je potrebno izpostaviti še delovno okolje oz. sredino, v kateri mladi raziskovalci delate in živite, saj predstavlja raziskovalno okolje pravzaprav vaš drugi dom. Verjamem, da se v tem drugem domu dobro počutite. Ob tem čas hitro mineva in ne gledate le na obvezni čas, pač pa delate tudi v poznih urah, ob sobotah, nedeljah, pa tudi praznikih. Vse to vam omogoča, da ste vzpostavili in še vzpostavljate delovne in prijateljske vezi, kar je velika vzpodbuda za vašo kreativnost na eni strani, po drugi strani pa za razvijanje profesionalnega odnosa do dela. Med vami so tudi mnogi mladi raziskovalci iz tujine, ki samo še bogatijo to raziskovalno okolje ter pomagajo pri vzpostavljanju mednarodnih stikov. Naj poudarim, da so izjemnega pomena kolegijski odnosi, spoštovanje vaših sodelavcev, mentorjev in sploh vseh, ki so prisotni in delujejo v tem raziskovalnem prostoru.

Vaši dosežki se izkazujejo v obliki objav v uglednih, pa tudi odličnih mednarodnih revijah, patentih, prikazovanju vaših rezultatov na mednarodnih in domačih konferencah, kratkih usposabljanjih v tujini in še kaj. Med te dejavnosti se uvršča tudi naša tradicionalna konferenca konca maja, na kateri naši doktorandi in magistrandi prikazujete svoje dosežke.

Posebej bi še izpostavil tesno sodelovanje med Institutom »Jožef Stefan« in našo podiplomsko šolo, v zadnjem času pa tudi z Nacionalnim inštitutom za biologijo (NIB), pa še kom. Pri tem ni zanemarljivo sodelovanje z industrijo. Brez vsega tega uspešnega delovanja te šole ne bi bilo. Pri tem moram omeniti še Centre odličnosti s

svojo odlično opremo, ki pa žal iz nerazumljivih razlogov, lahko bi rekli tudi zaradi nerazumevanja njihovega pomena, niso več financirani s strani države. Smo med redkimi državami razvitega sveta, ki to počno! Nedvoumno je to zelo slabo! Posledice takega odnosa že čutimo vsi, da ne omenjam katastrofalnega, lahko bi rekel ignorantskega odnosa do te veje družbene dejavnosti. Naša država namenja znanosti v zadnjem letu okoli 0,4 % BDP, kar je sramotno in nas po tem merilu uvršča na dno EU. Kljub temu pa vztrajamo na začrtani poti! Zavedamo se, da le vrhunski kadrovski potenciali in mednarodne povezave omogočajo pridobivanje odličnih znanj, pridobljenih na temeljnih in aplikativnih raziskavah, ki se potem prenašajo tudi v gospodarstvo. Žal je tega v zadnjem času le malo, saj mnogi odhajajo po končanem dodiplomskem in doktorskem študiju v tujino in so tako večinoma izgubljeni za nas. To je tipičen »brain-drain«, saj v obratno smer praktično ni dotoka in s tem izmenjave znanj. Nobelovec de Duve je rekel »Znanost je del kulture naroda. Kdor tega ne spoštuje, ni kulturen!«

Slovenija je zabredla v globoko ekonomsko krizo, iz katere se le počasi rešuje – prepočasi. Temu so se v dobri meri izognile države, ki so se pravočasno zavedale pomena vlaganj v odlično znanost in raziskave. Tudi mnoge nove članice EU! Še posebej pa se moramo zavedati, da ekonomsko uspešne države vlagajo velika finančna sredstva v znanost in raziskave in ob tem privabljajo mnoge odlične raziskovalce, pa tudi talentirane podiplomce in dodiplomce, na delo in študije za potrebe njihovega nadaljnjega ekonomskega razvoja v tekmi na globalni ravni. Zaradi situacije, v kateri se je znašla Slovenija in ki nam je vsem poznana, je nujno, da odgovorni v Republiki Sloveniji končno spoznajo, da brez odličnega znanja in odličnih tehnologij ne bo gospodarskega napredka. Znašli smo se že na samem začetku Evrope in nadaljevanje takega početja nas bo prikovalo na dno.

Mladi ste upravičeni do boljše prihodnosti, kot vam jo ponuja sedanjost! Do novih delovnih mest! Pravico imate, da se vam omogoči uspešno spopadanje z izzivi v domačem okolju, ne pa da iščete izpolnitve svojih ambicij in eksistenčnih možnosti z odhodom v tujino. To desetletje ali še krajša doba bo ključnega pomena za slovensko gospodarstvo ter ekonomsko in politično neodvisnost Slovenije.

Naj še enkrat ponovim, kar sem že pred kratkim zapisal: znanje je vrednota, ki omogoča narodu ekonomski razvoj in obstoj. Mladi vrhunski raziskovalci, ki so pogoj za uspešen gospodarski in vsesplošen družbeni razvoj, pa so srce družbe znanja. Očitno so za to spoznanje potrebne globoke družbene spremembe!

Beseda dekanje prof. dr. Milene Horvat

Raziskovalno-izobraževalni proces v intenzivnem in inovativnem raziskovalnem okolju ključno prispeva h krepitvi razvojnega potenciala znanosti in visokih tehnologij v družbi. Prav to je vodilo izobraževalnega procesa na Mednarodni podiplomski šoli, ki prepleta temeljno raziskovanje s podiplomskim izobraževanjem in tehnološkim razvojem. V dobrih 10-ih letih delovanja beležimo številne uspehe takega delovanja na področjih nanotehnologij, informacijsko-komunikacijskih tehnologij in ekotehnologij. K temu šola v novem študijskem letu 2016/2017 dodaja še področje senzorskih tehnologij, ki bistveno dopolnjuje že obstoječe programe in ustvarja nove možnosti za povezovanje na področju medsektorskega sodelovanja. Senzorji namreč pomagajo prepoznavati določene pogoje v okolju in nanje ciljno reagirajo, zato njihova uporaba sega na skoraj vsa področja človekovih dejavnosti, kot na primer preskrbo z zdravo in varno hrano, kmetijstvo, zdravstvo, okoljevarstvo, energetiko itd. Ob vse večjih ekonomskih in okoljskih zahtevah postajajo senzorske tehnologije bistveni sestavni del vseh “pametnih” izdelkov in s tem obetavna priložnost za industrijo. Njihova proizvodnja terja hitro napredujoče visoke tehnologije, zato je to področje tudi znanstveni izziv.

Slogan letošnje konference “Znanost je seme razvoja” zgovorno kaže, da so študentje prepoznali, da je poslanstvo MPŠ dobro zastavljeno.

Poleg znanstvenih objav, ki so v izobraževalnem procesu na šoli ključni pokazatelji uspeha, so študentje MPŠ že pred leti prepoznali, da je prav posredovanje znanstvenih rezultatov izjemnega pomena pri prenosu znanja iz raziskovalne sfere do uporabnikov. Prav tako izmenjava znanj in izkušenj med študenti in raziskovalci krepí in bogati raziskovalno delo, ki je po naravi večinoma interdisciplinarno. Letošnja konferenca k temu pridaja še posredovanje rezultatov širši javnosti, zato je program konference posvečen tudi pridobivanju veščin javnega nastopanja.

V Sloveniji je vloga javnosti v znanstveni sferi pogosto zanemarjena, čeprav Evropa prepoznava, da je ta segment ključen pri prenosu znanja v prakso, zato je to zapisano tudi v strateških ciljih, kar se odraža v zahtevah tematskih razpisov Obzorja 2020.

Tudi naša šola prepoznava pomen komunikacije širši javnosti kot sestavni del izobraževalnega procesa, zato bo tovrstne dejavnosti še naprej podpirala.

V sodelovanju s partnerskimi raziskovalnimi institucijami in industrijo želimo na MPŠ ustvariti pogoje, ob katerih študentje lahko ustvarjajo odlično mednarodno primerljivo znanost, hkrati pa razvijajo svoje kreativne in poslovne sposobnosti, s čimer bodo prispevali tudi k zagotavljanju pogojev za uspešen razvoj poslovnih modelov in posledično k vidnim rezultatom v družbi.

Vsem udeležencem študentske konference želim uspešno delo, ki bo ostalo v spominu kot kreativno in prijetno druženje.



Predstavnica gospodarstva dr. Jožica Rejec

Predstavitev rezultatov raziskav na letni študentski konferenci Mednarodne podiplomske šole Jožefa Stefana je odlična priložnost za hiter in celovit pregled dosežkov in raziskovalnih področij šole.

V industriji potrebujemo za dvig dodane vrednosti rešitve, ki so inovativne in konkurenčne na svetovnem trgu. V sodelovanju s kupci dobimo informacije o potrebah trga in,



kjer smo razvojni dobavitelj, oblikujemo z njimi ciljne karakteristike. Dobavitelji smo vedno bolj vključeni v zgodnji razvojni fazi idejnih rešitev izboljšav in novih platform končnih izdelkov. Ideje za inovativne in prebojne rešitve črpamo iz različnih virov in lastnih raziskav. Za uvrščanje izdelkov in rešitev v sam svetovni vrh in razumevanje delovanja sistemov rešitev že davno ni več dovolj eksperimentiranje. Potrebne so jasne teoretične fizikalne slike in uporaba računalniških simulacij za rešitve, ki so zato na dovolj varnem robu tveganj in prav zaradi tega konkurenčne.

Za odlične rešitve je potrebna širina različnih znanj in izkušnje. Študentska konferenca in predstavitev rezultatov raziskav je priložnost za spoznavanje novih odkritij z različnih področij. Na osnovi predstavitve se bo rodila kakšna ideja za prebojno rešitev in sodelovanje industrije z raziskovalci Mednarodne podiplomske šole Jožefa Stefana.

Znanost je seme razvoja – prispevaj svoj delež!

Za nami je že kar nekaj uspešno izpeljanih študentskih konferenc Mednarodne podiplomske šole Jožefa Stefana (MPŠ) in letos bo to že osma po vrsti. Organizacijski odbor 8. študentske konference sestavlja deloma stara, deloma nova ekipa študentov MPŠ, kjer smo predstavniki vseh treh študijskih smeri, Nanoznanosti in nanotehnologij, Informacijskih in komunikacijskih tehnologij ter predstavniki Ekotehnologije. Pri organizaciji dogodkov ves čas stremimo k temu, da so vsi dogodki, ki jih pripravljamo, za študente koristni in zanimivi.

V osnovi konferenca predstavlja druženje in povezovanje študentov med seboj, pomembno vlogo pa imajo predstavitve njihovega raziskovalnega dela podjetjem, industriji (industrijskim partnerjem) ter širši javnosti. Hiter razvoj in vse večja konkurenčnost na trgu dela kažejo na vse večjo potrebo po povezovanju raziskovalnega sektorja z industrijo in razvojno naravnanimi podjetji, saj bomo le tako lahko dosegli visokokvalitetne storitve in produkte. Letošnji slogan "Znanost je seme razvoja – prispevaj svoj delež!" zgovorno kaže na to, da pri tem lahko prvi korak naredimo tudi sami.

V želji, da konferenca ne bi bila samo neka formalna obveznost, ampak tudi družaben dogodek, ki nam bo ostal v lepem spominu, smo program in cilje letošnje konference zastavili nekoliko drugače. Dodatna znanja, ki jih pridobimo tekom študija oziroma na različnih področjih dela, so izredno pomembna, saj so zahteve pri vstopu na trg dela vedno višje in nam je to lahko v pomoč ne samo pri iskanju nove službe, ampak tudi ko bomo že vključeni v proces dela na drugem delovnem mestu ali pa bomo nadaljevali delo v raziskovalni sferi. Z namenom pridobivanja dodatnih veščin (znanj) smo začeli z organizacijo različnih delavnic, ki se do sedaj s strani študentskega sveta še niso izvajale, so pa zagotovo poučne in zaželene s strani študentov. Pri načrtovanju programa letošnje konference smo tako prišli na idejo, da bi bile lahko



delavnice v sklopu same konference. Namen letošnje konference tako ni samo predstavitev raziskovalnega dela mladih raziskovalcev ter povezovanje raziskovalne sfere z industrijo, pač pa je namenjena tudi pridobivanju informacij na področju javnega nastopanja in posledično predstavitvi ideje oziroma rezultatov na način, ki bi pritegnil širšo javnost, predvsem potencialne investitorje. Odločili smo se za izvedbo štirih delavnic, ki so vse tematsko usmerjene. V začetku maja je bila organizirana delavnica "Elevator pitch", saj je naloga vsakega študenta, ki na konferenci sodeluje, da v zelo kratkem času jasno predstavi svojo idejo oziroma raziskovalno delo. Z omenjeno delavnico smo želeli študente že mesec pred samim dogodkom informirati o tem, kako mora biti govor sestavljen in kaj so tiste bistvene lastnosti, ki jih mora poleg vsebine predstavitev vsebovati. Interes in sam obisk študentov je bil kar velik, saj se je dogodka udeležilo vsega skupaj 40 mladih raziskovalcev. Pozitiven odziv in želja po izvedbi dodatnih delavnic kaže na to, da imajo študenti poleg strokovnega znanja, ki ga pridobijo tekom dodiplomskega študija in podiplomskega izobraževanja na različnih fakultetah oziroma MPS, željo po pridobivanju še dodatnih veščin, saj je tega v samem izobraževalnem programu zagotovo premalo. Naše poslanstvo je, da poskusimo v dogovoru s šolo takim željam čim bolj ustreči in zato se bomo tudi v prihodnje trudili, da bo izvedenih še več tovrstnih delavnic z najrazličnejšimi tematikami.

Na sami konferenci sta bili izpeljani dve delavnici; prva s splošno tematiko javnega nastopanja (in neverbalne komunikacije) ter druga z napotki, kako mora izgledati predstavitev oziroma daljši govor, kot na primer "TED" govori oziroma predavanje na konferenci. Pred samo konferenco smo poskrbeli tudi za praktičen del, ki je pri vsem tem najbolj pomemben. Študente smo razdelili v štiri skupine, kjer je vsako skupino prevzel zunanji mentor – novinar, ki zna pristopiti k znanstveni tematiki in se strokovno ne spozna na tematiko njihovega dela, ima pa izkušnje na področju poljudnega podajanja znanosti. Mladim raziskovalcem so svetovali, kako naj pripravijo privlačen nadnaslov, jim pomagali izluščiti bistvene informacije posameznega raziskovalnega dela in jih predstaviti na način, da je privlačno za publiko in tudi potencialne vlagatelje.

Torej namen letošnje konference je predvsem pokazati, kako naj delo, idejo ali morebitni produkt predstavimo širšemu občinstvu na kratek, jasen in zanimiv način, ki bo hkrati dovolj strokoven in bo izpostavil uporabno vrednost, kar pa je zelo pomembno pri povezovanju in širjenju znanja na področje industrije in visokotehnoloških podjetij.

Tudi letos smo povabili predstavnike štirih podjetij in jih uvrstili v sklop predstavitev "Od ideje do uspeha", in sicer Pipistrel, Animacel, Viarbox in partnerja šole Cosylab. S kratkimi predavanji naj bi podjetja predstavila svojo pot do uspeha, kaj jih je vodilo v podjetniško pot in kako so se in se še soočajo z izzivi in ovirami pri svojem delu. Uspešna podjetja so odlični primer, kako se lahko dobra ideja udejanji, pri čemer pa je potrebno kar nekaj potrpljenja, ogromno vloženega dela in seveda želje po uspehu.

Konferenca je tudi odlični način za samo promocijo šole, tako preko spletnih socialnih omrežij kot tudi na osebni ravni. S pomočjo konference se študenti naše šole večkrat pojavijo v kakšnem časopisnem ali radijskem intervjuju, kar kaže na to, da ima šola res kvalitetne študente in da šola sama pridobiva na prepoznavnosti.

Temelj konference so kvalitetni študentski prispevki. Na povabilo k sodelovanju se je odzvalo 31 podiplomskih študentov (17 na smeri Ekotehnologije, 6 na smeri Nanoznanosti in nanotehnologije in 8 prispevkov na smeri Informacijske in komunikacijske tehnologije) in dodiplomska študentka, skupaj torej 32 prispevkov, kar je nekaj več kot lani. Za pregled prispevkov je skrbelo kar 20 članov redakcijskega odbora, ki so prispevke temeljito pregledali (pravilnost in strokovnost znanstvenega besedila) in podali mnenje, oceno ter predloge za popravke. Letošnja novost je tudi možnost objave razširjenega povzetka poleg članka, ki je že ustaljena praksa.

Poleg številnih sprememb in novosti v samem programu konference pa je prišlo do sprememb tudi pri sestavi vodstva na šoli. Štiriletni mandat dekanje se je iztekel prof. dr. Aleksandri Kornhauser-Frazer, ki je bila vedno zelo naklonjena študentski konferenci in je bila tudi letos v času do izteka mandata vedno na voljo za kakršne koli informacije in pomoč pri sami organizaciji, za kar smo ji zelo hvaležni.

Za uspešno izvedbo konference bi se v prvi vrsti radi zahvalili predvsem študentom in mentorjem, ki so s svojimi kakovostnimi deli, sodelovanjem in trudom prispevali k odličnosti in bistvu te konference. Za zanimiva predavanja in predstavitve izzivov, ki jih prinaša prenos znanosti na trg dela, se zahvaljujemo vsem sodelujočim podjetjem, organizacijam in predavateljem, ki so pokazali veliko zanimanje za sodelovanje in so poskrbeli, da je bila konferenca nadvse uspešna in zanimiva. Zahvaljujemo se redakcijskemu odboru za njihov čas in znanje, ki so ga porabili za pregled in tako poskrbeli za visoko kvaliteto prispevkov. Posebne zahvale grede tudi celotnemu osebju Mednarodne podiplomske šole Jožefa Stefana in sponzorjem za pomoč pri organiziranju konference. Še posebej bi se radi zahvalili sedanji dekanji prof. dr. Mileni Horvat za pomoč pri pridobivanju finančnih sredstev ter predvsem za podporo in zavzemanje za naše ideje. Nazadnje pa gre velika zahvala tudi Sergeji Vogrinčič, Tadeji Samec in Maši Matijašević, ki so zelo pomemben člen pri organizaciji in vodenju konference ter za skrbno lektoriranje in popravo zbornika. Hvala tudi sodelujočim novinarjem Renati Dacinger, Maji Ratej, Denisu Oštirju in Lenartu J. Kučiču za pomoč študentom pri pripravi kratkih predstavitev in novinarjem, ki so sodelovali pri ocenjevanju. Zahvala gre tudi prof. dr. Saši Novak za nasvete pri organizaciji sekcije »3 minute o mojem doktorskem delu« in društvu Satena, ki je v sklopu projekta Znanost na cesti prispevalo nagrado »Znanost pred mikrofonom«.

Uredniški odbor

Kazalo (Table of Contents)

Ekotehnologija (Ecotechnology)	2
Microstructural analysis of Bulk Molding Compounds and correlation with the flexural strength <i>Barbara Bertoneclj, Katarina Vojisavljević, Janez Rihtaršič, Gregor Trefalt, Barbara Malič</i>	3
Metal-free azidation of alcohols catalysed by molecular iodine <i>Klara Čebular, Monika Horvat, Stojan Stavber</i>	13
Building composites from fly ash, cement and electric arc furnace dust: Environmental impacts <i>Ana Drinčič, Irena Nikolić, Tea Zuliani, Radmila Milačič, Janez Ščančar</i>	20
HPGe gamma detector effective solid angle calculation <i>Lojze Gačnik, Radojko Jaćimović</i>	31
Implementing molecularly imprinted polymer (MIP) in the analytical method for determining sertraline residues in aqueous environment <i>Tjaša Gornik, Anja Krajnc, Amadeja Koler, Marko Turnšek, Ester Heath, Jernej Iskra, Peter Krajnc, Karel Jerabek, Tina Kosjek</i>	39
Maternal blood levels of selected elements and birth weight of mother-child pairs living in Slovenia <i>Marta Jagodic, Janja Snoj-Tratnik, Darja Mazej, Anja Stajnko, Majda Pavlin, Mladen Krsnik, Alfred B. Kobal, Lijana Kononenko, Milena Horvat</i>	46
Iodine and selenium content in buckwheat seed after foliar spraying of plants with I and Se solution <i>Ana Jerše, Ana Kroflič, Mateja Germ, Nina Kacjan-Maršič, Helena Šircelj, Vekoslava Stibilj</i>	52

Evidence of cave ventilation and its contribution to soil CO₂ flux	
<i>Bor Krajnc, Mitja Ferlan, Nives Ogrinc</i>	56
Does iodine affect selenium content in buckwheat sprouts?	
<i>Ana Kroflič, Ana Jerše, Nina Kacjan-Maršič, Mateja Germ, Helena Šircelj, Vekoslava Stibilj</i>	65
Mimicking nature-iron catalysed oxidation of alcohols	
<i>Štefan Možina, Stojan Stavber, Jernej Iskra</i>	69
Determination of polybrominated diphenyl ethers in sewage sludge with GC-ICP-MC	
<i>Petra Novak, Tea Zuliani, Radmila Milačič, Janez Ščančar</i>	76
Razvoj metod za pripravo aciloksialkilnih predzdravil fosfatov ter uporaba topil, primernih za farmacevtsko industrijo	
<i>Jerca Pahor, Ajda Podgoršek Berke, Alen Čusak, Gregor Kosec, Hrvoje Petković, Stojan Stavber</i>	81
A study of the thermal release of mercury compounds in FGD gypsum from the Šoštanj Thermal Power Plant using mass spectrometry	
<i>Majda Pavlin, Arkadij Popović, Radojko Jaćimović, Milena Horvat</i>	91
Stable isotope composition and elemental profile as a tool for determination of cheese species and geographical origin	
<i>Doris Potočnik, Marijan Nečemer, Nives Ogrinc</i>	96
Cadmium exposure biomarkers and their associations with renal function biomarkers at low level of exposure	
<i>Anja Stajniko, Janja Snoj-Tratnik, Darja Mazej, Marta Jagodic, Mladen Krsnik, Lijana Kononenko, Milena Horvat, Ingrid Falnoga</i>	106
The fate of zero valent iron nanoparticles after their use in	

wastewater remediation by single particle ICP-MS <i>Janja Vidmar, Primož Oprčkal, Ana Mladenovič, Radmila Mi- lačić, Janez Ščančar</i>	113
Speciation of mercury and microbial communities in the seawater of the Central Adriatic Sea <i>Igor Živković, Milena Horvat, Mladen Šolić, Vesna Fajon, Jože Kotnik</i>	122
Informacijske in komunikacijske tehnologije (Infor- mation and Communication Technologies)	129
NLOS Channel Detection with Multilayer Perception in Low-Rate Personal Area Networks for Indoor Localiza- tion Accuracy Improvement <i>Klemen Bregar, Andrej Hrovat, Mihael Mohorčič</i>	130
Passive Ankle Exoskeleton: Design and Practical Evalua- tion <i>Miha Dežman, Tadej Debevec, Jan Babič, Andrej Gams</i>	140
Knowledge extraction of evidence-based dietary recommen- dations <i>Tome Eftimov, Peter Korošec, Barbara Koroušič-Seljak</i>	149
Activity and stress monitoring using smartphone and wrist device <i>Martin Gjoreski, Vito Janko, Hristijan Gjoreski, Božidara Cvet- ković, Mitja Luštrek, Matjaž Gams</i>	154
Integrating predictive and decision modelling in decision support system for water protection from phytochemi- cals <i>Vladimir Kuzmanovski, Aneta Trajanov, Sašo Džeroski, Marko Debeljak</i>	165
Multi-dimensional analysis of PPMI data <i>Vanja Mileski, Dragi Kocev, Bogdan Draganski, Sašo Džeroski</i>	175

Model-based fault diagnosis with Gaussian process regression of nominal model residuals	
<i>Martin Stepančič, Boštjan Dolenc, Dani Juričič</i>	180
Low-cost spectrum sensor for ultra-narrowband transmissions	
<i>Tomaž Šolc</i>	193
Nanoznanosti in nanotehnologije (Nanosciences and Nanotechnologies)	205
New method for C-O and C-N bond formation catalysed by N-halo compounds under green reaction conditions	
<i>Njomza Ajvazi, Stojan Stavber</i>	206
Building thick spinel iron oxide layer onto the hexaferrite core nanoparticles using multiple co-precipitation of iron ions	
<i>Blaž Belec, Darko Makovec</i>	216
The formation of silica coating on barium hexaferrite nanoparticles and functionalization with 3-aminopropylsilane	
<i>Tanja Goršak, Slavko Kralj, Darko Makovec, Darja Lisjak</i>	227
Influence of concentration and size of Al₂O₃ particles on their distribution in reinforced austenitic stainless steel	
<i>Ana Kračun, Franc Tehovnik, Fevzi Kafexhiu, Bojan Podgornik</i>	239
An infrared study of Concanavaline A aggregation at pH 5 and 9	
<i>Urban Novak, Jože Grdadolnik</i>	250
Chemical speciation of third-row elements via valence-to-core x-ray emission spectroscopy	
<i>Marko Petrič, Klemen Bučar, Matjaž Žitnik, Matjaž Kavčič</i>	261
The effect of benzen ring and mercapto group in imidazoles	

on the corrosion inhibition of copper alloy with 10% zinc
Monika Žnidaršič, Črtomir Podlipnik, Ingrid Milošev **274**

Kazalo Avtorjev (List of Authors) **280**

Ekotehnologija (Ecotechnology)

Microstructural analysis of Bulk Molding Compounds and correlation with the flexural strength

Barbara Bertoncej^{1,2}, Katarina Vojisavljević³, Janez Rihtaršič¹, Gregor Trefalt⁴, Barbara Malič³

¹ Domel, d.o.o., Železniki, Slovenia

² Jožef Stefan International Postgraduate School, Ljubljana, Slovenia

³ Department of Electronic ceramics, Jožef Stefan Institute, Ljubljana, Slovenia

⁴ University of Geneva, Sciences II, Quai Ernest-Ansermet 30, 1205 Geneva, Switzerland

barbara.bertoncej@domel.com

Abstract. In this study, the influence of the glass fiber (GF) content on the microstructure and flexural strength of bulk molding compounds (BMCs) is investigated. Three sets of BMCs with different weight fractions of GF (5/10/12.5 wt%) were commercially prepared and compression molded into test specimens. The microstructure of the composites was analysed by scanning electron microscopy and further quantitatively characterized by Voronoi analysis in order to define the degree of the fiber distribution homogeneity. The experimental results were compared to the modelled microstructures. The results revealed that the fiber distribution in the composite with 5 wt% of GF is considered as the most homogeneous. Through the obtained microstructural descriptors, the fiber weight content and their distribution were correlated to the flexural strength of BMCs. The flexural strength was the highest for the composite with 10 wt% of GF.

Keywords: bulk molding compounds, glass fibers, microstructure, Voronoi analysis, flexural strength

1 Introduction

Bulk molding compounds (BMCs) are composite materials, consisting of a polymer matrix, discontinuous glass fibers (GF) and a mineral filler. Generally, polymers have

low strength and stiffness, therefore the addition of GF improves the mechanical strength of the material. BMCs are highly filled with the mineral filler, which modifies the viscosity of the polymer resin, improves the dimensional stability and surface quality, gives self-extinguishing properties and lowers the cost of the material. Finally, the function of the polymer is to hold together the fibers and particles of the filler in a proper spatial arrangement and helps in the stress transfer between the glass fibers. The overall properties of BMC composites are influenced by the weight content of individual constituents and their properties as well as on the type, shape, orientation and distribution of fibers.

The main area of application of such materials is in the electro and electronic industry for manufacturing of various products, ranging from switches and connection boxes to components for assembly of electro motors, such as housings, brush holders and yokes. The second major utilization area of such materials is automotive industry, e.g. for manufacturing under-the-hood components and headlamp reflectors. BMC products are usually manufactured by the injection molding technology, mainly used for mass production of small, complex shaped components.

The orientation and spatial distribution of fibers in the material depends on the molding process as well as on the geometry of the mold that is used to manufacture the composite product. Therefore, the formed product exhibits a complex microstructure with the preferred orientation of GF in the filling flow direction. However, the inhomogeneous fiber distribution can lead to a poorer mechanical strength of the material [1,2].

The Voronoi diagram analysis is one of the methods that can be used to quantitatively describe the microstructure of the fiber reinforced composites. In this way the microstructure can be described with statistical parameters in order to identify the level of the fiber distribution homogeneity. Several authors have applied Voronoi method to describe the microstructure and distribution of the second phases in composite materials [3-7]. The same method was used in our previous work, where we investigated the fiber distribution homogeneity in BMC composites with different GF fractions and where we concluded that the fiber distribution inhomogeneity affects the mechanical response of the composites. More details can be found in [8]. In this work we investigated another set of BMC samples with different weight contents of GF (5/10/12.5). Thus, the Voronoi diagram method was used to identify

and quantify the level of the fiber distribution homogeneity. Furthermore, the results of Voronoi analysis were related with the flexural strength of composites.

2 Experimental work

Three sets of BMC composites with varying contents of GF and mineral filler were commercially prepared. The polymer phase, based on the thermosetting unsaturated polyester, styrene and additives, was kept constant (21 wt%), while the GF with the initial length of 4.5 mm and diameter of 11 μm (confirmed by the scanning electron microscopy, SEM) were used for the polymer reinforcement. CaCO_3 was used as the mineral filler [9]. The formulation of the samples is listed in Table 1. Test specimens were prepared by compression molding, according to the standard ISO 3167 [10].

Table 1: Composition of the BMC samples.

	Polymer matrix	GF	CaCO_3
	Content [wt%]		
1	21	5	74
2	21	10	69
3	21	12.5	66.5

For individual composition, the test specimen was cut in half, perpendicular to the filling flow direction of the compound during the molding in order to obtain cross sections for microstructural characterization, as shown in Figure 1. The cross-sections of the test specimens were prepared by the standard metallographic technique, i.e. by grinding and polishing, and examined by field-emission scanning electron microscope FE-SEM (JSM-7600F JEOL Ltd., Tokyo, Japan). Prior to the SEM observations the samples were sputter-coated with a thin carbon layer. The micrographs were taken at the accelerating voltage of 15 kV in backscattered-electron mode.

The Voronoi diagrams were generated from the SEM micrographs. First, the center of each glass fiber on the micrograph was marked with a black point using Corel Paint Shop Pro X7 software. Next, the Voronoi diagrams were constructed using ImageJ software and then the area of each Voronoi polygon was measured using Image Tool software. Nine SEM micrographs of an individual sample were included in the analysis (see Figure 1) which accounts for 1.6 mm^2 of investigated area for each sample. As a

reference, for each composition of the composite material, a pattern of randomly distributed disks (by Poisson process) and a corresponding Voronoi diagram were generated.

For an easier comparison of the samples with different fractions of fibers, the absolute areas were normalized to the relative polygon areas, A_r , according to Equation (1):

$$A_r = A_p N / A_{\text{total}} \quad (1)$$

where A_p is the absolute polygon area, N is the number of polygons in the sample, A_{total} is the area of the sample. For individual sample, histograms of relative Voronoi polygon areas were generated.

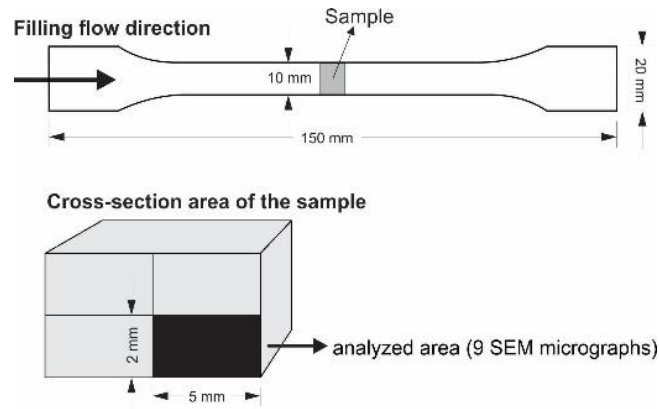


Figure 1: Schematic representation of the test specimen's dimensions, the cutting position of the sample and the sampling scheme of the cross-sectional area for the morphological characterization.

The flexural strength of the test specimens was measured by the three-point bending method (Alpha 50-5), according to standard ISO 178:2003 [11]. The span between the supports was 64 mm and the crosshead speed was 2.0 mm/min. The test was carried out on 15 specimens of each composition and calculated by the equation (2),

$$\sigma_f = \frac{3Pl}{2bh^2} \quad (2)$$

where σ_f is the flexural strength, P is the maximum fracture load, l is the span between the supports, b is the width of the sample and h is the height of the sample.

3 Results and discussion

3.1 Microstructure and Voronoi analysis

SEM micrographs of cross-sectional areas of the BMC composites with corresponding experimental and random Voronoi diagrams are shown in Figure 2. During the molding process, the fibers tend to orient in the preferred direction, i.e. they are mostly oriented parallel with the filling flow of the material. Therefore, depending on the orientation of the fibers, the cross-sections of the GF are circular to elliptical. The fibers are surrounded by the irregularly shaped particles of the CaCO_3 mineral filler. From the micrographs we observed that at lower glass fiber content, i.e. at 5 wt% to 10 wt% of GF, the distribution of the fibers is quite homogeneous. However, by increasing the glass fiber content above 12.5 wt%, the fibers tend to cluster together, forming a non-homogeneous microstructure with local areas where the number of fibers (i.e. fiber clusters) is high and areas filled only with polymer resin and CaCO_3 mineral filler.

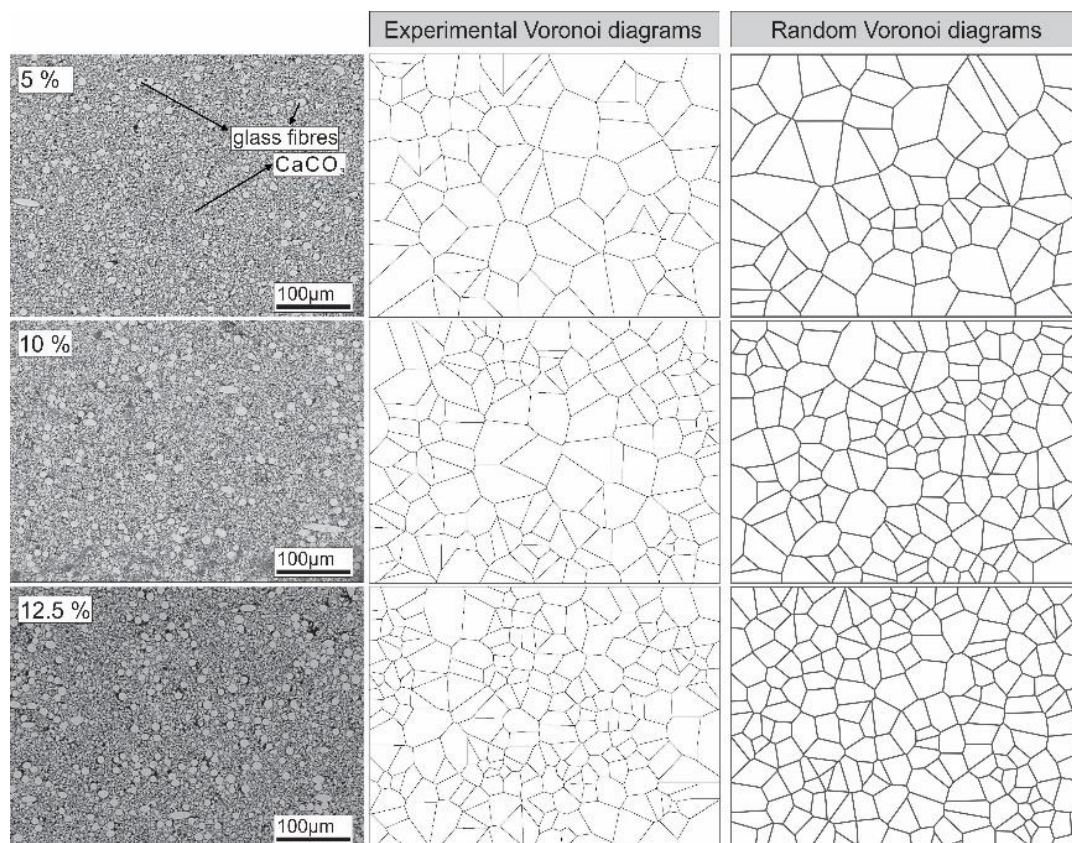


Figure 2: SEM micrographs of the BMC composites with different weight fractions of GF (5, 10 and 12.5 wt%) and the corresponding Voronoi diagrams from the experimental and randomly generated fiber distribution.

Therefore, in the next step we quantitatively characterized the microstructures to evaluate the homogeneity of the fiber distribution in the polymer matrix. To distinguish between the microstructures with possible fiber clustering and a more even fiber distribution in the polymer matrix, the experimental Voronoi diagrams were compared with Voronoi diagrams from the randomly generated microstructures (see Figure 2, central and right column). The experimental Voronoi polygons for the sample with 5 wt% of GF are quite large, but when the fiber content increases the polygons become smaller as a consequence of a larger number of fibers and therefore smaller spatial distances between them. Furthermore, it can be seen that there are more obvious differences between the sizes of polygons in experimental Voronoi diagrams of the samples with 10 and 12.5 wt% of GF. This is especially pronounced in the latter sample where relatively small polygons indicate fiber clustering. On the other hand, the sizes of Voronoi polygons obtained from random microstructures are almost equal across the whole area - as a result of a homogeneous fiber distribution. The histograms of relative Voronoi polygon areas from the experimental and random fiber distributions are shown in Figure 3. For the sample with 5 wt% of GF the experimental and random distribution plots are very close to each other, which confirms an even and homogeneous fiber distribution. However, we would like to note, that from the viewpoint of mechanical performance such composition could not be treated as the best since the mechanical properties are dependent on the fiber distribution as well as on fiber content (see section 3.2 Flexural strength).

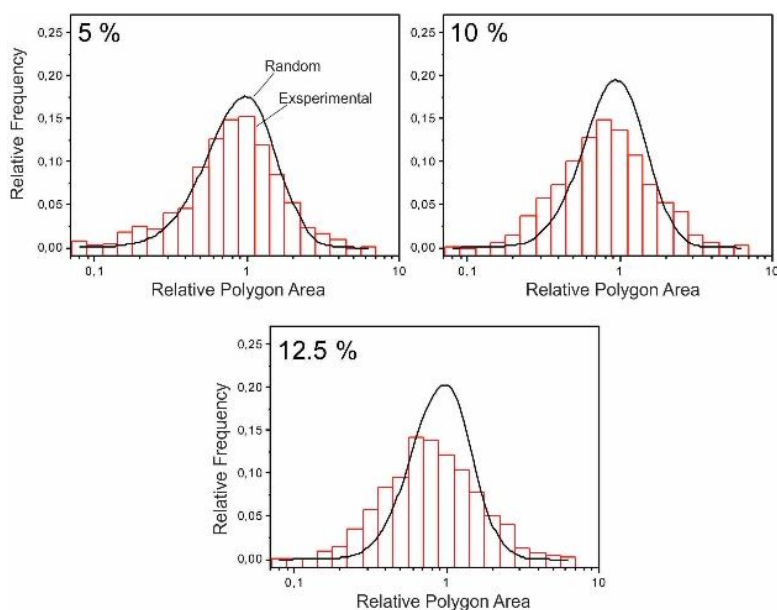


Figure 3: Histograms of the relative Voronoi polygon areas of BMC composites for the experimental and randomly generated fiber-distribution microstructure.

With increasing the GF content, the divergence of the experimental plot from the random plot is more pronounced, especially in the sample with 12.5 wt%. This indicates fiber clustering in the microstructure as a consequence of shorter distances between the fibers, i.e. only on local areas and not on the whole pattern.

The distribution of the random Voronoi polygons is becoming narrower with increasing the GF content which implies a more even distribution at higher fiber fractions. On contrary, the experimental distributions of all BMC samples have a similar width, with a peak slowly shifting to lower values when the GF content increases, which suggests that the fiber clustering is more prominent in the samples with a higher fiber content due to the lack of space for a homogeneous fiber distribution.

3.2 Flexural strength

The results of the flexural strength measurement and standard deviation of the BMC composites with different weight fractions of GF are listed in Table 2. The flexural strength is increasing with GF content from 61 MPa for the sample with 5 wt%, reaching a maximum value of 82 MPa for the sample with 10 wt% of GF. However, with further increase in the fiber content the flexural strength decreases to 76 MPa, which could be related to increased contacts between the fibers that contribute to the less efficient stress transfer in the composite material. The value of standard deviation for the latter sample is the highest (± 7) indicating uneven load capacity. Even so, that the decrease in flexural strength from 82 to 76 MPa is within the experimental error, the deterioration of flexural strength and uneven load capacity can be a consequence of fiber clustering that is reflected in non-homogeneous fiber distribution. This is more pronounced in the composites with higher fiber contents, i.e. in the sample with 12.5 wt% of GF as confirmed by Voronoi analysis, cf. Figures 2, 3.

Table 2: Flexural strength and standard deviation of BMC composite samples.

	GF content [wt%]		
	5	10	12.5
σ_f [MPa]	61 ± 3	82 ± 5	76 ± 7

4 Conclusions

Voronoi diagram analysis was used to quantitatively characterize the microstructures of BMCs with different weight fractions of GF and to correlate the derived microstructural features with the flexural strength of the composites. According to the results of Voronoi analysis the fiber distribution in the sample with 5 wt% of GF most closely approximates to the values of the random distribution. With increasing the fiber content, the divergence from the random distribution is more pronounced, especially in the sample with 12.5 wt%, which indicates fiber clustering at higher fiber contents. Such non-homogeneity of the fiber distribution can then affect the mechanical performance of the composites. The flexural strength increases with increased fiber content, however, only to a certain level. The highest value was measured for the sample with 10 wt%. A suitable combination of properties, i.e. a high level of fiber distribution homogeneity and high flexural strength can be achieved by tailoring the glass fiber content in BMCs. Moreover, the microstructure in critical parts of complex shaped BMC products from serial production can be quantitatively analyzed with Voronoi diagrams to obtain information about the fiber distribution. In this way the microstructure can be related to the mechanical response of the material which may be useful if mechanical testing cannot be performed, for example due to a non-standard shape of a selected part.

Acknowledgements

B.B. gratefully acknowledges the financial support of the Ministry for education, science and sport of Republic of Slovenia and European Commission through the European Social Fund. B.M. and K.V. acknowledge the support of the Slovenian Research Agency (P2-0105).

References:

- [1] L. T. Harper, T. A. Turner, N. A. Warrior, J. S. Dahl, C. D. Rudd. Characterisation of random carbon fibre composites from a directed fibre preforming process: Analysis of microstructural parameters. *Composites Part A: Applied Science and manufacturing*, 37: 2136-2147, 2006.
- [2] V. S. Sreenivasan, D. Ravindran, V. Manikandan, R. Narayanasamy. Mechanical properties of randomly oriented short *Sansevieria cylindrica* fibre/polyester composites. *Materials and Design*, 32: 2444-2455, 2011.

- [3] M. J. G. W. Heijman, N. E. Benes, J. E. ten Elshof, H. Verweij. Quantitative analysis of the microstructural homogeneity of zirconia-toughened alumina composites. *Materials Research Bulletin*, 37:141-149, 2002.
- [4] G. Trefalt, A. Benčan, M. Kamplet, B. Malič, Y. Seo, K. G. Webber. Evaluation of the homogeneity in Pb(Zr,Ti)O₃-zirconia composites prepared by the hetero-agglomeration of precursors using the Voronoi-diagram approach. *Journal of the European Ceramic Society*, 34:669-675, 2014.
- [5] J. Summerscales, F. J. Guild, N. R. L. Pearce, P. M. Russell. Voronoi cells, fractal dimensions and fibre composites. *Journal of Microscopy*, 201:153-162, 2001.
- [6] Z. Sun, X. Zhao, J. Ma. Characterization of microstructures in sisal fiber composites by Voronoi diagram. *Journal of Reinforced Plastics & Composites*, 32:16-22, 2012.
- [7] Z. Samardžija, U. Kunaver, M. Čeh, S. Novak. Determination of ZrO₂ distribution in an Al₂O₃ matrix by digital image analysis and point pattern analysis. *Scanning* (17):186-191, 1995.
- [8] B. Bertoneclj, K. Vojisavljević, J. Rihtaršič, G. Trefalt, M. Huskić, E. Žagar, B. Malič. A Voronoi-diagram analysis of the microstructures in bulk-molding compounds and its correlation with the mechanical properties. *Express polymer letters* 10 (6): 493-505, 2016.
- [9] B. Bertoneclj, K. Vojisavljević, J. Rihtaršič, G. Jelenc, B. Malič. Characterization of glass fiber reinforced composites for housing of electrical motors. In A. Žemva (Ed.), P. Šorli (Ed.), I. Šorli, (Ed.). *Proceedings of the 49th MIDEM International Conference on Microelectronics, Devices and Materials*, Kranjska Gora, Slovenia, 2013.
- [10] ISO 3167: Plastics-Multipurpose test specimens. International Organization for Standardization. <https://www.iso.org>.
- [11] ISO 178:2003: Plastics. Determination of flexural properties. International Organization for Standardization. <https://www.iso.org>.

For wider interest

Bulk Molding Compounds (BMCs) are a combination of polymer matrix, glass fibers and CaCO_3 mineral filler. Each constituent is having its own role that contributes to the final properties. The latter are dependent on chemical and physical properties of individual constituents, their relative amounts and spatial orientation and distribution of fibers.

BMCs are a preferred replacement for metals, such as steel and aluminum, because of their properties such as high strength and stiffness in combination with low density, low thermal expansion, corrosion resistance, etc. Moreover, the manufacturing process (injection molding) is energy efficient. Because the product is made in one piece there is no need for additional operations, such as machining and drilling.

The main use of BMCs is in mass production of components and products in automotive, electro and electronic industry. In such products, the mechanical response, for example, flexural strength, is important, but is sometimes hard to measure due to the complexity of the shape. Therefore, the microstructural analysis, i.e. Voronoi diagram analysis, can be applied to critical parts of BMCs products to obtain an insight about the mechanical response and to identify the causes for products failure or poor quality.

Metal-free azidation of alcohols catalysed by molecular iodine

Klara Čebular^{1,2,3}, Monika Horvat¹, Stojan Stavber^{1,3}

¹ Department of Physical and Organic Chemistry, Jožef Stefan Institute, Ljubljana, Slovenia

² Jožef Stefan International Postgraduate School, Ljubljana, Slovenia

³ Centre of Excellence for Integrated Approaches in Chemistry and Biology of Proteins, Ljubljana, Slovenia

klara.cebular@ijs.si

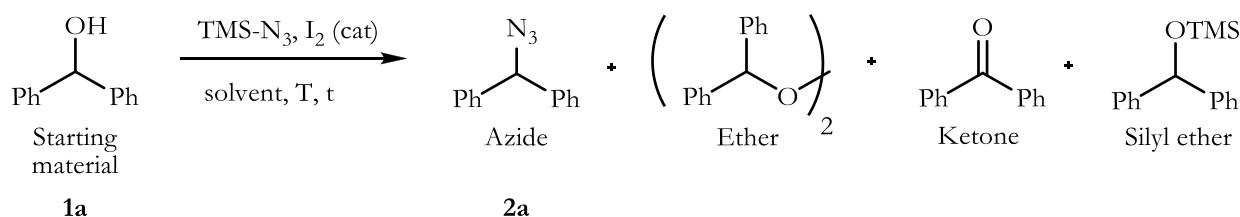
Abstract. In our continuous interest in greener chemical approach to transformations of organic compounds, we present a new metal- and solvent-free method for direct azidation of alcohols catalysed by iodine. Iodine was used in substoichiometric amounts as a Lewis acid promoter of nucleophilic substitution of hydroxyl group in alcohols and trimethylsilyl azide was used as the azide nucleophile donor for one-pot transformation of secondary benzylic alcohols to corresponding azidated products. Until now the method has proved efficient for transformation of secondary benzyl alcohols.

Keywords: azidation, azides, alcohols, solvent-free, metal-free, iodine, trimethylsilyl azide.

1 Introduction

Azides are useful compounds with significant application in organic synthesis in preparation of amines [1], nitrenes [2] and heterocyclic compounds, such as 1,2,3-triazoles. The latter are stable to reduction and oxidation as well as to hydrolysis in acidic and basic conditions due to their aromatic stabilization. Their structural and electronic properties are similar to those of a peptide bond, which makes them pharmaceutically interesting molecules in peptidomimetic research [3,4], especially since general methods for their synthesis are available. Cu or Ru catalysed azide alkyne cycloaddition (CuAAC or RuAAC) reactions are such general synthetic approaches, known as key examples of the Click Chemistry concept [5].

In most cases, classic nucleophilic substitution reaction is a commonly used method for preparation of alkyl azides and a typical reaction for direct transformation of alcohols to azides is the Mitsunobu reaction [6]. Although known methods for direct conversion of alcohols to azides are effective, they have several disadvantages, such as multi-step synthesis and prefunctionalisation with demanding manipulation, use of metal catalysts (e.g. Bi(III) [7], Cu(II) [8], In(III) [9], Fe(III) [10], ...), toxic solvents or expensive reagents.



^a Reaction conditions for solvent screening: Diphenylmethanol (1 mmol), TMS-N₃ (1 equiv), I₂ (10 mol%), no solvent, T = 70 °C, t = 4 h. ^b The yields were determined by ¹H NMR spectroscopy.

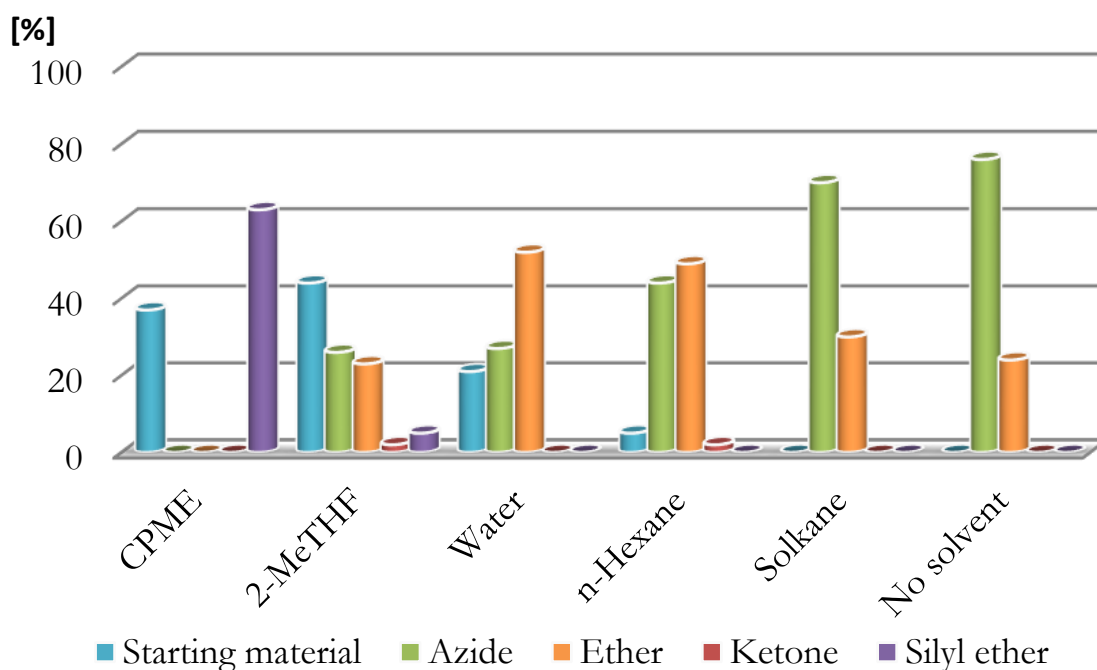
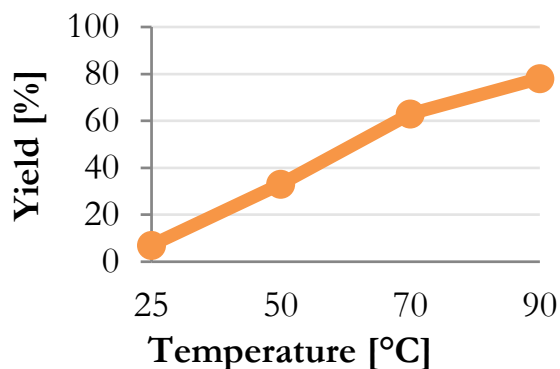
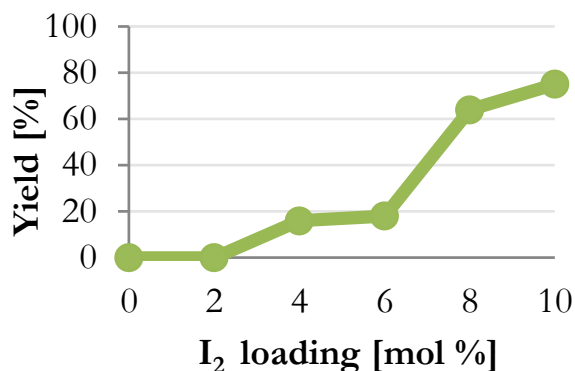


Figure 1 : Indication of possible products and effect of different solvents on distribution in the reaction mixture.

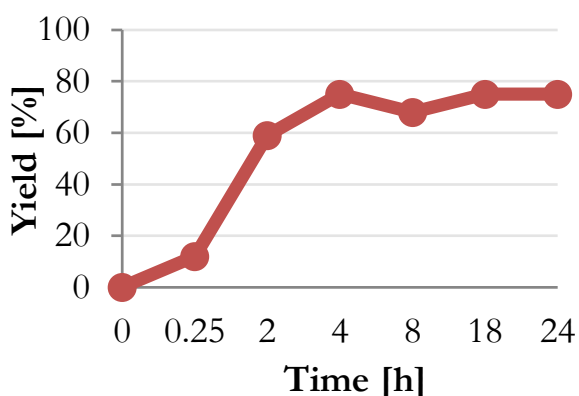
In our continuous interest in green chemical approach to transformations of organic compounds, here we present a new *one-pot metal- and solvent-free method for azidation of alcohols catalysed by iodine*. Iodine was used in substoichiometric amounts as a Lewis



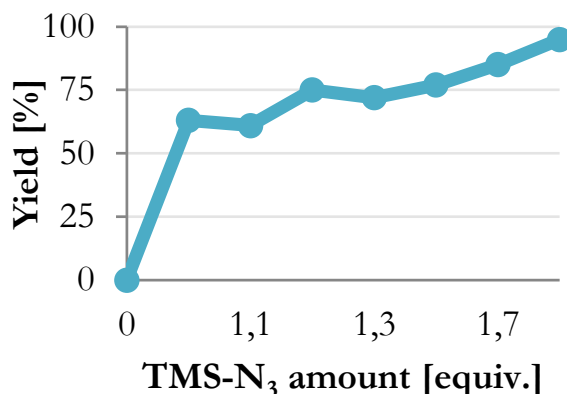
^a Reaction conditions: Diphenylmethanol (1 mmol), TMS-N₃ (1 equiv), I₂ (10 mol%), no solvent, T, t = 4 h.



^a Reaction conditions: Diphenylmethanol (1 mmol), TMS-N₃ (1 equiv), I₂, no solvent, T = 70 °C, t = 4 h.



^a Reaction conditions: Diphenylmethanol (1 mmol), TMS-N₃ (1 equiv), I₂ (10 mol%), no solvent, T = 70 °C, t.



^a Reaction conditions: Diphenylmethanol (1 mmol), TMS-N₃, I₂ (10 mol%), no solvent, T = 70 °C, t = 4 h.

^b All the yields were determined by ¹H NMR spectroscopy.

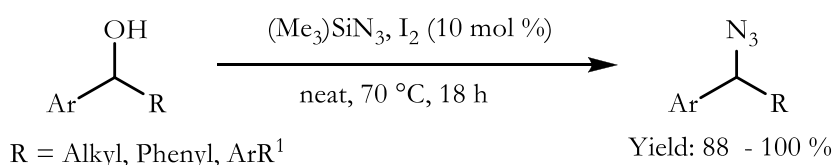
Figure 2 : The effect of temperature, time, amount of catalyst and amount of TMS-N₃ reagent on azide yield.

acid promoter of nucleophilic substitution of hydroxyl group in alcohols, resulting in formation of corresponding azides. Trimethylsilyl azide was used as the azide nucleophile donor for transformation of benzylic alcohols to corresponding azidated products. Silyl azides are valuable reagents in organic synthesis, since, unlike sodium

azide and hydrogen azide, they have no immediate explosive properties [11]. However, they hydrolyze in the long term to the volatile, toxic and explosive hydrogen azide and therefore must be stored in the absence of moisture and acids.

2 Results and discussion

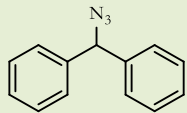
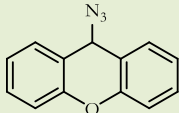
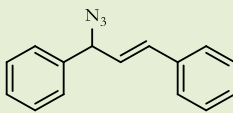
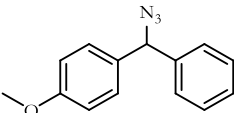
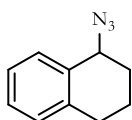
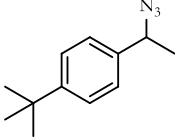
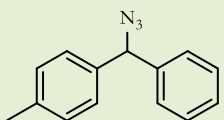
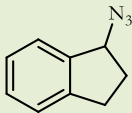
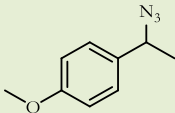
Initially, we have chosen the azidation of benzhydrol (**1a**) as a model reaction to optimise different reaction conditions, such as solvent screening, catalyst loading, amount of nucleophile, reaction temperature and time, as shown in Figure 2. It was found that among the solvents studied, the most selective and efficient conversion was achieved when no solvent was used (Figure 1), therefore further studies were carried out under neat reaction conditions. Furthermore, the effect of catalyst I₂ loading on the reaction yield was also examined.



Scheme 1 : The reaction system after optimisation of reaction conditions.

A significant increase in the yield was observed, when more than 6 mol% of iodine was used and the best result was obtained with 10 mol% of the catalyst. A quantitative conversion to **2a** was achieved under reaction conditions shown in Scheme 1.

Table 1 : Efficiency of the method applied to nine different alcohols.

Structures and yields [%] ^b of synthesized azides					
	100		88		100
	100		93		100
	100		100		95

^a Reaction conditions: Alcohol (1 mmol), TMS-N₃ (1.2–2 equiv), I₂ (10 mol%), no solvent, T = 70 °C, t = 18 h.^b The yields were determined by ¹H NMR spectroscopy.

After applying these conditions to other substrates, it was found that the method is most efficient on secondary benzyl alcohols. Since dimeric ether is formed during the reaction, the mechanism is assumed to proceed through carbocation intermediate, nevertheless, the exact course of the reaction is still under investigation. We have successfully applied the reaction system on nine different substrates so far, however, broader reaction scope is still being examined.

3 Conclusions

A new method for direct transformation of alcohols to azides under solvent-free reaction conditions was developed, using iodine as a cheap metal-free Lewis acid catalyst. The reaction is assumed to proceed through carbocation intermediate, however, the mechanism of reaction is still under investigation. Up till now the reaction system has proved to be efficient on secondary benzyl alcohols, nevertheless, broader reaction scope is still being examined.

Acknowledgments

The author (KČ) is greatly thankful to the Centre of Excellence for Integrated Approaches in Chemistry and Biology of Proteins, Jožef Stefan Institute and Slovenian Research Agency for their financial support.

References:

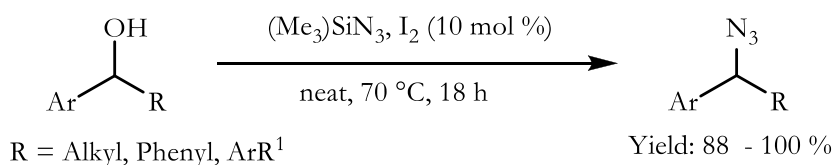
- [1] M. Köhn and R. Breinbauer. The Staudinger Ligation—A Gift to Chemical Biology. *Angewandte Chemie International Edition*, 43(24): 3106-3116, 2004.
- [2] A. Radomska and R. Drake. [20] Synthesis and uses of azido-substituted nucleoside diphosphate sugar photoaffinity analogs. *Methods in Enzymology*, 230: 330-339, 1994.
- [3] D. S. Pedersen and A. Abell. 1,2,3-Triazoles in Peptidomimetic Chemistry. *European Journal of Organic Chemistry*, 2011(13): 2399-2411, 2011.
- [4] S. Haider, M. S. Alam and H. Hamid. 1,2,3-Triazoles: Scaffold With Medicinal Significance. *Inflammation and Cell Signaling*, 1(2): 1-10, 2014.
- [5] H. C. Kolb, M. G. Finn and K. B. Sharpless. Click Chemistry: Diverse Chemical Function from a Few Good Reactions. *Angewandte Chemie International Edition*, 40(11): 2004-2021, 2001.

- [6] S. Bräse, C. Gil, K. Knepper and V. Zimmermann. Organic Azides: An Exploding Diversity of a Unique Class of Compounds. *Angewandte Chemie International Edition*, 44(33): 5188-5240, 2005.
- [7] J. Tummatorn, C. Thongsornkleeb, S. Ruchirawat, P. Thongaram and B. Kaewmee. Convenient and Direct Azidation of sec-Benzyl Alcohols by Trimethylsilyl Azide with Bismuth(III) Triflate Catalyst. *Synthesis*, 47(03): 323-329, 2015.
- [8] P. Khedar, K. Pericherla and A. Kumar. Copper Triflate: An Efficient Catalyst for Direct Conversion of Secondary Alcohols into Azides. *Synlett*, 25(04): 515-518, 2014.
- [9] A. Kumar, R. K. Sharma, T. V. Singh and P. Venugopalan. Indium(III) bromide catalyzed direct azidation of α -hydroxyketones using TMSN₃. *Tetrahedron*, 69(50): 10724-10732, 2013.
- [10] L. Y. Chan, S. Kim, W. T. Chung, C. Long and S. Kim. Fe(OTf)₃-Catalyzed Reaction of Benzylic Acetates with Organosilicon Compounds. *Synlett*, 2011(03): 415-419, 2011.
- [11] W. C. Groutas and D. Felker. Synthetic Applications of Cyanotrimethylsilane, Iodotrimethylsilane, Azidotrimethylsilane, and Methylthiotrimethylsilane. *Synthesis*, 1980(11): 861-868, 1980.

For wider interest

Since the preparation of the first organic azide, phenyl azide, by Peter Griess in 1864, these energy-rich and flexible intermediates have enjoyed considerable interest. They have assumed an important position at the interface between chemistry, biology, medicine, and materials science. Industrial interest in organic azide compounds began with the use of azides for the synthesis of heterocycles such as triazoles and tetrazoles as well as with their use as blowing agents and as functional groups in pharmaceuticals. In more recent times in particular, completely new perspectives have been developed for their use in peptide chemistry, combinatorial chemistry, and heterocyclic synthesis. Thus, for example, azidonucleosides attract international interest in the treatment of AIDS.

Alcohols are cheap and readily available chemical resources. From economical and green-chemical point of view their direct efficient transformation to other useful synthons without the need for prefunctionalisation is a desired pathway, by which additional synthetic steps as well as additional solvent and reagent consumption can be avoided. Accordingly, a new method for direct transformation of alcohols to azides under solvent-free reaction conditions was developed, using iodine as a cheap metal-free catalyst. Untill now the reaction system has proved to be efficient on secondary benzyl alcohols, nevertheless, broader reaction scope is still being examined.



Building composites from fly ash, cement and electric arc furnace dust: Environmental impacts

Ana Drinčić^{1,2}, Irena Nikolić³, Tea Zuliani¹, Radmila Milačić^{1,2}, Janez Ščančar^{1,2}

¹Department of Environmental Sciences, Jožef Stefan Institute, Ljubljana, Slovenia

²Jožef Stefan International Postgraduate School, Ljubljana, Slovenia

³University of Montenegro, Faculty of Metallurgy and Technology, Podgorica, Montenegro

ana.drincic@ijs.si

Abstract. The potential use of recycled building materials composed in 99% from a mixture of fly ash (80%) and cement (20%) and addition of 1% of electric arc furnace (EAF) dust, was investigated regarding the environmental impacts. For this purpose, the leachability test was performed using synthetic sea water and synthetic surface water as leaching solutions. To study the diffusion and dissolution of contaminants, leaching solutions were not replenished. Total element concentrations were determined in leachates over a time period of 16 days. The results revealed that Cr, Mo, V and As, which are predominantly present in the form of oxoanions, are at high pH of the leachate (pH 12), released in greater amounts from building materials, while the other elements remained below, or were close to their limits of detection of ICP-MS. It was experimentally found that chemical composition of the leaching solution influenced the release of matrix constituents from the building composites and consequently governed the extent of leaching of selected elements. The concentrations of toxic Cr, Mo, and As arose mainly from EAF dust, while V was leached from EAF dust, fly ash and cement. To prevent harmful effects to the environment and living organisms, the use of EAF dust, which was incorporated to the building material investigated, should be omitted.

Keywords: Building materials, fly ash, cement, electric arc furnace dust, leachability test, synthetic surface water, synthetic sea water

1 Introduction

In the last decades industrial by-products and waste materials, which are widely used in civil engineering, are being exploited as alternative materials that successfully substitute natural raw materials. Utilization of different industrial by-products and waste materials leads to preservation of natural resources [1] and substantially decreases landfills load [2]. The use of materials originating from wastes and industrial by-products is possible only, when such materials possess appropriate technical qualities and are environmentally acceptable. Their incorporation into building materials can even improve the quality of products [3-8]. Materials which contain different industrial wastes should fulfil the requirements on hygiene, health and the environmental aspects, set by Construction Product Declaration [9]. To prevent potential environmental hazard, it is necessary to estimate the extent of contaminants release from the final products during their service life [10]. The amount of substances that can be leached from building composites containing waste by-products is estimated by applying various leaching tests. In order to evaluate leaching characteristics of solid earthy and stony building and waste materials, the Dutch leaching test NEN 7375, which is based on diffusion was developed [11]. At the particular time specified leaching solution is replenished in to estimate the diffusion of inorganic components from composites investigated. Later, modified NEN 7375 test was applied to assess the long-term environmental impacts regarding leaching of elements and Cr(VI) from cement composites with the addition of electric arc furnace (EAF) dust [12] or ladle slag [13] and asphalt mixes with the addition of EAF dust [14] or EAF steel slag [8]. In the modified NEN 7375 test [8, 12, 13, 14] composites were immersed into MilliQ and salt water. In order to simulate the diffusion and dissolution of contaminants, the leaching solutions were not replenished.

In the present work modified NEN 7375 test was used to assess the long-term environmental impact of building composites composed in 99% of the mixture of flay ash (80%) and cement (20%), and in remaining 1% of EAF dust. For this purpose, total concentrations of elements in leachates were determined by ICP-MS.

2 Methods and materials

2.1 Instrumentation

Total element concentrations in leachates were determined by ICP-MS on an Agilent (Tokyo, Japan) 7700× instrument under optimal measurement conditions. A CEM Corporation (Matthews, NC, USA) CEM MARS 5 Microwave Acceleration Reaction System was used for the digestion of fly ash, cement and EAF dust samples.

2.2 Reagents and materials

Merck (Darmstadt, Germany) suprapur acids and MilliQ water (Direct-Q 5 Ultrapure water system, Millipore Water town, MA, USA) were used for the preparation of samples and standard solutions. NaOH and Na₂CO₃ (Merck) were used to prepare alkaline buffer solutions (pH 12). Stock standard solutions of metals (1000 ± 2 mg/L in 5% HNO₃) were also obtained from Merck. Leachates were filtered through 0.45 μm Minisart membrane filters (Sartorius Stedim Biotech GmbH, Göttingen, Germany). The certified reference materials CRM 320 Trace Elements in River Sediment, Community Bureau of Reference (Geel, Belgium) and SLRS-5, River water reference material purchased from the National Research Council (Ottawa, Ontario, Canada), were used to check the accuracy of the analytical procedures. For the preparation of building composites, the fly ash and electric arc furnace dust were supplied by the coal-fired power station “Pljevlja” and the steel-mill “Nikšić” in Montenegro. Portland cement CEM II/B-M(S-LL) 42.5 N was used.

2.3 Experimental design

In the present study, building composites made of 99% from fly ash (80%) and cement (20%) and remaining 1% of EAF dust, were used. Compact composites casts were cylinders 7 cm in height and of 5 cm in diameter, with a volume of approximately 0.137 L. To assess the long-term environmental impacts of building composites, the modified NEN 7375 leachability test, which is based on diffusion and dissolution of contaminants, was applied. As leaching solution synthetic sea water composed of 3.8 % NaCl, MgCl (1500 mg/L Mg), CaCl₂ (600 mg/L Ca) and KCl (420 mg/L K) and synthetic surface water composed of CaCO₃ (5 mg/L Ca) and MgCO₃ (1 mg/L Mg) were used. The experiments were carried out in 1 L polyethylene flasks. The volume

ratio of the tested composites to the added leaching solution was 1:5, as set by the NEN 7375 test. Blank samples of alkaline leaching solutions (buffer with pH 12) were analysed along with the samples investigated. Prior to each sampling, the solution was mixed with a glass rod. 0.7 mL of the sample was taken and filtered. After each sampling (0.25, 1, 1.5, 7, 9 and 16 days), the same amount of leaching solution as taken, was added. In each leachate sample, the pH was also measured. The total element concentrations were determined in 10-times diluted samples by ICP-MS. All the experiments were carried out in triplicate.

2.4 Quality control of the analytical data

The accuracy of the determination of total element concentrations in fly ash, cement and EAF dust was checked by the analysis of certified sediment reference material CRM 320 and of total element concentrations in the leachates, by the analysis of the SLRS-5 river water reference material. The determined concentrations agreed well with the reported certified values (agreement better than $\pm 5\%$).

3 Results and discussion

3.1 Total concentrations of selected elements in fly ash, cement and EAF dust

Total element concentrations of selected elements in fly ash, cement and EAF dust determined by ICP-MS are presented in Table 1. The concentrations of the elements in fly ash and EAF dust are comparable to those previously reported by Nikolić et al. [5], while the content of the elements in Portland cement CEM I 52.5R is similar to that reported by Zalar Serjun et al. [13]. Since EAF dust and fly ash are by-products of the steel-making industry and thermal power plants, they contain elevated concentrations of selected elements. The major components of EAF dust represent Zn (around 250 g kg⁻¹) and Fe (around 210 g kg⁻¹). The other components like Pb and Cr are present in moderate concentrations, while the content of As, Mo and V is appreciably lower. With exception of V the concentrations of these elements in fly ash and cement were substantially lower.

3.2 Leachability of selected elements

The data on the leachability of selected elements in the building composite investigated showed that during the course of the experiment the concentrations of Ba, Fe, Mn, Co, Ni, Cu, Zn, Cd, Sb, Hg and Pb in all samples investigated remained in general, below the limits of detection of ICP-MS (Table 2). The pH of leachates was during the course of the experiment rather constant, around 12. The high pH of leachates arose from solubilisation of Ca(OH)_2 and CaCO_3 from building composites. At highly alkaline pH's the majority of the elements were precipitated and effectively immobilized in the lattice of aluminosilicate geopolymers [4-6]. Therefore, the leaching of these elements did not represent environmental hazard.

Table 1: Total element concentrations in fly ash, cement and EAF dust determined by ICP-MS after microwave assisted digestion (RSD of measurement below $\pm 2\%$).

Element	Fly ash (mg/kg)	Cement (mg/kg)	EAF dust (mg/kg)
As	30.0	15.0	178
Se	4.95	2.50	9.0
Ba	630	420	680
Fe	37000	14800	213450
Mn	278	750	18555
Co	27.0	15.0	30.0
Ni	150	90	385
Cu	90	135	3510
Zn	26.0	120	293330
Cd	65.4	74.5	980
Sb	2.65	2.45	302
Hg	<15	<15	<15
Pb	52.7	110	31860
Cr	160	91	4170
Mo	3.32	22.4	64.6
V	180	107	69.2

Table 2: The concentration ranges of the elements in the synthetic surface and synthetic sea water leachates from compact composites during the course of the experiment. The concentrations of the elements were determined by ICP- MS.

Element	Concentration ranges of elements in synthetic sea water ($\mu\text{g/L}$)	Concentration ranges of elements in synthetic surface water ($\mu\text{g/L}$)
Ba	<0.3 – 12	0.6 – 1
Fe	<0.6 – <0.2	4 – 6
Mn	<0.02 – <0.6	<0.6 – 0.2
Co	0.02 – <1	0.07 – <1
Ni	0.2 – 1	<0.8 – 0.1
Cu	<0.9 – 11	<0.9 – 3
Zn	<0.2 – <0.6	<0.6 – 4
Se	6 – 40	14 – 99
Cd	<0.8 – 0.2	<0.8 – 0.2
Sb	<0.7 – 3	2 – 9
Hg	<0.04 – 0.2	<0.04 – 0.2
Pb	<0.7 – 0.2	<0.7 – 0.6

On the other hand, Cr, Mo, V and As, which are at highly alkaline pHs present mainly in the form of oxoanions (as highly soluble chromates, molybdates, vanadates and arsenates), were leached in greater amounts from building composites (Figure 1).

As evident from data of Figure 1, the leachability of Cr was during the course of the experiment higher in synthetic surface, than in sea water. This phenomenon is related to precipitation of MgCl_2 from synthetic sea water under highly alkaline pHs (pH 12) of the leachate, and co-precipitation of soluble Cr(III). Since the release of soluble Cr(III) from composite is inhibited, its oxidation to Cr(VI) is also hindered. In addition, Friedel's salt is formed by the hydration of cement from building composite. It is a double-layered hydroxide and good adsorbent for the immobilization of Cr(VI) [15]. Data from Figure 1 further indicate that the concentrations of Cr were gradually increased until the ninth day, and then tend to decrease. The maximal amount of Cr (445 $\mu\text{g/L}$) leached from compact building composite into synthetic surface water may potentially represent the environmental hazard. Namely, at high pH the leached Cr is most probably present predominantly in its hexavalent form. From data of Table 1 it may be concluded, that leaching of Cr from building composite investigated, arises mainly from EAF dust.

Similar behaviour as for Cr, was observed for leaching of Mo in synthetic sea water (Figure 1). The extent of leaching was slightly higher than that of Cr. After nine days, the maximal concentration of Mo leached was 400 µg/L. In synthetic surface water Mo leachability was gradually increased with time, and during the course of the experiment showed no tendency to equilibrate. After sixteen days, the concentration of Mo leached from synthetic surface water was similar to that determined after nine days of leaching in sea water. From data of Table 1 it is evident, that the leachability of Mo originates mainly from EAF dust.

Different behaviour than for Cr and Mo is observed for V (Figure 1). Its concentrations in synthetic sea and surface water leachates are equilibrated already nine days after experiments starts. It can be seen that V leachability is considerably higher than that of Cr and Mo. The extent of leaching is significantly higher in synthetic surface water (maximal concentration 7100 µg/L of V) than in sea water (maximal concentration 1250 µg/L of V). It may be presumed that at high pH of the leachates and by the presence of the dissolved oxygen V is oxidised to its pentavalent oxidation state. Oxoanions (vanadates) are highly soluble under alkaline conditions. The lower V solubility in synthetic sea than in surface water is related to co-precipitation of vanadates with MgCl₂. The leaching of V from the building composite examined came from the EAF dust, cement, and fly ash (Table 1). Due to the large extent of leaching of V, this building composite is not environmentally acceptable.

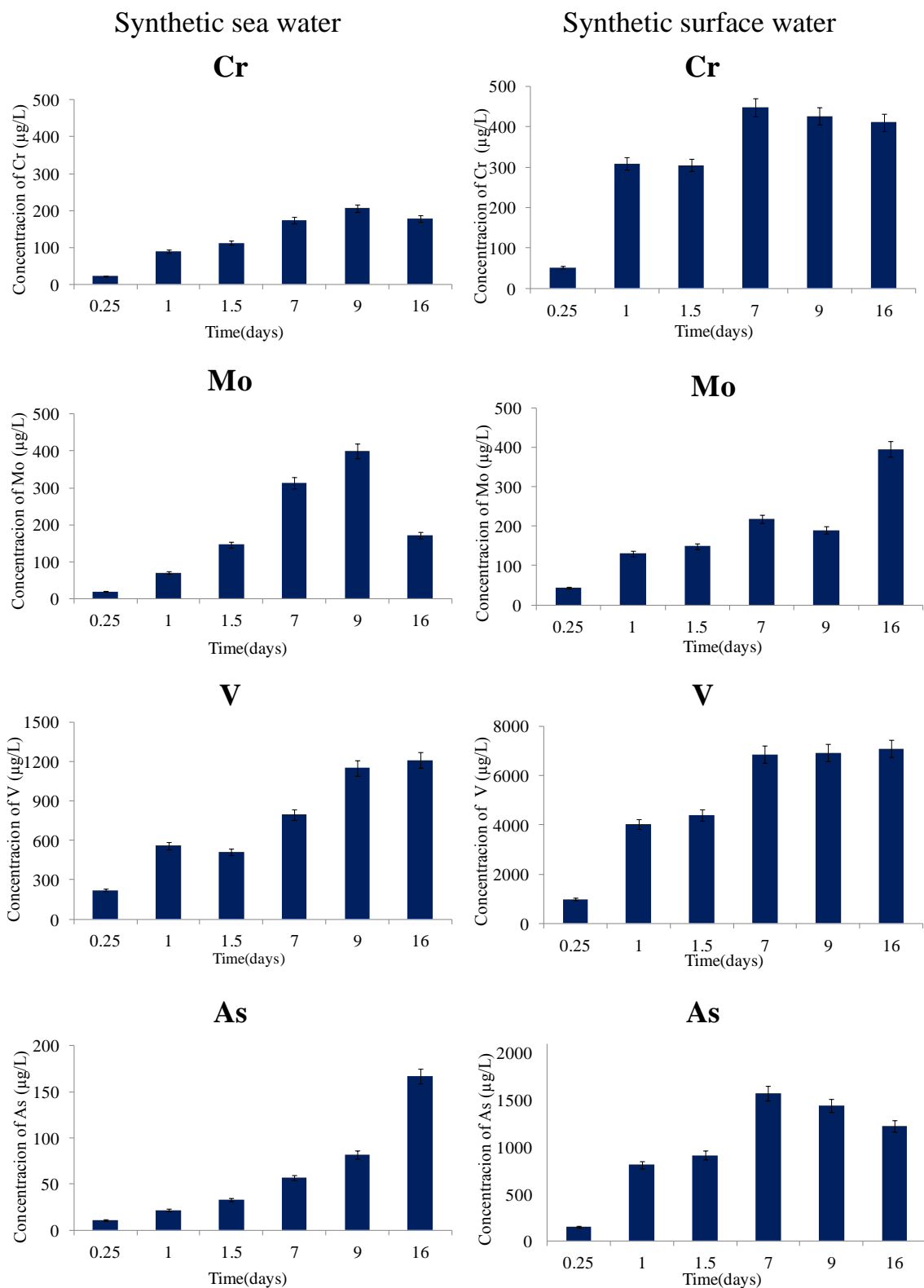


Figure 1: Leachability of Cr, Mo, V and As over time from compact composite (99% mixture of fly ash (80%) and cement (20%) with addition of 1% of EAF dust.

In synthetic sea water As is leached in similar concentrations as Cr, but its concentration was not equilibrated during the course of the experiment. On the contrary, in synthetic surface water As concentration was increased till seventh day and then indicated tendency of gradual decrease with time. However, the maximal leached concentration in synthetic surface water was appreciably high (1570 µg/L of As). Therefore, the release of As from the composite investigated is of environmental concern. Based on the data from Table 1 it may be concluded that leachability of As originated mainly from EAF dust.

4 Conclusions

The environmental impacts of building material prepared in 99% from a mixture of fly ash (80%) and cement (20%) and in remaining 1 % from EAF dust were investigated by the use of modified NEN 7375 test. In the applied leachability test synthetic sea and synthetic surface water were used as leaching solutions, which were not replenished during the course of the experiment (16 days). This enabled to follow the diffusion and dissolution of contaminants. The data demonstrated that leaching of Ba, Fe, Mn, Co, Ni, Cu, Zn, Cd, Sb, Hg and Pb from building composite was negligible in synthetic sea and surface water, since these elements were precipitated under highly alkaline conditions of the leachates. The high pH (pH 12) of the leachates arose from the Ca(OH)_2 and CaCO_3 , which were released from the building composite with the synthetic surface and sea water. On the contrary, Cr, Mo, V and As that were present predominantly in the form of highly soluble oxoanions, were leached from building composite with synthetic sea and surface water in high concentrations, which were not environmentally acceptable. The data revealed, that leachability of Cr, Mo and As from the building composite investigated arose mainly from EAF dust, while of V from EAF dust, cement and fly ash. It can be concluded, that the use of EAF dust, which was incorporated as additive to composites from fly ash and cement, should be omitted.

References:

- [1] B. Nadjoua, H. Hacene. Waste and by-products recycled for concrete. *International Journal of Scientific & Technology Research*, 2:190-196, 2013.

- [2] R. Siddique. Utilization of cement kiln dust (CKD) in cement mortar and concrete - an overview. *Resources, Conservation and Recycling*, 48:315-338, 2006.
- [3] R. Siddique. Performance characteristics of high-volume Class F fly ash concrete. *Cement and Concrete Research*, 34: 487-493, 2004.
- [4] I. Nikolić, R. Zejak, I. Janković-Častan, Lj. Karanović, V. Radmilović, V.R. Radmilović. Influence of alkali cation on the mechanical properties and durability of fly ash based geopolymers. *Acta Chimica Slovenica*, 60:636–643, 2013.
- [5] I. Nikolić, D. Đurović, D. Blečić, R. Zejak, Lj. Karanović, S. Mitsche, V.R. Radmilović. Geopolymerization of coal fly ash in the presence of electric arc furnace dust. *Minerals Engineering*, 49:24–32, 2013.
- [6] I. Nikolić, D. Đurović, R. Zejak, Lj. Karanović, M. Tadić, D. Blečić, V.R. Radmilović. Compressive strength and hydrolytic stability of fly ash-based geopolymers. *Journal of the Serbian Chemical Society*, 78:851–863, 2013.
- [7] R. Zejak, I. Nikolić, D. Blečić, V. Radmilović, V.R. Radmilović. Mechanical and microstructural properties of the fly-ash-based geopolymer paste and mortar. *Materials Technology*, 47:535–540, 2013.
- [8] R. Milačić, T. Zuliani, T. Oblak, A. Mladenović, J. Ščančar. Environmental impacts of asphalt mixes with electric arc furnace steel slag. *Journal of Environmental Quality*, 40:1153-1161, 2011.
- [9] Official Journal of the European Union. Regulation (EU) No. 305/2011 of the European parliament and of the council laying down harmonised conditions for the marketing of construction products and repealing Council Directive 89/106/EEC, 88:5-43, 2011.
- [10] P. Chaurand, J. Rose, V. Briois, I. Olivi, J-L. Hazemann, O. Proux, J. Domas, J-Y. Bottero. Environmental impacts of steel slag reused in road construction: A chrystallographic and molecular (XANES) approach. *Journal of Hazardous Materials*, 139:537-542, 2007.
- [11] NEN 7375, Leaching characteristics of moduled or monolithic building and waste materials. Determination of inorganic components with the diffusion test. “*The rank test*”, (2004).
- [12] T. Šturm, R. Milačić, S. Murko, M. Vahčić, A. Mladenović, J. Strupi Šuput, J. Ščančar. The use of EAF dust in cement composites: Assessment of environmental impact. *Journal of Hazardous Materials*, 166:277-283, 2009.
- [13] V. Zalar Serjun, A. Mladenović, B. Mirtič, A. Meden, J. Ščančar, R. Milačić. Recycling of ladle slag in cement composites: Environmental impacts. *Waste Management*, 43:376–385, 2015.
- [14] M. Vahčić, R. Milačić, A. Mladenović, S. Murko, T. Zuliani, M. Zupančič, J. Ščančar. Leachability of Cr(VI) and other metals from asphalt composites with addition of filter dust. *Waste Management*, 28:2667-2674, 2008.
- [15] Y. Dai, G. Quian, Y. Cao, Y. Chi, Y. Xu, J. Zhou, Q. Liu, Z.P. Xu, S.Z. Qia,. Effective removal and fixation of Cr(VI) from aqueous solution with Friedel’s salt. *Journal of Hazardous Materials*, 170:1086-1092, 2009.

For wider interest

Industrial waste materials may be re-used as substitute for natural raw materials in different building composites, if the final products possess appropriate mechanical properties and are environmentally acceptable. The main environmental impacts of building materials that contain waste by-products are estimated by applying different leachability tests. In the present study, the modified NEN 7375 test was applied for the evaluation of the long-term environmental impacts of the building composite, prepared in 99% from fly ash (80%) and cement (20%) and in the remaining 1% from EAF dust. Leachability of selected elements was followed in different time intervals over a period of sixteen days, using synthetic surface and synthetic sea water as leaching solutions. During the course of the experiment the leaching solutions were not replenished, enabling to follow diffusion and dissolution of contaminants. The data of the present investigation revealed, that leaching of Cr, Mo, V and As from the building composite investigated represent a limiting factor for its use due to negative environmental impacts.

HPGe gamma detector effective solid angle calculation

Lojze Gačnik^{1,2}, Radojko Jaćimović^{1,2}

¹Department of Environmental Sciences, Jožef Stefan Institute, Ljubljana, Slovenia

²Jožef Stefan International Postgraduate School, Ljubljana, Slovenia

lojze.gacnik@ijs.si

Abstract. For the purposes of the k_0 -standardization method, we calibrate high-purity Germanium (HPGe) gamma detectors, using reference point gamma sources with absolutely known activities. Because sample sources have geometries different to those of the reference sources, we calculate the effective solid angle the detector presents to the source, which is used by the efficiency transfer method to translate the efficiency from the reference source geometry to the sample source geometry. Our contribution is to take into account the inhomogeneous activation of the sample when calculating the effective solid angle, eliminating this source of systematic error. As side effect of our implementation of solid angle computation, we are able to apply our method to a wide variety of source and sample geometries.

Keywords: k_0 -standardization method, HPGe calibration, efficiency transfer method

1 Introduction

k_0 instrumental neutron activation analysis (k_0 -INAA) is a powerful multi-elemental analytical method, based on irradiating a sample with neutrons, and measuring the gamma spectrum of the resulting radioactive products. The high penetrability of neutrons and gamma rays in matter makes k_0 -INAA almost, but not completely, matrix insensitive. It is also based on strong theoretical foundations, and all of its sources of systematic and random error are quantifiable down to the limits of detection. When performed properly, it is able to determine multiple elements simultaneously, at combined standard uncertainties reaching 3.5% or better [1].

We present an improvement to k_0 -INAA by considering the effect of inhomogeneous sample activation, thus eliminating this source of systematic error [2].

2 k_0 instrumental neutron activation analysis

k_0 -INAA consists of irradiating a sample together with a monitor, usually an Al-Au alloy, in a nuclear reactor. The resulting radioactive sample and monitor are separately measured on an HPGe gamma detector, and the elemental mass fractions ρ are calculated using the ratio of activities between the sample and monitor:

$$\rho_a = \left(\frac{N_p / t_m}{SDCW} \right)_a \cdot \frac{1}{A_{sp,m}} \cdot \frac{k_{0,c}(m)}{k_{0,c}(a)} \cdot \frac{G_{th,m}f + G_{e,m}Q_{0,m}(\alpha)}{G_{th,a}f + G_{e,a}Q_{0,a}(\alpha)} \cdot \frac{\varepsilon_{p,m}}{\varepsilon_{p,a}} \quad (1)$$

where:

- a signifies the analyte – the element to be determined
- m signifies the monitor
- N_p is the number of counts in the full-energy peak area
- t_m is the measurement time
- S is the saturation factor, which accounts for the balance between activation and decay rates during irradiation
- D is the decay factor, and corrects for the decay of the measured radionuclide between the end of irradiation and start of measurement
- C is the measurement factor, accounting for the decay during the measurement
- W is the mass of the entire sample
- $A_{sp} = \frac{N_p / t_m}{SDCW}$ is the specific count rate of a single gamma peak, with W

being the mass of the element the gamma peak corresponds to

- $k_{0,c}(x)$ are the k_0 constants, published in literature, with c and x referring to elements. We usually select the monitor so that $m = c$, and therefore $k_{0,m}(m) \equiv 1$
- G_{th} and G_e are the thermal and epithermal neutron self-shielding correction factors, respectively
- f and α describe the reactor neutron flux distribution
- $Q(\alpha)$ describes the nuclear neutron cross-section in relation to the neutron flux distribution
- ε_p is the detector full-energy peak efficiency

Additionally, N_p must be corrected for true coincidence effects – when two or more gamma rays are emitted in a rapid cascade, and are both absorbed in the detector, the detector will see them as a single ray, and register the sum of their energies. This will place the energy outside the gamma peak, reducing its size. This is known as coincidence loss. Coincidence summing occurs when the sum of energies of gamma rays emitted in a cascade is equal to a different gamma peak, thus inflating it. Because the likelihood of any coincidence occurring is proportional to the absolute efficiency of the detector in order to calculate the coincidence correction factor, merely knowing the efficiency ratios, as they appear in equation (1), is insufficient - we need the absolute efficiency as well [1].

3 Reference sources

HPGe gamma detectors are calibrated using point reference sources – sources of very small dimensions compared to the detector, and with known absolute activities. Measuring them lets us determine the detector total and peak efficiency at different counting positions. We measure all sources at the furthest, reference position, which is chosen such that coincidence effects may be ignored, and measure only coincidence-free sources at nearer positions. As the selection of coincidence-free reference sources is limited, this results in many calibration points at the furthest position, and fewer at all others, as shown in Figure 1. The sources used were ^{241}Am , ^{133}Ba , ^{109}Cd , ^{57}Co , ^{60}Co , ^{137}Cs , ^{152}Eu , ^{203}Hg , ^{54}Mn , ^{226}Ra , and ^{65}Zn . Their

standardization dates ranged between 1988 and 2014, and their activities at time of standardization ranged between 20080 and 236000 Bq. They were produced by the Czech Metrology Institute, the Metrology Laboratory of Ionizing Radiation (France), and the German National Metrology Institute.

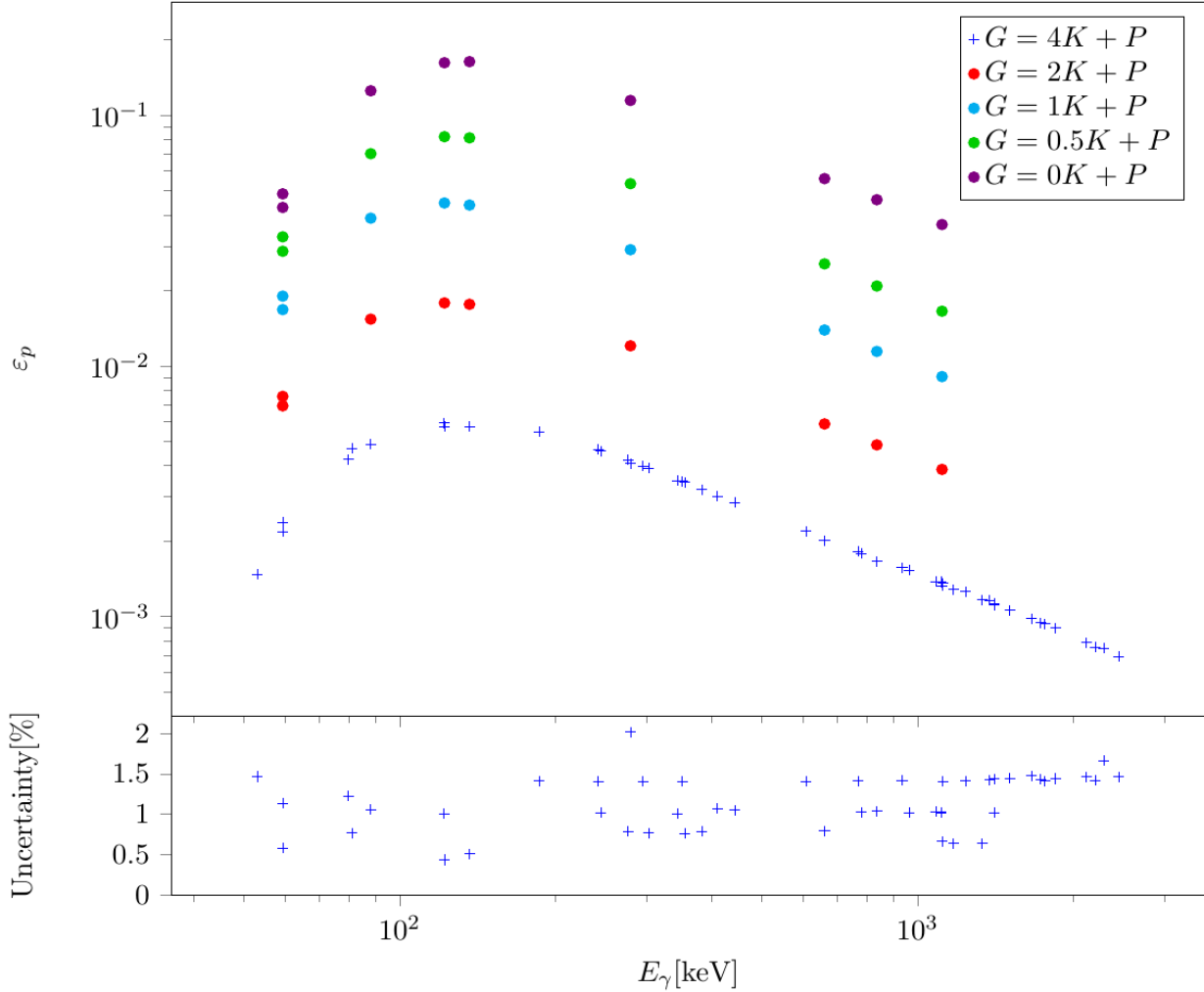


Figure 1: Peak efficiency determined at different counting positions (marked by G , for geometry). Uncertainties are given as combined standard uncertainties. In the expression $G = nK + P$, n marks the number of 4 cm high cylinders K .

4 Efficiency transfer

To determine the detector efficiency at more energies at closer counting positions, as well as for different source geometries, we use the *efficiency transfer method*. It is based on the relation

$$\varepsilon_p^{geo} = \varepsilon_p^{ref} \cdot \frac{\overline{\Omega}^{geo}}{\overline{\Omega}^{ref}} \quad (2)$$

where $\overline{\Omega}$ is the effective solid angle, and is proportional to the likelihood of a gamma ray interacting incoherently with the active detector volume, *ref* signifies a point source at the reference position, and *geo* signifies the sample [1].

5 Effective solid angle calculation

Knowing the source and detector geometry, we can calculate $\overline{\Omega}$ as

$$\overline{\Omega} = \iint_{source, detector} F_{eff} F_{att} d\Omega \quad (3)$$

where F_{eff} is the probability for a photon with energy E_γ , emitted in the direction $d\Omega$, to interact incoherently with the active detector material, and F_{att} accounts for gamma attenuation caused by incoherent interaction in the materials between source and detector – including the source itself. [1]

Equation (3) assumes the activity in the source is homogeneously distributed, but this is rarely the case, because the neutron flux in the reactor, where samples are irradiated, varies with position [4]. So far, when performing k_0 -INAA, we sandwiched each sample between two Al-0.1% Au alloy foil monitors, and assumed the sample felt the average flux that the monitors felt, throughout its entire volume, activating it homogeneously.

To improve the accuracy of $\overline{\Omega}$ calculation, we take into account the inhomogeneous activation of the sample, assuming that the flux, and therefore the activation of the sample, varies linearly between the two monitor foils. Weighing the integral of equation (3) proportionally to the activation yields a more accurate estimate of $\overline{\Omega}$.

We used Monte-Carlo integration to arrive at $\overline{\Omega}$, with source and detector geometry defined using constructive solid geometry. As a side effect, this allows us to apply the method to an almost arbitrarily large range of geometries, including ones without cylindrical symmetry, which is otherwise a common limitation.

6 Experimental setup

Until now, we were unable to calculate the solid angle of a wire lying flat on the detector platform, and were forced to approximate it with a centered upright cylinder. To evaluate the error we made this way, we used a 0.1 mm high upright cylindrical sample with a 0.5 cm radius, and a 1 cm long wire with a 0.5 mm radius, lying horizontally - both with the same volume, composition, and center of mass. We ran the wire calculation twice – once for a homogeneously activated wire, and once where the activity ratio between the ends of the wire was 0.5, changing linearly between those two points. The sample-detector distances are all typical for routine k_0 -INAA work, while the activation inhomogeneity is exaggerated – a typical value for a 1 cm long sample is 0.95.

7 Results

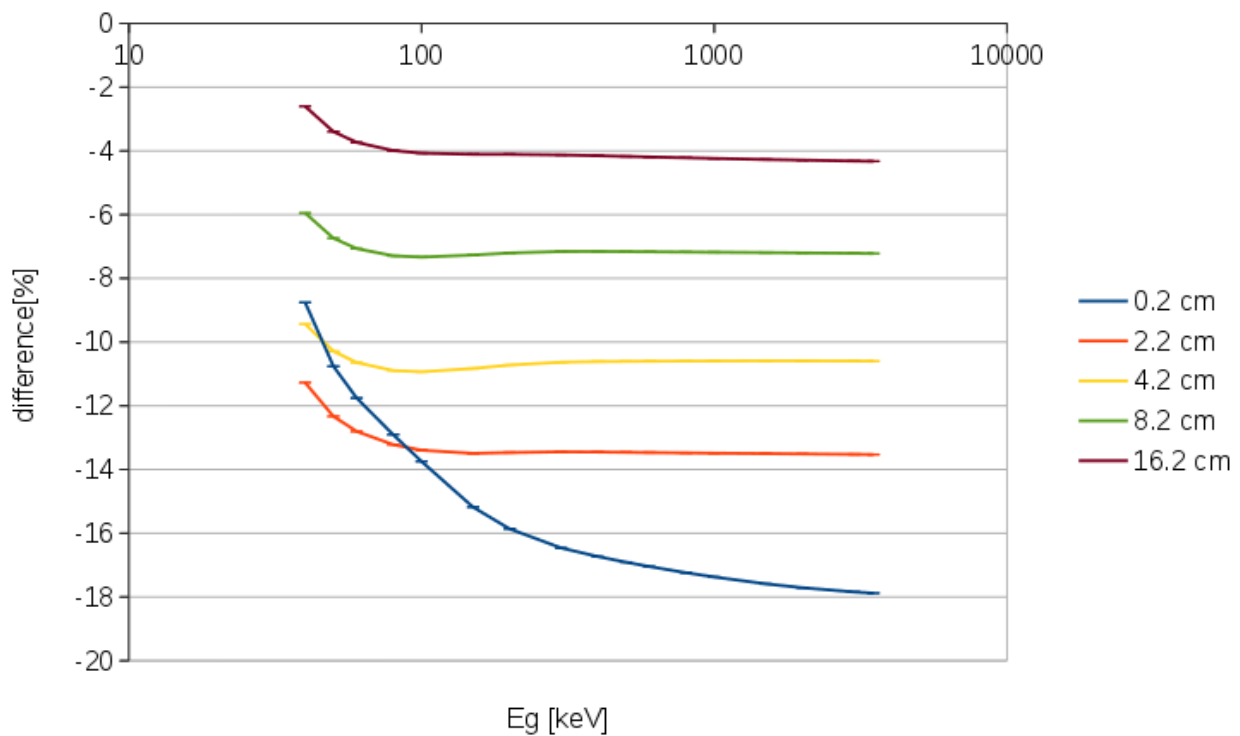


Figure 2: Solid angle difference of a horizontal wire versus a short, upright cylinder.

E_g stands for gamma energy, and the legend signifies sample-detector distance.

It can be seen from Figure 2, that the difference between an upright short cylinder and horizontal wire is very large. On the other hand, the effect of inhomogeneity is, in this case, very small – calculations yielded an upper limit of 0.01 %.

8 Conclusions

Despite inhomogeneity being a small correction in this case, the stronger dependence of the solid angle on the vertical position than the horizontal, as well as self-absorption in the sample, suggest it may be larger in other cases. The approximation of a horizontal wire as a vertical cylinder has, on the other hand, turned out to be very poor, so our more flexible method of calculation is a substantial improvement.

Acknowledgments

The work was performed in the scope of program group P1-0143 at the Jožef Stefan Institute, within the project PR-06174, financed by the Slovenian Research Agency.

References:

- [1] F. de Corte. *The k_0 -standardization method: a move to the optimization of neutron activation analysis* (habilitation thesis), State University of Ghent, Ghent, Belgium, 1987.
- [2] R. Jaćimović. Validation of the standard procedure of the k_0 -INAA using soil and sediment reference materials. *14th International Conference on Modern Trends in Activation Analysis*, Delft, August 23-28, 2015, *11th International Conference on Nuclear Analytical Methods in Life Sciences*, Delft, August 23-28, 2015. Program and abstracts. Reactor Institute Delft, 2015.
- [3] L. Gačnik. Absolute calibration of CA5 HPGe detector, *JSI work report IJS-DP-12061*, Jožef Stefan Institute, Ljubljana, Slovenia, 2016.
- [4] R. Jaćimović, V. Stibilj, L. Benedik, B. Smodiš. Characterization of the neutron flux gradients in typical irradiation channels of a TRIGA Mark II reactor. *Journal of radioanalytical and nuclear chemistry*, (257): 545-549, 2003.

For wider interest

k_0 instrumental neutron activation analysis (k_0 -INAA) is a powerful multi-elemental analytical method, based on irradiating a sample with neutrons, and measuring the gamma spectrum of the resulting radioactive products. The high penetrability of neutrons and gamma rays in matter makes k_0 -INAA almost, but not completely, matrix insensitive, and it is able to achieve combined standard uncertainties of 3.5 % or better.

We identified and corrected a source of systematic error, however, it turned out to be negligible for the chosen sample. We also improved the flexibility of a computational step, enabling us to perform the method on samples of arbitrary shapes, which resulted in a 4%-18% correction over the previous approximation for the case of a wire-shaped sample.

Implementing molecularly imprinted polymer (MIP) in the analytical method for determining sertraline residues in aqueous environment

Tjaša Gornik^{1,2}, Anja Krajnc¹, Amadeja Koler³, Marko Turnšek³, Ester Heath^{1,2}, Jernej Iskra^{3,4}, Peter Krajnc³, Karel Jerabek⁵, Tina Kosjek^{1,2}

¹ Department of environmental sciences, Jožef Stefan Institute, Ljubljana, Slovenia

² Jožef Stefan International Postgraduate School, Ljubljana, Slovenia

³ University of Maribor, Faculty of Chemistry and Chemical Engineering, PolyOrgLab, Smetanova 17, Maribor, Slovenia

⁴ Department of Physical and Organic Chemistry, Jožef Stefan Institute, Ljubljana, Slovenia

⁵ Institute of Chemical Process Fundamentals of the Czech Academy of Sciences, v. v. i., Rozvojova 2/135, Prague, Czech Republic

tjasa.gornik@ijs.si

1 Introduction

Sertraline is one of the most widely prescribed antidepressant in Europe and the USA. It has been approved for treating major depressive, panic, obsessive compulsive, social anxiety and post-traumatic stress disorders. It acts as a selective serotonin reuptake inhibitor. The majority of the drug is metabolised in the liver and its main metabolites are N-demethyl-sertraline (Figure 1) also known as norsertraline (phase I metabolic reactions) and its glucuronide (phase II) [1]. After excretion, a mixture of sertraline and its metabolites enter municipal wastewaters and eventually at a wastewater treatment plant where, if not completely removed, they can enter surface waters. Concentrations in the ng/L range for both the parent compound and norsertraline have been detected in waste and surface waters. Evidence for their bioaccumulation in sediments and aquatic organisms has also been reported [2].

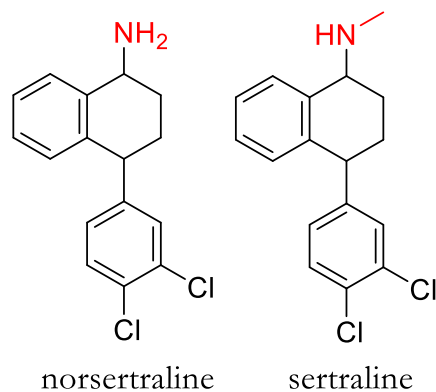


Figure 1: Chemical structures of nortsertraline and sertraline.

Most analytical methods used to determine sertraline in aqueous samples involve solid phase extraction (SPE) followed by liquid chromatography coupled with mass spectrometry [3]. The trend is to improve the selectivity and sensitivity of existing analytical methods. This can be achieved by using molecularly imprinted polymers (MIPs) in SPE. Molecularly imprinted polymers are synthetic polymeric materials with high selectivity for their target molecule. The target molecule is used as a template, forming either covalent or non-covalent interactions with the polymer. After polymerisation, the template is removed leaving an imprint behind for future binding of the target molecule. The selectivity of these materials makes them ideal for different applications, including sensors, capillary electrochromatography, enantiomeric separation, catalysis and solid phase extraction [4].

The objective of our research is to develop a highly selective method for environmental and biological samples using molecularly imprinted solid phase extraction (MISPE) for identifying and quantifying sertraline, its metabolites and environmental transformation products in aqueous samples. Therefore, we have to prove the MIP effect, where the adsorption of our compounds to MIP is larger than the adsorption to blank polymers.

2 Material and Methods

Materials: A sertraline hydrochloride reference standard was donated by pharmaceutical industry. Sertraline-D3 hydrochloride, norsetraline hydrochloride, nortsertraline 13C6 hydrochloride, acetanhydride and pyridine were purchased from Sigma-Aldrich, Switzerland. The solvents dichloromethane, ethyl acetate, methanol,

acetonitrile and hydrochloric acid were from J. T. Baker, USA. MilliQ (18M Ω) water was used to prepare all aqueous solutions. All pharmaceutical standards were of high purity grade (>90 %), while other chemicals were of p.a. grade or higher.

Methods: The analytical method for determination of sertraline in water samples involves sample preparation with SPE, derivatization and instrumental analysis.

Solid Phase Extraction (SPE): Oasis HLB 3 cc, 60 mg cartridges were used for solid phase extraction. The sorbent is a reverse-phase copolymer of N-vinylpyrrolidone and divinylbenzene. The analytical method is based on one previously developed in the Group for organic analyses at the Department of Environmental Sciences, Jožef Stefan Institute [5]: the sorbent was activated using 3 mL of ethyl acetate and 3 mL of methanol, and equilibrated with 3 mL of MilliQ water. Samples (200 mL) were spiked with the isotopically labelled sertraline D₃ and norsertraline ¹³C₆ internal standards at concentrations of 1 μ g/mL. Samples were loaded on the column at a flow rate of 1-2 mL per minute. The cartridge was washed with 3 mL of MilliQ water to remove impurities and vacuum-dried for 30 minutes. The analytes were eluted with 3 x 0,6 mL of different mixtures of solvents: ethyl acetate, dichloromethane, methanol, combinations of the two (1:1) and combination of all three solvents (1:1:1). We achieved the highest recoveries with methanol and the 1:1:1 mixture. The selected solvents were further tested with 2, 5 and 10 % of triethylamine, where methanol with addition of 2 % triethylamine showed the highest recovery.

Derivatization: The solvents were removed under N₂ at 40°C. The analytes were derivatized with a mixture of acethanhydride (15 μ L) and pyridine (5 μ L) at room temperature for 15 minutes. The samples were again reduced to dryness (N₂ at 40°C) and dissolved in 0.5 mL of ethyl acetate.

Instrumental analysis: Identification and quantification of the compounds was achieved using gas chromatography coupled to a mass spectrometer (GC-MS, 7890B/5977A Agilent Technologies, USA). Oven temperature programme: 100°C held for 2 min, then 25°C/min to 300°C and held for 6 min. Total runtime was 16 min. Separation was achieved on a HP-5ms Ultra Inert, 30 m long capillary column,

with a 0.25 mm i.d. and film thickness of 0.25 μm . Carrier gas was helium at a flow rate of 1 mL/min. Samples (1 μL) were injected in splitless mode and the inlet temperature was 270°C. The ionisation mode was EI at 70 eV.

Polymerisation: Polymers were synthesized at the Faculty for Chemistry and Chemical Engineering at the University of Maribor. The three chosen monolithic MIPs with the best characteristics were prepared from divinylbenzen monomers and acrylic acid, a porogen mixture of tetrahydrofuran and water (9:1), azobisisobutyronitrile as a thermo initiator and sertraline as a template. The only difference in their synthetic procedure was the quantity of sertraline added: 1.5 g for MT86, 0.82 g for MT87 and 0.43 g for MT88.

Removal of the template from molecularly imprinted polymers (MIP): To optimise the removal efficiency of the sertraline template, the MIP sorbents were washed with 12 mL of the following solvents: dichloromethane, ethyl acetate and methanol individually and a mixture of all three (1:1:1). Additional washing experiments were conducted using Soxhlet extraction with dichloromethane, ethyl acetate, acetone and 0.05 M HCl. The concentration of sertraline in the residue was determined using the analytical method described.

Extraction of norsesraline using MIP: MilliQ water (200 mL) was spiked with 20 μL of a 97.8 $\mu\text{g}/\text{mL}$ standard solution of norsesraline and 50 μL of a 10 $\mu\text{g}/\text{mL}$ solution of norsesraline $^{13}\text{C}_6$. Samples were then extracted according to the SPE procedure given. The analytes were eluted with a mixture (12 mL) of ethyl acetate, dichloromethane and methanol in the ratio 1:1:1.

3 Results

The optimized Oasis HLB method for sertraline gave recoveries of $65.2 \pm 5.9 \%$ and $50.2 \pm 1.6 \%$ for norsesraline. Optimization included the following:

- 2 % of triethylamine in methanol was used for elution;
- derivatization time was shortened from 1 hour to 15 minutes.

The peaks corresponding to sertraline and norsesraline were separated by GC and identified by MS using a full scan method in the mass range from m/z 50 to m/z 550. The retention times of sertraline and norsesraline were 13.5 minutes and 12.7

minutes, respectively. For quantification a SIM method was developed and m/z selected were **347**, 349 for sertraline; 350, **352** sertraline D3, **274**, 333 for norsesertraline and **280**, 282 for norsesertraline $^{13}\text{C}_6$. Quantification ions are in bold.

Despite thoroughly washing the MIP, we still observed continued leaching of sertraline from 40 to 160 $\mu\text{g}/\text{mL}/\text{g}$ of MIP. This made the evaluation of the MIP effect in comparison to blank polymers for sertraline at sample concentrations of up to 25 $\mu\text{g}/\text{mL}$ impossible. The MIP effect for norsesertraline was observed. The ratios of bound norsesertraline between the control polymer and the two MIPs MT88 and MT87 were 110 % and 160 %, respectively, whereas for MT86 no MIP effect was observed. Based on the presented results, MT87 was selected for further testing.

4 Conclusions

This work describes a potential new selective method based on MIP for analysing sertraline, its metabolites and transformation products in aqueous samples with the MIP effect proven for the metabolite norsesertraline. Future work will involve continued optimization for the Oasis HLB method, e.g. improved recovery, sensitivity and precision, which will be employed as a reference method for assessing the performance of MIP. The MIP effect for other identified metabolites and transformation products of sertraline will also be determined. In addition, a LC-MS method will be developed for analysing of sertraline residues in the aquatic environment. The final aim will be to develop a MIP-based analytical method for selective determination of sertraline residues.

Acknowledgments

The authors acknowledge the financial support of the Slovenian Research Agency (J1-6744: “Razvoj polimerov z molekularnimi odtisi in njihova uporaba na področju okoljske in bio-analitike” and P1-0143: “Kroženje snovi v okolju, snovna bilanca in modeliranje okoljskih procesov ter ocena tveganja”).

References:

- [1] C. L. De Vane, H. L. Liston, and J. S. Markowitz. Clinical pharmacokinetics of sertraline, *Clin. Pharmacokinet.*, 41 (15): 1247–1266, 2002.
- [2] M. M. Schultz, E. T. Furlong, D. W. Kolpin, S. L. Werner, H. L. Schoenfuss, L. B. Barber, V. S. Blazer, D. O. Norris, and A. M. Vajda. Antidepressant pharmaceuticals in two US effluent-

- impacted streams: occurrence and fate in water and sediment, and selective uptake in fish neural tissue, *Environ. Sci. Technol.*, 44 (6): 1918–1925, 2010.
- [3] J. G. Silva, L. M. Meisel, C. M. Lino, and A. Pena. Profiling Serotonin Reuptake Inhibitors (SSRIs) in the Environment: Trends in Analytical Methodologies, *Crit. Rev. Anal. Chem.*, 44 (1): 41–67, 2014.
- [4] E. Caro, R. Marce, F. Borrull, P. Cormack, and D. Sherrington. Application of molecularly imprinted polymers to solid-phase extraction of compounds from environmental and biological samples, *TrAC Trends Anal. Chem.*, 25 (2): 143–154, 2006.
- [5] A. Krajnc. *Posnemanje fotorazgradnje sertralina v okolju. Magistrska naloga*, Ljubljana, 2015.

For wider interest

Molecularly imprinted polymers or MIPs are materials with high selectivity towards a target molecule, because it is used as a template during polymerization. Based on their selectivity, different applications including sensors, capillary electrochromatography, enantiomeric separation, catalysis and solid phase extraction, have been proposed. The focus of our research is the antidepressant sertraline, a highly prescribed pharmaceutical that poses a threat to the environment due to its toxic effects on aquatic organisms. Our aim is to develop an analytical method using a MIP as a solid-phase extraction sorbent highly selective for sertraline, its metabolites and transformation products. First results showed that the assessment of the MIP effect for sertraline, the template and concurrently the target molecule, is hindered due to its continuous leaching from the MIPs. The MIP effect was proven for the metabolite nortriptyline. In the future we would like to use MIPs to selectively isolate structurally related sertraline compounds from environmental aqueous samples and adapt the method for bioanalytical and forensic applications.

Maternal blood levels of selected elements and birth weight of mother-child pairs living in Slovenia

**Marta Jagodic^{1,2*}, Janja Snoj Tratnik^{1,2}, Darja Mazej¹, Anja Stajnko^{1,2},
Majda Pavlin^{1,2}, Mladen Krsnik³, Alfred B. Kobal⁴, Lijana Kononenko⁵,
Milena Horvat^{1,2}**

¹ Department of O2, Jožef Stefan Institute, Ljubljana, Slovenia;

² 'Jožef Stefan' International Postgraduate School, Ljubljana, Slovenia;

³ Institute of Clinical Chemistry and Biochemistry, University Medical Centre Ljubljana, Ljubljana, Slovenia;

⁴ Ex-Department of Occupational Health, Idrija Mercury Mine, Arkova 43, 5280 Idrija, Slovenia;

⁵ Ministry of Health, Chemicals Office of the Republic of Slovenia, Ljubljana, Slovenia

marta.jagodica@ijs.si

The objective of the present study was to evaluate the impact of maternal blood levels of selected toxic and potentially toxic elements (manganese (Mn), copper (Cu), zinc (Zn), arsenic (As), selenium (Se), cadmium (Cd), lead (Pb) and mercury (Hg)) on the birth weight of their babies, taking into account maternal socio-demographic characteristics and dietary habits, since the literature suggest that trace exposures to some elements may influence birth weight [1, 2].

Five-hundred thirty-five pregnant women (19-39 years old) were recruited from 12 regions across Slovenia (Figure 1) as a part of the National Human biomonitoring study (2007-2015). Maternal blood was collected approximately 4-6 weeks after delivery. Mothers also completed a questionnaire in which they reported their age, prior areas of residence, familial background, social factors, education, weight before and through pregnancy, height and weight post-partum, parity, detailed reproductive, medical and occupational history, life style, relevant paternal/pregnancy related information, information about the newborn, and dietary information (frequency of food consumption and type of food consumed– vegetables, fruits, nuts, milk and

dietary products, eggs, poultry, game, other meat, fresh-water fish, fresh, frost and tinned-fish or other sea food, coffee or tea, and alcoholic drinks).

The levels of selected toxic and potentially toxic elements were analysed at Jožef Stefan Institute using a Direct Mercury Analyser (DMA-80, Milestone Srl, Italy) for Hg, where the system integrates thermal decomposition, sample preparation, amalgamation and atomic absorption detection; absorbance was measured as a function of mercury concentration at 254 nm [3]. An Octapole Reaction System (ORS) Inductively-coupled plasma mass spectrometry (ICP-MS, 7500ce, Agilent) equipped with an ASX-Autosampler (Cetac) was used to measure As, Cd, Cu, Mn, Pb, Se and Zn. Briefly, an aliquot of whole blood sample was diluted ten times with an alkaline solution containing Triton X-100 and ethylenediaminetetraacetic acid disodium salt dehydrate (EDTA) in contamination free tubes [4]. An aliquot of internal standard solution was added. For calibration a standard addition procedure was performed. Quantitation on selected isotopes was performed using one central point of the spectral peaks and three repetitions. A reference material Seronorm Trace Elements Whole Blood L-1 (SERO AS, Norway) was used to check the accuracy of the results for all selected elements in whole blood.

Statistical analyses were performed using SPSS software. Non-normally distributed data were log₁₀-transformed. Concentrations of elements below the detection limit (DL) were arbitrarily assigned the value of ½ DL. Associations between birth weight and a) the predictors obtained through the questionnaires and b) the levels of selected elements in women blood samples were tested using univariate analysis (Spearman for categorical data, Pearson for continuous data and analysis of variance (ANOVA)) and multiple linear regression analysis, whereas predefined confounders were fixed into the models (age of mother, education, pre-pregnancy body mass index (BMI) and living residence).

Characteristics of the study group are presented in Table 1. The levels of exposure to selected toxic elements (As, Cd, Pb and Hg) (Table 2) were generally low and the levels of essential elements (Mn, Zn, Cu and Se) were consistent with other studies, indicating that these factors do not represent any health risk for the mother-child pairs. Univariate correlations are presented in Table 3. The multiple regression model for the Slovenian population included 319 women (R Square=0.28, p<0.001) and showed that the gender of the baby, gestational age, maternal age and pre-pregnancy body

mass were the main predictors for birth weight, and that Mn in maternal blood was significantly and positively associated with newborn weight.

Dietary habits showed insignificant correlations with birth weight, with the following food items being tested: vegetable, fruits, nuts, milk, eggs, poultry, game, other meat, freshwater fish, and fresh, tinned and frozen seafood.

Associations between birth weight and the main predictors of birth weight (gender of the baby, gestational age, maternal age and pre-pregnancy BMI) were in agreement with the literature data. The positive association between birth weight and Mn in mother's blood could be explained by the essential role of Mn in foetal development as an important cofactor in enzymatic reactions in bone formation and metabolic regulation of amino acids, lipids, proteins and carbohydrates [5, 6].

Acknowledgments

This work was supported by the National Human Biomonitoring program financed by the Chemicals Office of the Republic of the Republic of Slovenia and the Slovenian Research Agency and the EU founded CROME-LIFE+ program (Cross-Mediterranean Environment and Health Network program).

References:

- [1] K. P. Stillerman, D. R. Mattison, L. C. Giudice, T. J. Woodruff. Environmental Exposures and Adverse Pregnancy Outcomes: A Review of the Science. *Reprod Sci*, 15:631–650, 2008.
- [2] C. V. Rudge, H. B. Röllin, C. M. Nogueira, Y. Thomassen, M. C. Rudge, J. Ø. Odland. The placenta as a barrier for toxic and essential elements in paired maternal and cord blood samples of South African delivering women. *J Environ Monit*, 11:1322–30, 2009.
- [3] US EPA: Mercury in solids and solutions by thermal decomposition, amalgamation, and atomic absorption spectrophotometry - method 7473 - total Mercury. *SW-846, Test Methods Eval Solid Waste, Phys Methods* 2007(February):1–17.
- [4] E. Barany, I. A. Bergdahl, A. Schültz, S. Skerfving, A. Skarsson. Inductively Coupled Plasma Mass Spectrometry for Direct Multi-element Analysis of Diluted Human Blood and Serum. *J Anal At Spectrom*, 12:1005–1009, 1997.
- [5] ATSDR: Toxicological profil for manganese, 2012.
- [6] A. M. Mora, B. van Wendel de Joode, D. Mergler, L. Córdoba, C. Cano, R. Quesada, D. R. Smith, J. A. Menezes-Filho, B. Eskenazi. Maternal blood and hair manganese concentrations, fetal growth, and length of gestation in the ISA cohort in Costa Rica. *Environ Res*, 136:47–56, 2015.
- [7] M. Horvat, D. Mazej, J. Snoj Tratnik, Z. Šlejkovec, M. Jagodic, V. Fajon, M. Pavlin, A. Stajniko, M. Krsnik, M. Prezelj, M. Skitek. *Monitoring Kemikalij v Organizmih 2011-2014*. 2015.

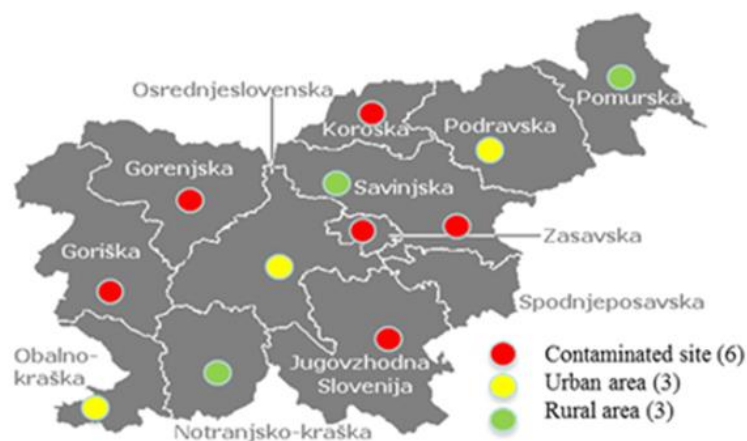


Figure 1: 12 regions in Slovenia [7].

Table 1: General characteristics of the study group.

Characteristic of study group		N	Mean (min-max) or % of answers
Women	Age (years)	493	29.0 (19-39)
	Pre-pregnancy body mass index (kg/m ²)	483	23.1 (16.6-44.8)
	Estimated gestational length (weeks)	473	39.7 (28-42)
	Education - Primary Secondary University	470	7.4 % 42.6 % 50.0 %
Children	Gender – male female	494	53.8 % 46.2 %
	Birth weight (kg)	494	3.38 (1.40-5.17)
	Birth length (cm)	493	51.4 (44-59)

N=sample number, min=minimal level, max=maximal level.

Table 2: Concentration of selected elements in maternal blood samples.

Concentration of elements in maternal blood	Geometric Mean	95% Conf. Interval of GM	min – max
Mn (ng/ml)	17.2	16.7 - 17.8	5.8 – 35.2
Cu (ng/ml)	1077	1057 - 1084	657 – 2004
Zn (ng/ml)	6731	6644 - 6819	3010 - 11733
As (ng/ml)	0.929	0.866 - 0.997	0.201 – 16.798
Se (ng/ml)	94.7	93.2 - 96.3	53.9 – 175.9
Cd (ng/ml)	0.346	0.328 - 0.365	0.20 – 3.084
Pb (ng/ml)	16.8	16.2 - 17.4	4.2 – 71.9
Hg (ng/ml)	1.11	1.03 - 1.19	0.20 – 10.17

GM=geometric mean, N=sample number, min=minimal level, max=maximal level. N: 370 for Mn, 493 for Cd and Hg, 494 for other elements.

Table 3: Univariate linear correlation between birth weight and selected variables.

Correlations with birth weight (kg)			
Variable	r_s	p -value	N
Residential location*	0.000	0.994	448
Age of mother (years) - groups	-0.043	0.346	493
Pre-pregnancy body mass index - groups	0.092	0.042	483
Education - groups	-0.033	0.469	470
Estimated gestational age (week)	0.325	0.000	473
Gender of baby	-0.096	0.033	494
Variable	r_p	p -value	N
Log10 Mn (ng/mL)	0.178	0.001	370
Log10 Cu (ng/mL)	-0.074	0.102	494
Log10 Zn (ng/mL)	0.004	0.938	494
Log10 As (ng/mL)	0.018	0.689	494
Log10 Se (ng/mL)	-0.042	0.347	494
Log10 Cd (ng/mL)	0.053	0.239	493
Log10 Pb (ng/mL)	0.076	0.091	494
Log10 Hg (ng/mL)	-0.04	0.376	493
Baby length (cm)	0.717	0.000	493
* Potentially contaminated, rural, and urban areas. N=sample number, r_s -Spearman correlation coefficient, r_p -Pearson correlation coefficient.			

For wider interest

The aim of our study was to assess the influence of selected elements in maternal blood samples (manganese (Mn), copper (Cu), zinc (Zn), arsenic (As), selenium (Se), cadmium (Cd), lead (Pb) and mercury (Hg)) on birth weight. In the evaluation of these associations we took into account the mother's and baby's social-demographic characteristics and the mother's dietary and lifestyle habits. Maternal blood was sampled 4-6 weeks after delivery.

The concentrations of selected elements did not represent any health risk for the mother-child pairs. Statistical analyses showed that the gender of the baby, gestational age, maternal age and pre-pregnancy body mass index were the main predictors for birth weight, and that the concentration of Mn in maternal blood was significantly and positively associated with birth weight.

This work was supported by the National Human Biomonitoring program financed by the Chemicals Office of the Republic of Slovenia and the Slovenian Research Agency and the EU funded CROME-LIFE+ program (Cross-Mediterranean Environment and Health Network program).

Iodine and selenium content in buckwheat seeds after foliar spraying of plants with I and Se solution

Ana Jerše^{1,2}, Ana Kroflič^{1,2}, Mateja Germ³, Nina Kacjan-Maršič³, Helena Šircelj³, Vekoslava Stibilj^{1,2}

¹ Department of Environmental Sciences, Jožef Stefan Institute, Ljubljana, Slovenia

² Jožef Stefan International Postgraduate School, Ljubljana, Slovenia

³ Biotechnical Faculty, University of Ljubljana, Ljubljana, Slovenia

ana.jerse@ijs.si

Iodine and selenium are essential elements for humans and animals, important for normal thyroid function and thyroid hormones synthesis. Both elements come into the body by food consumption. The main source of iodine for humans is iodized salt, but recommended decrease of salt in nutrition [1] would reduce also the intake of iodine. Slovenia is known as a country with low selenium content in soil and consequently also food contains low amounts of selenium. Naturally plants are low in concentrations of both elements. To avoid health problems caused by iodine or selenium deficiency, other sources of these two elements should be found. Iodine and/or selenium enriched cultivated plants could be an effective way to provide sufficient intake of these elements for humans [2–5].

The aim of our study was to investigate the iodine and selenium uptake in buckwheat seeds after foliar spraying of plants with solutions of both elements. Buckwheat that is commonly consumed in Slovenia belongs to the group of pseudo-cereals. It contains high amounts of vitamins B1 and B2, amino acid lysine and antioxidants such as tocopherols and phenolic substances and is therefore considered as food component of high nutritional value [6]. However, buckwheat seeds contain low amounts of iodine (25 ng/g) and selenium (49 ng/g) [7].

Buckwheat was grown on the field in summer 2014 (started in mid July). The plants were foliar sprayed just before blooming with water (control) or solutions of iodide I(–I), iodate I(V), selenite Se(IV), selenate Se(VI) or their combinations. The concentrations for spraying were 1000 mg I/L (7.88 mmol I/L) and 10 mg Se/L

(0.127 mmol Se/L). Seeds were harvested in mature phase, dried at 40 °C and milled. Each treatment was performed in three replicates.

Iodine content was determined by ICP-MS after alkaline microwave-assisted extraction (high extraction efficiency has previously been proven by independent method, k0-NAA) and selenium content by ICP-QQQ after acid microwave-assisted digestion. Concentrations of iodine and selenium in enriched buckwheat seeds are summarized in Table 1.

Buckwheat seeds were successfully enriched with both investigated elements since concentrations of both were higher in seeds from treated plants in compared to control. Iodine concentrations in seeds were not dependent on the form of iodine used for foliar spraying but there was a significant difference in selenium content regarding the form of treatment. Approximately 6-fold higher selenium concentrations were found when treated with less toxic form of selenium for plants [8], Se(VI) in comparison with Se(IV) treatment. Studied treatments did not affect the plant growth since there were no statistically significant differences between control and treated plants in plant height or dry seed mass.

There were also some significant interactions when combinations of both elements were used for spraying. When I(-I) was applied in combination with Se(IV), the final iodine content remained the same while the combination I(-I) + Se(VI) increased the iodine content in seeds. The opposite trend was observed when I(V) was combined with selenium since combination I(V) + Se(IV) increased iodine content in seeds but I(V) + Se(VI) had no influence on the final amount of iodine. The selenium content was also influenced by iodine presence in spraying solution – I(-I) decreased the uptake of both selenium forms in comparison with selenium treatments alone while I(V) increased the uptake of Se(IV) but decreased the uptake of Se(VI) even more than I(-I).

In the present study we proved that buckwheat seeds may be enriched with iodine and selenium by foliar spraying with no influence on plant growth. Both forms of iodine may be equally used for plant treatment while in case of selenium, higher final concentrations were observed when spraying with Se(VI) solution. Although some

interactions may be observed when mixed solutions of I and Se were applied, the enrichment might still be performed simultaneously. Therefore we concluded that the approach can be used for the production of functional food.

References:

- [1] F. Delahaye. Should we eat less salt? *Archives of Cardiovascular Disease*, 106:324–332, 2013.
- [2] Y.G. Zhu, Y. Huang, Y. Hu and Y. Liu. Interactions between selenium and iodine uptake by spinach (*Spinacia oleracea* L.) in solution culture. *Plant and soil*, 261:99–105, 2004.
- [3] S. Smolen, I. Kowalska and W. Sady. Assessment of biofortification with iodine and selenium of lettuce cultivated in the NFT hydroponic system. *Scientia Horticulturae*, 166:9–16, 2014.
- [4] P. Cuderman, L. Ožbolt, I. Kreft and V. Stibilj. Extraction of Se species in buckwheat sprouts grown from seeds soaked in various Se solutions. *Food Chemistry*, 123:941–948, 2010.
- [5] P. Smrkolj, M. Germ, I. Kreft and V. Stibilj. Respiratory potential and Se compounds in pea (*Pisum sativum* L.) plants grown from Se-enriched seeds. *Journal of Experimental Botany*, 57:3595–3600, 2006.
- [6] M. Holasova, V. Fiedlerova, H. Smrcinova, M. Orsak, J. Lachman and S. Vavreinova. Buckwheat – the source of antioxidant activity in functional foods. *Food research International*, 35:207–211, 2002.
- [7] S.W. Souci, W. Fachmann and H. Kraut. *Food Composition and Nutrition Tables, 6th Edition*. H. Scherz and F. Sensler, 2000.
- [8] N. Terry, A.M. Zayed, M.P. de Souza and A.S. Tarun. Selenium in higher plants. *Annual Review of Plant Physiology and Plant Molecular Biology*, 51:401–432, 2000.

Table 1: Iodine in selenium contents in I and/or Se enriched buckwheat seeds (given as mean value \pm standard error; superscripts indicate statistically significant differences between the results).

Treatment	c_I [ng I/g DW]	c_{Se} [ng Se/g DW]
Control	33 ± 9^c	29 ± 4^g
I(–I)	333 ± 21^b	-
I(V)	294 ± 45^b	-
Se(IV)	-	115 ± 8^e
Se(VI)	-	653 ± 16^a
I(–I) + Se(IV)	381 ± 24^b	92 ± 4^f
I(–I) + Se(VI)	535 ± 25^a	460 ± 15^b
I(V) + Se(IV)	609 ± 31^a	221 ± 25^d
I(V) + Se(VI)	347 ± 36^b	299 ± 30^c

For wider interest

Iodine and selenium are essential elements that are necessary for thyroid hormones synthesis. They both come into the body by food consumption. Deficiency problems caused by insufficient intake mainly results from the low content of the two elements in soils. Consequently, the transfer of both elements to the food chain, where plants are the first level, is low. To avoid health problems caused by iodine and/or selenium deficiency, other food sources of the elements should be found.

Our aim was to enrich buckwheat seeds with iodine and selenium. Plants were foliar sprayed with different forms of iodine and/or selenium. The results showed increased concentrations of both elements. According to World Health Organizations, recommended daily intakes (RDI) are 150 μg I/day and 30–70 μg Se/day. By one portion (100 g) of untreated buckwheat seeds a person would intake approx. 2 % of RDI for iodine and 4–10 % of RDI for selenium (on the supposition that all of iodine and selenium present in seeds are absorbed). By consuming a portion of treated buckwheat seeds from the present study, 20–40 % of iodine RDI and 13–220 % of selenium RDI would be ingested. Therefore some further optimizations regarding the concentrations used for foliar spraying are still needed, but this is a promising approach to provide sufficient iodine and selenium intake for humans.

Evidence of cave ventilation and its contribution to soil CO₂ flux

Bor Krajnc¹, Mitja Ferlan², Nives Ogrinc^{1,3}

¹Jožef Stefan International Postgraduate School, Ljubljana, Slovenia

²Department of Forest Ecology, Slovenian Forestry Institute, Ljubljana, Slovenia

³ Department of Environmental Sciences, Jožef Stefan Institute, Ljubljana, Slovenia

bor.krajnc@ijs.si

Abstract. The main objective of this research is to detect and estimate the contribution of cave air CO₂ to soil CO₂ fluxes above the cave. Research was performed in the forest above known subterranean cave near Postojna. Carbon stable isotope composition ($\delta^{13}\text{C}_{\text{CO}_2}$) and CO₂ concentration were measured in soil gas, atmospheric and cave air together with soil CO₂ fluxes at two selected sampling sites. A time series of a modelled “isotopically light” end-member revealed large shifts in the data values, due to the presence of an abiotic CO₂ source. Results suggest that the subterranean CO₂ pool and its ventilation is the main source of soil CO₂, accounting for up to 80% of the soil air, during cold periods. This source potentially contributes up to 20% to the annual CO₂ flux indicating to be an important source of soil CO₂ in karstic areas and should be taken into account during carbon cycling studies.

Keywords: Soil CO₂, Flux, Stable isotopes, Abiotic sources, Ventilation, Karst region

1 Introduction

Studying and understanding global carbon cycle is attracting attention due to increased concern regarding concentrations of “greenhouse” gasses in the atmosphere. Due to the ability of soil to act as a significant sink or source of atmospheric CO₂ [1; 2] increasing number of researches focuses on studies of soil CO₂ flux dynamics and its sources. Accurate measurements of soil CO₂ fluxes are important for understanding the mechanisms that are affecting the soil CO₂ efflux and for determining whether the ecosystem under investigation acts as a sink or source of CO₂. Soil CO₂ flux measurement provides only the information of the

bulk CO₂ fluxes originating from different sources. To gain deeper understanding of soil carbon dynamic it is important to distinguish and study those sources and could also help to develop reliable methodology to detect and quantify different anthropogenic sources. Recently different methodologies of CO₂ (and other gasses) capturing methods to decrease industrial CO₂ emissions have been developed along with different storage possibilities of captured CO₂. One possibility for CO₂ storage is so called “geological storage” where captured CO₂ is transported to underground spaces in impermeable geological layers [3; 4]. It is imperative to develop reliable monitoring system above those storage spaces to detect possible leaches of the stored gas to the atmosphere. Soil CO₂ sources in natural ecosystems are mainly deriving from two biological sources, namely autotrophic and heterotrophic respiration. Both of those two biological sources and their interactions can be further divided into more subdivisions as it was done by Kuzyakov [5]. CO₂ from these sources is defined as soil-respired CO₂ [6; 7]. CO₂ in soil can also originate from other, abiotic sources, such as atmospheric CO₂ transported into soil by diffusion, convection or rain water. Another abiotic source which has been generally considered of minor importance [5] is CO₂ derived from carbon dissolution/precipitation processes in soil and its parent material. Its importance has been recently demonstrated for soils on karstic areas and can have significant contribution to bulk soil CO₂ [8; 9; 10; 11]. One of the characteristics of karstic areas is the presence of different subterranean cavities which can act as temporal storage of CO₂ that would otherwise leach out of the system e.g. dissolved in percolating water. Those temporal storages can act as instantaneous soil CO₂ source when favorable conditions occur (e.g. water fill of cavities or ventilation caused by changes of outside temperature, pressure, wind etc.). Stable isotope techniques can be used to partition between different CO₂ sources due to their distinctive isotopic composition. Soil respiration CO₂ reflects the $\delta^{13}\text{C}$ values of the local flora whose $\delta^{13}\text{C}$ values in the case of C3 type flora are about -27‰ (-35‰ to -20‰) [12; 5]. Atmospheric CO₂ has average isotopic composition ($\delta^{13}\text{C}_{\text{atm}}$) of about -8‰ [13]. The $\delta^{13}\text{C}$ value of the carbonate bedrock ($\delta^{13}\text{C}_{\text{CaCO}_3}$) has normally a narrow, close to zero range (0‰ - 4‰).

The aim of this study is to evaluate the ventilation of the subterranean CO₂ pool, as the main source of soil CO₂ flux during the ventilation period, and estimate its contribution on an annual basis. Our previous study indicates that cave ventilation

does affect soil CO₂ above the cave. It was estimated that during ventilation period up to 80% of soil CO₂ originates from cave air [14].

2 Material and Methods

Study area. Velika Jeršanova dolina (45°47' N, 14°12' E) is a collapse doline located in the forest near Postojna, Slovenia (**Figure 1**). Its collapse blocks on the south side of the doline define the end of the northernmost part of the subterranean corridor called “Pisani rov”. Study area lies in the Omphalodo-Fagetum forest with mainly C3 vegetation. Two sampling sites were selected: the first, the test site, (above the cave - AC) is located directly above the last hall of Pisani rov (575 m.a.s.l.) and the second, the control site, where no cave (NC) influence is expected, is located at the bottom of the doline underneath (539 m.a.s.l.). Thickness of the cave ceiling between Rdeča dvorana and the AC is estimated to be ~30 m [15]. It is expected that air between Rdeča dvorana and AC can be exchanged through different fractures and conduits.

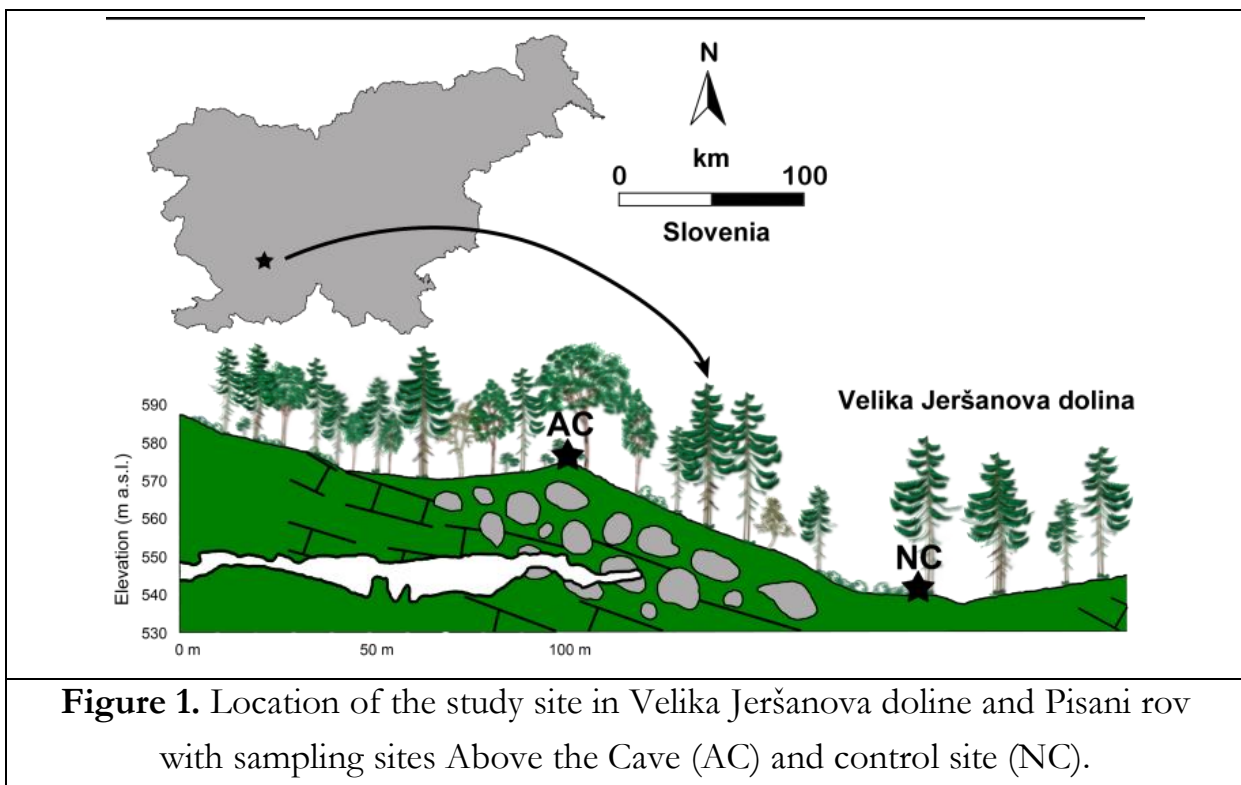


Figure 1. Location of the study site in Velika Jeršanova dolina and Pisani rov with sampling sites Above the Cave (AC) and control site (NC).

Sampling and Measurements. Soil CO₂ fluxes were measured with automatic soil respiration system “Ukulele”, which is a system of closed dynamic chambers developed in the Laboratory for Electronic Devices at the Slovenian Forestry Institute [16]. The system measures the increment of CO₂ concentration in a

closed space above soil surface using infrared gas analyzer (IRGA) LI-840 (LI-COR, USA). IRGA has measurement range from 0 to 20000 ppm with the accuracy of <1.5% of the reading. Three flux chambers were installed at each site. Each chamber has integrated thermocouples and FDR sensors for measuring soil temperature (TS) and soil water content (SWC), respectively. All data were measured continuously in hourly intervals from 21.6.2014 to 2.9.2015. Each CO₂ flux measurement consisted of TS, SWC and 210 individual CO₂ concentration measurements for each chamber. Average flux values for four seasons (a year) were calculated. Season lengths were chosen based on astronomical seasons, with exception of the ventilation period (winter), which was chosen based on soil CO₂ source calculation from our previous research [14]. All calculations were made using R statistical environment (R Development Core Team).

3 Results and Discussion

Different trends in soil CO₂ fluxes across the year were observed between AC and NC sites. Average season fluxes for site AC and NC are plotted in **Figure 2**. It can be seen that at AC site (**Figure 2c**) soil fluxes follow typical trends, with the highest values during warm periods and lowest values during colder seasons. The maximum fluxes were measured in autumn 2014 with autumn average value of $1.62 \pm 0.73 \mu\text{mol m}^{-2} \text{s}^{-1}$, while the minimum average value of $1.18 \pm 0.37 \mu\text{mol m}^{-2} \text{s}^{-1}$ was determined during cave ventilation period in winter 2014/15. Average flux values for summer 2014, spring 2015 and summer 2015 were $1.25 \pm 0.60 \mu\text{mol m}^{-2} \text{s}^{-1}$, $1.43 \pm 0.60 \mu\text{mol m}^{-2} \text{s}^{-1}$ and $1.39 \pm 0.60 \mu\text{mol m}^{-2} \text{s}^{-1}$, respectively. At NC site (**Figure 2d**) the minimum average flux was obtained for summer 2014 ($0.50 \pm 0.4 \mu\text{mol m}^{-2} \text{s}^{-1}$), similar average value was observed in autumn and during the cave ventilation period ($0.62 \pm 0.37 \mu\text{mol m}^{-2} \text{s}^{-1}$ and $0.63 \pm 0.27 \mu\text{mol m}^{-2} \text{s}^{-1}$, respectively). Relatively low average fluxes for the summer season can be attributed to non-typical rainy and cold summer in 2014. The highest average flux of $2.33 \pm 0.90 \mu\text{mol m}^{-2} \text{s}^{-1}$ was determined at NC site in spring 2015. Significantly higher value of average soil CO₂ fluxes were recorded in spring and summer in 2015, which could be caused by a heavy forest sanitation cutting in that area after a Scolytidae outbreak as a consequence of freezing rain damage in February 2014. After cutting, more sunlight

reached the forest floor increasing soil respiration and thus influencing the soil CO₂ fluxes.

The results from our previous study, which include the stable isotope approach, indicate that soil CO₂ in this region is also influenced by abiotic source probably from cave ventilation. Based on isotope mass balance two end-member mixing model calculation and equations proposed by Davidson [17], this contribution was estimated to be up to 80% to soil CO₂. The influence of the non-biogenic source to the soil CO₂ is presented in **Figure 2a**. In case that only biogenic source is influencing CO₂ flux, $\delta^{13}\text{C}_{\text{light}}$ values should be relatively constant or could eventually shift for $\sim 1\text{-}2\text{‰}$. The value is indeed relatively uniform at the NC site (**Figure 2b**) with slightly scattered values during colder periods (autumn 2014 and winter 2014/15), while during the warmer period (spring and summer 2015) a small increase was observed. However, all these deviations are small and can be explained by environmental factors affecting isotopic composition of soil respired CO₂. At AC, this shift is much higher and cannot be attributed solely to the differences in biotic sources caused by environmental factors. At AC the $\delta^{13}\text{C}_{\text{light}}$ is relatively constant until late November 2014 and returns to its starting value in April 2015. It can be seen from the **Figure 2a**, that the period when $\delta^{13}\text{C}_{\text{light}}$ values start to increase coincide with the period when $\delta^{13}\text{C}_{\text{cave}}$ values were higher (orange line). The increase in $\delta^{13}\text{C}_{\text{cave}}$ values together with lower cave atmosphere CO₂ concentrations was the consequence of cave ventilation. Under these assumptions the contribution of cave CO₂ to soil CO₂ and consequently soil CO₂ flux was estimated to be up to 80%. Based on this calculation, the overall annual contribution of cave CO₂ to soil CO₂ fluxes was estimated to be 410 gm² of cave air CO₂ during the ventilation period to overall 1870 gm² per year to soil CO₂. This suggests that if during all ventilation period the cave contribution to soil CO₂ would be 80%, it would contribute 20% to overall annual CO₂ release from soils at AC site. However, it should be stressed out that this estimation is most certainly overestimated, because the maximum observed cave CO₂ contribution was used for calculation for all the ventilation period.

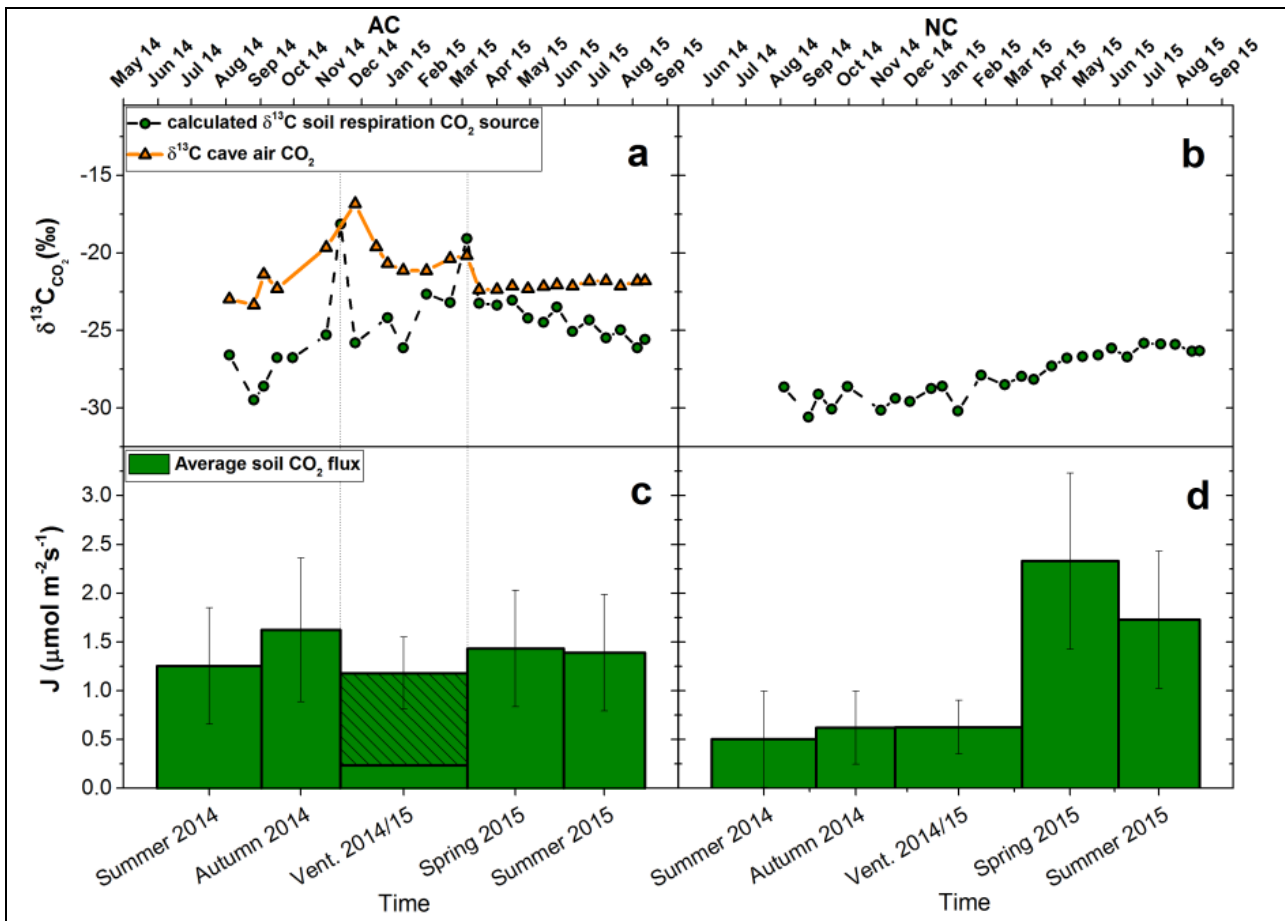


Figure 2. Time series of calculated isotopic composition of the isotopically light end-member from samples gathered at AC (a) and NC (b) site at the depth of 80 cm. Orange line represents carbon isotopic composition of cave atmosphere CO₂ [14]. Bar-plots of average fluxes for particular season and cave ventilation period at AC (c) and at NC (d). Hatchet part of the bar-plot is the estimated contribution of cave air. Dotted lines represent the ventilation period at AC site (a and c).

4 Conclusions

This study revealed the presence of an abiotic source of CO₂ in soil above the cave during cold periods. Those periods coincided with the period of cave ventilation. A rough estimate indicates that cave air CO₂ can account for up to 80% of the overall soil CO₂ during the ventilation and potentially up to 20% of annual CO₂ flux from soil above the cave. This shows that subterranean cavities act as a temporal storage of CO₂ and can be released during favourable conditions. However for a more accurate interpretation of carbon cycling over carbonate and karst ecosystems more knowledge and methodologies are required involving more than one tracer e.g. ¹⁴C and/or ²²²Rn.

Acknowledgments

The study is a part of PhD thesis of B. Krajnc supported by the Innovative scheme for co-financing of doctoral studies financed by the European Union through the European Social Fund. We appreciate the support of cave guides Stanislav Glažar, Janez Margon and Erik Rebec for their dedication during fieldwork. We would also like to acknowledge the Karst Research Institute, the managers of the Postojnska Jama d.d. and the Ministry of Agriculture and Environment of Slovenia for the permission to access and work in the cave and the forest.

References:

- [1] R. Amundson. The carbon budget in soils. *Annual Review of Earth and Planetary Sciences*, 29 (1): 535–562, 2001.
- [2] J.W. Raich, C.S. Potter, D. Bhagawati. Interannual variability in global soil respiration, 1980–94. *Global Change Biology*, 8 (8): 800–812, 2002.
- [3] ECCSEL European Carbon Dioxide Capture and Storage Laboratory Infrastructure. <http://www.eccsel.org/>, 5.3.2016.
- [4] CIUDEN experiences in CO₂ capture by oxycombustion. http://www.gecarbon.org/boletines/articulos/BoletinGEC_035_art3.pdf, 5.3.2016.
- [5] Y. Kuzyakov. Sources of CO₂ efflux from soil and review of partitioning methods. *Soil Biology and Biochemistry*, 38 (3): 425–448, 2006.
- [6] T.E. Cerling, D.K. Solomon, J. Quade, J.R. Bowman. On the isotopic composition of carbon in soil carbon dioxide. *Geochimica et Cosmochimica Acta*, 55 (11): 3403–3405, 1991.
- [7] H. Doerr and K.O. Münnich. Annual variations of the (super 14) C content of soil CO (sub 2). *Radiocarbon*, 28 (2A): 338–345, 1986.
- [8] A.S. Kowalski, P. Serrano-Ortiz, I.A. Janssens, S. Sánchez-Moral, S. Cuezva, F. Domingo, A. Were, L. Alados-Arboledas. Can flux tower research neglect geochemical CO₂ exchange? *Agricultural and Forest Meteorology*, 148 (6–7): 1045–1054, 2008.
- [9] P. Serrano-Ortiz, M. Roland, S. Sanchez-Moral, I.A. Janssens, F. Domingo, Y. Godderis, A.S. Kowalski. Hidden, abiotic CO₂ flows and gaseous reservoirs in the terrestrial carbon cycle: review and perspectives. *Agricultural and Forest Meteorology*, 150 (3): 321–329, 2010.
- [10] M. Čater and N. Ogrinc. Soil respiration rates and in natural beech forest (*Fagus sylvatica* L.) in relation to stand structure. *Isotopes in environmental and health studies*, 47 (2): 221–237, 2011.
- [11] G. Plestenjak, K. Eler, D. Vodnik, M. Ferlan, M. Čater, T. Kanduč, P. Simončič, N. Ogrinc. Sources of soil CO₂ in calcareous grassland with woody plant encroachment. *Journal of soils and sediments*, 12 (9): 1327–1338, 2012.

- [12] J.R. Ehleringer and T.E. Cerling. C3 and C4 photosynthesis. *Encyclopedia of Global Environmental Change, The Earth system: biological and ecological dimensions of global environmental change*, 2 (1): 186–190, 2002.
- [13] GLOBALVIEW-CO2C13: Cooperative Atmospheric Data Integration Project - $\delta^{13}\text{C}$ of Carbon Dioxide. http://www.esrl.noaa.gov/gmd/ccgg/globalview/co2c13/co2c13_intro.html, 2009.
- [14] B. Krajnc, M. Ferlan, N. Ogrinc. Soil CO₂ sources above a subterranean cave – Pisani rov (Postojna Cave, Slovenia). *Journal of Soils and Sediments*, Under review, 2016.
- [15] S. Šebela and J. Čar. Velika Jeršanova dolina - a former collapse doline. *Acta carsologica*, 29 (2): 201–212, 2000.
- [16] M. Ferlan. The use of micro-meteorological methods for the monitoring of the carbon fluxes in Karst ecosystems, *Doctoral dissertation*, Ljubljana, Slovenija, 2013.
- [17] G.R. Davidson. The stable isotopic composition and measurement of carbon in soil CO₂. *Geochimica et Cosmochimica Acta*, 59 (12): 2485–2489, 1995.

For wider interest

Studying and understanding carbon cycle is important due to increased concern regarding concentrations of “greenhouse” gasses in the atmosphere. Special attention in last decades is given to its natural sinks and sources and possible artificial storage of CO₂ “captured” from industrial sources. One of the important natural CO₂ sink /source are also soils. Different soils and environments dictate different carbon dynamics. Soils developed on karstic areas are globally widely distributed. Beside carbon originating (in different forms) from plants and plant material, the presence of carbonate rocks affects soil carbon dynamics with its dissolution and precipitation processes. Furthermore, below soils there can be a presence of subterranean caves and cavities, which can act as temporal reservoirs for CO₂. This “captured” CO₂ can migrate back to the soil and to atmosphere when favorable conditions are present. Different pathways and sources of soil CO₂ can be studied using stable isotope techniques. In present study natural abundance stable isotopes of carbon were used to detect and quantify the influence of subterranean cave to soil CO₂ and soil CO₂ fluxes. Soil CO₂ fluxes were measured with special chambers and a rough estimation for contribution of cave air to the CO₂ flux was made. Although present research is of great importance for understanding soil carbon dynamics in such areas, it has a potential applicability also in detection of carbon leakage from artificial subterranean storing of carbon captured from industrial sources.

Does iodine affect selenium content in buckwheat sprouts?

Ana Kroflič^{1,2}, Ana Jerše^{1,2}, Nina Kacjan Maršič³, Mateja Germ³, Helena Šircelj³, Vekoslava Stibilj¹

¹ Department of Environmental Sciences, Jožef Stefan Institute, Ljubljana, Slovenia

² Jožef Stefan International Postgraduate School, Ljubljana, Slovenia

³ Biotechnical Faculty, University of Ljubljana, Ljubljana, Slovenia

ana.kroflic@ijs.si

Selenium and iodine are essential trace elements for humans and animals. Two-third of the whole human population is suffering from their deficiency [1]. Supplementation of the diet with selenium and iodine is promising approach to improve human nutrition of both elements. Cereals, meats and fish are main source for Se [2], while iodine is supplemented mainly with salt iodination. Agronomic Se fortification is more advantageous approach than direct Se supplementation in form of Se(IV) or Se(VI), especially because plants assimilate Se into more available organic forms for humans (SeMet) [2]. Se(IV) and Se(VI) are both bioavailable for plants, but Se(IV) is less toxic form. In literature, the data about iodine supplementation in plants are scarce.

Buckwheat is considered as a functional food with high nutritional value. It is rich in vitamin B₁, B₂, lysine and potential antioxidants, such as tocopherols and phenolic substances (3-flavanols, rutin, phenolic acids) [3]. Buckwheat sprouts are widely consumed in Japan and Korea.

The aim of present work was to found out (1) how treatment with Se and I influence germination, height and mass of buckwheat sprouts, (2) the impact of different forms of Se and I on Se content in sprouts and (3) use of treated buckwheat sprouts for Se fortified food.

Approximately 30 g of buckwheat seeds were soaked for 4 h in solutions of selenite Se(IV), selenate Se(VI), iodide I(-I), iodate I(V) and combination of different forms of both elements. Each treatment were made in three replicates. Concentration of

selenium in the soaking solution was 10 mg/L and concentrations of iodine were 1000 and 1500 mg/L. Control seeds were soaked in tap water. After 10 days of germination, plants were sampled, lyophilized (Gamma 1-16 LSC, Martin Christ, Germany) and milled in the MM 200 mill (Retsch, Germany). For Se determination powder of sprouts were digested with HNO₃ in UltraWAVE digestion system (Milestone, USA), diluted to appropriate volume and detected with inductively coupled plasma – tandem mass spectrometry ICP-QQQ (Agilent Technologies, Tokyo, Japan). Se were determined in each replicate in duplicates. Accuracy and precision were checked with certified reference material Spinach leaves (NIST 1570a) and good agreement between reference value (117 ± 8) ng/g and found value (122 ± 12) ng/g was obtained.

We found out that different treatments of buckwheat sprouts with Se and/or I have minor effect on germination, height and mass. Germination in all treatments was similar (71-89 %), with exception of treatment with Se(IV) and I(V), where only 49-54 % were germinated. Height and masses in control and treated sprouts were similar.

Treatment of buckwheat sprouts increase Se content according to control plant (Table 1). Standard deviation was high, due to various Se uptake between replicate. There were no differences in Se content between soaking in different Se solutions. The uptake of Se(VI) is higher than Se(IV), because of its active transport via sulphate transporters [4]. When buckwheat sprouts were treated with Se and I (in both forms and concentrations), Se contents were increased. The highest Se content was found in buckwheat sprouts treated with Se(VI) and 1500 mg I/L in both forms. In literature, there is no data about Se-I interactions in plant. So we can only conclude, that determined Se contents showed that Se and I treated buckwheat sprouts can potentially be used for functional food to increase amount of consumed Se from food.

Acknowledgments

Research was financed by Ministry of Higher Education, Science and Technology, the Republic of Slovenia, through the program “Young researcher” PR-01678, project PR-5524 and program P1-0143.

References:

- [1] S. Smoleń, I. Kowalska, and W. Sady. Assessment of biofortification with iodine and selenium of lettuce cultivated in the NFT hydroponic system. *Scientia Horticulturae (Amsterdam)*, 166:9–16, 2014.
- [2] M. P. Rayman. Selenium and human health. *Lancet (London, England)*, 379(9822):1256–68, 2012.
- [3] M. Holasova, V. Fiedlerova, H. Smrcinova, M. Orsak, J. Lachman, and S. Vavreinova. Buckwheat—the source of antioxidant activity in functional foods. *Food Research International*, 35(2–3):207–211, 2002.
- [4] N. Terry, A. M. Zayed, M. P. de Souza, and A. S. Tarun. Selenium in higher plants. *Annual Review of Plant Physiology and Plant Molecular Biology*, 51:401–432, 2000.
- [5] C. F. L. Gonçalves, C. F. Lima Gonçalves, M. C. de S. dos Santos, M. C. de Souza dos Santos, M. G. Ginabreda, R. S. Fortunato, R. Soares Fortunato, D. P. de Carvalho, D. Pires de Carvalho, and A. C. Freitas Ferreira. Flavonoid rutin increases thyroid iodide uptake in rats. *PLoS One*, 8(9):e73908, 2013.

Table 1: Se content in Se and I enhanced buckwheat sprouts

Treatment*	c (Se) [ng/g]
Control	29 ± 13
Se(IV)	161 ± 35
Se(IV)+I(-I) ^a	242 ± 30
Se(IV)+I(-I) ^b	460 ± 23
Se(IV)+I(V) ^a	153 ± 17
Se(IV)+I(V) ^b	276 ± 70
Se(VI)	167 ± 78
Se(VI)+I(-I) ^a	213 ± 16
Se(VI)+I(-I) ^b	963 ± 257
Se(VI)+I(V) ^b	1350 ± 944

* each treatment made in three replicates

^a 1000 mg I/L

^b 1500 mg I/L

For wider interest

Selenium and iodine are essential trace elements for human and animals health. Two-third of the whole human population is suffering from selenium and iodine deficiency. Supplementation of the diet with selenium and iodine is promising approach to improve human nutrition with both elements. Cereals, meats and fish are main source for Se, while iodine is uptaken mainly with salt iodination.

Buckwheat is considered as a functional food with high nutritional value, rich in vitamin B₁, B₂, lysine and potential antioxidants, such as tocopherols and phenolic substances. Buckwheat is consumed also as buckwheat sprouts.

The aim of present work was to research (1) how treatment with Se and I influence on germination, height and mass of buckwheat sprouts, (2) the impact of different forms of Se and I on Se content in sprouts and (3) use of treated buckwheat sprouts for Se fortified food.

In our research we found out, that Se and I treatment have minor effect on agricultural parameters (germination, height and mass of sprouts). Se content were enhanced in all treatments. Se and I enhanced buckwheat sprouts can potentially be used for functional food to increase amount of consumed Se from food.

Mimicking nature – iron catalysed oxidation of alcohols

Štefan Možina^{1,2}, Stojan Stavber^{1,3}, Jernej Iskra³

¹Centre of Excellence for Integrated Approaches in Chemistry and Biology of Proteins (CIPKeBiP), Ljubljana, Slovenia

²Jožef Stefan International Postgraduate School, Ljubljana, Slovenia

³Department of Physical and Organic Chemistry, Jožef Stefan Institute, Ljubljana, Slovenia

stefan.mozina@ijs.si

Abstract. Use of molecular oxygen for oxidation is desired however its low reactivity needs to be overcome by additional activation. We have developed new method for selective aerobic oxidation of secondary alcohols. By mimicking nature we were able to obtain ketones in excellent yields by oxidation of alcohols with oxygen. Nitric acid and FeCl₃ worked as catalysts in 1,1,1,3,3,3-hexafluoro-propan-2-ol which as activator and solvent is essential for reaction to proceed. Method is selective for secondary alcohol as no oxidation occurred on primary alcohol group.

Keywords: Oxidation, iron catalyst, fluorinated alcohols, nitric acid

1 Introduction

Oxygen is the most abundant element on Earth and a third in our solar system. Free oxygen represent 21 % of Earth atmosphere though during the first half of Earth's 4.5 billion old history levels were as low as 0.001 % [1]. A cause for increasing the oxygen level was occurrence of cyanobacteria also known as chloroplast which emerged around 2.8 billion years ago. First biological production of O₂ was offset by reactions with reduced compounds originating from Earth crust. Compounds such as hydrogen, carbon, sulphur, and iron were being oxidized which consumed produced oxygen from bacteria. Consumption of molecular oxygen decreased through time. . From around 2.4 billion years ago production of O₂ was higher than its consumption and it's concentration in atmosphere started to increase. Permanent

rise of levels of molecular oxygen in atmosphere began which is now known as "Great oxidation event" [1]. Although oxygen is powerful oxidant, its low reactivity towards typical organic compounds is major obstacle. In nature this unfavourable kinetics of direct oxidation was solved by creation of aerobic respiratory chain, which takes place in the inner mitochondrial membrane of eukaryotic cells [2].

Selective oxidation of organic molecules is primary transformation in industry. Fine chemistry and pharmaceutical industry are especially in need of highly selective oxidation of alcohol group into desired products. In man-made chemistry for long time stoichiometric and toxic oxidants were used which usually were based on heavy metals. This changed at the beginning of 1990s when concept of Green chemistry was formulated. Its purpose was to design chemical products and processes which reduce or eliminate the use and generation of hazardous substances and achieve sustainability. Paul Anastas collected and summarised ideas of Green chemistry in "12 principles of Green chemistry" which work as guidelines in designing new products as well as processes to all chemists today [3]. Green chemistry was not only reducing hazards through all stages of life cycles of compounds but it has been shown to be economically profitable. Because of sustainability, non-hazardous nature, synergy and economics, Green chemistry found its way in all industry sectors (automobile, electronics, pharmaceutical, agriculture...) [4]. Nature's respiratory chain was inspiration to chemists to design new green methods for oxidation of organic compounds using molecular oxygen as oxidant. [5]. This was made possible by using different catalyst such as TEMPO [6] and/or transition metals [7-11]. Iron and copper being highly abundant, low risk metals became point of interest recently for catalysis. Developed systems range from simple catalyst [7] to bioinspired catalyst [12]. Even though iron has very desired properties, developing efficient and selective catalyst proved to be challenging compared to noble metals such as platinum, palladium etc. Course of reactions can be strongly modified by choice of solvent. Reactions in fluorinated alcohols, especially 1,1,1,3,3,3-hexafluoro-2-propanol (HFIP) and 2,2,2-trifluoroethanol (TFE), could proceed though this might not be the case in other common organic solvent. The course of reactions in fluorinated alcohols is modified due to their unique properties such as high hydrogen bonding donor ability, low hydrogen bond acceptor ability, low nucleophilicity and high ionizing power. Highly fluorinated alcohols have higher melting point and lower

boiling point (TFE – 74 °C, HFIP – 59 °C) then their non-fluorinated counterparts. This means they can be removed simply with distillation even when substrates are heat sensitive. Fluorine atoms have strong negative inductive effect that consequently increase acidity of hydroxyl group (pK_a [TFE]=12.4, pK_a [HFIP]=9.3) [13, 14]. Fluorinated alcohols act as template catalyst where they provide template which stabilizes transition state of the reaction. This effect is similar to enzyme’s function that provide complementary charge which decreases energy barrier and enables reaction to proceed [15].

In our research we combined activation of nitric acid with fluorinated alcohol and iron catalyst for aerobic oxidation of alcohols to discover method for oxidation of alcohols to ketones with remarkable selectivity and conversion.

2 Results and discussion

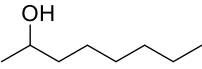
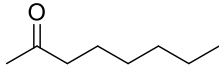
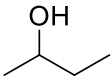
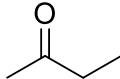
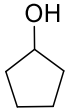
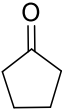
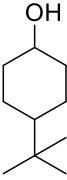
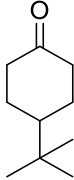
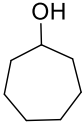
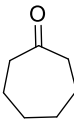
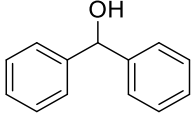
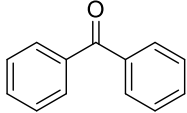
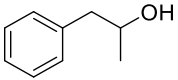
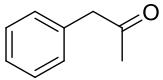
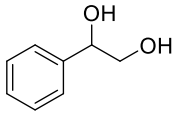
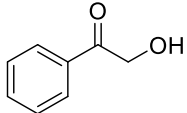
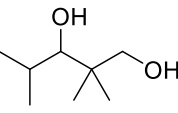
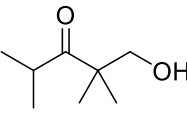
It is well known that HNO₃ has oxidative properties. NO_x gases in conjunction of TEMPO and Br₂ were successfully used for oxidation of alcohols [16]. TEMPO and its derivatives are expensive substrates and good recovery is problematic. In our study we simplified oxidation method by getting rid of need for TEMPO. Therefore we screened simple metal salts to work as co-catalyst for aerobic oxidation of 2-octanol catalysed by nitric acid and activated by HFIP. In the search of metal co-catalyst we focused mostly on iron and copper salts because of their non-toxicity, good availability and low price. We found out that of different catalysts tested 1 mol% FeCl₃ gave the best result and quantitative conversion (Table 1). HCl (3 mol%) gave also quantitative conversion of 2-octanol to 2-octanone but had lower conversion on other substrates compared to FeCl₃. Interestingly choice of counter ion was found to be important as high yield was obtained only when chlorine anions were presents. There is significant difference of conversion of 2-octanol between Fe²⁺ and Fe³⁺ which indicates there is no cycle of reduction of Fe³⁺ to Fe²⁺ and reoxidation.

Table 1: Conversion of 2-octanol into 2-octanone with aerobic oxidation catalysed with HNO₃ was depended on choice of co-catalyst.

Salt	FeCl ₃	FeCl ₂	CuI	CuCl	CuCl ₂	AlCl ₃	HCl (3 mol%)	NaCl (3 mol%)	K ₃ [Fe(CN) ₆]	Fe(NO ₃) ₃
Conv. [%]	100	57	7	12	2	1	100	1	2	8

We investigated further the effect of other solvents such as MeCN, EtOH, DCM, n-hexane, etc. on the oxidation. However, in all of them product was found only in trace amounts. This indicates HFIP has catalytic properties and is key component of reaction to proceed. We applied our method to other substrates and we obtained very good conversions and excellent selectivity (Table 2). Reaction method was selective for secondary alcohols and no reaction occurred on primary alcohol group.

Table 2: Oxidation of secondary aliphatic alcohols into ketones using HNO₃/FeCl₃/HFIP system.

Entry	Substrate	HNO ₃ [mol%]	Time [h]	Conversion (yield) [%]	Product
1		5	24	100	
2		12	7	100	
3		10	23	43	
		15	23	100	
4		15	6,5	100 (66)	
5		15	23	90 (43)	
6		12	5	100	
7		10	5	100	
8		15	22	90 (72)	
9		12	5	100 (96)	

3 Conclusion

We developed new efficient system for selective aerobic oxidation of secondary alcohols with catalytic amount of HNO_3 , molecular oxygen as terminal oxidant, while solvent played very important role. Reactions proceeded with high selectivity and excellent yield in HFIP. It is worth mentioning no reaction occurred on primary alcohol group. This makes this method very useful for selective oxidation of alcohols into ketones on big and complex substrates with no need for protection of primary alcohols which is usually done to avoid undesired products. Catalysts used are inexpensive and commercially available as well solvent can be easily recovered with distillation.

4 Acknowledgment

The financial support of the Slovenian Research Agency is greatly appreciated.

5 References

- [1] T. W. Lyons, C. T. Reinhard and N. J. Planavsky. The rise of oxygen in Earth's early ocean and atmosphere. *Nature*, 506(7488): 307-315, 2014.
- [2] J. M. Berg, J. L. Tymoczko and L. Stryer. *Biochemistry, Fifth Edition*, W.H. Freeman, 2002.
- [3] P. T. Anastas and J. C. Warner. *Green Chemistry: Theory and Practice*, Oxford University Press, Incorporated, 1998.
- [4] P. Anastas and N. Eghbali. Green Chemistry: Principles and Practice. *Chemical Society Reviews*, 39(1): 301-312, 2010.
- [5] D. V. Deubel. From Evolution to Green Chemistry: Rationalization of Biomimetic Oxygen-Transfer Cascades. *Journal of the American Chemical Society*, 126(4): 996-997, 2004.
- [6] S. Wertz and A. Studer. Nitroxide-catalyzed transition-metal-free aerobic oxidation processes. *Green Chemistry*, 15(11): 3116-3134, 2013.
- [7] M. J. Schultz and M. S. Sigman. Recent advances in homogeneous transition metal-catalyzed aerobic alcohol oxidations. *Tetrahedron*, 62(35): 8227-8241, 2006.
- [8] R. A. Sheldon. Recent advances in green catalytic oxidations of alcohols in aqueous media. *Catalysis Today*, 247(4-13), 2015.
- [9] B. L. Ryland and S. S. Stahl. Practical Aerobic Oxidations of Alcohols and Amines with Homogeneous Copper/TEMPO and Related Catalyst Systems. *Angewandte Chemie International Edition*, 53(34): 8824-8838, 2014.
- [10] S. E. Davis, M. S. Ide and R. J. Davis. Selective oxidation of alcohols and aldehydes over supported metal nanoparticles. *Green Chemistry*, 15(1): 17-45, 2013.
- [11] Q. Cao, L. M. Dornan, L. Rogan, N. L. Hughes and M. J. Muldoon. Aerobic oxidation catalysis with stable radicals. *Chemical Communications*, 50(35): 4524-4543, 2014.
- [12] L. Que and W. B. Tolman. Biologically inspired oxidation catalysis. *Nature*, 455(7211): 333-340, 2008.
- [13] J.-P. Bégué, D. Bonnet-Delpon and B. Crousse. Fluorinated Alcohols: A New Medium for Selective and Clean Reaction. *Synlett*, 2004(01): 18-29, 2004.
- [14] I. A. Shuklov, N. V. Dubrovina and A. Boerner. Fluorinated alcohols as solvents, cosolvents and additives in homogeneous catalysis. *Synthesis*(19): 2925-2943, 2007.
- [15] S. P. de Visser, J. Kaneti, R. Neumann and S. Shaik. Fluorinated Alcohols Enable Olefin Epoxidation by H₂O₂: Template Catalysis. *The Journal of Organic Chemistry*, 68(7): 2903-2912, 2003.
- [16] R. Liu, X. Liang, C. Dong and X. Hu. Transition-Metal-Free: A Highly Efficient Catalytic Aerobic Alcohol Oxidation Process. *Journal of the American Chemical Society*, 126(13): 4112-4113, 2004.

For wider interest

We have developed new method for selective aerobic oxidation of secondary alcohols. By mimicking nature we were able to obtain ketones in excellent yields. Nitric acid and FeCl_3 worked as catalyst in 1,1,1,3,3,3-hexafluoro-propan-2-ol solvent which is essential for reaction to proceed. Reaction was selective for secondary alcohols and no reaction occurred on primary alcohol group. This makes method very useful in synthesis of complex molecules where protection of primary alcohol is needed to avoid undesired reaction. Our method reduces number of steps in synthesis and material used.

Determination of polybrominated diphenyl ethers in sewage sludge with GC-ICP-MS

Petra Novak^{1,2}, Tea Zuliani¹, Radmila Milačič^{1,2}, Janez Ščančar^{1,2}

¹ Department of Environmental Sciences, Jožef Stefan Institute, Ljubljana, Slovenia

² Jožef Stefan International Postgraduate School, Ljubljana, Slovenia

petra.novak@ijs.si

Polybrominated diphenyl ethers (PBDEs) belong to the group of brominated flame retardants. They are added to different industrial materials such as plastics, furniture, electronics, textiles and building materials. When such materials are used, recycled or disposed on landfills, PBDEs can be released into the environment by leaching and volatilization. Consequently, their presence has been confirmed in all compartments of the environment. PBDEs have a high binding affinity to particles and organic matter and have been found in sediments, soils, sewage sludge, house dust, and in outdoor and indoor air [1]. They are present in biota and human tissues. Increasing concentrations of PBDEs in humans have caused health concerns due to their toxic effects on nervous system and tendency to disrupt the thyroid hormones and the reproductive organs [2]. Because of their environmental persistence, capability for long-range atmospheric transport, bioaccumulation and health-hazard potential, the European Union Water Framework Directive (WFD) listed six PBDEs (BDE 28, BDE 47, BDE 99, BDE 100, BDE 153, BDE 154) as priority hazardous substances. PBDEs enter wastewater treatment plants (WWTPs) through urban and agricultural runoffs, household domestic wastewater and industrial discharges [3]. Because of their low aqueous solubility and resistance to biodegradation, PBDEs preferentially partition into the sludge during wastewater treatment. In municipal wastewater treatment plants, up to 90 % of the PBDEs from wastewater end up in sewage sludge [4]. Therefore, the determination of PBDEs in sewage sludge is a useful strategy for assessing the environmental fate of PBDEs originally present in wastewaters. In Europe the majority of sewage sludge is disposed in landfills or applied to the land. When sewage sludge is used as fertilizer, it contributes to the release of PBDEs into the environment. Consequently, PBDEs may accumulate and transfer via the food chain, threatening the environment and human health. The

analysis of sewage sludge for PBDEs provides important information about the risks associated with the re-use of sewage sludge as biosolids for land application.

Most analytical procedures for the determination of PBDEs in sewage sludge developed in recent years employ the time- and solvent-consuming Soxhlet extraction method, accelerated solvent extraction (ASE), microwave-assisted extraction (MAE) or ultrasound-assisted extraction. Those based on the separation of PBDEs by gas chromatography (GC) coupled with different highly developed detector systems, such as high resolution mass spectrometry (HR-MS), mass spectrometry operating in the negative chemical ionization mode (NCI-MS) or electron capture detectors (ECNI-MS) are applied almost exclusively. All these analytical procedures are comprised of extraction, clean-up and instrumental analysis. Despite the fact that inductively coupled plasma mass spectrometry (ICP-MS) is a versatile and sensitive detector, it is not commonly used for the detection of separated PBDEs.

The aim of this study was to develop a simple analytical procedure with minimal sample preparation for a sensitive and reliable determination of the six PBDEs in sewage sludge samples by GC-ICP-MS.

Sewage sludge consists of a complex sample matrix, which is mostly composed of organic matter. To release the hydrophobic PBDEs from the organic and particulate matter an appropriate extraction method must be applied. For this purpose the influence of different extracting agents (methanol (MeOH), acetic acid (AcOH)/MeOH mixture (3:1) and 0.1 mol L⁻¹ HCl in MeOH) and the subsequent addition of the Tris-citrate buffer (co-extracting agent) and iso-octane on the extraction efficiency was studied when applying different modes of extraction (mechanical shaking, microwave- and ultrasound-assisted extraction). For the quantification of the PBDEs a standard addition calibration method was applied. The accuracy of the developed analytical procedure was checked by the spike recovery test and the species-specific isotope-dilution (ID) GC-ICP-MS analysis. A flow chart of the optimized analytical procedure for the determination of the six PBDEs in sewage sludge is presented in Fig. 1 and the chromatogram of the sewage sludge spiked with internal standard BDE 77 is shown in Fig. 2. The developed GC-ICP-MS analytical procedure was applied for a determination of the PBDEs in sewage sludge samples from WWTP Domžale-Kamnik, Slovenia, collected in 1998, 2000 and 2014. These results are presented in Table 1. The most abundant BDE

congeners in the samples analysed were BDE 47 and BDE 99, which is in accordance with the typical profile usually found in sewage sludge. The concentrations of the BDEs decreased with time. The decreasing concentration changes are reasonable, based on the regulatory actions and the reduced usage of PBDEs in society.

Accuracy checks were made by the spike recovery test of sludge samples spiked with PBDEs and by the ID-GC-ICP-MS analysis. The recoveries for the six PBDEs ranged from 95 to 104 %, while the differences between the results determined by both techniques did not exceed 4%. Good repeatability and reproducibility of measurements RSDs (2.2 to 5.7 %) was obtained. The procedure is very sensitive with LODs for six PBDEs congeners ranging from 0.2 to 0.3 ng g⁻¹.

The procedure is simple and requires minimal sample preparation, which is the main advantage over commonly applied procedures based on GC-MS analysis that consume much more reagents and solvents and require tedious clean-up steps before the MS detection. In general, the RSDs are better and the LODs lower as those reported in the literature. Due to its simplicity, reliability and sensitivity, the developed method is appropriate for use in laboratories that routinely monitor the PBDEs in sewage sludge. To demonstrate the applicability of the newly developed procedure, PBDEs were determined in sewage sludge from WWTP Domžale-Kamnik.

Acknowledgments

This work was supported by the Ministry of Higher Education, Science and Technology of the Republic of Slovenia (Programme group P1-0143).

References:

- [1] R.C. Hale, M.J. La Guardia, E. Harvey, M.O. Gaylor, T.M. Mainor. Brominated flame retardant concentrations and trends in abiotic media. *Chemosphere*, 64:181-186, 2006.
- [2] J.L. Lyche, C. Rosseland, G. Berge, A. Polder. Human health risk associated with brominated flame-retardants (BFRs). *Environment International*, 74:170-180, 2015.
- [3] B. Gevao, S. Muzaini, M. Helaleh. Occurrence and concentrations of polybrominated diphenyl ethers in sewage sludge from three wastewater treatment plants in Kuwait. *Chemosphere*, 71(2):242-247, 2008.
- [4] K.D. North. Tracking Polybrominated Diphenyl Ether Releases in a Wastewater Treatment Plant Effluent, Palo Alto, California. *Environmental Sciences and Technologies*, 38:4484-4488, 2004.

Table 1: Concentrations of PBDEs found in sewage sludge samples from WWTP Domžale-Kamnik.

Sampling year	BDE congener (ng g ⁻¹ dw)					
	BDE 28	BDE 47	BDE 99	BDE 100	BDE 153	BDE 154
1998	<0,209	49,9±2,1	66,6±1,5	13,4±0,3	4,20±0,4	4,7±0,2
2000	1,12±0,03	38,6±1,6	29,30±0,7	8,1±0,2	7,3±0,4	5,3±0,2
2014	1,40±0,04	20,1±0,9	12,7±0,3	6,4±0,1	9,6±0,18	3,11±0,03

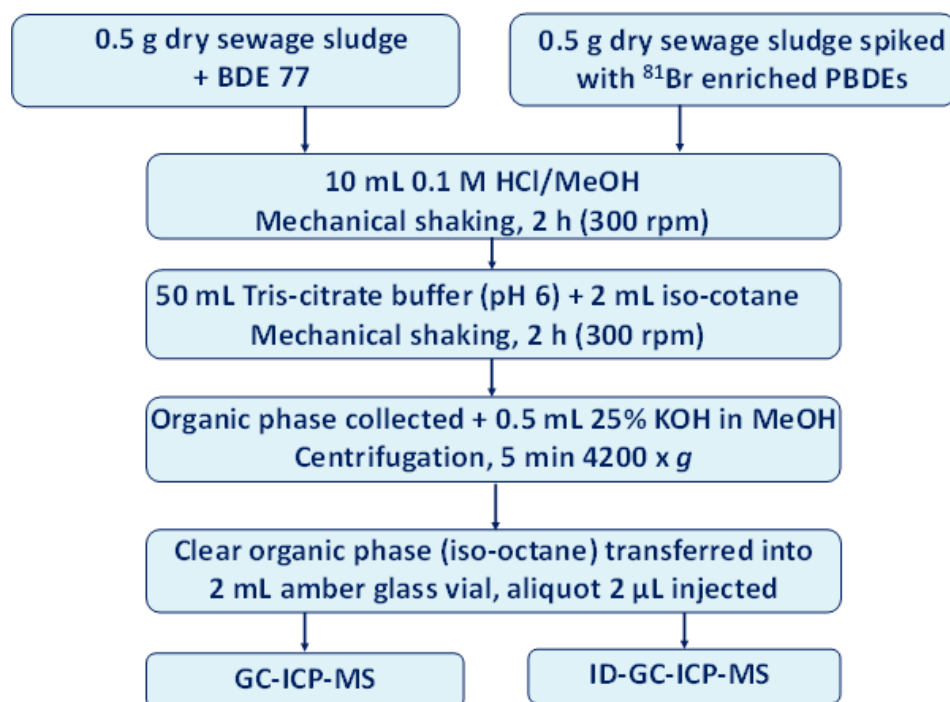


Figure 1: Flow chart of the analytical procedure for the determination of PBDEs in sewage sludge.

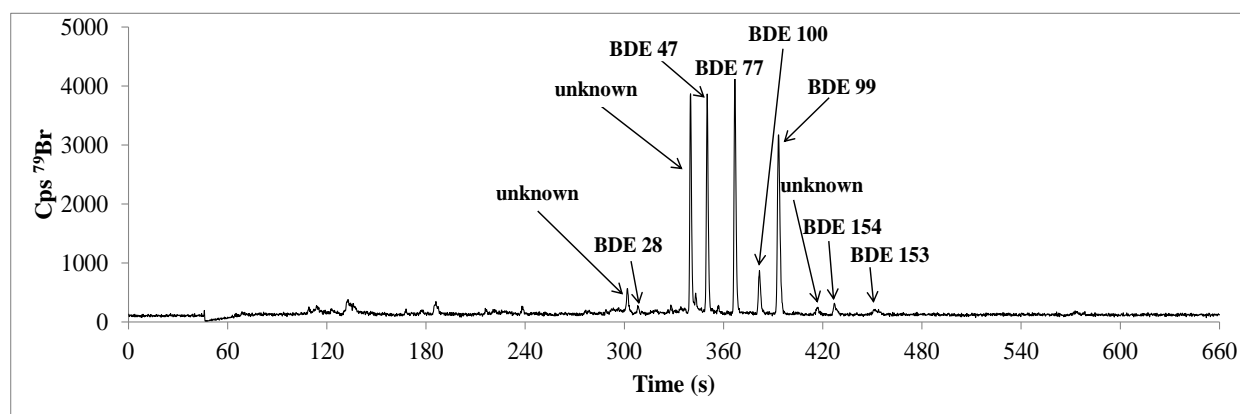


Figure 2: Chromatogram of the sewage sludge (WWTP Domžale-Kamnik, sampling year 2000) spiked with internal standard BDE 77 (12ng mL⁻¹ iso-octane).

For wider interest

Polybrominated diphenyl ethers (PBDEs) belong to the group of brominated flame retardants. They are persistent organic pollutants that are via food chain bioaccumulated or biomagnified in living organisms. Increasing concentrations of PBDEs in humans have caused health concerns due to their toxicity. In municipal wastewater treatment plants, up to 90 % of the PBDEs from wastewater end up in sewage sludge. The analysis of sewage sludge for PBDEs provides valuable information about the risks associated with the re-use of sewage sludge as biosolids for land application. Thus, reliable analytical methods are needed in order to evaluate the contribution of contaminated sewage sludge to the PBDEs' pollution of the environment. The newly developed method is simple, reliable and sensitive. To demonstrate the applicability of the procedure, PBDEs were determined in sewage sludge samples from WWTP Domžale-Kamnik.

Razvoj metod za pripravo aciloksialkilnih predzdravil fosfatov ter uporaba topil, primernih za farmacevtsko industrijo

Jerca Pahor,^{1,2} Ajda Podgoršek Berke,^{2,3} Alen Čusak,^{3,4} Gregor Kosec,³
Hrvoje Petković,³ Stojan Stavber,^{1,2,5}

¹ Laboratorij za organsko in bioorgansko kemijo, Odsek za fizikalno in organsko kemijo, Institut »Jožef Stefan«, Ljubljana, Slovenija

² Mednarodna podiplomska šola Jožefa Stefana, Ljubljana, Slovenija

³ Acies Bio d.o.o., Ljubljana Slovenija

⁴ Alkemika LTd., Kukovčeva 1, 3000 Celje, Slovenija.

⁵ Center odličnosti za integrirane pristope v kemiji in biologiji proteinov, Ljubljana, Slovenija

jerca.pahor@ijs.si

Povzetek. Fosfatna skupina je zaradi svojih specifičnih lastnosti pogost strukturen element v različnih zdravilnih učinkovinah. Pri razvoju učinkovin, ki imajo fosfatno skupino, pa je potrebno precej pozornosti posvetiti njihovi omejeni biološki dostopnosti, ki jo lahko izboljšamo s pripravo predzdravila. Med predzdravili fosfatov je najobetavnejša sinteza različnih aciloksialkilnih estrov, vendar je nabor metod za njihovo učinkovito pripravo omejen. V okviru naših raziskav na področju razvoja novih metod smo pripravili nov klorofosfatni reagent, ki omogoča pripravo predzdravil fosfatov, maskiranih z izobutiriloksimetilnimi skupinami. Preverili smo uporabnost reagenta za fosforiliranje različnih tipov alkoholov, pri čemer smo uporabili mile in ekonomične reakcijske pogoje. Poleg tega smo preverjali tudi možnost uporabe topil, sprejemljivejših za farmacevtsko industrijo in pokazali, da je pripravljen reagent možno uporabiti tudi v manj strupenih topilih.

Ključne besede: Predzdravila fosfatov, Aciloksialkilne maskirne skupine, Fosforiliranje alkoholov

1 Uvod

Fosfatna skupina je zaradi svojih specifičnih lastnosti pogost strukturen element v različnih spojinah z biološko aktivnostjo. Mednje sodi širok nabor učinkovin za zdravljenje virusnih in rakavih obolenj [1], poleg tega pa farmacevtski interes zbuja tudi fosforilirani derivati pantotenske kisline, ki bi lahko bistveno izboljšali kakovost življenja bolnikov z redko dedno nevrodegenerativno boleznijo – nevrodegeneracijo, povezano s pantotenat kinazo (PKAN) [2]. Pri razvoju potencialnih učinkovin, ki imajo fosfatno skupino, pa je potrebno precej pozornosti posvetiti tudi njihovi omejeni biološki dostopnosti. Fosfatni monoestri imajo namreč običajno nizke vrednosti pK_a , zaradi česar so pri fiziološkem pH deprotonirani [3]. Zaradi močnega negativnega naboja so zato spojine, ki vsebujejo fosfatno skupino, večinoma nezmožne pasivnega prehoda čez celične membrane in zato biološko neaktivne. Temu problemu se lahko učinkovito izognemo s pripravo predzdravila, in sicer z uvedbo maskirnih skupin, ki nevtralizirajo negativen naboj ter omogočijo prehod fosfata v notranjost celic ter tako povečajo biološko uporabnost spojine. Znanih je kar nekaj različnih predzdravilnih pristopov, ki lahko povečajo zmožnost fosfatov prehajanja čez membrane [1,3,4]. Najpogosteje uporabljen tip predzdravila za fosfate in fosfonate so aciloksialkilni estri [1]. Večina objavljenih procedur za pripravo tovrstnih predzdravil fosfatov je vezanih na pripravo pivaloiloksimetilnih (POM) estrov ter vključuje več-stopenjske reakcije in večinoma zelo nizke izkoristke. Še manj obetavni pa so objavljeni sintezni postopki za pripravo drugih aciloksialkilnih estrov, ki jih je v literaturi mogoče zaslediti precej redkeje. Kemijska stabilnost posameznih aciloksialkilnih skupin močno variira glede na njihovo strukturo, zato je za optimalen razvoj aktivnih učinkovin nujna dostopnost metod za učinkovito pripravo različnih aciloksialkilnih predzdravil, ki omogočajo pripravo derivatov z različnimi maskirnimi skupinami in primerjavo njihove bioaktivnosti ter farmakokinetičnih lastnosti med seboj. Razvoj metod za učinkovito pripravo najrazličnejši aciloksialkilnih predzdravilnih oblik je zato ključen za optimalen razvoj novih zdravil, ki vsebujejo fosfatno skupino.

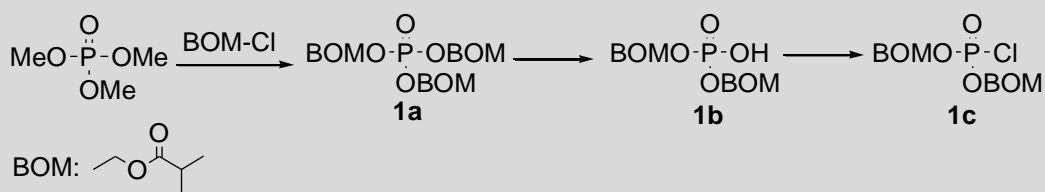
2 Materiali in metode

Vse kemikalije, ki smo jih uporabil pri delu, so komercialno dostopne pri znanih dobaviteljih (Sigma Aldrich, Merck, Fluka, AKos GmbH). Razen reakcij, ki smo jih

izvedli v vodnem mediju, smo reakcije izvedli pod argonovo atmosfero, v sušeni steklovini in z uporabo brezvodnih topil. Brezvodna topila smo hranili na aktiviranih molekulskih sitih (4 \AA) ali brezvodnem Na_2SO_4 pod dušikovo atmosfero. Tankoplastno kromatografijo smo izvajali na ploščah Silica gel/TLC-cards DC-Alufolien-Kieselgel proizvajalca Fluka z $0,2 \text{ mm}$ nanosom silikagela na aluminijastem nosilcu. V primerih, ko spojine niso absorbirale v UV območju, smo za vizualizacijo produktov uporabljali raztopino kalijevega permanganata. Za kolonsko kromatografijo smo uporabljali silikagel: Silicagel 60 Angstrom proizvajalca Fluka s premerom delcev $0.040 - 0.063 \text{ mm}$. ^1H , ^{13}C in ^{31}P NMR spektre smo posneli na Kemijskem inštitutu (NMR center) z Varian Inova 300 spektrometrom (300 MHz) pri $25 \text{ }^\circ\text{C}$. Kemijske premike (δ) smo določevali v ppm glede na interni standard (Me_4Si) v ^1H NMR, glede na signal topila (CDCl_3) v ^{13}C NMR ali glede na zunanji standard ($85 \text{ \% H}_3\text{PO}_4$) v ^{31}P NMR spektrih. Meritve na visokoločljivostnem masnem spektrometru (HR-MS) so nam posneli na Centru za masno spektroskopijo Instituta »Jožef Stefan«.

3 Rezultati

Pregled literature je pokazal, da večina razsikav s področja priprave aciloksialkilnih predzdravil fosfatov zajema zgolj pripravo POM predzdravil. Za uvedbo te maskirne skupine na fosfatno skupino spojin je v literaturi moč zaslediti tri različne sintezne pristope [5-7]. O najboljših izkoristkih poročajo avtorji, ki uporabljajo metodo, ki vključuje pripravo ustreznega klorofosfatnega reagenta bis(POM) klorofosfata [7]. Do enake ugotovitve smo prišli tudi sami in sicer na podlagi izkušenj, pridobljenih na področju priprave predzdravil fosforiliranih spojin [8]. Zato smo želeli ta učinkovit pristop preizkusiti tudi za pripravo drugih aciloksialkilnih predzdravil fosfatov, saj priprava klorofosfatnih reagentov z drugimi aciloksialkilnimi skupinami v literaturi še ni bila raziskana. Sklepali smo, da je priprava drugih sorodnih reagentov možna, in sicer z manjšo modifikacijo recepture za pripravo POM reagenta [7]. V prvi stopnji sinteze reagenta smo tako namesto pivaloilmetil klorida uporabili klorometil isobutirat in uspešno pripravili klorofosfatni regent z isobutiriloksimetilnimi (BOM) skupinami **1c (Shema 1)**.



Shema 1. Sinteza bis(isobutiriloksimetil) klororfosfata **1c**.

S tem smo pokazali, da je metodo za pripravo bis(POM) klorofosfata [7] mogoče razširiti tudi za pripravo klorofosfatnih reagentov z drugimi aciloksialkilnimi skupinami, kot je BOM. Uporabnost novo pripravljenega reagenta **1c** za fosforiliranje različnih substratov smo tudi preizkusili. Pred tem smo s pomočjo modelnega sistema optimizirali reakcijske pogoje. Pri tem smo si za prvi substrat izbrali benzilni alkohol (**2a**) ter ga fosforilirali z komercialno dostopnim dietil klorofosfatom (**3**). Preizkusili smo različne baze ter različna topila, ki se tipično uporabljajo za fosforiliranje z klorofosfatnimi reagenti (**Tabela 1**). Najboljši izkoristek smo dobili pri reakciji, ki smo jo izvedli v diklorometanu (DCM) s kombinacijo baze *N,N*-diisopropiletil amina (DIPEA) in katalitskih količin 4-dimetilaminopiridina (DMAP) (**Tabela 1**, Vrstica 12). To kombinacijo baz je mogoče pogosto zaslediti v literaturi za fosforiliranje različnih bioloških molekul [9-11], zato nas rezultati niso presenetili. V nadaljevanju optimizacije pogojev smo s pomočjo primerjalnih eksperimentov določili še količine reagentov ter reakcijski čas. Končni optimizirani pogoji vključujejo: 1,5 ekvivalenta DIPEA, 0,1 ekvivalenta DMAP v kombinaciji 1,3 ekvivalenta klorofosfatnega reagenta **3**, reakcija pa je bila uspešno zaključena v 2 urah s 94-odstotnim izkoristkom.

Tabela 1. Fosforiliranje na modelnem sistemu z različnimi reagenti ^a

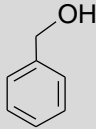
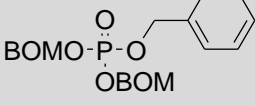
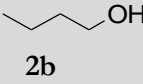
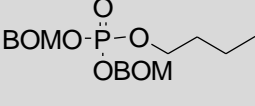
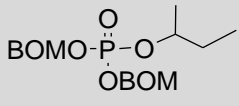
c1ccc(cc1)CO (**2a**) + CCOP(=O)(Cl)OCC (**3**) $\xrightarrow[\text{Topilo}]{\text{Amin}}$ c1ccc(cc1)COP(=O)(OCC)OCC (**3a**)

Vhod	Amin	Ekv. amina	Ekv. 3	Topilo	Izkoristek [%] ^b
1	Et ₃ N	1.5	1.5	THF	10
2	Et ₃ N	1.5	1.5	MeCN	21
3	Et ₃ N	1.5	1.5	DCM	34
<hr/>					
4	Pyridine	1.5	1.5	THF	13
5	Pyridine	1.5	1.5	MeCN	78
6	Pyridine	1.5	1.5	DCM	83
<hr/>					
7	DABCO	1.5	1.5	THF	84
8	DABCO	1.5	1.5	MeCN	68
9	DABCO	1.5	1.5	DCM	84
<hr/>					
10	DIPEA, DMAP	1.5, 0.1	1.5	THF	83
11	DIPEA, DMAP	1.5, 0.1	1.5	MeCN	42
12	DIPEA, DMAP	1.5, 0.1	1.5	DCM	93

^aRekcijski pogoji: benzil alkohol **2a** (0,5 mmol) in amin sta bila raztopljena v topilu (2,5 ml), dietil klorofosfat **3** je bil dodan po kapljicah pod Ar, reakcijsko zmes pa smo mešali pri sobni temperature še dodatni dve uri. ^bKonverzijo v **3a** smo določili z ¹H NMR spektroskopijo surove reakcijske zmesi.

V nadaljevanju študije smo uporabili optimizirane reakcijske pogoje z modelnega sistema za fosforiliranje z bis(BOM) klorofosfatnim reagentom **1c**. Izbrali smo si tri različne alkohole in sicer benzilni (**2a**), butan-1-ol (**2b**) ter alkohol butan-2-ol (**2c**) (Tabela 2). Oba primarna alkohola (**2a** in **2b**) smo fosforilirali z dobrim izkoristkom (72-77 %), sekundarni alkohol (**2c**) pa pričakovano z nekoliko nižjim izkoristkom (39 %). Pri tem velja poudariti, da smo za fosforiliranje uporabili neprimerno bolj mile in ekonomične pogoje od tistih, ki so bili v literaturi objavljeni za uporabo s sorodnim bis(POM) klorofosfatom. V primerih iz literature so avtorji za uspešno fosforiliranje uporabili 5 ekvivalentov bis(POM) klorofosfata ter od 7 do 13 ekvivalentov baze [7,12]. V našem primeru pa smo uspešno fosforiliranje dosegli z zgolj 1,5 ekvivalenta bis(BOM) klorofosfata (**1c**), 1,5 ekvivalenta DIPEA ter 0,1 ekvivalenta DMAP (Tabela 2).

Tabela 2. Fosforiliranje različnih alkoholov z bis(BOM) klorofosfatom (1c).^a

$\text{R-OH} + \text{BOMO}-\overset{\text{O}}{\underset{\text{OBOM}}{\text{P}}}-\text{Cl} \longrightarrow \text{BOMO}-\overset{\text{O}}{\underset{\text{OBOM}}{\text{P}}}-\text{O-R}$		
Vhod	Alkohol	Produkt, izkoristek ^b
1	 2a	 4a, 72 %
2	 2b	 4b, 77 %
3	 2c	 4c, 39 %

^aReakcijski pogoji: alkohol **2a**, **2b** ali **2c** (1 mmol), DIPEA (1,5 ekv.) in DMAP (0,1 ekv.) so bili raztopljeni v DCM (10 ml). Bis(BOM) klorofosfat **1c** (1,5 equiv.) je bil dodan kot raztopina v 5 ml DCM pod Ar pri 0°C. Reakcijsko zmes smo pri sobni temperaturi mešali še dodatnih 12 h. ^bIzkoristek izoliranega in očiščenega produkta.

V zadnjem delu raziskave smo želeli preveriti možnost fosforiliranja s pripravljenim klorofosfatnim reagentom v topilih, ki so manj strupena in nevarna za človekovo zdravje (3. razred topil v farmacevtski industriji, [13]). V ta namen smo se ponovno vrnili k modelnemu sistemu, s katerim smo želeli primerjati potek fosforiliranja v različnih topilih: heptanu, *tert*-butil metil etru, etil acetatu ter v 2-metiltetrahydrofuranu (**Tabela 3a**). Izkoristka doseženega v diklorometanu sicer nismo dosegli (94 %), smo pa se mu približali, in sicer z uporabo 2-metiltetrahydrofurana (82 %) (**Tabela 3a**, Vhod 5). Topilo smo zato uporabili tudi za fosforiliranje z novim reagentom **1c** in tudi v tem primeru uspešno izolirali željen produkt z nekoliko manjšim, pa vendar uporabnim izkoristkom (**Tabela 3b**, Vhod 2).

Tabela 3. (a) Primerjava topil za fosforiliranje na modelnem sistemu,^a (b) Fosforiliranje z **1c** v 2-metiltetrahydrofuranu.^c

(a)			(b)		
<p style="text-align: center;"> <chem>c1ccc(cc1)CO + ClP(=O)(OCC)OCC >> c1ccc(cc1)COP(=O)(OCC)OCC</chem> 2a 3 3a </p>			<p style="text-align: center;"> <chem>c1ccc(cc1)CO + ClP(=O)(OBOM)OBOM >> c1ccc(cc1)COP(=O)(OBOM)OBOM</chem> 2a 1c 4a </p>		
Vhod	Topilo	Izkoristek ^b	Vhod	Topilo	Izkoristek ^d
1	DCM	94	1	DCM	72
2	heptan	31	2	2-Me-THF	30
3	<i>t</i> -BuOMe	50			
4	EtOAc	74			
5	2-Me-THF	82			
^a Rekcijski pogoji: benzil alkohol 2a (0,5 mmol), DIPEA (1,5 ekv.) in DMAP (0,1 ekv.) so bili raztopljeni v DCM (2,5 ml), dietil klorofosfat 3 je bil dodan po kapljicah pod Ar, reakcijsko zmes pa smo mešali pri sobni temperature še dodatni dve uri. ^b Konverzijo v 3a smo določili z ¹ H NMR spektroskopijo surove reakcijske zmesi.			^c Reakcijski pogoji: benzil alkohol 2a (1 mmol), DIPEA (1,5 ekv.) in DMAP (0,1 ekv.) so bili raztopljeni v DCM (10 ml). Bis(BOM) klorofosfat 1c (1,5 equiv.) je bil dodan kot raztopina v 5 ml DCM pod Ar pri 0°C. Reakcijsko zmes smo pri sobni temperaturi mešali še dodatnih 12 h. ^d Izkoristek izoliranega in očiščenega produkta.		

4 Zaključki

Z namenom razvoja učinkovitih metod za pripravo različnih aciloksialkilnih predzdravil fosfatov smo uspešno sintetizirali nov klorofosfatni reagent, primeren za fosforiliranje različnih tipov alkoholov. Tako pripravljen reagent bis(BOM) klorofosfat omogoča uspešno uvedbo BOM skupin skupaj s fosfatno skupino, kar se je v primeru uvajanja POM maskirnih skupin izkazalo za najučinkovitejši način priprave tovrstnih predzdravil. Z novim reagentom smo uspešno fosforilirali več različnih tipov alkoholov, s čimer smo dokazali uporabnost reagenta za fosforiliranje. Pri tem smo uporabili reakcijske pogoje, ki so neprimerljivo bolj ekonomični od pogojev uporabljenih v literaturi. V zadnjem delu študije, pa smo pokazali, da je reagent mogoče uporabiti tudi v manj toksičnem topilu 2-metiltetrahydrofuranu.

Zahvala

Avtorji se zahvaljujemo za finančno pomoč Javni agenciji za raziskovalno dejavnost Republike Slovenije (PR-05021 and PR-0134). Delo je bilo financirano tudi s Sedmim okvirnim programom Evropske Komisije (št. FP7/2007-2013, HEALTH-F2-2011, št. sporazuma 277984, TIRCON podjetju Acies Bio d.o.o.). Za pomoč pri NMR analizah se zahvaljujemo Slovenskemu NMR centru Kemijskega inštituta ter Centru za masno spektroskopijo Inštituta »Jožef Stefan« za meritve na visokoločljivostnem masnem spektrometru. Za pomoč ter souporabo laboratorijev se zahvaljujemo raziskovalcem podjetja Acies Bio.

Literatura:

- [1] Hecker SJ, Erion MD. Prodrugs of Phosphates and Phosphonates. *Journal of Medicinal Chemistry*. 2008;51(8):2328-2345.
- [2] Srinivasan B, Baratashvili M, van der Zwaag M, et al. Extracellular 4[prime]-phosphopantetheine is a source for intracellular coenzyme A synthesis. *Nature Chemical Biology*. 2015;11(10):784-792.
- [3] Schultz C. Prodrugs of biologically active phosphate esters. *Bioorganic & Medicinal Chemistry*. 2003;11(6):885-898.
- [4] Krise JP, Stella VJ. Prodrugs of phosphates, phosphonates, and phosphinates. *Advanced Drug Delivery Reviews*. 1996;19(2):287-310.
- [5] Rutschow S, Thiem J, Kranz C, Marquardt T. Membrane-Permeant derivatives of mannose-1-phosphate. *Bioorganic & Medicinal Chemistry*. 2002;10(12):4043-4049.
- [6] Farquhar D, Khan S, Srivastva DN, Saunders PP. Synthesis and Antitumor Evaluation of Bis[(pivaloyloxy)methyl] 2'-Deoxy-5-fluorouridine 5'-Monophosphate (FdUMP): A Strategy To Introduce Nucleotides into Cells. *Journal of Medicinal Chemistry*. 1994;37(23):3902-3909.
- [7] Hwang Y, Cole PA. Efficient Synthesis of Phosphorylated Prodrugs with Bis(POM)-phosphoryl Chloride. *Organic Letters*. 2004;6(10):1555-1556.
- [8] Jenko B, Kosec. G, Petkovic H, et al., Inventors. Stable pantetheine derivatives for the treatment of pantothenate kinase associated neurodegeneration (pkan) and methods for the synthesis of such compounds. US patent WO2015063177. 7 May 2015.
- [9] Parry RJ, Burns MR, Skae PN, Hoyt JC, Pal B. Carbocyclic analogues of d-ribose-5-phosphate: Synthesis and behavior with 5-phosphoribosyl α -1-pyrophosphate synthetases. *Bioorganic & Medicinal Chemistry*. 1996;4(7):1077-1088.
- [10] Soliveri G, Bertolotti A, Panza L, Poletti L, Jones C, Lay L. Synthesis of phosphorylated fragments of Streptococcus pneumoniae type 19F capsular polysaccharide. *Journal of the Chemical Society, Perkin Transactions 1*. 2002(19):2174-2181.

- [11]Walker SR, Jiao W, Parker EJ. Synthesis and evaluation of dual site inhibitors of 3-deoxy-d-arabino-heptulosonate 7-phosphate synthase. *Bioorganic & Medicinal Chemistry Letters*. 2011;21(17):5092-5097.
- [12]Hwang Y, Ganguly S, Ho AK, Klein DC, Cole PA. Enzymatic and cellular study of a serotonin N-acetyltransferase phosphopantetheine-based prodrug. *Bioorganic & Medicinal Chemistry*. 2007;15(5):2147-2155.
- [13]Residual solvents - US Pharmacopeial Convention. http://www.usp.org/sites/default/files/usp_pdf/EN/USPNF/generalChapter467Current.pdf. Accessed March 2016.

Za širše zanimanje

Za uspešno pripravo zdravil je ključna učinkovitost kemijskih metod, ki omogočajo sintezo učinkovin. V primeru aktivnih učinkovin, ki vsebujejo fosfatno skupino, je potrebno te dodatno modificirati, da lahko dosežemo želeno delovanje, t.j. pripraviti »predzdravilo«, ki omogoči učinkovito delovanje zdravila. Ker metod na tem področju primanjkuje, smo tekom naših raziskav razvili novo metodo, ki omogoča uspešno pripravo enega izmed tovrstnih predzdravil. Pri tem smo uporabili ekonomične reakcijske pogoje, s čimer je mogoče zmanjšati stroške sinteze tovrstnih učinkovin in topila, ki so manj škodljiva od topil, ki se jih običajno uporabljajo v sintezni kemiji in so primerna tudi za sintezo v farmacevtski industriji.

A study of the thermal release of mercury compounds in FGD gypsum from the Šoštanj Thermal Power Plant using mass spectrometry

Majda Pavlin^{1,2}, Arkadij Popović¹, Radojko Jačimović¹, Milena Horvat^{1,2}

¹ Department of Environmental Sciences, Jožef Stefan Institute, Ljubljana, Slovenia

² Jožef Stefan International Postgraduate School, Ljubljana, Slovenia

majda.pavlin@ijs.si

The Šoštanj Thermal Power Plant (ŠTPP) is important for generating electricity (1304 MW) and district heating energy (300-350 GWh) [1]. The power plant burns lignite (brown coal), which is comes from the nearby Velenje Coal Mine. At the power station different air pollution control devices (APCD), such as electrostatic precipitators (ESP) for removing particulates and a wet flue gas desulphurization system (FGD) to remove SO₂, have been installed with the purpose of reducing emissions (trace elements, particles, gases) into the environment [2]. An important by-product of flue gas desulphurization is gypsum (CaSO₄·2H₂O), which is produced by reacting sulphur dioxide (contained in the flue gas) with a CaCO₃-water suspension. There are many uses of FGD gypsum for example in the production of construction materials (e.g., wallboard), concrete and in agricultural applications.

Flue gas can contain a significant amount of elemental Hg and different Hg species, which can end up in waste materials (fly ash) and importantly in FGD gypsum. Mercury is a well-known environmental pollutant that affects human and ecosystem health. Understanding the potential release Hg, therefore, is important when using FGD gypsum as a feedstock in further applications.

The factors that affect the final partitioning of Hg and its compounds during coal combustion are the: mineral content and their distribution in the coal; particle size since small particles pass through the ESP and enter into the wet FGD system, and physical process factors such as the presence of emission control devices (FGD process) and the temperature and turbulence of the flue gases [3,4]. During combustion, mercury undergoes various oxy/redox processes and can even precipitate in the wet FGD system [5]. As the FGD slurry settles, gypsum separates into a heavy coarse fraction (grey colour) at the bottom and a light fine fraction (brown colour) at the top. This fine fraction contains less CaSO₄·2H₂O, but has a

higher concentration of mercury. Particle size, therefore, is also an important factor in the accumulation of mercury and other (trace) elements in FGD [6].

The aim of this study was to develop a new method for identifying the various mercury compounds present in the FGD gypsum from the ŠTTP. To achieve this cold vapour atomic absorption spectrometry (CV AAS), typically used to measure Hg, was replaced by mass spectrometry (MS). Mass spectrometry has several advantages over CV AAS. It is more sensitive and a variety of different volatile compounds can be detected, whereas CV AAS only detects elemental mercury. In principle, the method is similar to temperature fractionation, where AAS is used to identify the mercury compounds in gypsum and represents a continuation of work already published [7]. Briefly, samples of gypsum from the ŠTTP were separated into fine and coarse fractions. Prior to analysis, all the samples were dried, washed and homogenized. Each sample (1-10 mg) was loaded into a quartz tube, heated to 650 °C at 10 °C/min and analysed by MS. Identification of mercury compounds was based on a comparison of the thermograms of different mercury standards (e.g., HgCl₂, Hg₂Cl₂, HgS, HgSe, HgO, HgSO₄ and Hg₂SO₄ mixed with pure CaSO₄·2H₂O) with the thermograms of the FGD gypsum samples.

In the MS, ions originating from the sample matrix can interfere with the measurement and the overlapping of these ions with mercury ions can significantly influence the shape of the mercury releasing peak. Background optimization is, therefore, an important if not essential step in obtaining reliable results at low mercury concentrations. For this reason, a washing step was included in the method as an efficient means of reducing background interference. The concentration of total mercury in FGD gypsum (mixture of finer and coarser fraction) is typically low (< 1 µg·g⁻¹) and in the coarse fraction is even lower and often close to or below the LOD (< 0.2 µg g⁻¹ of Hg) for CV AAS. Fortunately, the much higher sensitivity of the MS enables a reliable release profile in samples containing as little as 0.05 µg g⁻¹ of Hg. These release profiles are presented as thermograms of intensity versus temperature where the ²⁰⁰Hg isotope was chosen due to its smaller background influence compared to the ²⁰²Hg. The thermograms of the fine fraction and the coarse fraction reveal differences in the mercury desorption/decomposition peaks, especially in peak intensity and peak shape (Fig. 1). This suggests that particle size and the concentration of mercury in the different size fractions of the gypsum are important parameters in the retention of Hg.

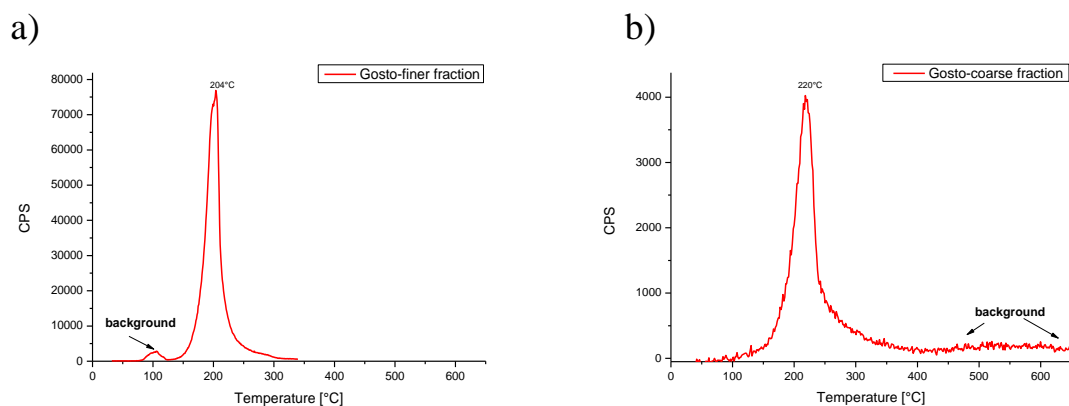


Figure 1: (a) Finer fraction and (b) coarse fraction.

Identifying, the peaks in relation to authentic mercury compounds remains problematic, since the observed peaks do not that match exactly with the peak maximum in the samples and despite MS allowing multiple species to be observed, the simultaneous interpretation of the decomposition profile of mercury compounds present in the samples remains challenging. This is especially true when mercury is present at low concentrations.

In summary, understanding the stability of mercury compounds is important since knowledge of the temperature at which Hg is released can aid in the design of the whole production process of new construction materials. This also applies weather waste material (fly ash) must be treated prior to being landfilled since conditions of disposal can affect the release of mercury into its surroundings. Both MS and CV AAS are useful methods for observing the stability of mercury compounds, but MS is more sensitive than CV AAS with LOD as low as $0.05 \mu\text{g g}^{-1}$. Method optimization further improved sensitivity allowing Hg decomposition profiles to be obtained. The interpretation of the measurements using MS is also easier since decomposition products such as SO_2 and HCl can be determined. Nevertheless, identifying the different mercury compounds present in actual samples from the power station remains a challenge, and this study represents work-in-progress and additional experiments will be performed to identify the different mercury compounds present in FGD gypsum samples.

Acknowledgments

This work was supported by the ARRS program P1-0143 and the ARRS young researcher program. I would like to thank my supervisor prof. dr. Milena Horvat and the guidance of dr. Arkadij Popović and his help in the preparation of this extended abstract.

References:

- [1] Webpage of Šoštanj Thermal Power Plant. <http://www.te-sostanj.si/si>, March 2016.
- [2] J.H. Pavlish, E.A. Sondreal, M.D. Mann, E.S. Olson, K.C. Galbreath, D.L. Laudal, S.A. Benson. Status review of mercury control options for coal-fired power plants. *Fuel Processing Technology* 82, 89–165, 2003.
- [3] R. Meij, Trace element transformations in coal-fired power systems: Trace element behaviour in coal-fired power plants, *Fuel Processing Technology*, 39(1), 199-217, 1994.
- [4] M. Xu, R. Yan, C. Zheng, Y. Qiao, J. Han, C. Sheng, Status of trace element emission in a coal combustion process: a review, *Fuel Processing Technology*, 85 (2–3), 215-237, 2004.
- [5] A. Stergaršek; M. Horvat; P. Frkal, S.R. Guevara, R. Kocjancic. Removal of Hg⁰ in wet FGD by catalytic oxidation with air - A contribution to the development of a process chemical model. *Fuel*, 107, 183-191, 2013.
- [6] A. Stergaršek, M. Horvat, J. Kotnik, J. Tratnik, P. Frkal, D. Kocman, R. Jaćimović, V. Fajon, M. Ponikvar, I. Hrastel, J. Lenart, B. Debeljak, M. Čujež, The role of flue gas desulphurisation in mercury speciation and distribution in a lignite burning power plant, *Fuel* 87 (17–18), 3504-3512, 2008.
- [7] M. Sedlar, M. Pavlin, R. Jaćimović, A. Stergaršek, P. Frkal, and M. Horvat. Temperature Fractionation (TF) of Hg Compounds in Gypsum from Wet Flue Gas Desulfurization System of the Coal Fired Thermal Power Plant (TPP). *American Journal of Analytical Chemistry*, 6, 939-956, 2015.

For wider interest

The Šoštanj Thermal Power Plant (ŠTPP) is the biggest power plant in Slovenia and is important in generating the electricity and district heating energy. Flue gas desulphurization (FGD) gypsum ($\text{CaSO}_4 \cdot 2\text{H}_2\text{O}$) is a useful by-product of FGD, which is produced by reacting sulphur dioxide (contained in the flue gas) with a CaCO_3 -water suspension. FGD gypsum is used in many application including new construction materials (e.g., wallboard), agriculture, etc. The burning of coal is also major emission source of mercury, a major global pollutant and mercury compounds are present in wet FGD gypsum as well as other waste product from the power station (fly-ash). These compounds, that are unstable over a long period can decompose and/or released into the environment. Different Hg compounds have different decomposition temperatures and knowledge about the stability of the compounds is important.

A heating furnace coupled with cold vapour atomic absorption spectrometer is the normal method used to measure mercury solid samples. FGD gypsum, however, contains very low concentration of mercury and determining/observing mercury compounds at higher temperatures is almost impossible using this method. To overcome this limitation we have developed a new method based on mass spectrometry. The advantage of the mass spectrometer is its better sensitivity and that it allows us to observe different ions simultaneously. Our work has shown have shown that particle size is an important factor for retaining of Hg in gypsum where much higher concentration of mercury is present in finer compared to coarser fraction. This is important information in the production of new material where low amounts of Hg and other toxic metals might be present.

In our further studies, we will carry out further method optimization this and apply our method to the identification of mercury compounds in other industrial relevant solid matrices.

Stable isotope composition and elemental profile as a tool for determination of cheese species and geographical origin

Doris Potočnik^{1,2}, Marijan Nečemer³, Nives Ogrinc^{1,2}

¹ Department of Environmental Science, Jožef Stefan Institute, Ljubljana, Slovenia

² Jožef Stefan International Postgraduate School, Ljubljana, Slovenia

³ Department of Low and Medium Energy Physics, Jožef Stefan Institute, Ljubljana, Slovenia

doris.potocnik@ijs.si

Abstract. Sheep, cow and goat cheeses produced in close Slovenian regions, at a distance of 10 to 150 km, were characterized using stable isotope ratio of C and N in casein and elemental contents of P, S, Cl, K, Ca, Zn, Br, Rb, Sr, in order to determine regional provenance and to differentiate between the different cheese species. Linear discriminate analysis based on K, $\delta^{15}\text{N}$ in casein, Br, Ca, Zn, S and P is used to distinguish sheep and goat cheese from cows. Furthermore, sheep cheese could be distinguish according to different geographical origin with a prediction ability of 94.0 %, where K, $\delta^{13}\text{C}$ in casein, Mn, S, Cl and P are identified as the most significant parameters.

Keywords: cheese, stable isotopes composition, elemental composition, LDA

1 Introduction

Increasing consumer awareness and quality expectations resulted in an increasing interest in demand for high quality dairy products with clear geographical origin, such as product with a Protected Denomination of Origin (PDO) or protect geographical indication (PGI). The typical characteristic that determine PDO products is a unified geographical location of production, processing and preparation using recognized known-how, while PGI covers products that has at least one said stage that takes place in a certain area [1].

The consumption of dairy product is steadily increasing in recent years, rendering the proof of provenance a vital issue in food and consumer protection. It is known that

over 18 million metric tons of cheese per year are produced worldwide, mostly in USA, Germany, France and Italy and according to popularity in the diet, adulteration of cheese is becoming more widespread [2]. Since the adulteration can be highly sophisticated, the quality and efficient analytical techniques are required to monitor the presence of the main compounds that characterize PDO products. Stable isotope techniques, either on its own or in a combination with other techniques mainly with elemental profile, are at the moment the most recognize techniques for differentiation of PDO dairy products and between different species of cheese.

Several papers describe the usefulness of stable isotopes analysis of light elements ($^{13}\text{C}/^{12}\text{C}$, $^{15}\text{N}/^{14}\text{N}$, $^{18}\text{O}/^{16}\text{O}$, $^{34}\text{S}/^{32}\text{S}$) to obtain dietary regime in order to characterize dairy products and provide useful information in origin discrimination. It is well-known that $\delta^{13}\text{C}$ of casein fraction discriminates between C_3 (grass) and C_4 (maize) plants, since $\delta^{13}\text{C}$ values are more negative under grass feeding regime in comparison with regime, where higher amounts of maize are included in the diet [3, 4, 5, 6, 7]. While the isotopic composition of nitrogen ($\delta^{15}\text{N}$) is not only dependent on the dietary habits, but also influenced by many factors such as agricultural practice, aridity, salinity and distance from the sea. The differences arise, because some plants (leguminosae) use both atmospheric and soil nitrogen source for nitrogen-fixation pathway [8, 9, 10, 11].

The contents of major and trace elements in milk are not constant and decisively reflect the contents of these elements in soil and animal feed and thus represents unique markers in dairy products, which are useful for distinguish geographical origin [12]. For example, Del Signore [13] and co-workers proved that elemental composition of Li, K, Mn, Se, Rb, Cs allows discrimination of cheese, origin from three Italian regions, regardless of the type of milk (cow or sheep), while Fresco and co-workers [14] reported that major and trace element composition of P, K, Mg, Zn, Fe and Mn enable differentiation between cows' and goats milk. Elemental composition of K and Li are also useful markers for distinguish milk and mozzarella cheese from two areas in Southern Italy [15].

Until now, only a few studies combine both methods for determining origin of cheese. Pillonel et al [10] allow separation of Emmental cheese from Finland, Bretagne and Savoie, while Bontempo et al. [16], successfully distinguished between traditional alpine and pre-alpine Italian cheese. Furthermore, Camin and co-workers [5] present two models with excellent classification success rates ($> 98\%$), one for predicting

geographic origin of the 7 European hard cheese production, and another for discriminate PDO Parmigiano Reggiano cheese from 9 European and 2 non-European producers.

The aim of our work is to identify the pattern that allow us to distinguish among cow, sheep and goat cheese and to discriminate cheese according to their region of production in order to protect their authenticity. Our study include cow, sheep and goat cheese obtained from different Slovenian regions. Two type of cheese have EU PDO certification (cow cheese Tolminc and Bovški sheep cheese) and one type of sheep cheese has local Slovenian PDO name; Kraški sheep cheese.

2 Experimental work

2.1 Samples

During August 2012, 17 samples of sheep cheese and 6 samples of goat cheese and 9 samples of cow cheese were systematically collected, limited to only few regions in Slovenia namely: Bovec, Karst, Vipava, Brkini, Central Slovenian region and South region. Special feature of these cheeses are in their status, since two types of cheese, Bovški sheep cheese (Bovški ovčji sir) and cow cheese Tolminc have EU PDO status, while Kraški sheep cheese (Kraški ovčji sir) has local PDO status. In addition 5 cheese samples of mixed origin; sheep-goat-cow (1 sample), sheep-goat (1 sample), goat-cow (2 samples) and sheep-cow (1 sample) were also analysed.

2.2 Stable isotope analysis

Determination of stable isotopic composition for nitrogen ($\delta^{15}\text{N}$) and carbon ($\delta^{13}\text{C}$) was performed in casein fraction of cheese.

Isolation of casein in cheese: 10 g of fresh cheese was grated. Fat from cheese was removed by extraction using a Soxhlet extractor (8h of extraction) with petrol ether:ethyl ether (2:1) mixture. After extraction, the sample was centrifuged (e.g. 4100 rpm for 6 min) to separate the ether from the residue. The skimmed cheese was warmed to 40°C to remove any possible residual of ether. Then the residue was washed twice with 20 ml of water, centrifuging each time (e.g. 4100 rpm for 3 min). The residue, made up mainly of casein, was freeze-dried and conserved at room temperature until analysis.

Isotope ratio mass spectrometry: Casein samples were weighed directly into a tin capsule, closed with tweezers and put into the automatic sampler of the elemental analyser. All stable C and N analyses were performed separately on a Europa Scientific 20-20 continuous flow mass spectrometer with an ANCA-SL solid-liquid preparation module.

Stable isotope composition is expressed in δ -notation in units of per mil (‰) using the general formula:

$$\delta (\text{‰}) = \left[\left(R_{\text{sample}} / R_{\text{standard}} \right) - 1 \right] \times 1000 \quad (1)$$

where R represents the ratio between the heavier and the lighter isotope ($^{13}\text{C}/^{12}\text{C}$, $^{15}\text{N}/^{14}\text{N}$) in the sample and standard. Values are reported relative to the following international standards: for carbon the Vienna Pee Dee Belemnite (VPDB) and atmospheric N_2 (AIR) for nitrogen. The results were calibrated against the following international reference materials collected in Table 1. Reproducibility of the measurements was $\pm 0.2\text{‰}$ for $\delta^{13}\text{C}$ and $\pm 0.3\text{‰}$ for $\delta^{15}\text{N}$.

Table 1: List of certified reference material used for stable isotopes analysis.

	Name	Analyte	Material	δ value (‰)
Certified Reference Materials	NBS 22	$\delta^{13}\text{C}$	Oli	-30.031 ± 0.043
	IAEA-CH-6		Sucrose	-10.449 ± 0.033
	IAEA-CH-7		Polyethylene foil	-32.151 ± 0.050
	IAEA-N-1	$\delta^{15}\text{N}$	Ammonium sulphate	$+4.0 \pm 0.2$
	IAEA-N-2		Ammonium sulphate	$+20 \pm 0.2$

2.3 Elemental analysis

Multielemental determination of macro and micro elemental content (P, S, Cl, K, Ca, Zn, Br, Rb, Sr) was non-destructively performed by Energy Dispersive X-ray Fluorescence Spectrometry (EDXRF). The pellets were prepared from approximately 1g of frozen-dried samples. For excitation the source of Cd-109 (20mCi) and ^{55}Fe (25mCi) from Eckert and Ziegler were used. The emitted fluorescence radiation was measured by Si(Li) detector (Canberra). The spectrometer was equipped with a vacuum chamber (^{55}Fe) for measurement of light elements P-Cl, while the energy resolution of the spectrometer was 175 eV at 5.9 keV. The analysis of complex X-ray

spectra was performed by AXIL spectral analysis program [17, 18]. The overall uncertainty of the spectral measurement and analysis was in most cases better than 10%.

2.4 Statistical analysis

Statistical calculations and multivariate analysis were carried out using XLSTAT software package (Addinsoft, New York, USA) Basic statistics included mean values (median and arithmetic mean), standard deviation (SD), minimum and maximum, while multivariate analysis involved linear discriminant analysis (LDA).

3 Results and discussion

The results and statistical analysis of our research indicate that, for verification of correct declared geographical origin and determination of different species of cheeses, it is possible to use stable isotope composition of light elements and elemental composition.

3.1 Differentiation of cheese in relation to animal variety

The $\delta^{13}\text{C}$ and $\delta^{15}\text{N}$ values in casein and macro and microelements; Zn, Br, Sr, Rb, P, S, Cl, K, Ca are parameters used for linear discriminant analysis (LDA). Only Ca, Zn, Br and Sr were significant to distinguish between goat, sheep and cow cheese. Ca and Zn enable separation of sheep cheese from cow and goat cheese, Br allow differentiation between sheep and cow cheese, whereas based on Sr it is possible to differentiate between sheep, goat and cow cheese.

The efficiency of LDA classification was then examined by five cheese samples prepared from different type of milk, sheep-goat-cow (1 sample), sheep-goat (1 sample), goat-cow (2 samples) and sheep-cow (1 sample). Results are collected in Table 2. Mixes samples with added cow milk are identified as pure sheep or goat cheese, due to low content of cows' milk and prevailing sheep or goat milk in the sample. The most influent parameters that distinguish cheese type were in the first function K, $\delta^{15}\text{N}$, Br, Ca and Zn, S, P and Ca in the second one. These results indicated that LDA could be a useful method for verifying species of milk in cheese according to its declaration.

Table 2: Classification of mixed cheese samples: Sheep (S), cow (C), goat (G).

Sample description mixture	Predicted group
S+C+G	S
S+G	S
G+C	G
S+C	S

3.2 Differentiation of cheese according to geographical origin

In the second study the LDA analysis was used to determine the geographical origin of sheep's cheeses. The results are present in Figure 1. It is possible to distinguish between six different geographical production locations of sheep cheese BO-Bovec, BR-Brkini, KRA- Karst, O-Central Slovenia, VI-Vipava and V-Dolenjska region. The groups are well separated between each other. The function 1 explains 57.3% of variance, while function 2 explains 36.7%. The main discriminating variables were K, $\delta^{13}\text{C}$, Mn, S, Cl, and P for function 1. The overall correct classification rate was 94.0%. The classification functions reveal that all samples were correctly classified into their original group; Bovec, Brkini, Karst, Central Slovenia, Vipava and South region.

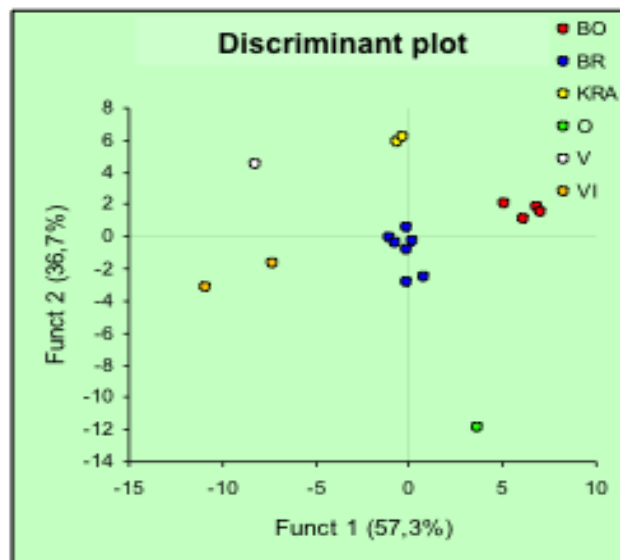


Figure 1: Distribution of sheeps' cheeses according to the location of production: BO-Bovec, BR-Brkini, KRA-Karst, O-Central Slovenia, VI-Vipava, V-South region.

Our results show that elemental profile in a combination with stable isotope composition is a suitable technique used for verifying the geographical origin of sheep's cheese in close regions of production, since the samples were taken at a distance of 10 to 150 km.

4 Conclusion

Characterization of Slovenian cow, sheep and goat cheeses was performed by stable isotope composition of carbon and nitrogen in casein in a combination with elemental composition of macro and micro elements (P, S, Cl, K, Ca, Zn, Br, Rb, Sr). Based on linear discriminant analysis a discrimination of cheeses according to animal species and geographical origin was obtained. This preliminary study can contribute to support and protect the existence of PDO status of Bovški and Kraški sheep cheese and Tolminc cow cheese and protect the consumers, which can in turn promote local products and contribute to the local economy.

Acknowledgements

The work was performed within the project V4-1108 entitled "The use of specific methods for determination and prevention of adulteration of milk and dairy products" financially supported by Slovenian Research Agency and Ministry of Agriculture and the Environment. The research represents a part of the ERA Chair ISO-FOOD project. We thank Mlekarna Planika for supply cow cheese Tolminc, and Kmetijski gozdarski zavod Nova Gorica and all local producers of goat and sheep milk and cheese for providing the samples.

References:

- [1] A. Gonzalez, S. Armenta, M. de la Guardia. Trace-element composition and stable-isotope ratio for discrimination of foods with Protected Designation of Origin. *Trends in Analytical Chemistry*, 28 (11): 1295-1311, 2009.
- [2] S. A. Drivelos, C. A. Georgiou. Multi-element and multi-isotope ratio analysis to determine the geographical origin of foods in the European Union. *Trends in Analytical Chemistry*, 40, 38-51, 2012

- [3] F. Camin, K. Wietzerbin, A. B. Cortes, G. Haberhauer, M. Lees, G. Versini. Application of multielement stable isotope ratio analysis to the characterization of French, Italian, and Spanish cheeses. *Journal of Agricultural and Food Chemistry*, 52, 6592–6601, 2004
- [4] F. Camin, M. Perini, G. Colombari, L. Bontempo, G. Versini. Influence of dietary composition on the carbon, nitrogen, oxygen and hydrogen stable isotope ratios of milk. *Rapid Communications in Mass Spectrometry*, 22, 1690–1696, 2008
- [5] F. Camin, R. Wehrens, D. Bertoldi, L. Bontempo, L. Ziller, M. Perini, G. Nicolini, M. Nocetti, R. Larcher. H, C, N and S stable isotopes and mineral profiles to objectively guarantee the authenticity of grated hard cheeses. *Analytica Chimica Acta*, 711, 54–59, 2012
- [6] Ill-M.Chung, I. Park, J.Y. Yoon, Y.S. Yang, S.-H. Kim. Determination of organic milk authenticity using carbon and nitrogen natural isotopes. *Food Chemistry*, 160, 214–218, 2014
- [7] G. Manca, M. A. Franco, G. Versini, F. Camin, A. Rossmann, A. Tola. Correlation Between Multielement Stable Isotope Ratio and Geographical Origin in Peretta Cows' Milk Cheese. *Journal of Dairy Science*, 89, 831–9, 2006
- [8] N. Knobbe, J. Vogl, W. Pritzkow, U. Panne, H. Fry, H. M. Lochotzke, A. Preiss-Weigert. C and N stable isotope variation in urine and milk of cattle depending on the diet. *Analytical and Bioanalytical Chemistry*, 386, 104–108, 2006
- [9] L. Bontempo, G. Lombardi, R. Paoletti, L. Ziller, F. Camin. H, C, N, and O stable isotope characteristics of alpine forage, milk and cheese. *International Dairy Journal*, 23, 99–104, 2012
- [10] L. Pillonel, R. Badertschera, P. Froidevaux, G. Haberhauer, S. Holzld, P. Hornd, A. Jakobe, E. Pfammatterf, U. Piantinig, A. Rossmannh, R. Tabacchii, J. O. Bosset. Stable isotope ratios, major, trace and radioactive elements in emmental cheeses of different origins. *Lebensmittel Wissenschaft Und Technologie Food Science and Technology*, 36, 615–623, 2003
- [11] D. Sacco, M. A. Brescia, A. Sgaramella, G. Casiello, A. Buccolieri, N. Ogrinc, A. Sacco. Discrimination between Southern Italy and foreign milk samples using spectroscopic and analytical data. *Food Chemistry*, 114, 1559–1563, 2009
- [12] S. Kelly, K. Heaton, J. Hoogewerff. Tracing the geographical origin of food: The application of multi-element and multi-isotope analysis. *Trends in Food Science and Technology*, 16, 555–567, 2005
- [13] A. Del Signore, F. Di Giacomo, M. Giaccio. Determining the regional origin of cheeses with trace metal analysis using statistical classifiers. *Journal of Commodity Science*, 43, 133–144, 2004
- [14] J. M. Fresno, B. Prieto, R. Urdiales, R. M. Sarmiento, J. Carballo. Differentiation by source of milk and by variety from their content of main and trace elements. *Journal of the Science of Food and Agriculture*, 69, 339–345, 1995
- [15] M. A. Brescia, M. Monfreda, A. Buccolieri, C. Carrino. Characterisation of the geographical origin of buffalo milk and mozzarella cheese by means of analytical and spectroscopic determinations. *Food Chemistry*, 89, 139–147, 2005
- [16] L. Bontempo, R. Larcher, F. Camin, S. Hölzl, A. Rossmann, P. Horn, G. Nicolini. Elemental and isotopic characterisation of typical Italian alpine cheeses. *International Dairy Journal*, 21, 441–446, 2011

- [17]M. Nečemer, P. Kump, J. Ščančar, R. Jaćimović, J. Simčič, P. Pelicon, K Vogel-Mikuš. Application of X-ray fluorescence analytical techniques in phytoremediation and plant biology studies. *Spectrochimica Acta - Part B Atomic Spectroscopy*, 63, 1240–1247.,2008
- [18]M. Nečemer, P. Kump, K. Vogel-Mikuš. Use of X-ray fluorescence-based analytical techniques in phytoremediation. In I. Golubev (Ed.), *Handbook of phytoremediation (Environmental science, engineering and technology)* (pp. 331–358). New York: Nova Publishe, 2011.

For wider interest

Consumer awareness about importance of nutrition in today's lifestyle is leading to increasing demands for safety and quality control of foodstuff. Adulteration of food, due to large economic profits motivation, is nowadays in various consumer sectors commonly practiced. In recent years the demand for authentic dairy product (especially sheep and goat cheese) is steadily increasing, thus the proof of provenance is becoming a vital issue in food and consumer protection. For verification of correct declared geographical origin and distinguishing cheeses according to animal species, the use of stable isotope composition of light elements in a combination with elemental profile is becoming the industry standard. Obtained researched data can serve to support and protect existence of PDO status of Bovški and Kraški sheep cheese and Tolminc cow cheese, and consequently also for promoting local products and contributing to the local economy.

Cadmium exposure biomarkers and their associations with renal function biomarkers at low level of exposure

**Anja Stajnik^{1,2}, Janja Snoj Tratnik¹, Darja Mazej¹, Marta Jagodic^{1,2},
Mladen Krsnik³, Lijana Kononenko⁴, Milena Horvat^{1,2}, Ingrid Falnoga¹**

¹ Department of environmental science, Jožef Stefan Institute, Ljubljana, Slovenia

² Jožef Stefan International Postgraduate School, Ljubljana, Slovenia

³ University Medical Centre Ljubljana, Ljubljana, Slovenia

⁴ Ministry of Health, Chemical Office of the Republic of Slovenia, Slovenia

anja.stajniko@ijs.si

Cadmium (Cd) is a non-essential metal to which general population is primarily exposed through diet, drinking water and/or tobacco smoke. It readily accumulates in human body, mostly in kidneys, which are also the major target of Cd toxicity. Its excretion takes part through urine and faeces. Cd levels in urine (U-Cd) and in blood (B-Cd) are primarily used for Cd exposure assessment, occupational or environmental. In general it is stated that B-Cd is an indicator of recent exposure (due to its short half-life), whereas U-Cd better reflects Cd body burden accumulated over a long term. Cd health risk assessment – regarding kidney damage - relies on association between U-Cd and renal function biomarkers (RFBs). Although U-Cd is a well-established biomarker at elevated (occupational) levels of exposure (>4 µg/g Crea) its use and associations with RFBs at low levels (<1.0 µgCd/g Crea) has recently been seriously questioned [1],[2],[5].

The objective of present study was to assess the correlations between various biomarkers of exposure or/and renal function (B-Cd, U-Cd, U-Alb, U-IgG, U-NAG, U-A1M) and to identify factors influencing these associations, in order to evaluate the appropriateness and reliability of U-Cd or/and B-Cd as biomarker(s) of choice at low level of exposure.

The study was focused on Slovenian population consisting of 1081 occupationally unexposed healthy individuals from Slovenian Human biomonitoring Survey (2007-2015): 533 primiparous lactating females and 548 males, aged 18 to 49 years. Data

from questionnaire (age, socio-economic status, medical history, life style and nutritional habits) and data on levels of B-Cd (also B-Pb, B-Hg, B-As and B-Se), U-Cd, urine creatinine (U-Crea), specific gravity (SG) and four urine RFBs - albumin (Alb), immunoglobulin G (IgG), N-acetyl- β -glucosaminidase (NAG) and α_1 -microglobulin (A1M), were used for Cd exposure assessment and assessment of correlations between various biomarkers. Correlations were estimated by Pearson's correlation coefficient (r_p) and by multiple linear regression analysis (adjustment for diuresis (U-Crea or SG), age, smoking, BMI, B-Pb, B-Hg, B-As and B-Se). Differences between groups were assessed by one way ANOVA.

The mean urine and blood Cd levels in studied population were 0.22 ng/g and 0.33 ng/g in blood and 0.16 μ g/g Crea and 0.26 μ g/g Crea in urine for males and females, respectively. Geometric mean values of all four renal function biomarkers were far below critical levels. Females had significantly higher B-Cd levels than males ($p < 0.001$), while the gender differences in levels of urine biomarkers were inconsistent due to the correction for diuresis by either U-Crea or SG (Table 1).

Weak positive association between U-Cd and B-Cd was observed (irrespective of gender and correction for diuresis; $r_p \sim 0.2$, $p < 0.001$). U-Cd also positively correlated with all four renal function biomarkers (irrespective of gender) (r_p 0.252 - 0.453, $p < 0.001$) although the associations were considerably weaker when correction for diuresis by U-crea or SG was used. After consideration of all possible confounders the overall correlations of renal function biomarkers with U-Cd stayed significant. On the contrary B-Cd was in a weak, gender specific, positive association with two renal function biomarkers only, with A1M in males ($r_p \sim 0.16$, $p < 0.001$) and with NAG ($r_p \sim 0.1$, $p < 0.05$) in females. However, after testing the associations for possible confounders, we observed that A1M was in fact related to age (positively), smoking (positively), B-Pb (positively) and B-Hg (negatively) rather than to B-Cd, while NAG stayed correlated with B-Cd with marginal significance ($r_p \sim 0.12$, $p < 0.1$).

Although we had incomplete (self-reporting) dataset of current and/or former smoking, the existing data were suitable to estimate smoking effects on Cd levels. So in the present study the significant influence of current smoking, on B-Cd and U-Cd levels was confirmed for males. For females the former smoking, with cessation of

smoking ~1 year ago, was found to influence the levels of B-Cd, but not that of U-Cd.

According to Bernard [2], we suggest that positive associations between Cd exposure biomarkers (U-Cd and B-Cd) and renal function biomarkers observed in present study, at levels as low as $<0.5 \mu\text{g/g}$ Crea (or ng/g), could not be attributed to Cd renal effects (toxicity). Bernard [2], [3] is inclined to explanation that associations at such low levels of Cd are a consequence of normal physiological variations and influence of other factors such as smoking, age and a co-exposure to other metals. Positive correlations of U-Cd with renal function biomarkers could be simply explained by their co-excretion; Cd in plasma is mainly bound to metal protective proteins metallothioneins (MTs) and in this form it uses the same transport pathways of renal function biomarkers, consequently both U-Cd and renal function biomarkers are affected by variations in renal function in the same way, as also previously reported [3],[4]. Consequently, low levels of U-Cd more likely reflects renal function than Cd exposure. Additionally, correlations of renal function biomarkers with B-Cd were in general absent or in case of A1M confounded by smoking, age and presence of other metals.

An additional issue in evaluation of Cd exposure and its associations with urine renal function biomarkers represents correction for diuresis by U-Crea or SG, which in some cases gave incomparable results. It is also important to point out that both U-Crea and SG are determined by a far less accurate method than U-Cd, which introduce an important additional uncertainty and could lead to misinterpretation of results when we are dealing with Cd levels below $<1 \mu\text{g/g}$ Crea. Beside that recently, in a study on environmentally exposed individuals Hoet et al., 2016 reported that for low levels of U-Cd correction for diuresis is not recommended [5]. As already mentioned above, U-Cd is also influenced by both recent (smoking) and/or past (kidney Cd deposits) exposure. The same can be considered for B-Cd levels as shown in present study based on a case of current and former smokers, which makes it difficult or impossible to differentiate recent and past Cd exposure at low levels.

Based on observations from our and also other studies it could be concluded, that blood Cd (normalized by hemoglobin or hematocrit) can represent better alternative as a biomarker of exposure at low levels.

Future directions:

Although, the associations of Cd exposure and renal function biomarkers observed at low environmental exposure are most probably driven by a normal physiological variations, it is important to consider that there are individuals in the general populations which could be more susceptible to Cd exposure. Of big importance are deficiencies of particular essential elements; their absence can considerably influence Cd uptake and excretion and consequently physiological response to exposure.

Similarly important are genetic variations of several genes involved in Cd metabolisms. Well known example are genes coding for metallothioneins (MTs), metal binding cysteine-rich low molecular weight proteins with important role in homeostasis and transport of essential metals (Cu, Zn) and scavenging of radicals (Figure 1). Due to physicochemical similarities between metals they are also involved in immobilization and detoxification of Cd and other potentially toxic metals (As, Hg, Pb).

Our future work will be to determine whether the selected MT polymorphisms (or their combination) and levels of essential metals are associated with levels of Cd and also other potentially toxic metals.

References:

- [1] G. Nordberg, B. Fowler, M. Nordberg. *Handbook on the Toxicology of Metals. 4th edition*. USA: Elsevier Life Science; 2015.
- [2] A. Bernard: Confusion about cadmium risks. The unrecognized limitations of an extrapolated paradigm. *Environmental Health Perspective*, 124:1–5, 2016.
- [3] M. Akerstrom, G Sallsten, T Lundh, L Barregard. Associations between urinary excretion of cadmium and proteins in a nonsmoking population: renal toxicity or normal physiology? *Environmental Health Perspective*, 121:187–91, 2013.
- [4] A. Bernard. Biomarkers of metal toxicity in population studies: research potential and interpretation issues. *Journal of Toxicology and Environmental Health*, 71:1259–65, 2008.
- [5] P. Hoet, G. Deumer, A. Bernard, D. Lison, V. Haufroid. Urinary trace element concentrations in environmental settings: is there a value for systematic creatinine adjustment or do we introduce a bias? *Journal of exposure science & environmental epidemiology* (January):1–7, 2015.
- [6] B. Ruttkay-Nedecky, L. Nejdil, J. Gumulec, O. Zitka, M. Masarik, T. Eckschlager, M. Stiborova, V. Adam, R. Kizek. The role of metallothionein in oxidative stress. *International Journal of Molecular Sciences*, 14:6044–6066, 2013.

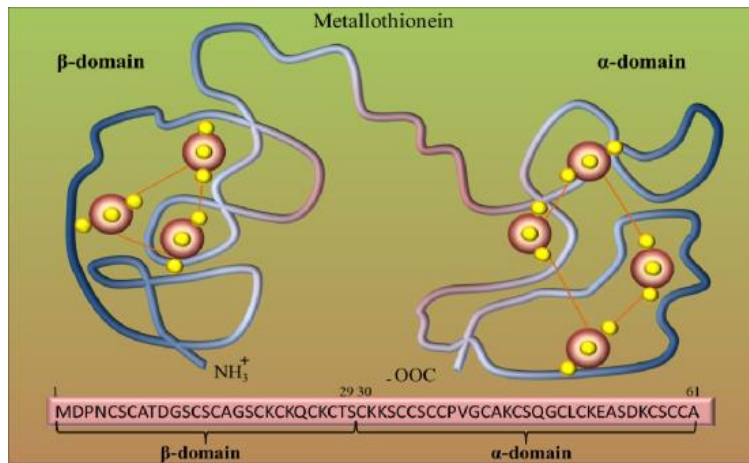


Figure 1: Structure of metallothionein (MT)[6].

Table 1: Levels of biomarkers in blood and urine expressed as GM (min-max), stratified by gender.

BIOMARKERS	MALE	FEMALE	p-value female vs male
B-Cd (ng/g)	0.22 (0.1 – 4.54)	0.33 (0.1 – 2.93)	<0.001
B-Hg (ng/g)	1.18 (0.1 – 29.3)	0.33 (0.1 – 2.93)	0.042
B-Pb (ng/g)	18.3 (3.65 – 109)	15.9 (4.04-68.3)	<0.001
U-Cd (ng/mL)	0.21 (0.015 – 1.75)	0.17 (0.015 – 3.83)	<0.001
U-Cd/Crea (µg/g)	0.16 (0.03 – 1.14)	0.36 (0.02 – 2.79)	<0.001
U-Cd/SG (ng/mL)	0.22 (0.03 – 1.11)	0.21 (0.04 – 3.65)	0.153
U-IgG (mg/L)	2.52 (1.70 – 88.1)	2.80 (1.70 - 363)	0.035
U-IgG/Crea (mg/g)	1.84 (0.53 – 144.76)	3.99 (0.28 - 535)	<0.001
U-IgG/SG (mg/L)	2.63 (0.50 – 152.2)	3.26 (0.82 - 471.9)	<0.001
U-Alb (mg/L)	6.80 (1.06 – 1090)	6.91 (1.06 - 2190)	0.784
U-Alb/Crea (mg/g)	5.05 (0.50 - 1791)	10.0 (0.18 - 3227)	<0.001
U-Alb /SG (mg/L)	7.17 (0.81 – 1883)	8.24 (0.66-2847)	0.029
U-A1M (mg/L)	5.11 (2.62– 49.5)	3.34 (2.62 -116.1)	<0.001
U-A1M/Crea (mg/g)	3.67 (0.82 – 60.1)	4.81 (0.47-38.1)	<0.001
U-A1M/SG (mg/L)	5.26 (0.82 – 62.7)	3.93 (1.28-45.7)	<0.001
U-NAG (nkat/L)	30.7 (2.0 - 296)	23.5 (2.0-204)	<0.001
U-NAG/Crea (µkat/g)	22.0 (1.15 – 283.0)	33.6 (0.17-295)	<0.001
UNAG/SG (nkat/L)	31.9 (1.72 – 234.3)	27.5 (0.68-292.5)	0.006

Reference values: B (U)-Cd <1 ng/g (µg/g Crea), B-Hg <5 ng/g, B-As <20 ng/g, B-Pb <90 or <70 ng/g for female and male, respectively, B-Se 60-130 ng/g; Critical levels: U-Cd > 4 mg/g Crea; U-IgG > 12.8 mg/g Crea, U-Alb > 30 mg/g Crea, U-A1M >10 mg/g Crea, U-NAG > 81 mg/g Crea.

For wider interest

Cadmium (Cd) is a non-essential metal to which general population is mostly life-long exposed through diet, drinking water and/or tobacco smoke. Cd accumulates mostly in kidneys, which are also the major target of its toxicity. To estimate the exposure of population to Cd its levels in urine and blood are measured. To evaluate its possible kidney effects, association between urine Cd levels and levels of urine proteins, which are indicators of kidney function, are studied. Cd levels in urine at elevated exposure (occupational; $>4 \mu\text{g/g Crea}$) are well established as a biomarker, but its use at low environmental exposure ($< 1 \mu\text{g/g Crea}$) has recently been questioned.

The aim of present study was to estimate the appropriateness and reliability of U-Cd and blood Cd (B-Cd) as biomarker(s) of choice at low level of exposure ($< 0.5 \mu\text{g/g Crea}$).

Our results confirmed recent observations that urine Cd at low levels of exposure is not a reliable biomarker. Such low levels are significantly influenced by variations observed in normal physiology (kidney function) or pathology related to unidentified cardiovascular diseases and uncertainties introduced by data normalization for diuresis (by creatinine or SG). For that matter Cd in blood seemed to be much better biomarker for Cd exposure at very low levels.

The fate of zero valent iron nanoparticles after their use in wastewater remediation by single particle ICP-MS

Janja Vidmar^{1,3}, Primož Oprčkal^{2,3}, Ana Mladenovič^{2,3}, Radmila Milačič^{1,3}, Janez Ščančar^{1,3}

¹ Department of Environmental Sciences, Jožef Stefan Institute, Ljubljana, Slovenia

² Slovenian National Building and Civil Engineering Institute, Ljubljana, Slovenia

³ Jožef Stefan International Postgraduate School, Ljubljana, Slovenia

janja.vidmar@ijs.si

Abstract: Application of zero-valent iron nanoparticles (nZVI) exhibits great potential in efficient removal of metal contaminants in wastewater treatment. After their application in nanoremediation, risk exists that nZVI remain in remediated waters, presenting potential threat to the environment and living beings. Therefore, the occurrence and behaviour of nZVI need to be studied. In our study, a novel approach with the use of single particle ICP-MS was first optimized for sizing and quantification of iron nanoparticles in wastewater matrix. The method was then applied for studying the aggregation and dissolution rate of nZVI as well as mechanism of Cd²⁺ removal in synthetic wastewater. Results showed that 70 % of initial 100 ng/mL Cd²⁺ concentration was adsorbed on nZVI and removed, while 97 % of the initially added nZVI aggregated and settled, losing their nano properties. This indicates that the use of nZVI does not present environmental threat and that nanoremediation is efficient in removing Cd from the wastewaters.

Keywords: nanoremediation, zero-valent iron nanoparticles, single particle ICP-MS, nZVI aggregation, removal of Cd²⁺

1 Introduction

For the past 15 years, nanoscale zero valent iron nanoparticles (nZVI) have been investigated as a new tool for the treatment of contaminated water and soil [1]. They can efficiently remove pollutants due to their small particle size, large surface area, and greater density of reactive and adsorptive site. Metals are removed by adsorption, reduction and coprecipitation with iron (Fe) hydroxides, during which oxidation from Fe⁰ to Fe²⁺ and Fe³⁺ occurs [2]. One of the common industrial and environmental pollutant is cadmium (Cd) which is found in environmental waters in the

concentrations below 10 ng/mL. Cd is extremely toxic and classified as a human carcinogen [3]. Therefore, its removal from such contaminated waters is mandatory. Nanoremediation has the potential not only to improve treatment efficiency of the wastewater, but it also efficiently reduces most contaminant concentrations, enabling the reuse of cleaned wastewater for secondary purposes. Despite their extensive use in the wastewater remediation, risk exists that nZVI potentially remain in remediated waters. Investigations on the fate of nanoparticles (NPs) after the nanoremediation are scarce. nZVI are toxic due to their extremely strong reducing properties, which can cause severe damage to tissues (e.g. lung [4] or nerve cells [5]).

In order to use nZVI for remediation purposes in a way that remediated water does not present a risk to the environment and living beings, concentration, size, aggregation as well as dissolution of nZVI after nanoremediation have to be studied. For this purpose, single particle inductively coupled plasma mass spectrometry (SP-ICP-MS) that provides information about nanoparticles (NPs) number/mass concentration and size distributions, at mass concentration levels down to the low ng/L, can be applied. The major advantages of SP-ICP-MS over other characterization techniques are its superior sensitivity and ability to simultaneously measure soluble and particulate form of the element [6].

The determination of very low Fe concentrations in complex matrices by ICP-MS is challenging due to polyatomic interferences produced by oxygen, argon and calcium on ^{56}Fe ($^{40}\text{Ar}^{16}\text{O}^+$ and $^{40}\text{Ca}^{16}\text{O}^+$) [7]. Polyatomic interferences on ICP-MS can be reduced by the application of collision or reaction cell technology [8]. Gases can collide or react either with the polyatomic interfering ions ($^{40}\text{Ar}^{16}\text{O}^+$ and $^{40}\text{Ca}^{16}\text{O}^+$), thus removing their interference with Fe on m/z , 56 or transform the analyte ions to other species that do not interfere with ^{56}Fe . To the best of our knowledge, the use of reaction cell for measuring NPs in SP-ICP-MS mode has so far not been reported in the literature.

The aim of this study was to find the optimal instrumental parameters for sensitive and interference-free measurement of nZVI by SP-ICP-MS on the most abundant ^{56}Fe isotope and to apply this method for following the aggregation, dissolution and settlement of nZVI after their usage for the remediation of synthetic wastewater. In addition, mechanism of Cd^{2+} removal with nZVI was studied. Measuring Cd in SP-ICP-MS mode enables to distinguish and quantify Cd adsorbed on nZVI from Cd dissolved in solution.

2 Materials and methods

SP-ICP-MS measurements were performed on a model 8800 Triple Quadruple ICP-MS instrument (Agilent Technologies, Tokyo, Japan). The operating parameters, including the use of optimal reaction/collision gas and gas flow rate, were optimized for plasma robustness and sufficient sensitivity of monitored ^{56}Fe isotope. For the SP-ICP-MS measurements, the instrumental data acquisition was set to time-resolved-analysis mode. The measurement duration for each run was 120-180 s with a short integration time of 3 ms. The peristaltic pump was set to 0.1 rps for all the experiments, which corresponded to a sample flow rate of 0.3 mL/min. For the optimization of SP-ICP-MS measurements with the use of reaction/collision gas, $\text{Fe}_3\text{O}_4\text{NPs}$ (Sigma-Aldrich, St. Louis, USA) with the particle size less than 50 nm were used. Simulated nanoremediation processes were performed with nZVI Nanofer star (NANO IRON, s.r.o., Czech Republic) that are stabilized by the Fe_3O_4 surface layer (15 % of mass content). In order to determine transport efficiency, gold NPs (AuNPs RM 8012) (NIST, Maryland, USA) with 30 nm particle size were applied. The dissolved Fe and Cd stock standard solutions (Merck, Germany) of 1000 ± 4 mg/L were used for the preparation of the calibration curves. Synthetic wastewater [9] was prepared by dissolving 160 mg of peptone, 30 mg of urea, 28 mg of K_2HPO_4 , 7 mg of NaCl, 4 mg of $\text{CaCl}_2 \cdot 2\text{H}_2\text{O}$ and 2 mg of $\text{Mg}_2\text{SO}_4 \cdot 7\text{H}_2\text{O}$ in 1 L of Milli-Q water. Milli-Q water (18.2 M Ω cm) (Millipore, Bedford, MA, USA) was used for all sample preparations and sample dilutions.

3 Results and discussion

3.1. Optimization of nZVI determination by SP-ICP-MS

In order to achieve satisfactory limits of detection (LOD) for measuring trace levels of Fe in wastewater (ng/L) by SP-ICP-MS, different gases, e.g. helium (He) as a collision gas in high energy collision mode (HECM) and hydrogen (H_2), oxygen (O_2) and ammonia (NH_3) as reaction gases, were tested. LOD for the $\text{Fe}_3\text{O}_4\text{NPs}$ size and mass concentration, dissolved Fe as well as sensitivity and signal to noise ratio determined in SP-ICP-MS were calculated in different modes (Table 1). Based on the results, H_2 as a reaction gas was chosen. Measurements of $^{56} \rightarrow ^{56}\text{Fe}$ in collision cell with H_2 gas (5.5 mL/min) is sensitive with all the interferences efficiently reduced, which results in the decrease of the background noise and low LOD. LODs for mass concentration of nZVI and dissolved Fe (0.980 ng/L and 329 ng/L, respectively) were

calculated as three times the standard deviation of 6 blanks (Milli-Q water), while the size LOD of nZVI (30 nm) was calculated as the size equivalent of the three times the standard deviation of the blank signal in the size calibration plot.

Table 1: Calculated limits of detection for the Fe₃O₄NPs size and mass concentration, dissolved Fe, sensitivity and signal to noise ratio with the use of different collision/reaction gases determined by SP-ICP-MS.

Tune mode	56 Fe [HEHe]	56→56 Fe [H ₂]	56→56 Fe [O ₂]	56→56 Fe [NH ₃]	56→72 Fe [O ₂]	56→124 Fe [NH ₃]
LOD _{size} nm	64	46	46	49	70	146
LOD _{NPconc} ng/L	0.302	0.607	0.878	0.260	0.738	45
LOD _{diss} ng/L	691	231	306	213	321	483
Sensitivity cps/(ng/mL)	22602	61699	43377	29262	8913	229
Signal/noise	2.718	5.700	6.343	6.078	7.554	3.293

3.2 Studying the behaviour of nZVI after their use for the remediation of synthetic wastewater

Laboratory scale nanoremediation experiment was carried out at room temperature. To simulate environmental conditions, such as the presence of organic matter and ionic strength, a batch experiment was performed in 1L of synthetic wastewater to which nZVI and Cd²⁺ solution was added in order to achieve final concentration of 0.25 g/L nZVI and 100 ng/mL Cd²⁺. The bottle was capped and shaken for 4h at 150 rpm on horizontal shaker.

To study the aggregation, settling and dissolution behaviour of nZVI as well as adsorption of Cd²⁺ on nZVI with time, 5 mL sample aliquots were taken from the top at different time intervals. Behaviour of nZVI after their use in nanoremediation is presented in Figure 1A and 1B.

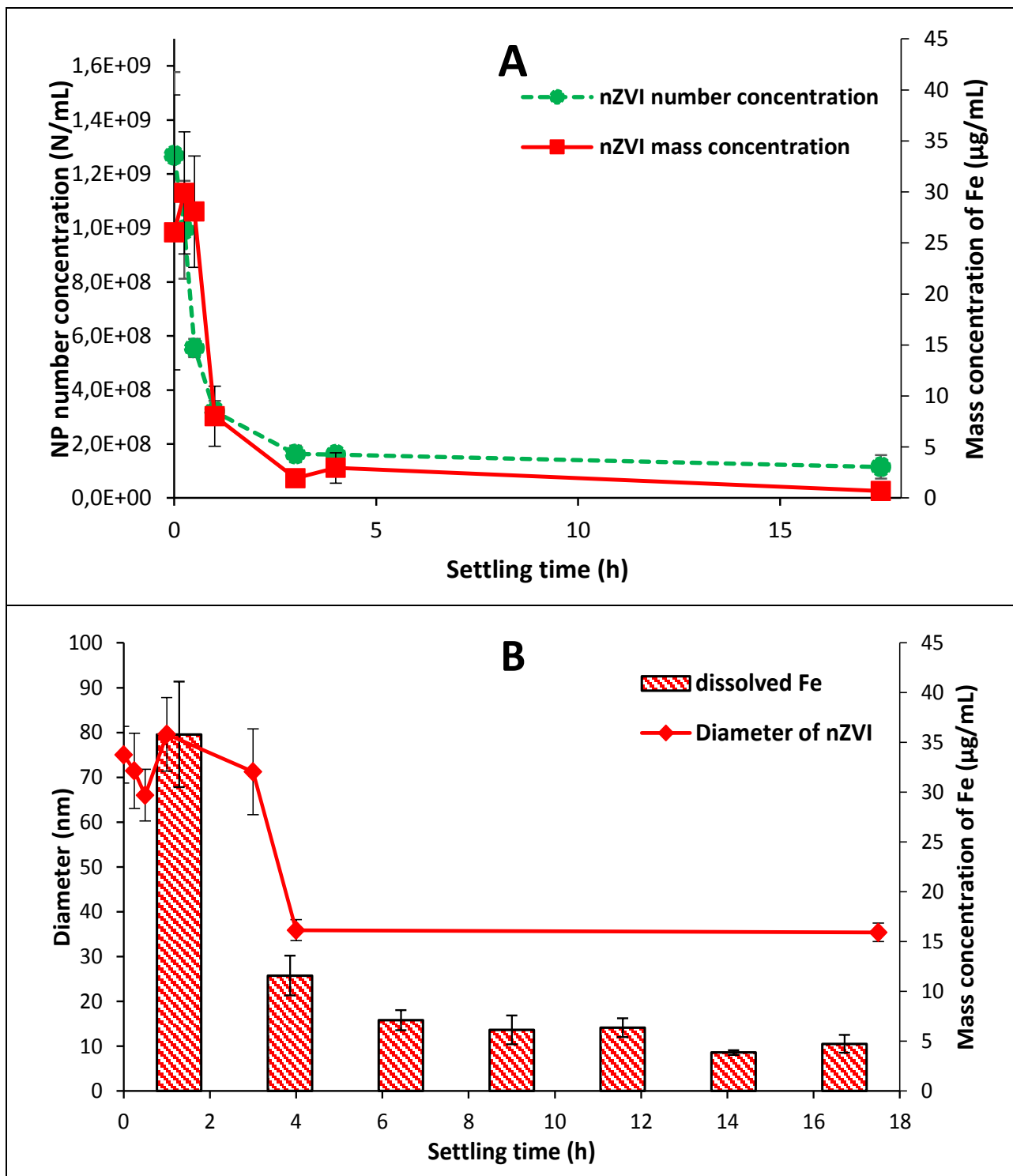


Figure 1: Influence of settling time on (A) the nZVI mass and number concentration, and (B) on concentration of the dissolved Fe and nZVI size.

It can be seen that most of nZVI aggregate and settle already 3 h after the shaking was stopped. When equilibrium is achieved (after 18 h of settling), 97 % of Fe in the nanoscale and 87 % of Fe in the dissolved form is removed from the solution. It can be further seen that the size of nZVI, which remained dispersed in water, decreases

from the initial 75 nm to 36 nm after 18 h of settling (Figure 1B), indicating that only NPs with smaller sizes remained dispersed. It can be concluded that the use of nZVI in nanoremediation does not present environmental threat since nZVI after the treatment quickly aggregate and settle, thus no longer have their nano properties.

3.3 Studying the mechanism of Cd²⁺ removal

Adsorption mechanism of Cd on nZVI is shown on Figure 2, which indicates that percentage of Cd²⁺ removal remains more or less constant (about 70 %) during 18 h of settling. After the nZVI treatment, Cd was removed by adsorption and coprecipitation with Fe hydroxides. The amount of Cd²⁺ adsorbed on nZVI decreases gradually with the increase of the settling time. The initial rapid adsorption of Cd²⁺ on nZVI (from 8.5 ng Cd/mL to 10.5 ng Cd/mL after 15 min of settling) and consequently its removal by settling of nZVI, is related to the initially available large amounts of adsorptive sites on nZVI [3]. When the adsorptive sites are saturated, the adsorption of Cd²⁺ starts to decrease until it approaches equilibrium concentration (0.5 ng Cd/mL after 18 h of settling).

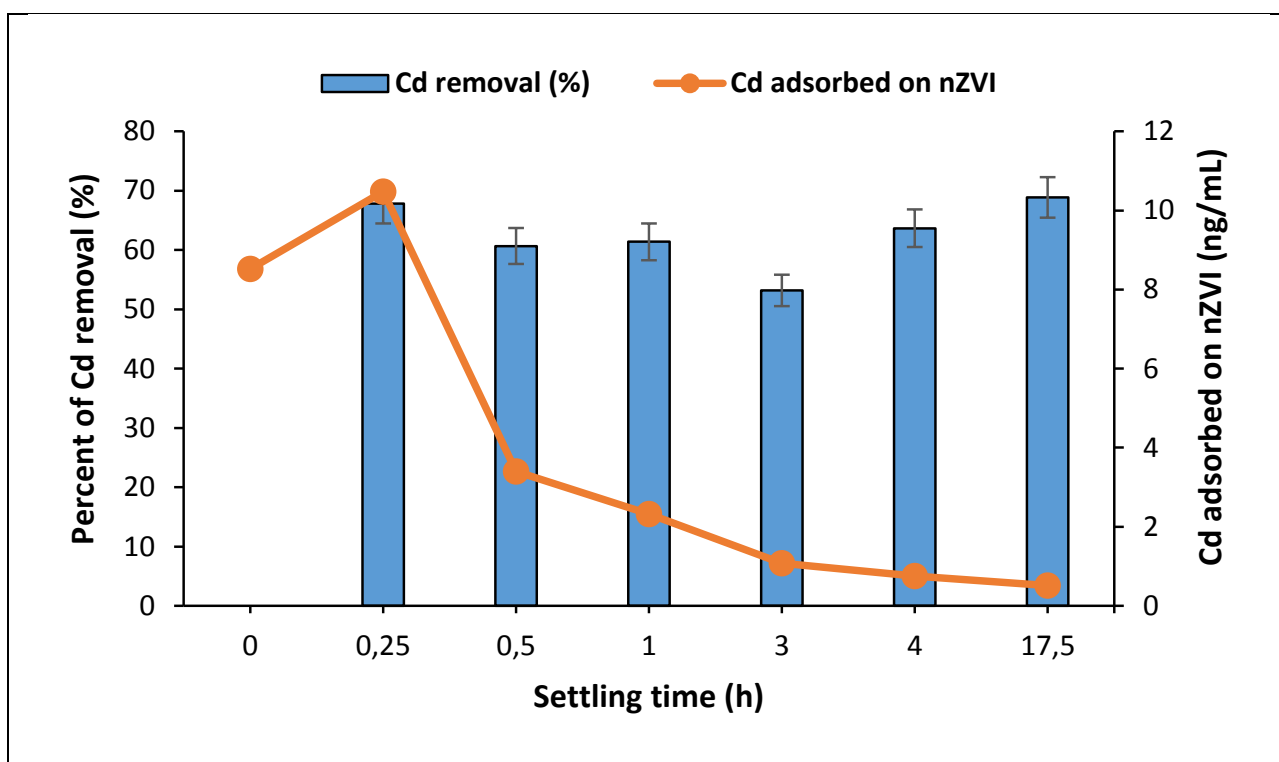


Figure 2: Influence of settling time on Cd²⁺ removal from the synthetic wastewater and the amount of Cd²⁺ adsorbed on nZVI.

4 Conclusions

Due to the strong spectral interferences, measurement of low concentrations of nZVI by SP-ICP-MS is possible only with the use of reaction cell technology in MS/MS mode. It was found experimentally that by the use of H₂ as a reaction gas signal of noise at m/z 56 is effectively reduced, enabling sensitive measurements with the lowest LODs among all the collision/reaction gases tested. Optimized SP-ICP-MS method was applied for studying the fate of nZVI and Cd²⁺ after their use in nanoremediation of synthetic wastewater contaminated with 100 ng/mL of Cd²⁺. 97 % of the initially added nZVI aggregated and settled, losing their nano properties, while 70 % of Cd²⁺ concentration was adsorbed on nZVI and removed. Understanding the processes of the nZVI behaviour after the treatment of contaminated waters and mechanisms of Cd²⁺ removal is essential to achieve effective nanoremediation and to ensure conditions, which enable rapid settlement of nanosized Fe, thus preventing nano threat towards environment and living beings. In the future, SP-ICP-MS method will be applied for studying the behaviour and removal efficiency of nZVI in real wastewater samples.

Acknowledgments

This work has been supported by the Ministry of Higher Education, Science and Technology of the Republic of Slovenia (Programme group P1-0143) and EU funded project LIFE12 ENV/SI/000443: LIFE RusaLCA Nanoremediation of water from small wastewater treatment plants and reuse of water and solid remains for local needs.

References:

- [1] R.A. Crane, T.B. Scott. Nanoscale zero-valent iron: Future prospects for an emerging water treatment technology. *Journal of Hazardous Material*, 211-212:112–125, 2012.
- [2] C. Noubactep, S. Caré. On nanoscale metallic iron for groundwater remediation. *Journal of Hazardous Material*, 182:923–927, 2010.
- [3] H. K. Boparai, M. Joseph, D. M. O'Carroll. Cadmium (Cd²⁺) removal by nano zerovalent iron: Surface analysis, effects of solution chemistry and surface complexation modeling. *Environmental Science and Pollution Research*, 20:6210–6221, 2013.
- [4] C.R. Keenan, R. Goth-Goldstein, D. Lucas, D.L. Sedlak. Oxidative stress induced by zero-valent iron nanoparticles and Fe(II) in human bronchial epithelial cells. *Environmental Science of Technology*, 43:4555–4560, 2009.
- [5] T. Pisanic, J. Blackwell, V. Shubayev, R. Finones, S. Jin. Nanotoxicity of iron oxide nanoparticle internalization in growing neurons. *Biomaterials*, 28:2572–2581, 2007.
- [6] F. Laborda, E. Bolea, J. Jimenez-Lamana. Powerful Tool for Nanoanalysis. *Analytical Chemistry*, 86:2270–2278, 2014.

- [7] M. Segura, Y. Madrid, C. Camara. Elimination of calcium and argon interferences in iron determination by ICP-MS using desferrioxamine chelating agent immobilized in sol-gel and cold plasma conditions. *Journal of Analytical Atomic Spectrometry*, 18:1103-1108, 2003.
- [8] S.D. Tanner, V.I. Baranov, D.R. Bandura. Reaction cells and collision cells for ICP-MS: A tutorial review. *Spectrochimica Acta - Part B*, 57:1361–1452, 2002.
- [9] L.E. De-Bashan, M. Moreno, J.P. Hernandez, Y. Bashan. Removal of ammonium and phosphorus ions from synthetic wastewater by the microalgae *Chlorella vulgaris* coimmobilized in alginate beads with the microalgae growth-promoting bacterium *Azospirillum brasilense*. *Water Research*, 36:2941–2948, 2002.

For wider interest

Providing clean and affordable water to meet human needs is a major global challenge of the 21st century. Current water and wastewater treatment technologies and facilities are reaching their limit for providing adequate water quality to meet human and environmental needs. Therefore, the sustainable use of water, including the efficient use of renewable sources of water, is needed. Nanotechnology with the use of zero valent iron nanoparticles (nZVI) exhibits great potential in efficient wastewater treatment, enabling the reuse of wastewater for secondary purposes. After their use in nanoremediation, nZVI can either agglomerate – lose their nano properties and settle, or they can remain dispersed in water. Their small size and high redox reactivity make them potentially harmful to living organisms. In order to ensure that the use of nZVI does not present a risk to living beings and the environment, single particle ICP-MS method was used for following the removal efficiency and nZVI behaviour after their use in the nanoremediation.

Speciation of mercury and microbial communities in the seawater of the Central Adriatic Sea

Igor Živković^{1,2}, Milena Horvat^{1,2}, Mladen Šolić³, Vesna Fajon¹, and Jože Kotnik¹

¹ Department of Environmental Sciences, Jožef Stefan Institute, Ljubljana, Slovenia

² Jožef Stefan International Postgraduate School, Ljubljana, Slovenia

³ Laboratory of Marine Microbiology, Institute of Oceanography and Fisheries, Split, Croatia

igor.zivkovic@ijs.si

Mercury (Hg) is the main trace metal contaminant in the Mediterranean Sea. Its biota contains high Hg levels and engages human consumers at risk. Methylmercury (MeHg) is the main toxic form of mercury that can cause adverse health effects to organisms at higher trophic levels. Measurements of Hg levels in the open Mediterranean water indicate that Hg is present due to natural and anthropogenic sources [1, 2]. However, it is still unknown how much of the deposited Hg finds its way up the food chain. Inorganic Hg needs to be transformed into MeHg in order to bioaccumulate along marine food webs. This is of particular importance in the Adriatic Sea where the mercury water levels are higher than in the rest of the Mediterranean [3]. Pathways for mercury methylations include abiotic mechanisms (by methylcobalamin and humic matter) and biotic methylation in anoxic conditions by sulfate-reducing bacteria [4]. However, there are evidences that suggest that oxic environment may also host biotic methylation [5]. Remineralisation of particulate organic matter controls the methylation of Hg by providing inorganic Hg and by activating methylating bacteria. The rates of formation of MeHg and the structure of the food web determine Hg accumulation rates in the marine food web. The highest water column MeHg levels are found alongside the presence of nano- and picophytoplankton, as shown in the Western Mediterranean [5]. Relative importance of prokaryotes and microbial food web to matter and energy fluxes is the greatest in oligotrophic conditions [6]. Therefore, these organisms possess great potential for bioaccumulation of mercury. The same factors that enable scavenging nutrients at low concentrations (small size, large surface to volume ratio, rapid metabolism) may also facilitate mercury accumulation in their biomass for subsequent transfer to other

components of the food web. Our research tries to identify relationship between mercury species and fractions in the seawater and the abundance of individual microbial specie. This could show whether methylation, or other transformation processes, can occur directly within microbes in the Adriatic Sea. We will compare results obtained during cooler (November – March) and warmer (April – October) part of the year.

The investigated coastal area is located in the central Adriatic Sea, covering the coastal zone from Kaštela to Split and is partly under the influence of the karstic rivers Jadro (Kaštela Bay) and Cetina (Split area). The Bay of Kaštela is an enclosed bay in the Central Adriatic with the average water renewal time of about one month [6]. It had been affected by previous contamination from chlor-alkali industrial waste waters. The switch from eutrophic to oligotrophic conditions occurred after the sewage outfalls had been completed in 2005. This switch was observed by decreases in concentrations of dissolved nitrogen and phosphorus, bacterial abundance, bacterial production and chlorophyll *a*, and increase in heterotrophic nanoflagellate abundance and bacterial specific growth rate [6]. Bacterial production and bacterial biomass abundance is generally the highest at the station nearest to the coast (Vranjic) and decreasing towards the open sea [7]. The Split Channel is a near-shore passage separated from the open sea by the islands of Šolta and Brač. It is mostly influenced by domestic and industrial waste waters from the city of Split. Open sea samples were collected at the station located near the island of Vis, which can be considered a pristine environment. In order to establish relationship between mercury and microbial species, we performed series of samplings, usually at monthly intervals, from March 2014 to December 2015 during oceanographic cruises aboard the Croatian research vessel Bios Dva. Samples were taken from four locations: two in the Bay of Kaštela (Vranjic and central station), one in the Split Channel and one near the island of Vis. Non-filtered seawater samples were collected using 5 L Niskin bottles at several depths between the surface and the bottom (at 5- to 10-m intervals for the upper 50 m and at 75 and 100 m at the island of Vis). For the determination of total mercury (THg) and MeHg concentrations, seawater was transferred to 1 L glass bottle and acidified with 1 mL of concentrated HCl. Un-acidified seawater samples were stored at 5°C in 0.5 L glass bottles for the determination of dissolved gaseous mercury (DGM). For the picoeukaryotes cells count, 2 mL samples were

preserved in 0.5% glutaraldehyde and frozen at -80 °C until analysis. THg was determined by sample digestion with BrCl/UV irradiation, reduction with SnCl₂, double amalgamation on gold traps, and using cold vapour atomic fluorescence (CVAFS) detection on Tekran 2600. DGM was determined by sample sparging with argon gas, double amalgamation, and CVAFS detection by Brooks Rand III. MeHg was measured by conversion to hydride with NaBH₄, cryotrapping on GC column immersed in liquid nitrogen followed by column heating and species separation, pyrolysis and CVAFS detection by Brooks Rand III. Number of picoeukaryotes was determined by Beckman Coulter, Epics XL-MCL flow cytometer.

THg in the Adriatic seawater ranged from 256 – 2780 pg/L. Higher concentrations were almost always found during the warmer periods (April - October) when compared to cooler periods (November - March). This is the best displayed in the pristine environment of the island of Vis, where winter THg concentrations of 297 ± 29.8 pg/L are approximately 25% lower than during summer (397 ± 28.6 pg/L). However, in the central part of the Bay of Kaštela, average concentrations were the same throughout the year (~800 pg/L). The highest annual THg concentrations (~2700 pg/L) were found at the bottom layer of the most contaminated part of the Bay of Kaštela, which is probably the consequence of resuspension from the sediment. DGM concentrations range from 80.6 – 186 pg/L. Slightly higher concentrations were observed during the warmer period in the coastal area (152 ± 17.9 pg/L) compared to cooler period (140 ± 21.9 pg/L). On the contrary, in the open sea, DGM is higher during cooler (115 ± 13.2 pg/L) than warmer period (97.2 ± 13.8 pg/L), which is possibly connected to higher UV radiation in cleaner atmosphere. This emphasises the importance of photoreduction and photooxidation as two important driving forces for the presence of DGM concentrations in the seawater [1]. Interestingly, the highest difference between DGM concentrations during cooler and warmer period (19%) is found at the Split Channel station (109 ± 6.52 pg/L and 130 ± 9.56 pg/L, respectively). MeHg concentrations were mostly the same throughout the year (5.12 – 20.6 pg/L) with an average levels of 10.1 ± 3.29 pg/L. Slightly higher MeHg concentrations were observed during warmer period (11.1 ± 2.08 pg/L) than during cooler (10.2 ± 2.25 pg/L) at the island of Vis. This may be attributed to the increased biological production at the beginning of warmer period when particulate organic carbon remineralisation occurs [5].

However, the highest MeHg concentration (20.6 $\mu\text{g/L}$) was found during cooler period at the bottom of the most polluted part of the Bay of Kaštela, indicating possible MeHg input from the sediments to the water column due to strong winter winds and low depth (15 m). Number of picoeukaryotes ranged from $3.04 - 18.1 \times 10^6/\text{L}$. The lowest number was found at the island of Vis ($4.87 \pm 1.07 \times 10^6/\text{L}$) due to low nutrients in the pristine environment. On the contrary, high nutrient input from three surrounding cities [6] is responsible for the highest number of picoeukaryotes observed in the Bay of Kaštela. Here, also higher biological production was observed with the higher number of picoeukaryotes during warmer period ($14.2 \pm 2.95 \times 10^6/\text{L}$) compared to cooler ($11.9 \pm 2.05 \times 10^6/\text{L}$). Just outside the Bay of Kaštela, in the Split Channel, lower nutrients input can be observed through the 42% drop in average annual number of picoeukaryotes ($7.57 \pm 1.62 \times 10^6/\text{L}$).

Vranjic (in the Bay of Kaštela) is the closest station to Hg source and shows the highest values for THg, while the lowest were found at island of Vis. MeHg has similar values for both stations in the Kaštela Bay, except after strong wind, which might have changed distribution. The Bay of Kaštela has the highest number of picoeukaryotes due to occasional eutrophic conditions for which surrounding cities are responsible. The data presented in here showed variability of mercury fractions and microbial species, and has raised a question about their relationships that will be further investigated through the statistical data analysis. This analysis could possibly provide answer to question of picoplankton promoted Hg methylation in the sea water under oligotrophic conditions. We speculate that specific structure of the Adriatic microbial net has an influence on MeHg biomagnification in the whole marine food web. As mercury bioaccumulation has the highest factor in the first step of the marine food web, this could explain why Mediterranean fish have higher MeHg content than Atlantic ones.

Acknowledgments

Authors would like to thank for funding to the Slovenian Research Agency P1-0143 programme, PR-06179 project, and 7 FP GMOS project.

References:

- [1] M. Horvat, J. Kotnik, M. Logar, V. Fajon, T. Zvonarić, N. Pirrone. Speciation of mercury in surface and deep-sea waters in the Mediterranean Sea. *Atmospheric Environment*, 37(1):S93-S108, 2003
- [2] J. Kotnik, M. Horvat, E. Tessier, N. Ogrinc, M. Monperrus, D. Amouroux, V. Fajon, D. Gibičar, S. Žižek, F. Sprovieri, N. Pirrone. Mercury speciation in surface and deep waters of the Mediterranean Sea. *Marine Chemistry*, 107:13-30, 2007
- [3] J. Kotnik, F. Sprovieri, N. Ogrinc, M. Horvat, N. Pirrone. Mercury in the Mediterranean, part I: spatial and temporal trends. *Environmental Science and Pollution Research*, 21(6):4063-4080, 2013
- [4] J. H. Weber. Review of possible paths for abiotic methylation of mercury(II) in the aquatic environment. *Chemosphere*, 26(11):2063-2077, 1993
- [5] L.-E. Heimbürger, D. Cossa, J.-C. Marty, C. Migon, B. Averty, A. Dufour, J. Ras. Methyl mercury distributions in relation to the presence of nano- and picophytoplankton in an oceanic water column (Ligurian Sea, North-western Mediterranean). *Geochimica et Cosmochimica Acta*, 74:5549-5559, 2010
- [6] M. Šolić, N. Krstulović, G. Kušpilić, Ž. Ninčević Gladan, N. Bojanić, S. Šestanović, D. Šantić, M. Ordulj. Changes in microbial food web structure in response to changed environmental trophic status: A case study of the Vranjic Basin (Adriatic Sea). *Marine Environmental Research*, 70:239-249, 2010
- [7] D. Šantić, S. Šestanović, M. Šolić, G. Kušpilić, M. Ordulj, Ž. Ninčević Gladan. Dynamics of the picoplankton community from coastal waters to the open sea in the Central Adriatic. *Mediterranean Marine Science*, 15(1):179-188, 2014

For wider interest

Among the trace metals, mercury is one of the contaminants of most concern because of its high toxicity, persistence and accumulative behaviour in the environment and biota. Mercury can reside in the atmosphere for a long time and be transported over a large geographical distance and is therefore considered a global environmental problem. Due to transformation and transport processes mercury can travel between environmental compartments; from atmosphere to water, soil and biota. Natural bacterial processes in seawater and in sediments can convert inorganic Hg into its most toxic form, methylmercury, where it can be rapidly incorporated into the food web. The uptake of methylmercury by organisms is much quicker than its elimination from the body, so MeHg concentrations will increase with continuing exposure as organisms grow older. This increase with age is referred to as bioaccumulation. Species with longer lifespan are more likely to bioaccumulate higher amounts of methylmercury with continued exposure. Persistent bioaccumulative contaminants, like methylmercury, build up in much greater levels in predators than in their prey. This increase with each step up the food web (trophic level) is called biomagnification. So, in the marine food chain, methylmercury is bioaccumulated and biomagnified with the highest levels found in older predatory fish. But the initial bioaccumulation of methylmercury by phytoplankton represents the biggest single contribution to overall bioaccumulation in marine food webs.

**Informacijske in komunikacijske tehnologije
(Information and Communication Technologies)**

NLOS Channel Detection with Multilayer Perceptron in Low-Rate Personal Area Networks for Indoor Localization Accuracy Improvement

Klemen Bregar^{1,2}, Andrej Hrovat^{1,2}, Mihael Mohorčič^{1,2}

¹ Department of Communication Systems, Jožef Stefan Institute, Ljubljana, Slovenia

² Jožef Stefan International Postgraduate School, Ljubljana, Slovenia

klemen.bregar@ijs.si

Abstract. Indoor localization takes an important part in several areas. It enables indoor navigation for visitors, inventory monitoring, wireless network optimization etc. Among different existing indoor localization approaches the scheme which defines distances via measuring time of flight of the wireless packets and combines them with multilateration is one of the most promising in terms of accuracy and simplicity. The main drawbacks of the multilateration positioning are its sensitivity to noisy measurements, non-line-of-sight (NLOS) signal path effect and positioning anchors fixed in straight line. To mitigate accuracy degradation NLOS ranges should be effectively detected and discarded. In this paper we propose accurate classifier for NLOS signal detection with multilayer perceptron (MLP).

Keywords: IEEE 802.15.4-2011, ultra-wide band (UWB), non-line-of-sight (NLOS), NLOS detection, multilayer perceptron (MLP)

1 Introduction

Information about location is important in modern communication systems, social networks, location-specific applications and other areas [1],[2],[3]. There are numerous approaches for localization based on received signal strength (RSS), time of arrival (TOA), time difference of arrival (TDOA), angle of arrival (AOA), two-way TOA (or round-trip) [4],[5] and fingerprinting methods [1]. RSS measurements are highly variable, TOA and TDOA schemes require accurate time synchronization

between wireless devices while for the fingerprinting methods extensive and time consuming training phase is required for radio environment mapping [4],[6].

Two-way TOA or two-way ranging (TWR) is a method, where wireless packet is time stamped on both receiver and transmitter and takes two round trips. Since two times of flight needed for distance calculation between two nodes can be acquired from accumulated time stamps in a packet, the need for time synchronization of nodes is eliminated.

TWR capability has been already enabled by an extension of base IEEE 802.15.4 standard IEEE 802.15.4-2011 for low-rate personal area network devices [7]. The extension defines an UWB pulse radio, which excels with its great multipath propagation characteristics, high time resolution, low power spectral density (reducing interference to other systems) and centimeter accuracy ranging [8]. This standard enables advent of low-cost radio devices designed for widespread use in sensor networks, industry automation, etc.

Device location can be estimated by multilateration which is a range-based localization method. Ranges between unknown node positions and anchor nodes can be estimated from TDOA, AOA, RSS or TWR data. But the problem of calculating estimated node locations with multilateration is high sensitivity to range errors where non-line-of-sight (NLOS) signal path is the most prominent source of range error [9]. NLOS signal path emerges when direct line between node and anchor is obstructed by an obstacle. Because signal needs to travel around obstacle signal path increases in length which makes path longer than direct line of sight path presumed by multilateration. Such measurements can be refined with post processing techniques or methods for detection of outliers in obtained data.

In this paper we propose an accurate NLOS signal classifier based on multilayer perceptron (MLP). It can be used to accurately detect NLOS range measurements that can be discarded prior localization to prevent localization errors.

2 Experimental setup

To build a classifier great amount of representative data is needed. For localization and data collection purposes we selected low-cost and low-power IEEE 802.15.4-2011 enabled UWB radios from DecaWave which are suitable for low-cost sensor nodes.

A. DecaWave UWB ranging radios

DecaWave DW1000 UWB radios incorporate efficient algorithm for detecting start of frame necessary for accurate packet time stamping and thus great ranging resolution. 10 centimeter localization accuracy is advertised in [10].

DW1000 radio supports 6 UWB channels with center frequencies from 3.5 GHz to 6.5 GHz, data rate options of 110 kbit/s, 850 kbit/s and 6.8 Mbit/s, and transmit power density lower than -41.3dBm/MHz guaranteeing low or no interference to other radio communication systems in the same bands, i.e. operating as an underlying technology. The communication is handled with transport of UWB frames. Each frame consists of synchronization header (SHR), containing SYNC field and start of frame delimiter (SFD), PHY header (PHR) and the data payload part as presented in Figure 1 [8]. SHR field is used by internal time stamping algorithm for channel impulse response estimation (frame quality analysis) and start of frame detection [8].

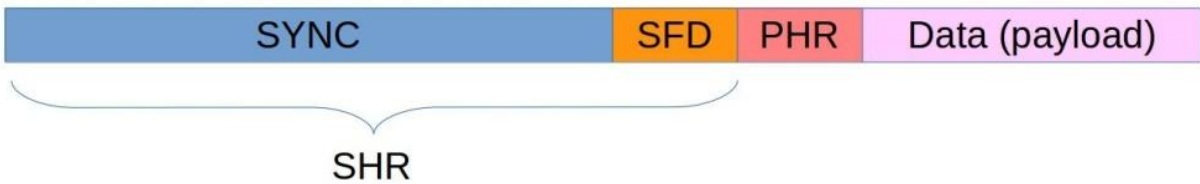


Figure 1: UWB frame structure

B. Localization with multilateration

The common 2-D localization method exploiting range measurements from more than 2 anchor nodes at known locations is called multilateration [9]. Range measurements r_i can be written as a system of equations

$$r_i = \sqrt{(x_i - x)^2 + (y_i - y)^2}, \quad (1)$$

where $\mathbf{P}_i = (x_i, y_i), i = 1, 2, \dots, n$ are known coordinates of an anchor node i . The problem of finding unknown node position with multilateration is similar to problem of finding the intersection points of n circles in 2-D space and is solved by squaring the equation (1) and subtracting the last equation from the first $n - 1$ equations [9].

The resulting system of linear equations can then be written as

$$\mathbf{A} = \begin{bmatrix} 2(x_1 - x_n) & 2(y_1 - y_n) \\ \vdots & \vdots \\ 2(x_{n-1} - x_n) & 2(y_{n-1} - y_n) \end{bmatrix} \quad (2)$$

$$\mathbf{b} = \begin{bmatrix} x_1^2 - x_n^2 + y_1^2 - y_n^2 + r_n^2 - r_1^2 \\ x_{n-1}^2 - x_n^2 + y_{n-1}^2 - y_n^2 + r_n^2 - r_{n-1}^2 \end{bmatrix}.$$

Therefore, for each location the linear system can be solved using

$$\mathbf{P}(x, y) = \hat{\mathbf{x}} = (\mathbf{A}^T \mathbf{A})^{-1} \mathbf{A}^T \mathbf{b}. \quad (3)$$

C. NLOS identification feature selection

To be able to detect the nature of received UWB frame, signal waveform metrics are needed to show the quality of current communication channel. DecaWave radios have several frame quality indicators that can be used as LOS/NLOS identification features [11]. They are obtained during received SHR frame processing inside built-in frame processing algorithm. Frame quality indicators can be obtained from radio registers through SPI interface. However because of the implementation complexity limitations those parameters are just highly accurate estimates of actual state.

Available frame quality indicators are:

- a) *Standard Deviation of Channel Impulse Response Estimate Noise (σ_{CIREN}):* σ_{CIREN} gives a measure of noise associated with measured estimation of channel impulse response. Low levels of noise compared to first path amplitude have little impact on the timestamp accuracy. In case of high noise values and NLOS signal path, first path can be buried in the noise, which results in incorrect timestamp detection [11].
- b) *Received channel power estimate (RCPE):* RCPE gives the estimated signal power at radio input for current ranging measurement (UWB packet). Due to the radio signal path loss the RCPE decreases with increasing distance between nodes. According to device specification relationship between actual received channel power and RCPE is not linear for entire range. For low signal levels RCPE shows accurate signal levels but when the signals are stronger (high transmission power, low ranges to neighbor nodes) RCPE shows lower signal levels than actual. [11].
- c) *First path received channel power estimate (RCPE_{FP}):* RCPE_{FP} shows the signal power of the detected first path signal. Relation between first path signal level and general RCPE level indicates the nature of received packet path. If RCPE_{FP} is significantly lower than RCPE, the signal is strongly affected

by multipath effects and consequently NLOS. Examples of channel impulse responses presenting distinction between the first path and multipath components of LOS and NLOS conditions are shown in Figure 2.

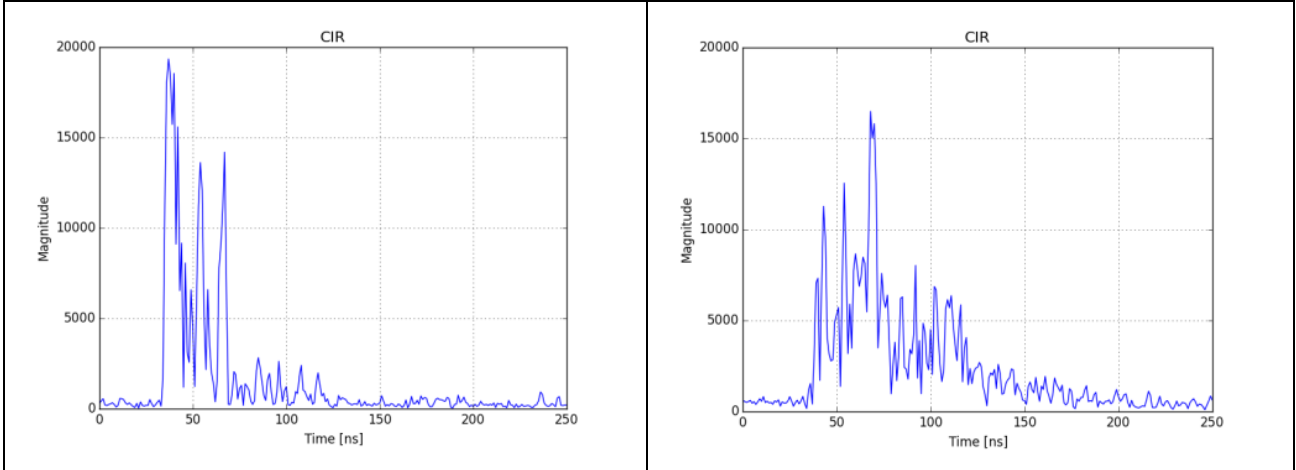


Figure 2: LOS channel impulse response and NLOS channel impulse response

D. Data collection

To make a good classification model, representative data for LOS and NLOS ranging measurements with different degrees of multipath effects and ranging errors in real world environment had to be collected. We selected an office space with nearby corridor and mapped it with measurement sites. Each measurement site had a fixed relative coordinate which simplified the calculation of the actual distances between two nodes. The location of the first radio was fixed throughout whole experiment while the other was moved through all the predefined positions.

Fixed sensor node was connected to the computer over virtual serial port. Since every new ranging report had to include packet performance information and channel impulse response estimation (CIRE), the default sensor node firmware was modified. Measurement samples were collected and later preprocessed with python script which also took care of radio setup and control.

To identify the most accurate ranging channel for current radio calibration we first performed test ranging measurements. According to the acquired data we selected channel 2 with central frequency of 3993.6 MHz and bandwidth of 499.2 MHz. To get the best performance in case of NLOS signals and consequently better accuracy in first path signal detection we selected the longest SHR preamble length of 4096

symbols. In addition, to extend the communication range, we choose the lowest available bit rate (110 kbit/s).

For each of the 36 locations 100 signal measurement samples were acquired which gave us 3600 overall samples.

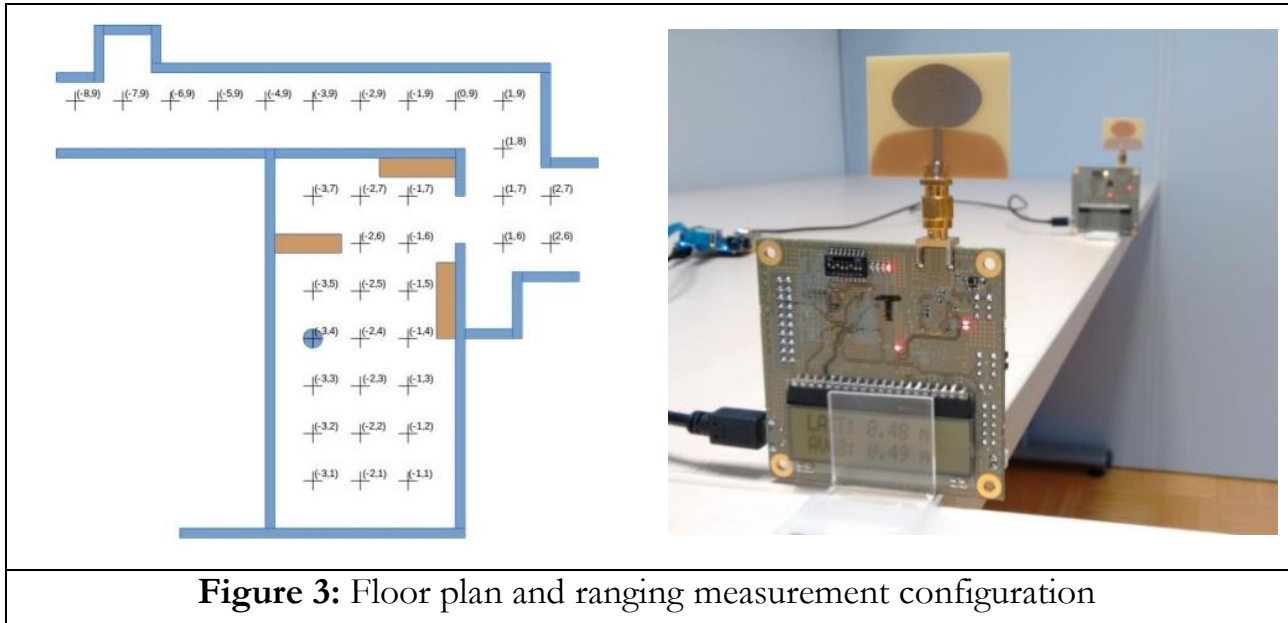


Figure 3: Floor plan and ranging measurement configuration

E. Building LOS/NLOS classifier

For the LOS/NLOS signal classifier we selected a multilayer perceptron (MLP). It is capable of building complex system models from multiparameter data where relations between parameters are difficult to obtain analytically. For learning and classification we used MLP implementation from scikit-learn machine learning package in Python.

In the first learning stage we split the acquired data and 60% of the data were used for perceptron training. Classification of the remaining 40% of samples was used for evaluation of NLOS predictor accuracy.

During learning process we experimented with different MLP configurations, according to their classification performance. The most effective configuration consists of three hidden layers with 5 neurons in first layer, 12 neurons in second layer and 3 neurons in third layer.

3 Results

Classification of the test samples acquired during measurement campaign shows good NLOS signal detection capability of previously trained MLP classifier. It

correctly detects the nature of acquired range measurement in 90% of the cases. Actual classification performance can be seen in Table 1. NLOS signal is correctly detected in 87% of cases and LOS signal in 93% of cases.

Table 1: Classification results

Training set:	2160 samples
Test set:	1440 samples
Incorrectly classified LOS:	97
Incorrectly classified NLOS:	48
Correctly classified NLOS:	642
Correctly classified LOS:	653
Sensitivity:	0.8687
Specificity:	0.9315
Accuracy:	0.8993

The actual impact on localization accuracy cannot be extracted from the Table 1. In order to evaluate their impact we attempted to localize unknown node position from all possible combinations of 3 and 4 anchors with known locations, extracted from our set of measurement points in data set acquired during measurement campaign. In this stage both LOS and NLOS signals were used and the results in Table 2 clearly show great multilateration sensitivity to ranges impacted by noise and signal path enlarged by NLOS conditions. Large part of error in worst case scenario combinations of anchors comes from numerical instability of multilateration in cases where all anchors are in straight line or at the same height. The closer anchors are to a straight line or more similar are their heights, the closer is the singularity of matrix \mathbf{A} (2) and therefore the bigger is the localization error regardless the real distance measurement errors.

Maximum location error inside entire dataset is 122 m for configuration A and almost 66 m for configuration B. If we filter the NLOS conditioned ranges out by eliminating them with perfect a priori knowledge taken from dataset, the maximum worst case scenario errors decrease to 4.23 m for configuration C and 2.78 m for configuration D.

In operational scenarios only ranges with strongest signals and shortest distances will be taken for localization. Thus, the occurrence of worst case scenario combinations

would be eliminated in most cases. It can be assumed that mean errors and standard deviations from calculated set of locations can be taken as good localization performance metrics. For unfiltered data where both LOS and NLOS ranges are used 1.93 m mean error for configuration A and 1.13 m mean error for configuration B is achieved with standard deviations of 3.98 m and 1.41 m respectively. We can conclude that with increasing number of anchor nodes used for localization, multilateration estimates location with better accuracy.

Table 2: Localization errors for different configurations

	Configuration	Mean [m]	Std_dev [m]	Median [m]	Max [m]
A	3 anchors: LOS and NLOS	1.93	3.98	0.86	122.05
B	4 anchors: LOS and NLOS	1.13	1.41	0.72	65.70
C	3 anchors: LOS only	0.28	0.29	0.19	4.23
D	4 anchors: LOS only	0.19	0.14	0.16	2.78
E	3 anchors: with classifier	0.59	0.97	0.32	33.36
F	4 anchors: with classifier	0.40	0.51	0.26	21.92

To evaluate classifier impact on localization accuracy improvement we filtered the test set of ranges with previously trained MLP classifier. Improvement in localization accuracy compared to unfiltered ranges can be observed. Ranges filtered by MLP classifier yields mean errors of 0.59 m for configuration E and 0.40 m for configuration F with standard deviations of 0.97 m and 0.51 m respectively. Maximum localization errors were reduced to 33.36 m for configuration E and 21.92 m for configuration F. All results can be seen in Table 2.

To make multilateration usable in real life scenarios the smart anchor selection algorithm should be applied. Selection algorithm should be checking geometric configurations of anchors in range and selecting only those with the most spread coordinates in space to prevent situations where anchors are aligned in straight line or at the same height thus preventing errors induced by numerical instability of multilateration.

4 Conclusion

We trained the MLP classifier to distinguish between LOS and NLOS ranging signals in indoor localization problem. It can be seen that positioning accuracy can be greatly degraded when NLOS ranging signals are used for localization and stays in

reasonable limits when classification is used for NLOS ranges elimination. With additional measurement activities the NLOS model should be further evaluated and extended at different environments than used in the experiment to eliminate possibility of NLOS model overfitting to current environment.

To prevent localization errors induced by numerical instability of multilateration when anchors are positioned in a straight line or at the same height the geometrical checking of selected ranges should be made to select only the anchors with most spread coordinates in space.

In the future NLOS model should be extended with measurements for all available communication channels and with additional channel quality parameters such as overall length of channel impulse response and channel impulse response itself.

The described solution should be further developed by NLOS ranging error predictor and range error mitigation which would make NLOS affected ranges more suitable for localization.

References:

- [1] T. Van Nguyen, Y. Jeong, H. Shin and N.Z. Win, Machine Learning for Wideband Localization, IEEE Journal on Selected Areas in Communications, vol. 33, no. 7, pp. 1357-1380, July 2015
- [2] H. Wymeersch, S. Marano, W. M. Gifford and M. Z. Win, A Machine Learning Approach to Ranging Error Mitigation for UWB Localization, IEEE Transactions on Communications, vol. 60, no. 6, pp. 1719-1728, June 2012
- [3] S. Marano, W. M. Gifford, H. Wymeersch and M. Z. Win, NLOS identification and mitigation for localization based on UWB experimental data”, IEEE Journal on Selected Areas in Communications, vol. 28, no. 7, pp. 1026-1035, September 2010
- [4] N. Patwari, J. N. Ash, S. Kyperountas, A. O. Hero, R. L. Moses and N. S. Correal, Locating the nodes: cooperative localization in wireless sensor networks, IEEE signal Processing Magazine, vol. 22, no. 4, pp. 54-69, July 2005.
- [5] Long Cheng, Chengdong Wu, Yunzhou Zhang, Hao Wu, Mengxin Li, and Carsten Maple, “A Survey of Localization in Wireless Sensor Network,” International Journal of Distributed Sensor Networks, vol. 2012, Article ID 962523, 12 pages, 2012. Doi:10.1155/2012/962523
- [6] Y. Luo, Y. P. Chen and O. Hoerber, Wi-Fi-Based Indoor Positioning Using Human-Centric Collaborative Feedback, 2011 IEEE International Conference on Communications (ICC), Kyoto, 2011, pp. 1-6.
- [7] IEEE Standard for Local and Metropolitan Area Networks – Part 15.4: Low-Rate Wireless Personal Area Networks (LR-WPANs), IEEE Std 802.15.4-2011, 2011
- [8] S. Gezici et al., Localization via ultra-wideband radios: a look at positioning aspects for future sensor networks, IEEE Signal Processing Magazine, vol. 22, no. 4, pp. 70-84, July 2005
- [9] R. Mautz, W. Ochieng, G. Brodin and A. H. Kemp, 3DWireless Network Localization from inconsistent Distance Observations, Ad Hoc & Sensor Wireless Networks 3, no. 2-3 (2007), pp. 141-170
- [10] DW1000 Product Brief, Available: <http://www.decawave.com/support>
- [11] DW1000 User Manual, Available: <http://www.decawave.com/support>

For wider interest

Wireless localization takes important part in several application areas. It can be used for indoor industrial robot navigation, visitor navigation at a fair, inventory monitoring, etc. One way to correctly position devices or people in space is to measure ranges from several points in space (in this case with wireless sensors communication) and combine this distances to a relative or an absolute position with method called multilateration.

Multilateration is efficient mathematical method to calculate position but is sensitive to distance measurement errors. Wireless ranging devices are susceptible to non-line-of-sight distance measurement bias. This happens because of longer signal traveling path caused by reflections in environment compared to actual shortest distance between devices which is not obstructed by obstacles.

To eliminate or at least mitigate the effects of non-line-of-sight distance measurements impacting positioning accuracy we proposed signal classifier based on multilayer perceptron machine learning algorithm which in 90% cases correctly decides on a nature of distance measurement (line-of-sight or non-line-of-sight) according to available frame quality indicators.

Correctly classified non-line-of-sight distances can be removed from localization set and thus preventing positioning accuracy degradation. In experimental setup this improved the localization accuracy from 1.93 m to 0.59 m.

Passive Ankle Exoskeleton: Design and Practical Evaluation

Miha Dežman^{1,2}, Tadej Debevec¹, Jan Babič¹, Andrej Gams¹

¹Department of Automatics, Biocybernetics and Robotics, Jožef Stefan Institute, Ljubljana, Slovenia

²Jožef Stefan International Postgraduate School, Ljubljana, Slovenia

miha.dezman@ijs.si

Abstract: With the recent advancements in technology, wearable devices or exoskeletons witness intense development. Passive unpowered exoskeletons are starting to emerge that have advantages compared to the powered solutions; simpler design, lower weight, no complex electronics and lower price. Such an exoskeleton has a higher chance of end-user acceptance. In this paper, the design and evaluation of an unpowered passive ankle exoskeleton is presented. Important design aspects such as ergonomics, comfort and robustness are outlined. The exoskeleton was evaluated in a short study, where its physiological effects were assessed by measuring the oxygen consumption and EMG muscle activity during five 10-min walking sessions with different boundary conditions for four participants. Results show that by choosing a proper spring, metabolic cost reduction of walking can be achieved.

Keywords: passive exoskeleton, metabolic cost, efficient walking, metabolic cost reduction

1 Introduction

Wearable robotic mechanisms [1] or exoskeletons hold great promise to improve our everyday lives in the near future. They have a wide range of potential users and applications and can be applied for rehabilitation, for assistance and augmentation of motion of patients with disabilities, workers, the elderly and even healthy people. The exoskeleton research is now most intense [2][3], however, a lot of issues still prevent the successful commercialization and wider use; like portability, energy consumption, social constraints and high cost of these devices [4].

An important everyday human activity is walking, since it provides social independence and has near-term and long-term effects on health [5]. A lot of

powered exoskeletons are therefore focused on augmentation of lower extremities to assist in human walking or running. One way the exoskeletons can help is by reducing the metabolic expenditure, which can be achieved in different ways. Ferris et al. [6] have shown that by assisting at the hip during walking, muscle effort reduction can be achieved in the hip as well as in the ankle. Gams et al. [7] showed that usage of a knee exoskeleton decreases the metabolic cost of squatting. Mooney et al. [8] showed significant decrease of metabolic cost when using a powered ankle exoskeleton during load carriage.

Another way to achieve metabolic cost reduction is with the use of passive solutions that do not rely on motors, batteries or controllers. Passive devices can be in some aspects superior to actuated solutions, because of their lower weight, simpler design and lower price, which makes them more affordable, user friendly and perhaps easier to introduce into everyday lives. Passive solutions can decrease the metabolic consumption for humans carrying heavy loads by transmitting some weight directly to the ground [9]. This solution, however, does not reduce metabolic consumption compared to normal walking. Collins et al. [10] presented an un-powered exoskeleton that achieved metabolic cost reduction of human walking with a completely passive device. The exoskeleton they presented used a spring between the insole and the frame around the calf. The spring is attached to a mechanical clutch, which allows the spring to store energy at some parts of the gait, release it at an appropriate time, and not hinder the motion of the leg while it is in the swing phase.

In this paper we present our implementation of such an un-powered exoskeleton. Our main goal was to evaluate the exoskeleton, described in [10] and find ways to improve the current concept. Different materials were used in the design and some minor changes were introduced to make the production cheaper and assembling more convenient. Lastly, a short study was performed to test the exoskeleton and to see if a reduction in metabolic cost of walking can be observed.

2 Passive Ankle Exoskeleton

We designed a prototype exoskeleton, shown in **Figure 1**, based on the work of Collins et al. [10]. Our goal was to achieve a working prototype in as few iterations

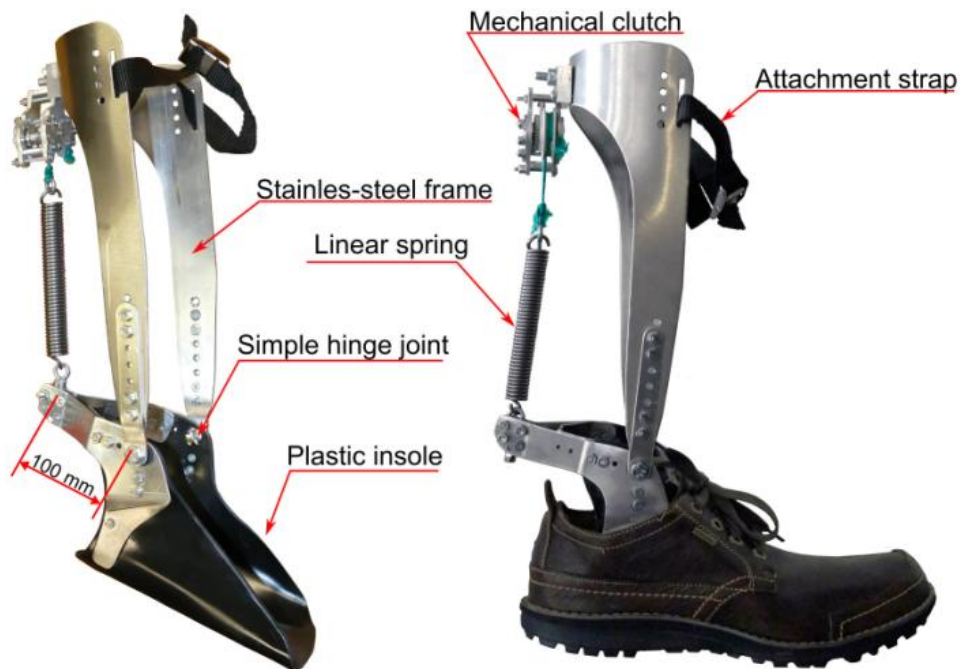


Figure 1. Our prototype version of the exoskeleton.

as possible. With this in mind, we incorporated some changes and used different materials to make the production faster, cheaper and more convenient. The working principle stayed the same as in the original.

The exoskeleton comprises of an insole part, a simple hinge joint, a stainless steel frame, an attachment strap, a mechanical clutch and a linear tension spring. The exoskeleton allows one degree of freedom motion at the ankle hinge joint. The user can don-on the exoskeleton by tightening the attachment strap. One exoskeleton was made for each leg. The exoskeleton frame was made out of stainless steel and no weight/strength optimization was performed. The prototype weights 0.8 kg. We believe, however, that the weight could be significantly reduced in the next iteration of design.

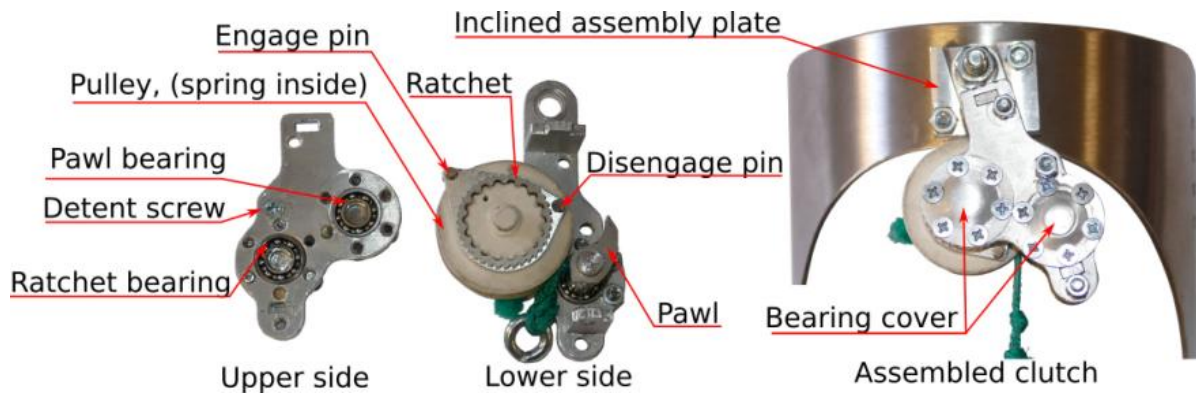


Figure 2. Our prototype version of the mechanical clutch.

The mechanical clutch shown in **Figure 2** is largely based on the original [10] with some modifications to make the production and assembly more convenient. Its components were manufactured out of aluminum, stainless-steel and plastic using laser-cutting process and 3D-addition technologies. We assembled the clutch onto the frame using an inclined assembly plate in order to improve the robust operation of the mechanical clutch.

The insole was manufactured out of plastic using heat-forming process and then reinforced with stainless-steel. Effort was made, so that the insole would fit into an average male shoe and still be comfortable. The possibility, where the user can use its own shoes when using the exoskeleton, gives the feeling of simplicity and trust. Ergonomic design and comfort are important and greatly affect the end-user acceptance. Since the foot must fit into the shoe and the exoskeleton, the design of such an insole is no easy feat. Our approach comprised of four major steps to design an insole that would not cause discomfort to the user. It is important that the insole is not thick and its overall width not too large. An insole which is too wide, would prevent the user from walking normally.

To design a comfortable insole, we first designed an approximate 3D sheet-metal model [**Figure 3a**], which we then flattened out and printed on a piece of paper. The paper insole [**Figure 3b**] was then fitted into a shoe, to estimate the positions where the aluminum should fold. Next the fold positions were incorporated into the 3D-model in the shape of rectangular holes, which were then present in the

manufactured aluminum insole [Figure 3c]. The rectangular holes helped in folding of aluminum insole, but introduced wear weak points in the overall insole design. Because of this, another insole was designed using plastic [Figure 3d], which was heat-formed over the aluminum insole and strengthened using stainless-steel frame.

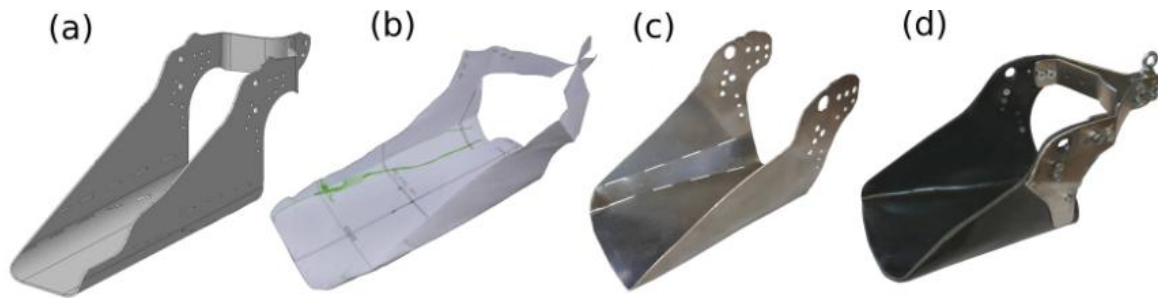


Figure 3. Process of the insole design.

3 Results

A randomized cross-over study was designed in order to see if the exoskeleton works as intended. Four healthy young males (age 23-37 years, weight 71-81 kg, height 175-181 cm) volunteered to participate in the study. After learning about the procedure and giving a free informed consent, the participants were asked to perform a series of 10-min walks on a treadmill moving with a speed of 4 km/h. Each participant performed five walks that consisted of a referential (exoskeleton free) walk; walk with the spring-less exoskeleton; and three walks with exoskeleton with springs of different stiffness (5 N/mm, 12 N/mm and 20 N/mm). Participants rested sitting on a chair for at least 10-min between sessions.

To evaluate the exoskeleton effect on the user, we measured the *oxygen consumption* ($\dot{V}O_2$) using a portable metabolic cart (K4b², Cosmed Italy). The change in average *oxygen consumption* was used as a way to assess the reduction/increase of metabolic cost of walking. The measurement system is shown in **Figure 4a** and a participant during a walking session in **Figure 4b**. To assess an approximation of the overall muscle effort during walking, we measured EMG activity of the *Vastus Medialis* and *Soleus* muscle on the right leg of each participant. The EMG signals were rectified

and integrated for a time of 7-min out of the 10-min walk to exclude the starting and ending discrepancies, and then normalized to the value at the referential walk.

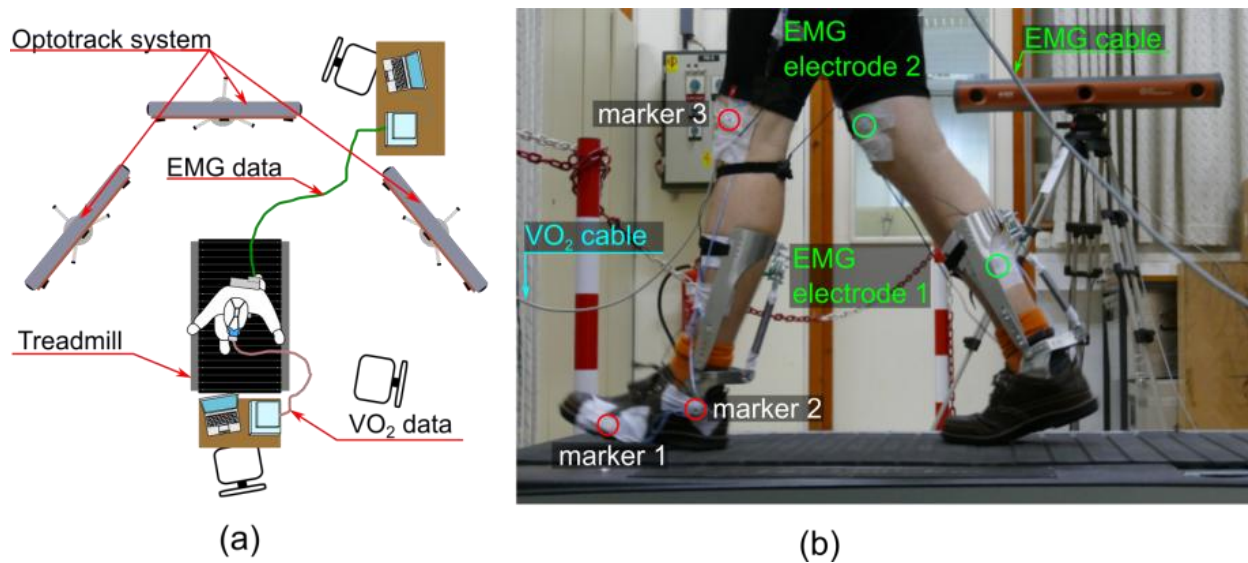


Figure 4. (a) Our measurement system, (b) exoskeleton test walk.

The collected data is presented in **Figure 5**. An increase of metabolic cost of walking can be seen when using the exoskeleton without a spring. The reason seems to be the increased weight (0.8 kg) and the introduced kinematic constraints. These aspects of the exoskeleton can be improved in the next iteration of design. When using a spring, the average metabolic cost does get lower in some cases. Results differ greatly from subject to subject, which can be seen in a relatively large standard deviation from the average. We assume that the metabolic cost reduction would be more apparent compared to the metabolic cost of normal walking, if the increase of the metabolic cost when donning the exoskeleton could be lowered. Apart from that it seems that the most appropriate spring stiffness is in the area near 5 N/mm.

The EMG activity data does not directly coincide with the data for oxygen consumption. For the Soleus muscle a reduction of muscle activity can be observed, when the spring stiffness increases. The appropriate spring stiffness according to soleus muscle activity would be near or over 20 N/mm. The muscle activity of the *Vastus Medialis* does seem to drop compared to the activity when walking with a spring-less exoskeleton, but compared to the activity of normal walking, the

reduction is not so apparent. It seems, that the reduced oxygen consumption results also from other muscles, apart from the *Soleus* and *Vastus Medialis* muscle, which could explain the discrepancy between the average oxygen consumption and average muscle activity. The metabolic cost reduction is heavily dependent on the quality of the clutch operation, ergonomic design and comfort of the exoskeleton and its weight and introduced kinematic constraints. All this should be taken into account in the exoskeleton design.

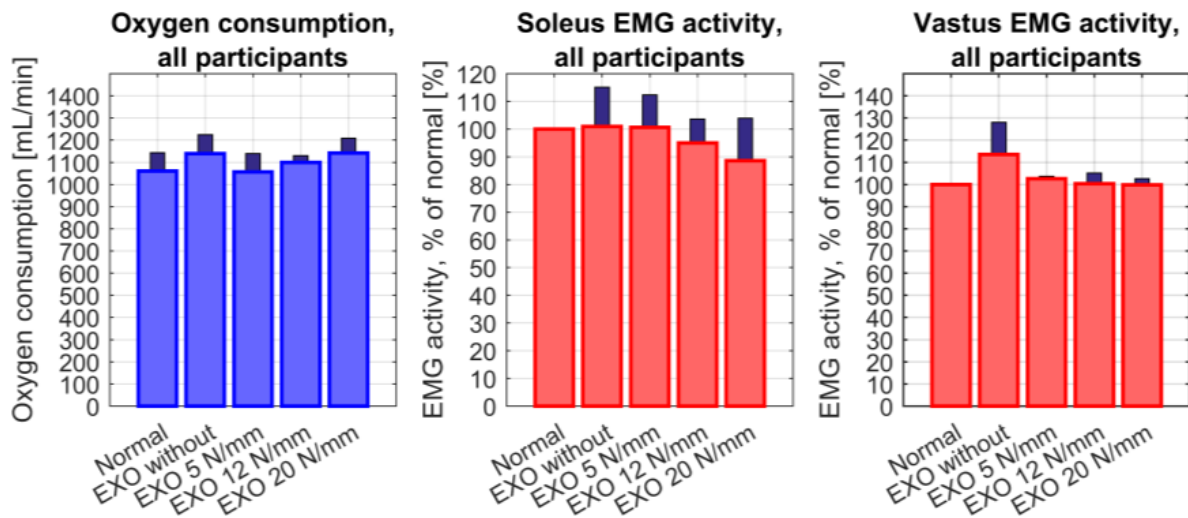


Figure 5. Comparison of oxygen consumption and muscle EMG activity (*Soleus* and *Vastus Medialis* muscles on right leg) for different boundary conditions.

4 Conclusions

The collected data shows that addition of a spring of appropriate stiffness does result in a reduced metabolic cost, but differs greatly from subject to subject. It would presumably get more apparent, when the introduced kinematic constraints on the user and weight of the exoskeleton get minimized. To achieve significant metabolic cost reduction, an appropriate spring must be chosen and the clutch timing setup correctly. Focus is advised in exoskeleton design to achieve minimal introduced kinematic constraints. Additionally, a light-weight frame structure should be designed and weight/strength optimization performed. Exoskeleton design should be ergonomic in order to achieve a greater comfort. Based on the results, the appropriate spring stiffness is deemed smaller than 12 N/mm and near 5 N/mm.

References:

- [1] J. L. Pons. *Wearable robots: Biomechatronic exoskeletons* Hoboken, NJ: Wiley, 2008.
- [2] D. P. Ferris. The exoskeletons are here, *Journal of Neuro-engineering and Rehabilitation*, 6(1): 1, 2009.
- [3] S. Viteckova, P. Kutilek, and M. Jirina, Wearable lower limb robotics: A review. *Biocybernetics and Biomedical Engineering*. 33(2):96–105, 2013.
- [4] S. Mohammed and Y. Amirat, Towards intelligent lower limb wearable robots: Challenges and perspectives - State of the art. *IEEE International Conference on Robotics and Biomimetics (ROBIO)*, Bangkok, pp. 312-317, 2009
- [5] J. N. Morris and A. E. Hardman. Walking to health. *Sports medicine*, 23(5):306–332, 1997.
- [6] D. P. Ferris, G. S. Sawicki, and A. Domingo. Powered lower limb orthoses for gait rehabilitation. *Topics in spinal cord injury rehabilitation*, 11(2):34, 2005.
- [7] A. Gams, T. Petric, T. Debevec, and J. Babic. Effects of robotic knee exoskeleton on human energy expenditure. *IEEE Transactions on Biomedical Engineering*, 60(6):1636–1644, 2013.
- [8] L. M. Mooney, E. J. Rouse, and H. M. Herr. Autonomous exoskeleton reduces metabolic cost of human walking during load carriage. *Journal of Neuro-engineering and Rehabilitation*, 11(1):1, 2014.
- [9] C. J. Walsh, D. Paluska, K. Pasch, W. Grand, A. Valiente, and H. Herr. Development of a lightweight, under-actuated exoskeleton for load-carrying augmentation. *IEEE International Conference on Robotics and Automation*, pp. 3485–3491, IEEE, 2006.
- [10] S. H. Collins, M. B. Wiggin, and G. S. Sawicki. Reducing the energy cost of human walking using an unpowered exoskeleton. *Nature*, 522(7555):212–215, 2015.

For wider interest

Exoskeletons or wearable robotic mechanisms are assistive robots, which now face intensive development. They can improve the quality of lives for patients with disabilities, older people, workers and even healthy people. Because of a rapidly aging population of industrial societies, the proportion of older people is getting larger. Exoskeletons could improve their lives and prolong their individual social independence, which could have benefits for the users as well as long-term benefits for the society.

Right now, many different actuated exoskeletons exist, some are also commercially available, but are not yet widely affordable. The high prices result from complicated mechanics, actuators, sensors, complicated controllers, electronics and the need for batteries. Unpowered passive exoskeleton solutions exist that have some distinct advantages over the actuated solutions, since they are simpler, lighter, easier to operate and do not use electronics or controllers, and are consequently cheaper. Because of this, they possess a better chance of integration and end-user acceptance.

In this paper a passive exoskeleton is presented with results from a study of its effect on the user during walking. The unpowered ankle exoskeleton reduced the metabolic cost of walking, when correct clutch timing was setup and when a spring with a proper stiffness was selected. The mechanism of clutch operation is at this stage not yet fully robust, so the average metabolic consumption reduction differs greatly from subject to subject. Additional research is still needed and the exoskeleton design could still be improved. The current results will help improve the concept, the design and robust clutch operation and bring the exoskeleton closer to the usage.

The concept could potentially be extended to other human joints, instead of only the ankle, which could result in novel new types of exoskeletons that work in a hybrid unpowered and powered combination to achieve greater energy efficiency and performance. The exoskeleton could be used by any user, that is able to walk, and would like to walk with less effort.

Knowledge extraction of evidence-based dietary recommendations

Tome Eftimov^{1,2}, Peter Korošec¹, Barbara Koroušić Seljak¹

¹ Department of Computer Systems, Jožef Stefan Institute, Ljubljana, Slovenia

² Jožef Stefan International Postgraduate School, Ljubljana, Slovenia

tome.eftimov@ijs.si, peter.korosec@ijs.si

barbara.korousic@ijs.si

1 Introduction and motivation

Unhealthy diet can lead to diseases such as diabetes, cardiovascular disease and stroke, and some types of cancer, among other health-related problems. For this purpose, generalized dietary guidelines and recommendations are presented in different forms, available in books, magazines, television programs and the Internet. For example, Dietary Reference Intakes (DRIs) are reference values that are quantitative estimates of nutrient intakes that can be used for planning and assessing the diets for healthy people [1]. In addition, there are food-composition studies, which are carried out to determine the chemical nature of components in food that affect human health [2]. Also the complete mapping of the human-genome sequence introduced the possibility of personalized dietary recommendations based on an individual's genetic profile, and give an opportunity to understand the relationship between food and gene expression.

The main goal of our research is to find some new methods that can be used for knowledge extraction of evidence-based dietary recommendations, which are crucial in public health and health informatics.

2 Methodologies for knowledge extraction

Three methods related to evidence-based dietary recommendations are presented. The first one is an information retrieval method that can be used for finding the most relevant food analysis from the food-composition database (FCDB) for given recipe's ingredient or food. The second one is a method that can be used for harmonization of the data that is coming from different data or service providers. And the third one is a named-entity linking method that can be used for knowledge extraction of evidence-based dietary recommendations.

2.1 POS tagging-probability weighted method

There is a lack of structure in the names of the ingredients used in the recipes and a lack of structure in the names of the food analyses from the FCDBs. In order to find the most relevant match for the ingredients used in the recipes using their names and the names of the food analyses presented in the FCDBs, an information retrieval method based on probability theory and string similarity is presented [3]. The method is evaluated using a collection of 721 lunch recipes, from which 1,615 different ingredients are extracted and the result shows that the method can match 91.82% of the ingredients with the FCDB. Also the method is tested with Slovenian recipes and the result is promising having in mind that there are still food analyses missing in the Slovenian FCDB.

2.2 Ontology learning using personalized dietary web services

Nowadays, there are several data sources that contain information about nutritional principles or provide personalized dietary services. The question that arises here is how to extract knowledge from heterogeneous data sources using different ways of describing and classifying the data. In order to help users and clinical dieticians access the relevant knowledge about food and nutrition data in e-health systems that use different data sources, ontologies about food and related domains, such as clinical medicine, individual user profile, etc., are very important in order to provide successful, smart e-health systems. For this purpose, an ontology-learning process using personalized dietary web services that are dealing with food-related data and knowledge rules is presented. The result is an ontology presented in Figure 1. The ontology is developed in a semi-automatic way using POS tagging probability-weighted method, which is based on string similarity and probability theory. The ontology can be used for harmonization of personalized dietary web services and will enable researchers to share information in this domain. To the best of our knowledge, this ontology is the first ontology that describes data including food-composition studies, biomarkers' analysis, dietary reference intakes and knowledge rules and the relation between them.

References:

- [1] J. P. Hellwig, J. J. Otten and L. D. Meyers. *Dietary Reference Intakes: The Essential Guide to Nutrient Requirements*. National Academics Press, 2006.
- [2] H. Greenfield and D. A. Southgate. *Food composition data: production, management, and use*. Food and Agriculture Organisation of the United Nations, 2003.
- [3] T. Eftimov and B. Koroušić Seljak. POS tagging-probability weighted method for matching the Internet recipe ingredients with Food Composition Data. In *Proceedings of 7th International Joint Conference on Knowledge Discovery, Knowledge Engineering and Knowledge Management (IC3K 2015)*, 2015, Lisbon, Portugal, 2015.

For wider interest

Food-based dietary guidelines (FDBGs) are simple advices on healthy eating, aimed at the general public. They give an indication of what a person should be eating in terms of foods, and provides a basic framework to apply when making healthy dietary choices and planning meals. The main goal of FDBGs is to improve public health and well-being.

The European Food Safety Agency (EFSA) is an example of the authority, which provides dietary reference values (DRVs) as a complete set of nutrient recommendations and quantitative reference values for nutritional intakes.

Most countries have established their own national DRVs and FDBGs that consider beside international recommendations and guidelines also local conditions and national eating culture and habits and are reviewed and updated from time to time.

In several chronic diseases, like diabetes, celiac disease, chronic kidney disease, some cancers, Parkinson's disease etc., nutritional therapy is used to help patients get energy and nutrients they need to deal with the effects of disease and its treatment.

Personalized dietary recommendations consider genetic predisposition to chronic disease and phenotypic information on anthropometry, physical activity, clinical parameters and biochemical markers of nutritional status, and give strategies to dramatically reduce the chronic–disease risk.

In public health as well as in clinical practice, dietary recommendations should be based on evidence-based principles, considering scientific knowledge, expert consensus and clinical experience. In case of chronic patients, the best available evidence must take into account individual circumstances, preferences, and cultural and ethnic preferences, and the patient should be involved in the decision-making process.

As today amount of information is massive and is quickly increasing, computer-based tools for systematic knowledge identification, extraction and exploration are welcome to support human experts in decision-making about appropriate nutritional care for specific disease states or conditions in typical settings.

Activity and stress monitoring using smartphone and wrist device

Martin Gjoreski^{1,2}, Vito Janko^{1,2}, Hristijan Gjoreski¹, Božidara Cvetković^{1,2}, Mitja Luštrek¹, Matjaž Gams¹

¹ Department of Intelligent Systems, Jožef Stefan Institute, Ljubljana, Slovenia

² Jožef Stefan International Postgraduate School, Ljubljana, Slovenia

vito.janko@ijs.si martin.gjoreski@ijs.si

Abstract. It is well known that physical and mental health are closely related and impact the overall quality of life simultaneously. Therefore, both these areas should be tackled together. In this paper we propose a smartphone application capable of monitoring physical activity and mental stress. The application consists of two machine learning modules, an activity recognition (AR) module and a stress detection module. The AR module continuously recognizes user's activity using accelerometer data and additional information such as phone orientation and location, with accuracy of 91%. The recognized activities are summarized and presented to the user including health advices, and are also fed to the second module of the application, the stress detection module. The stress detection module, in addition to the information provided by the AR module, uses data provided by a commercial wrist device equipped with standard bio-sensors and an accelerometer. The stress detection module was trained on 21 subjects in a laboratory setting and tested on 5 subjects in a real-life setting achieving accuracy of 92% for detection of stressful events.

Keywords: Activity recognition, stress detection, machine learning, sensors, wrist device.

1 Introduction

Regular physical activity can have a positive impact on one's life, yet only a small fraction of the modern population exercises sufficiently. To appropriately motivate people for increasing their physical activity, it is important to quantify it first. Modern phones are equipped with a variety of sensors that can constantly track the user, allowing us to deduce much about his/hers behavior. An average smart phone,

which most people already have, contains a tri-axial accelerometer, making it arguably the most convenient device to use for this task.

The first goal of our work was to detect person's basic activities, such as standing, sitting, walking, running, etc. with the information available on his/hers mobile phone. To do so, we first determine phone's orientation, relative to the user, and location of wear. Using that information in addition to the accelerometer data we show that user's current activity can be accurately determined. We enhance the application by allowing the user to wear an optional wristband, which provides additional data to the module. AR is a mature area of research that many have attempted with different wearable sensors [12]. AR using a smart phone device has also already been attempted [13]. Our improvement to the other smart phone solutions is that we explicitly calculate phone's location and use specialized classifiers for that location.

The second goal of our work was to implement a stress-detection module which complemented with the AR module (providing physical health care) would provide a mental health care to the users. The need for health monitoring was confirmed by the European Commission by estimating the costs of work-related stress at €20 billion a year due to absence from work and decreased productivity [1]. Therefore, a stress-detection module in combination with an AR module would be useful for self-management of mental and physical health of workers [3], students and others in the stressful environment of today's world.

Thanks to the recent technological advances, some of the “fight-or-flight” components (stress-response components) [11] can be captured using an unobtrusive wrist device equipped with sensors, e.g., Empatica [14] or Microsoft Band [17]. Our method for stress direction is also based on the data captured by such a device, on which we use advanced machine learning (ML) in combination with context information provided by the AR module.

Since 2005, when Healey and Picard who showed that stress can be detected using physiological sensors [5], various studies were conducted to implement stress detection using a combination of signal processing and ML. The problem of stress

detection was first analyzed in constrained environments such as a laboratory/office [10], car [5], and call center [6]. Some approaches in which the subjects were allowed to be active based on a predefined scenario came one step closer to the real world [9]. Most recently Hovsepian et al. [7] proposed cStress, a method for continuous stress assessment in real-life using a chest belt. Similarly, our stress detection method is tested in real life, but instead of a chest belt we use a commercial wrist device. As future work Hovsepian et al. [7] suggested better handling of physical activity (which can confuse stress detection) and including context information in the process of stress detection – which is what we have done by combining the stress detection module with an AR.. By combining the two modules we were able to implement a smartphone application for monitoring physical and mental health which is used in several projects [3][15][16].

In the next section we describe the two modules for activity recognition and stress detection, next we present experimental results and finally we present a discussion and conclusion.

2 Methods

In this section we are describing the AR and stress-detection modules which were developed and evaluated separately, and then combined in a fully functional Android application.

2.1 Activity recognition module

In this module we use ML classifiers to detect activities from accelerometer data. Our approach differs from the related work by explicitly determining phone's orientation and location of wear. Knowing phone's orientation allows to normalize the accelerometer data, so no requirement is placed on the user on how is he to wear his phone. Secondly, since every location of wear (trouser pocket, breast and bag) has different pattern of movement, a specialized classifier is used in each case. Our activity recognition module works in the following way:

- 1.) If the wrist device is detected, its accelerometer is used instead of phone's accelerometer. In this case, a wrist-device specific classifier is used.

- 2.) If the phone orientation and location of wear are unknown (at the beginning of application usage), a general orientation and location independent classifier is used.
- 3.) If a general classifier detects walking segment, orientation and location are calculated. Every location of wear (trouser pocket, breast, bag) has different pattern of walking that a dedicated classifier can learn to detect. Phone's orientation can be determined by its perceived direction of gravity (average of all accelerometer measurements approximates gravity vector). Knowing orientation, data is normalized by translation into an appropriately rotated coordinate system.
- 4.) If location is known, a location specific AR classifier is used.
- 5.) If the phone is detected as not worn (simple heuristics: screen is lit, phone is still for too long, phone detects light, etc.), orientation and location reset.

To implement this module, we needed to train 6 different classifiers. To do so, we created an AR learning dataset by measuring ten different people. Each had to follow a fixed scenario that lasted for roughly an hour. In this scenario the subject performed different activities that we aimed to recognize. Accelerometer data was captured by Microsoft Band and three phones (Samsung S4), each worn on a different body location: trouser pocket, breast pocket, bag. True labels of the activities were marked during the experiment. The accelerometer frequency was 50 Hz. The data was then split into 2-second windows. Each window became one instance, totaling to around 80000 instances. We started with 88 features per instance, including signal average, min, max, standard deviation, kurtosis, skewness, correlation between axis, number of times the signal crosses its mean, integral of the signal and also some features in the frequency domain. Using a feature selection technique (features were ranked with ReliefF algorithm, and then iteratively added to the set, until classification accuracy stopped increasing) the number of attributes was narrowed down to 20-40 (depending on the task). For each required task we then used ML to create an SVM [19] classifier for AR.

2.2 Stress detection module

For implementation and evaluation of the stress detection module (Figure 1) two datasets were recorded, a laboratory dataset, which included 21 subjects, and a real-life dataset, which included 5 subjects. In both datasets the Empatica wrist device

was used to collect data. The Empatica wrist device provides heart rate (HR), blood volume pulse (BVP), galvanic skin response (GSR), skin temperature (ST), time between heartbeats (RR intervals) and accelerometer data. For the laboratory data we used a standardized stress-inducing experiment as proposed by Dedovic et al. [2]. The main stressor was solving a mental arithmetic task under time and evaluation pressure. For the real-life data, five subjects were wearing the wrist device and were keeping track of their stressful events.

On the laboratory data, a laboratory stress detector is built using ML. The laboratory stress detector distinguishes stressful vs. non-stressful events using 4-minute data windows with a 2-minute overlap. For each data window of 4 minutes, features for stress detection are computed. From each physiological signal (BVP, HR ST and GSR), statistical and regression features are computed: mean, standard deviation, quartiles, quartile deviation, slope and intercept. Additional features to quantify the GSR response are computed with an algorithm for peak detection [8]. For the RR signal, we use features obtained through heart-rate-variability analysis in the frequency and time domain. These features are fed into a classifier trained with the Random Forest [18] ML algorithm, which was chosen experimentally by comparing performance measures (precision, recall, accuracy) of several ML algorithms.



Figure 1. Context-based output with LOSO evaluation.

On the real-life data, a context-based stress detector is built. The context-based stress detector was introduced to distinguish between genuine stress in real life and many situations which induce a similar physiological arousal (e.g., exercise, eating, hot weather, etc.). As features, it uses the distribution of the last 10 outputs of the laboratory stress detector, the previous output of the context-based detector, and context features: whether there was any high-level activity in the last 20 minutes, the hour of the day, the type of the day – workday/weekend, etc. It classifies every 20 minutes as stressful or non-stressful. The context-based stress detector was trained

with the SVM ML algorithm, which was again chosen experimentally by comparing performance measures (precision, recall, accuracy) of several ML algorithms.

3 Experimental results

In this section we present experimental results for the two modules, AR and stress detection. The AR module was evaluated on the AR dataset which consists of ten different people performing fixed activity scenario that lasted for roughly an hour. The stress-detection module was evaluated on the real-life data which summarizes in 55 days of data from five subjects. "Leave-one-person-out" (LOSO) evaluation method was used. That means that one subject is left out for testing, the rest data is used for learning and the results are averaged.

3.1 Experimental results for activity recognition

Each task was evaluated separately using LOSO evaluation technique. The results are listed in Table 1. They show accuracy for task. Note that activities that are classified depend on the phone's location, as some activities sometimes cannot be distinguished (for example: "sitting" and "standing" when the phone is in your breast pocket). As an example, the last row shows that when using data provided by the wrist device, the AR module achieves accuracy of 92,7% when distinguishing the activities walking, running, standing, sitting and cycling.

Table 1. LOSO evaluation for AR

Task	#	Class values	Accuracy %
Location	31	trouser pocket, breast pocket, bag	85.8
Activity No location	14	walking, running, cycling, other	92.2
Activity Breast Pocket	19	walking, running, cycling, upright, lying	92
Activity Bag	21	walking, running	92.5
Activity Trouser pocket	26	walking, running cycling, standing,	89
Activity Band	40	walking, running, standing, sitting, cycling,	92.7

3.2 Experimental results for stress detection

The evaluation of the stress-detection module was performed on the real-life data. Because labeling stress is quite subjective [10] and it is almost impossible to strictly define starts and ends of stressful situations, we split the stream of real-life data into discrete events. Each event had a minimum length of one hour. If there was a stressful situation in the event (labelled by the user), the event’s duration was extended to capture the stressful situation plus one hour before and after the situation. By this, we allow for a labeling lag of one hour. The 55 days of the real-life data was split into nearly 900 events, each lasting at least an hour.

Table 2 presents the confusion matrices for the event-based evaluation using leave-one-subject-out (LOSO) cross-validation. On the left are the results for classification without context (based only on the predictions of the laboratory stress detector) and on the right are the results for the context-based stress detector. The accuracy achieved by the context-based stress detector (for distinguishing stressful vs. non-stressful events) is 92%, which is for 16 percentage points better than the no-context classifier.

Table 2. Confusion matrices for event-based evaluation. Context vs. no-context.

	No Context		With context	
	0	1	0	1
0	638	175	790	23
1	44	70	51	63
Recall	78%	61%	97%	55%
Prec.	94%	29%	94%	73%
F1	85%	39%	96%	63%
Acc.	76%		92%	

Additionally, Figure 2 depicts the output of the context-based stress detector for the real-life dataset. On the x-axis is the day, on the y-axis is the hour of the day, the black stripes label to which subject belongs the data, and the colored squares correspond to the false positive (FP), false negative (FN), true positive (TP) and true negative events (TN). From the figure it can be seen that subject 1 (S1) has many FN events, and subject 2 (S3) has many FP events compared to the rest of the subjects.

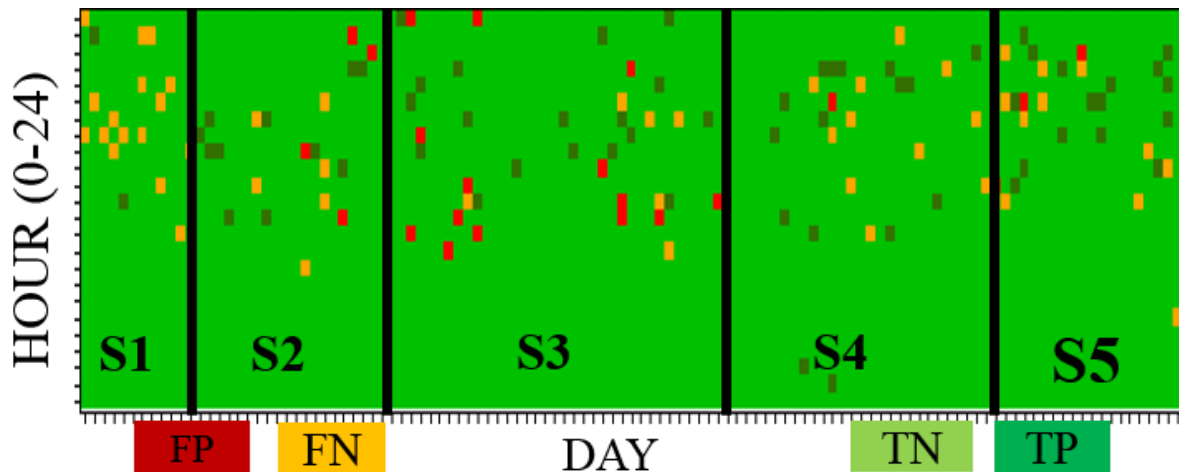


Figure 2. Context-based output with LOSO evaluation.

4 Discussion and conclusion

In this work we presented our modules for AR and stress detection. Both are implemented as an Android application (Figure 3) currently used in the Fit4Work project [3]. Our AR approach was additionally used in the projects Commodity12 [15] and E-Gibalec [16]. The AR experimental results were quite encouraging and comparable to other similar works [13]. In contrast to most other work, we are able to differentiate between “lying”, “sitting” and “standing” with phone alone. It also works robustly in practice independently on where and how the user wears the phone.

The stress detection module continuously tracks stress in real time, which makes it different from other related approaches. By introducing a context-based classifier we provided more information about real-life circumstances and the user, which improved the detection performance compared to no-context approach. The experimental results for stress detection show that there is still room for improvement, but they are encouraging for such a challenging problem. For now, the context-based stress detector receives information from the laboratory stress detector and from the activity recognizer. Additional context information can be provided from other components that recognize events which induce similar physiological arousal to a stress event (e.g., exercise, eating, hot weather etc.). Because stress is quite subjective and perceived differently by different subjects, we

also plan to implement personalization to allow to the general model to adapt to new users. The need for personalization was confirmed by the visualization in Figure 1, where it can be seen that distribution and the type of the classification errors (e.g., FP vs. FN) is subject-specific.



Figure 3. Smartphone application for physical (left) and mental (right) health monitoring.

Future work on the topic will also be focused on phone energy efficiency, as draining the battery too quickly is a major limitation in the practical use for such application.

References:

- [1] EU-OSHA – European Agency for Safety and Health at Work. Calculating the cost of work-related stress and psychosocial risks [Online]. Available: https://osha.europa.eu/en/tools-and-publications/publications/literature_reviews/calculating-the-cost-of-work-related-stress-and-psychosocial-risks, [Accessed 15.10.2014].
- [2] K. Dedovic, R. Renwick, N.K. Mahani, and V. Engert, The Montreal Imaging Stress Task : using functional imaging to investigate the effects of perceiving and processing psychological stress in the human brain. *Journal of Psychiatry & Neuroscience*. 30(5):319–325, 2005.

- [3] Fit4Work Project, <http://www.fit4work-aal.eu/>. [Accessed 30.04.2016].
- [4] H. Gjoreski, S. Kozina, M. Gams, M. Luštrek, Álvarez-García J.A, Hong J.H, Ramos J, Dey A.K, Bocca M, Patwari N. Competitive Live Evaluation of Activity-recognition Systems. *IEEE Pervasive Computing*. 14(1):70 – 77, 2015.
- [5] J.A. Healey and R.W. Picard. Detecting Stress During Real-World Driving Tasks Using Physiological Sensors. *IEEE Trans. Intell. Transp. Syst.*, 6(2):156–166, 2005.
- [6] J. Hernandez, R. R. Morris, and R. W. Picard. Call Center Stress Recognition with Person-Specific Models with Person-Specific Models. *Affective computing and intelligent interaction*. 6974:125–134, 2011.
- [7] K. Hovsepian, M. Absi, T. Kamarck, and M. Nakajima. cStress : Towards a Gold Standard for Continuous Stress Assessment in the Mobile Environment. In *proceedings ACM Int Conf Ubiquitous Comput*, Sep, 2015, pp. 493–504, 2015.
- [8] G.K. Palshikar. Simple Algorithms for Peak Detection in Time-Series. In the *Proc. 1st Int. Conf. Advanced Data Analysis, Business Analytics and Intelligence*, 2009.
- [9] J. Ramos, J. Hong, and A.K. Dey. Stress Recognition - A Step Outside the Lab. *Proc. Int. Conf. Physiol. Comput. Syst.*, 2014.
- [10] N. Sharma and T. Gedeon. Modeling a stress signal. *Appl. Soft Comput. J.*, 14(A):53–61, 2014.
- [11] S.C. Segerstrom, G.E. Miller. Psychological stress and the human immune system: a meta-analytic study of 30 years of inquiry. *Psychological Bulletin*, 2004.
- [12] L. Bao and S. S. Intille. Activity recognition from user-annotated acceleration data. In *Pervasive computing*, pp. 1-17. Springer, 2004.
- [13] N.D. Lane, E. Miluzzo, H. Lu, D. Peebles, T. Choudhury, and A.T. Campbell. A survey of mobile phone sensing. *Communications Magazine*, IEEE, 48(9): 140-150, 2010.
- [14] M. Garbarino, M. Lai, S. Tognetti, R. Picard, and D. Bender. Empatica E3 - A wearable wireless multi-sensor device for real-time computerized biofeedback and data acquisition. In *Proc. 4th Int. Conf. Wirel. Mob. Commun. Healthc. - Transforming Healthc. through Innov. Mob. Wirel. Technol.*, pp. 3–6, 2014.
- [15] Commodity12 project. www.commodity12.eu. [Accessed 12.05.2015].
- [16] E-gibalec project: www.e-gibalec.si. [Accessed 5.03.2016].
- [17] Microsoft Band: <https://www.microsoft.com/microsoft-band/en-us> [Accessed 5.11.2016].
- [18] T.K. Ho. Random Decision Forests. In *Proceedings of the 3rd International Conference on Document Analysis and Recognition*, pp. 278–282. Montreal, Canada, 1995.
- [19] S.R. Peter. *Artificial Intelligence: A Modern Approach. Second Edition*, Prentice Hall, 2003.

For wider interest

Physical and mental health are closely related and impact the overall quality of life simultaneously. The need for health monitoring was confirmed by the European Commission by estimating the costs of work-related stress at €20 billion a year due to absence from work and decreased productivity.

Regular physical activity has a positive impact on one's life, yet only a small fraction of the modern population exercises sufficiently. To appropriately motivate people for increasing their physical activity, it is important to quantify it first. Similarly, the stressful environment of today's world introduces another problem, stress, which should be addressed in order to prevent negative health consequences of chronic stress.

We propose a smartphone application capable of monitoring physical activity and mental stress using data provided from smartphone sensors and a commercial wrist device. The application consists of two modules, an activity recognition (AR) module and a stress detection module. The AR module continuously recognizes user's activity with accuracy of 91%.

The stress detection module uses data provided by the AR module and a commercial wrist device equipped with standard bio-sensors and an accelerometer. The stress detection module was trained on 21 subjects in a laboratory setting and tested on five subjects in a real-life setting achieving accuracy of 92% for detection of stressful events.

Integrating predictive and decision modelling in decision support system for water protection from phytochemicals

Vladimir Kuzmanovski^{1,2}, Aneta Trajanov^{1,2}, Sašo Džeroski^{1,2,3}, Marko Debeljak^{1,2}

¹ Department of Knowledge Technologies, Jožef Stefan Institute, Ljubljana, Slovenia

² Jožef Stefan International Postgraduate School, Ljubljana, Slovenia

³ Centre of Excellence for Integrated Approaches in Chemistry and Biology of Proteins, Ljubljana, Slovenia

vladimir.kuzmanovski@ijs.si

Abstract. Most real-world decision problem over multiple criteria are facing uncertain conditions during the decision making problem. Such uncertainty appears mainly due to lack of information about the state of the world and possible outcomes of a particular decision. Therefore, additional resources and analysis are required, in order to estimate the risk of uncertainty to influence the decision making process. In this paper we demonstrate integration of predictive and decision modelling within a decision support system, in order to avoid additional analysis of uncertain conditions. The former is proposed to take the role of oracle that will bring more accurate information within the decision making process and quantify its uncertainty. The latter considers such predictions and uncertainty quantification, and provides decision models with access to additional information. The proposed integration is applied to a decision problem from the domain of water protection from pesticides used in agriculture, which results in web-based decision support system.

Keywords: multi-criteria decision analysis, predictive modelling, decision modelling, decision support system

1 Background & Objectives

Multi-criteria decision analysis (MCDA) is a sub-field of operational research that aims to structure and solve decision problems over multiple criteria. The main challenge within the MCDA is dealing with potential risks and uncertainty that may

derive from different sources within the scope of a decision problem [1]. The scope of a decision problem (application area) is a domain that describes the actual or expected situation of nature (referred to as *world*), which reflects the conditions of observed domain in time of decision making. It is interpreted with a set of rules and situations (referred to as *the state of the world*) that can be completely or partially known accompanied with perfect or imperfect information, respectively.

The main objective of a decision making process is to choose the best option or *alternative* among many alternatives, considering multiple and possibly conflicting criteria. The term *best*, however, can be estimated upon realization of particular alternative, i.e., when *the outcome* of a particular alternative is known.

Most of the real world decision problems face the challenge to estimate possible outcome(s), in advance. Such estimation represents imperfect knowledge about the outcome of alternatives' realization (referred to as unknown consequences) and introduces uncertainty in the complete decision making process.

The problem of the uncertainties, due to the lack of information about the state of the world and unknown consequences of each alternative, in advance, constitute the main objective of the study. Namely, the presence of doubts in the decision making process, caused by uncertainty, required additional analysis (risk analysis) of all involved factors in the decision problem, which tries to reveal how the world will behave under different scenarios, considered as a risk that the imperfect knowledge will impact the whole process [2].

External analysis of uncertain conditions requires additional resources and time. Therefore, we propose an integration of predictive modelling and multi-attribute decision modelling within the scope of a decision support system (DSS). DSSs are set of computer tools that support decision makers in the decision making process [3]. Predictive modelling is proposed to take the role of oracle that will bring more accurate information within the decision making process and quantify its uncertainty.

The proposed integration of predictive modelling and decision modelling within a DSS is applied on a case-study from the domain of protection of surface and ground water from phytochemicals (referred to as pesticides) used in agriculture.

Agriculture acts as the major diffuse-source water polluter because of the application of plant protection products (referred to as *pesticides*) at a field scale [4]. Despite strict regulation of pesticides use in crop management [5], they can still be found in surface and ground water in concentrations above the permitted limits of pollution. Related work is mainly based on mechanistic models [4], out of which MACRO [10] and RZWQM [11] models are most popular in practice. Both require parametrization and calibration of the model with specific parameters retrieved with field analysis. To overcome the problem of water pollution with pesticides at the field level and to bypass the complexity of the state-of-the-art models, we applied the proposed integration of predictive modelling and decision modelling, which results in a web-based decision support system.

The state of the world is described with the current set of conditions that are presented on the field. Additionally, two conditions are marked as uncertain: water outflow at the time of pesticide application and the time period of intensive water outflows within a crop growing season. The case-study is limited to tile-drained fields, therefore, drainage water outflow is considered as a prevailing pathway of water outflow (e.g., other possible water pathways such as surface runoff and infiltration are not considered in our case study [6]). Consequently, the time period of intensive drainage outflow is considered as *drainage period*.

At the time of decision making, the decision maker does not possess any information regarding the both uncertain conditions on the field (i.e. water outflow and drainage period), which motivate the application of predictive modelling in order to acquire additional information accompanied with quantified uncertainty. Namely, the decision maker must decide in advance if the scheduled application time of selected pesticides would be risky or not for water pollution. Introduction of DSS in this decision process enables review of planned application of pesticides and if its assessment is risky for the environment, then the DSS should generate not risky pesticide management alternatives that the decision maker can consider as

substitutes of the originally planned actions. The alternatives should consist of similar actions with modified properties, such as: application time, application dose, change of active ingredient, and a set of agronomic actions (e.g., soil management measures, field margin management measures, ...).

Thus, the DSS should be able to perform a priori evaluation of planned application of pesticides in the field, and in case that the application would be risky for water pollution, it should find alternatives (mitigation measure) with the minimum changes of the original pesticide management plan that would not pose a threat of water quality, i.e., not risky pesticide application plan.

2 Materials & Methods

The data we used in our study are from the experimental site La Jaillière, run by the technical institute ARVALIS - Institut du Végétal. It is situated at the southern end of the Armorican massif in western France. The site has been dedicated to the study of the influence of agricultural management practices on water quality since 1987. It is a reference site for the European Commission FOCUS working group. The La Jaillière site is considered as a representative of the agricultural regions in Europe with shallow silty clay soils. The climate at the site is of oceanic type. The mean annual precipitation of 717 mm is evenly distributed along the year (monthly values between 40 and 62 mm). The mean annual potential evapotranspiration is 712 mm (meteorological station of La Jaillière, 1987-2012) [4].

Data from the experimental site of La Jaillière are collected since 1987 and include data about the agricultural practices (tillage, sowing, fertilizing and pesticides application dates), the amount of water flows and the concentration of the water solution (mineral and active substances) in the water pathways (drainage and runoff).

Additionally, for decision modelling, we use expert knowledge for water and pollutant pathways through the soil under certain crop management, field and landscape conditions, provided by experts from ARVALIS.

The predictive modelling of water flows from the fields and drainage periods has been done using machine learning and data mining methodology. Precisely, we use a

bagging approach [7] for building ensembles models of both regression and model trees. In literature, ensembles are also referred to as multiple classifier systems, committees of classifiers, classifier fusion, combination or aggregation [8]. Bagging is an approach for learning multiple predictive models and using them to get an aggregated prediction. The aggregation averages over the base predictive models outputs. The multiple base predictive models are automatically constructed on different bootstrap replicates. If the training set causes significant changes in the constructed models, then bagging can improve the predictive performance of the base predictive models.

The decision modelling task for building qualitative multi-criteria decision models, is done using DEX methodology [9]. In DEX, the qualitative attributes compose a hierarchical structure that represents a decomposition of the decision problem into less complex sub-problems, which are assumed to be easier to be solved. The hierarchical structure is represented as a decision tree, which assures that each attribute within the structure will be indirectly connected to the root of the tree. The hierarchical structure, set of basic and aggregated attributes and utility functions construct a DEX decision model. The methodology is implemented in the DEXi software package [3].

Within the predictive modelling task, predictive models are built for both uncertain conditions on the field, drainage outflow and drainage period. They are further incorporated into the final web-based DSS with a role to extract as much as possible valuable information about the uncertain conditions on the field.

The decision modelling task involves building DEX decision models for a priori ecological risk evaluation of planed application of pesticides at the field scale. These models also take a role to evaluate each possible mitigation measure in coordination with previously evaluated ecological risk and feasible crop management actions on the field, out of which mitigation measures (alternatives) are constructed.

3 Results & Discussion

The predictions of drainage outflow models are compared with the state of the art mechanistic models used for simulating drainage outflow MACRO [10] and

RZWQM [11]. The comparison regarding Root Relative Squared Error and Pearson correlation coefficient (Fig. 1) shows significant improvement of data mining models over the MACRO model, while exposing similar performance in comparison to the RZWQM [4]. However, the simplicity of usage of the data mining models which don't not require extensive field analysis, adds additional points over the RZWQM.

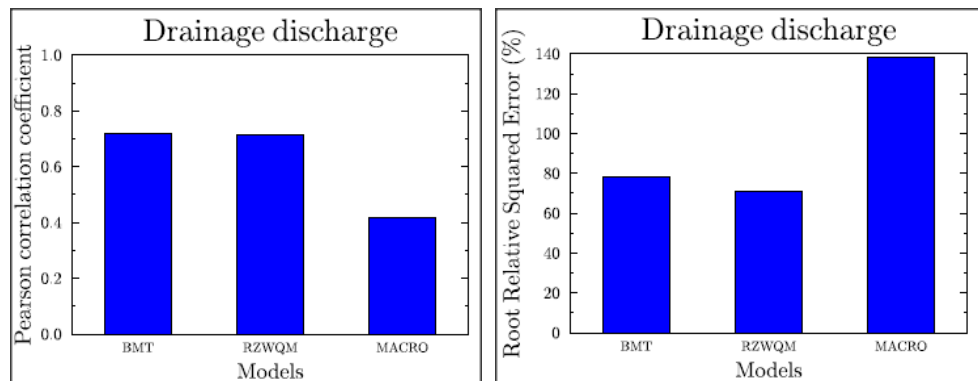


Figure 1: Comparison of the performances between data mining models (BMT – Bagging of model trees) for predicting drainage outflow and mechanistic models (MACRO and RZWQM)

The second predictive task is building predictive models for beginning and lasting of drainage periods. The built predictive model is compared to dates assigned by the experts and shows good performance expressed with upper bounded error of six days when predicting start and end of drainage period, for each campaign since 1987.

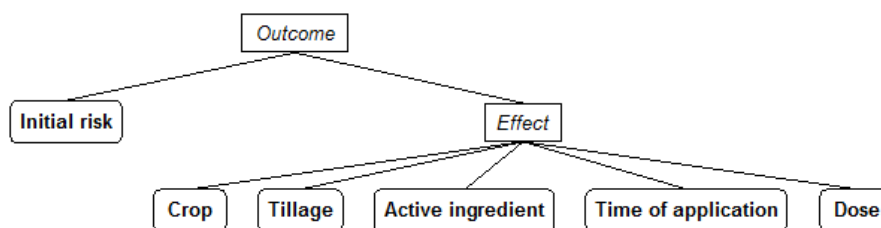


Figure 2: Hierarchical structure of DEXi decision model for evaluation of pesticide application

The developed DEX decision model for evaluation of planned application of pesticides, has a hierarchical structure as is shown in Fig. 2. Six basic (input)

attributes consist of one attribute that represent the initial risk (based on data mining predictions of drainage outflow and drainage period), five attributes describing planned soil and crop management measures to be applied in a field, and two aggregated attributes: *Effect* of the crop and soil management actions and the root attribute *Outcome* which gives the output value of the decision model.

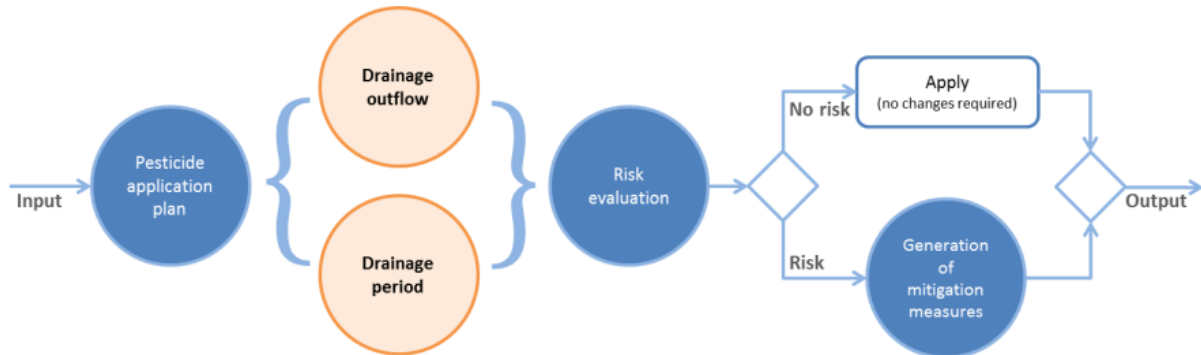


Figure 3: Conceptual structure and workflow of the DSS

The predictive models are used to evaluate the initial ecological risk of particular application of pesticides (Fig. 3). Their roles (in orange) appear between pesticide application plan and risk evaluation, which fulfill the uncertain conditions on the field with predictions. Evaluation of ecological risk gives information about the consequences of the realization of particular application on the field.

The following component redirects the workflow in adequate direction. If the planned application is evaluated as risky, then the DSS finds the optimal (in regard to the complexity) set of actions that represents a mitigation measure. In most of the cases there will be more than one mitigation measure available, so the system selects at least three most optimal mitigation measures and report them to the decision maker in order to made the final decision.

The DSS is implemented as a web-based application where DSS's graphical user interface contains two main parts: input (or scenario description) and evaluation report. The former is a web form that contains set of field for all required information about the planned application of pesticide, current state of the field and soil properties, which could be populated manually or automatically from the ARVALIS soil database (Fig. 4). The second part of the graphical interface is the web form composed of three main sections: initial state of the field with assessed

ecological risk, performance selector and a set of proposed mitigation measures as shown in Fig. 5.

Overall Progress: 0%

Scenario Description | Water Pathways | Water Quantity | Risk Characterization | Risk Management | Mitigation Report

Scenario Description

Provide and populate fields with the required information.

General Information	
Scenario	
Region	Pays-de-la-Loire
Location	Maine-et-Loire (La Jaillière)

Field Conditions	
Soil description	Choose soil type...
Soil conditions	Choose conditions ...
Tillage	Choose...
Slope	Choose a slope...
Slope disruption	Choose...
Thalweg	Choose...
Downhill	Choose...
Access area issues	Choose...
Corner issues	Choose...

Soil Conditions	
Cracks in soil	Choose...
Capping soil	Choose ...
Surface permeability	Choose ...
Permeability disruption	Choose a depth...
Substratum permeability	Choose...
Substratum	Choose a depth...

Crop Management	
Crop	Choose present crop...
Date of sowing	dd/MM/yyyy

Pesticide Application	
Date of application	dd/MM/yyyy
Active ingredients	Choose active ingredient...
Dose	<input type="text"/> g/ha

Start

Figure 4: Graphical user interface: input form where planned application is described

The second section contains checkboxes that help to decision maker to select a set of mitigation measures based on what agronomic actions are preferred. The third and main section of evaluation report lists at least three most optimal mitigation measures (if the initial planned application is assessed as risky) with detailed information about each required action on the field (Fig. 5).

The system is evaluated by the experts from ARVALIS institute using what-if analysis. Their conclusion is that the DSS satisfies their requirements and expectations regarding proposition of mitigation measures, and successfully overcomes the issue with the complex parametrization that comes across state-of-the-art models

(MACRO and RZWQM). Finally, current version of the DSS has limited useability and it is applicable over regions the provided data are representative for.

DRAINAGE DISCHARGE

Risk Management

Ranked strategies
The strategies are ordered by the complexity of agricultural practices.

1. Mitigation strategy

Practice required
The following changes are required for risk reduction:

Dosage recommendation
Applying Close to Winter Flow Period: **1600 g/ha**
Applying During Winter Flow Period: **1600 g/ha**

Notes
The following changes are given as possible management without risk:

Application time
NOTE: Without any consequences, could be applied **Close to Winter Flow Period** or **During Winter Flow Period**.

2. Mitigation strategy

Practice required
The following changes are required for risk reduction:

Active ingredient
Should be replaced with **pendiméthaline, isoproturon, bromoxynil, flurtamone or diflufénicanil**.

Dosage recommendation
Application of flurtamone: **250 g/ha**
Application of bromoxynil: **180 g/ha**
Application of isoproturon: **1000 g/ha**
Application of diflufénicanil: **120 g/ha**
Application of pendiméthaline: **1000 g/ha**

Figure 5: Graphical user interface: List of proposed mitigation measures

References:

- [1] C. Zopounidis and P. Pardalos. *Handbook of multicriteria analysis*. Applied Optimization. Springer Berlin Heidelberg, 2012.
- [2] S. Roeser, R. Hillerbrand, P. Sandin and M. Peterson. *Handbook of risk theory: epistemology, decision theory, ethics, and social implications of risk*. Handbook of Risk Theory. Springer, 2012.
- [3] M. Bohanec. *Dexi: program for multi-attribute decision making, v4.00*. Technical report No. IJS-DP 11340. Jožef Stefan Institute - Ljubljana, 2013.
- [4] V. Kuzmanovski, A. Trajanov, F. Leprince, S. Džeroski and M. Debeljak. Modeling water outflow from tile-drained agricultural fields. *Science of The Total Environment*, 505(1):390-401, 2015
- [5] European Parliament & Council. Commission implementing regulation (eu) no 540/2011. *Official Journal of the European Union*, 153(1):1-186, 2011
- [6] M. Tomer, D. Meek, D. Jaynes and J. Hatfield. Evaluation of nitrate nitrogen fluxes from a tile-drained watershed in central Iowa. *Journal of Environmental Quality*, 32(2):642-653, 2003
- [7] L. Breiman. Bagging predictors. *Machine Learning*, 24(2):123-140, 1996
- [8] S. Džeroski, P. Panov and B. Ženko. Machine learning, ensemble methods. In *Meyers R, editor. Encyclopedia of complexity and systems science*. Springer, New York, 2011.
- [9] M. Bohanec & V. Rajkovič. Dex: an expert system shell for decision support. *Sistemica*, 145-157, 1990
- [10] M. Larsbo & N. J. Jarvis. Simulating solute transport in a structured field soil: uncertainty in parameter identification and predictions. *Environmental Quality*, 34(1):621-634, 2005
- [11] L. Ahuja, K. Rojas and J. Hanson. *Root zone water quality model: modelling management effects on water quality and crop production*. Water Resources Publications, 2000.

For wider interest

In this paper we demonstrated an approach for integration of predictive and decision modelling into a decision support system. The described approach employed machine learning and data mining methodology for predictive modelling tasks, and DEX methodology for decision modelling task. The former is applied, in order, to build models that accurately predict uncertain conditions of the state of the world in decision making process, while the latter use such predictions in order to make a better evaluation of the defined alternatives. Finally, the approach of integration is implemented in a web-based decision support system for decision problem from the domain of water protection from pesticides used in agriculture. The web-based decision support system includes four steps in the workflow: description of the planned application of pesticides, prediction of drainage outflow (quantity) and periods of intensive drainage events (time period), risk evaluation, and, if the planned application of pesticides is evaluated as risky, generation of mitigation measures (alternatives) that leads to the solution of the given decision problem.

Multi-dimensional analysis of PPMI data

Vanja Mileski^{1,2}, Dragi Kocev^{1,2}, Bogdan Draganski³ and Sašo Džeroski^{1,2}

¹ Department of Knowledge Technologies (E8), Jožef Stefan Institute, Ljubljana, Slovenia

² Jožef Stefan International Postgraduate School, Ljubljana, Slovenia

³ Centre Hospitalier Universitaire Vaudois (CHUV), Lausanne, Switzerland

vanja.mileski@ijs.si

1 Introduction

Parkinson's disease (PD) is a chronic progressive neurodegenerative disease of unknown etiology that mainly affects body movement and progressively disables the patient for an independent life. The disease is characterized by the selective degeneration of dopamine nigrostriatal neurons and the consequent lack of the neurotransmitter dopamine in the striatum, which results in slower mobility (bradykinesia), muscle rigidity, rhythmical tremors (shaking while resting) and disturbance of body posture [1] [2]. The Parkinson's Progression Markers Initiative (PPMI) is an observational clinical study for identification and verification of disease biomarkers [3]. It combines the knowledge obtained from multiple cohort studies that are of a significant interest and consists of an exhaustive set of clinical, imaging and biosample data.

The disease progression is typically described with motor assessment scores of the motor impact of the disease on the patients (MDS-UPDRS). The goal of this work is to search for groups of subjects that exhibit similar behavior in terms of the multiple motor assessment scores. The identified groups/clusters of subjects are then described using image features including Regions of Interest (ROIs) from fMRI scans, as well as DaT scans. This can save time, money and effort from specialists and can also provide an insight or even detect the biomarkers that indicate Parkinson's disease at an early stage of the disease.

2 Methods and Materials

In this study, we use three data sets from the PPMI database: the regions of interest (ROIs [4]) of the patients' fMRIs, DaT (dopamine transporter) scans and the motor assessment scores (MDS-UPDRS) [5]. The joined table between these three data sets consists of examples that includes MDS-UPDRS scores of a patient and the both imaging data mentioned above. The time interval between the scoring date and the imaging date are less than 6 months. We distinguish two variants of the dataset: baseline and complete. In the baseline dataset, we consider only the earliest scores (baseline) and imaging data for each patient resulting in 374 examples. In the complete dataset, we take all scores and imaging data for each patient resulting in 716 examples.

The task at hand is multi-target regression: the goal is to predict all of the scores for the motor impairment assessments from the extracted ROIs (of the fMRIs) and the DaT scans features. To this end, we use CLUS – a multi-target system based on the predictive clustering framework. CLUS is a decision tree and rule induction system that unifies unsupervised learning (i.e., clustering) and predictive modeling [6]. We use predictive clustering trees (PCTs) - a generalization of the decision trees towards predicting structure outputs including multiple continuous target variables. Furthermore, we use two tree-based ensemble methods: bagging and random forests. Bagging builds different trees on different bootstrap replicates of the original training set and then aggregates their individual predictions to form a final prediction. Random forest also builds each tree in the ensemble from a bootstrap replicate from the training set, however, the node splits are chosen as the best splits among a random subset of the features. We used 10-fold cross validation to assess the predictive performance of the methods on unseen examples. The predictive performance is measured as normalized root mean squared error (nRMSE) – this normalizes the RMSE values of all of the target variables so that each variable contributes equally to the overall score.

3 Results and Conclusion

The results from the predictive modelling methods applied on the two datasets reveal that the lowest error (as estimated with 10-fold cross-validation) is achieved

using random forests on the complete dataset that uses all of the imaging data and scores.

More detailed analysis of the results follows. We begin by discussing the influence of the introduction of a hierarchy in the output space. The performance on the complete dataset is much better than the one obtained on the baseline dataset ranging from 0.603 to 0.883 for the complete dataset as opposed to 0.889 to 0.926 for the baseline. Furthermore, we can note that the hierarchy did not improve the predictive performance for the smaller baseline dataset (in both cases the training nRMSE is 0.889 and the cross-validated nRMSE with or without hierarchy was 0.923 and 0.926, respectively). Conversely, the use of hierarchy improves the performance of the model learned on the complete dataset (the training nRMSE with and without hierarchy is 0.702 and 0.603 respectively and the cross-validated nRMSE is 0.862 and 0.883, respectively). This indicates that the predictive model without hierarchy overfits more than the model with hierarchy.

Considering the ensemble methods, we can conclude that random forests yield slightly better results than bagging. More specifically, we discovered that the introduction of the hierarchy does not improve the predictive performance. However, the performance on the complete dataset is significantly better than on the baseline dataset: 0.758 compared to 0.91nRMSE score. Finally, the performance of the ensemble models is significantly better than the performance of a single tree.

The results from the analysis are indicative that both the descriptive and predictive power of all of the obtained models is good. The improved performance obtained on the complete dataset is mainly due to the fact that by using the additional records, we introduced more variability in the target space. Namely, the baseline dataset contains measurements from subjects that are, more or less, at an earlier stage of the disease, hence the motor assessment scores are lower. Moreover, since it is impossible to investigate subjects that are the same stage of disease simultaneously, including information obtained throughout various disease stages helps to construct a better predictive model.

References:

- [1] J. Konczak, D.M. Corcos, F. Horak, H. Poizner, M. Shapiro, P. Tuite, J. Volkmann, and M. Maschke. Proprioception and motor control in parkinson's disease. *Journal of motor behavior*, 41(6):543-552, 2009.
- [2] L.C.S Tan. Epidemiology of Parkinson's disease. *Neurology Asia*, 18(3):231-238, 2013.
- [3] K. Marek, D. Jennings, S. Lasch, A. Siderowf, C. Tanner, T. Simuni, C. Coffey, et al. The Parkinson progression marker initiative (PPMI). *Progress in neurobiology*, 95(4):629-635, 2011.
- [4] R.A. Poldrack. Region of interest analysis for fMRI. *Social cognitive and affective neuroscience*, 2(1):67-70, 2007.
- [5] C.G. Goetz, B.C. Tilley, S.R. Shaftman, G.T. Stebbins, S. Fahn, et al. Movement disorder society-sponsored revision of the unified parkinson's disease rating scale (mds-updrs): Scale presentation and clinimetric testing results. *Movement disorders*, 23(15):2129-2170, 2008.
- [6] D. Kocev, C. Vens, J. Struyf, and S. Džeroski. Tree ensembles for predicting structured outputs, *Pattern Recognition*, 46(3): 817-833, 2013.

For wider interest

The major goal in Parkinson's disease treatment is to look for a disease-modifying treatment that will hopefully slow, prevent or even reverse the effects of the disease. A crucial step towards that goal is the discovery and validation of disease biomarkers. The current set of identified biomarkers is not fully validated and is not optimal.

In this work, we used data acquired from the Parkinson's Progression Markers Initiative (PPMI). The goal is to search for groups of subjects that exhibit similar behavior in terms of their motor assessment scores. These scores tell us how much a person has a motor impairment in a certain region of his body (left arm, right leg, speech etc.). On the identified groups/clusters of subjects, their motor assessment scores were described using imaging data information from fMRIs (functional magnetic resonance imaging) and DaT scans (specialized imaging technique for detecting levels of dopamine in the brain).

The results from the use of predictive clustering trees for analysis of such data are promising. With this technique, we are able to predict all of the patients' motor scores from their imaging scans. This can save time, money and effort from specialists and can also give us an insight or even detect the biomarkers that indicate Parkinson's disease at a person before the disease even starts to manifest.

Model-based fault diagnosis with Gaussian process regression of nominal model residuals

Martin Stepančič^{1,2}, Boštjan Dolenc^{1,2}, Đani Juričić¹

¹Jozef Stefan Institute, Ljubljana

²International Postgraduate School Jožef Stefan, Ljubljana

`martin.stepancic at ijs.si`

Abstract. Discrepancy between a process and its model affects reliability of the diagnostic system, either through decreased sensitivity or frequent false alarm rates.

The problem tackled in this paper is how to handle unmodelled effects, caused by imperfect nominal models. We propose nonparametric statistical modelling of the error in nominal model. The Gaussian process model is used to predict the discrepancy between process and nominal model. Hence, the the two models together may represent a refined model of the plant. Since the Gaussian process model prediction is normally distributed, each realisation of (refined model) residual is a random variable with associated normal probability distribution.

The onset of a fault is inferred by comparing the statistical pattern of the refined model residuals, collected under current operating mode with the pattern in the nominal (fault-free) condition. Major novelty of the approach is the application of Jensen-Renyi divergence as a means to quantify the difference between the two corresponding ensembles of distributions.

The ideas of the approach and their potentials are demonstrated in an illustrative example of simulated solid oxide fuel cell system.

Keywords: Fault detection, Gaussian process model, Jensen-Renyi divergence.

1 Introduction

A number of fault detection and isolation techniques rely on verification of consistency between measured process variables and the process model. This step results in the variables referred to as residuals, which play central role in the diagnostic decision making. By definition, residuals should be (near) zero if the system is fault-free. A fault in the system destroys the consistency among measured variables. From the discrepancy between current residuals

pattern and the reference (fault-free) pattern, one can infer whether a fault is present in the system or not.

Unfortunately, non-zero residuals can also emerge due to modelling errors. Indeed, every model is derived under some restrictions, either in the form of lack of knowledge, missing prior data or simply limited resources. In all the cases the result is a model of limited precision in terms of bias. When such a model is used in diagnostic decision making, even if there is no fault, the residuals might take significant values. If alarm thresholds are not set high enough, false alarms may trigger. On the other hand, by increasing the alarm thresholds false alarm rates can be decreased, however on account of poor sensitivity of the detector with respect to the faults.

The problem we address here is how to quantify and appropriately handle the unmodelled portion of reality, that is not included in the nominal process model. The problem is relevant as it is challenging to reduce the destructive impact that model errors might have on diagnostic reliability. However, it has received relatively little attention, e.g. [1],[2].

More generally, the problem of quantification of modelling error has been studied more intensively in the context of robust identification where basically three different concepts have been proposed in [3, 4, 5] respectively. However, not much work was also focused on the characterisation of unmodelled nonlinearities [6]. The aim of this paper is to fill the gap. The idea falls in the category of stochastic embedding techniques since the residual of the nominal model (bias error), which can be caused by unmodelled nonlinear dynamics, is viewed as realisation of a second order stochastic process.

The idea of our approach is illustrated in Figure 1. Let $\mathcal{P} : u \mapsto y$ and $\mathcal{M}_0 : u \mapsto \hat{y}_0$ be process and nominal model respectively. The difference $z = y - \hat{y}_0$ is in the case of perfect model structure and parameters zero or white noise uncorrelated with the regressors. Unmodelled system dynamics z can be viewed as response of a nonlinear system $\Delta\mathcal{M} : u \mapsto z$. To realise $\Delta\mathcal{M}$ we apply the Gaussian process-based dynamical system model, which response to process inputs is the estimated nominal model error.

The rest of the paper goes as follows. In section II a brief review of the main ideas of GP models will be given. Section III deals with the design of the detection procedure, which basically breaks down to a statistical decision making problem. A novel diagnostic decision making based on entropy measures

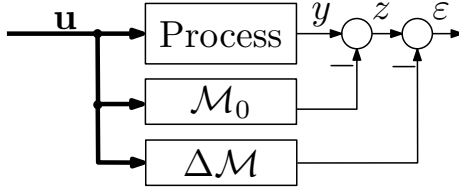


Figure 1: The idea of accounting for modelling error.

is proposed. In section IV the potentials of the approach are demonstrated on diagnosis of a simulated solid oxide fuel cell system.

2 Overview of dynamic systems modelling with Gaussian-process model

Let the system to be modelled be viewed as a mapping of vector of inputs \mathbf{v} into scalar output y , i.e. $\mathbf{v}(k) \mapsto z(k)$. The system output is modelled as Gaussian process (GP), meaning $[z(1), \dots, z(n)]^T = \mathbf{z} \sim \mathcal{N}(\mathbf{m}, \Sigma)$, where $m_i = \mathbb{E}[z(i)] = m(\mathbf{v}(i))$ and the elements of the covariance matrix Σ , namely, $\Sigma_{ij} = \text{cov}(z(i), z(j)) = C(\mathbf{v}(i), \mathbf{v}(j))$ is expressed as covariance function of inputs $\mathbf{v}(i)$ and $\mathbf{v}(j)$. Thus, the mean $m(\mathbf{v})$ and covariance $C(\mathbf{v}(i), \mathbf{v}(j))$ fully characterise the GP. Note that the covariance function $C(\cdot, \cdot)$ can be any positive semi-definite function. A frequently chosen (prior) mean function is zero and (prior) covariance function consists of the squared exponential covariance function and Kronecker delta operator δ_{pq} :

$$C(\mathbf{v}(i), \mathbf{v}(j)) = C_f(\mathbf{v}(i), \mathbf{v}(j)) + \delta_{ij}\sigma_n^2, \quad (1)$$

$$C_f(\mathbf{v}(i), \mathbf{v}(j)) = \sigma_f^2 \exp \left[-\frac{1}{2} \sum_{d=1}^D \frac{(v_{i,d} - v_{j,d})^2}{l_d^2} \right] \quad (2)$$

where l_d , σ_f , σ_n are the hyperparameters of the covariance function, D is the dimension of input space, and $\delta_{pq} = 1$ if $p = q$ and 0 otherwise. The hyperparameters can be written as a vector $\theta = [l_1 \dots l_D \sigma_f \sigma_n]^T$. This covariance function is smooth and continuous. It presumes that the noise is white. Other forms and combinations of covariance functions, suitable for various applications, can be found in [7]. For a given problem, the hyperparameter values are optimised or trained using the data at hand.

The predictive distribution of the GP-models can be done by means of Bayesian inference. Assume a GP model the trained on a set of observed out-

put data $\mathbf{z}_o = \{z(1), \dots, z(N)\}$ with corresponding inputs $\mathbf{V}_o = \{\mathbf{v}(1), \dots, \mathbf{v}(N)\}$. Then, for a new input \mathbf{v} the predicted distribution of the corresponding output reads

$$\mathbb{E}(z(\mathbf{v})) = m'(\mathbf{v}) = C(\mathbf{v}, \mathbf{V}_o)^T C(\mathbf{V}_o, \mathbf{V}_o)^{-1} \mathbf{z}_o, \quad (3)$$

$$\text{var}(z(\mathbf{v})) = C'(\mathbf{v}, \mathbf{v}) = C(\mathbf{v}, \mathbf{v}) - C(\mathbf{v}, \mathbf{V}_o) C(\mathbf{V}_o, \mathbf{V}_o)^{-1} C(\mathbf{V}_o, \mathbf{v}) \quad (4)$$

where $m'(\cdot)$ and $C'(\cdot)$ denote a posteriori mean and covariance function, respectively. To accurately reflect correlations present in the training data, the hyperparameters of the covariance function need to be optimised. Bayesian inference of hyperparameters probability distribution is infeasible [7]. However, only a point estimate of hyperparameters is calculated with Maximum Likelihood optimisation method. The problem may be restated as marginal likelihood $p(\mathbf{z}_o|\theta)$ that is to be maximised. The likelihood evaluation may involve such computational burden that the timeframe of optimisation method may be unacceptable. In order to avoid such computational complexity, we employ a computationally efficient approximation of likelihood $p(\mathbf{z}_o|\theta)$ from [8]. The evaluation of likelihood requires solving left matrix division that involves covariance matrix $C(\mathbf{V}_o, \mathbf{V}_o)$ of observed inputs. To speed up the left matrix division, a low-rank approximation of $C(\mathbf{V}_o, \mathbf{V}_o)$ is used instead of the original covariance matrix. Further information is provided in [8].

2.1 The structure of GP-based dynamical system

Regarding to modelling of dynamical systems, various structures of GP-based dynamical system model exist and are presented in [9]. The chosen structure in this paper is the nonlinear finite impulse response (NFIR) model structure, where the output at time step k depends on the delayed inputs \mathbf{u} :

$$z(k) = f(\mathbf{u}(k), \mathbf{u}(k-1), \dots, \mathbf{u}(k-m)) + \epsilon(k) \quad (5)$$

where f denotes the process model, $\epsilon(k)$ is white gaussian noise, and the output $z(k)$ depends on the state vector $\mathbf{v}(k) = \text{vec}([\mathbf{u}(k-1), \mathbf{u}(k-2), \dots, \mathbf{u}(k-m)]^T)$ at time step k . Validation of the GP-based NFIR model is naturally equivalent to simulation. Simulation, therefore, means that only on the basis of previous samples of a process input signal $u(k-i)$ we may simulate future outputs.

3 Detection procedure

3.1 Data sets

In the most general case we need to distinguish between three data sets: (i) $\mathcal{D}_0 = \{(\mathbf{u}(i), y(i)), i = 1, \dots, N_0\}$ containing data used to train the nominal model; (ii) $\mathcal{D}_n = \{(\mathbf{u}(j), y(j)), j = N_m, \dots, N_M\}$ data collected during nominal condition of the process (fault-free) in order to train the GP-NFIR corrective model $\Delta\mathcal{M}$; (iii) $\mathcal{D}_c = \{(\mathbf{u}(k), y(k)), k = t - N_c + 1, \dots, t\}$ representing sliding window with "current" data, $t > N_M + N_c$.

3.2 Residual generation

Nominal model \mathcal{M}_0 of the plant can be obtained in several ways, as for example by identification from \mathcal{D}_0 or by using first principles modelling. For the sake of simplicity, let us assume a residual z associated to \mathcal{M}_0 is defined as prediction error:

$$z(k) = y(k) - \hat{y}(k), \quad (6)$$

where $y(k)$ denotes the process output and $\hat{y}(k)$ is the output of the nominal model \mathcal{M}_0 , and k is time moment. In case the nominal model were free of bias, then only variance error would be present in the residual. That means the residual would be zero-mean white Gaussian noise $z(k) \sim \mathcal{N}(0, \sigma^2)$.

However, due to unmodelled dynamics, bias is also part of the model error. In order to cope with that, the residual z is modelled as Gaussian process \hat{z} conditioned on process data in the reference fault-free case $\mathcal{D}_n = \{\mathbf{z}_n, \mathbf{U}_n\}$, that is, given current state $\mathbf{v}(k)$ the estimated residual $\hat{z}(k) \sim \mathcal{N}(\mu(k), \sigma^2(k))$ where $\mu(k) = m'(\mathbf{v}(k))$ and $\sigma^2(k) = C'(\mathbf{v}(k), \mathbf{v}(k))$. Final residual $\varepsilon(k) = z(k) - \hat{z}(k)$ is obtained by correction contributed by the GP-NFIR model. Since $\hat{z}(k)$ is a random variable and $z(k)$ is a realisation, the residual $\varepsilon(k)$ is again a realisation and has the probability density function (pdf):

$$\varepsilon(k) \sim \mathcal{N}(z(k) - \mu(k), \sigma^2(k)). \quad (7)$$

3.3 Detection rule based on a statistical divergence measure

Intuitively, if the prediction error is low, we have good reason to infer that no fault is in the system. On the contrary, a change in the residual pattern indicates a fault either in sensors, actuators or internal process faults.

Detection of residual changes that is based only on current time-instant is simple, but is not recommended in practice as it is prone to fluctuations originated by process noise, thus resulting in poor *detection stability*. The detection stability can be improved if residuals from a time window $[k - M + 1, k]$ are employed to draw decision about presence of fault at time step k . The length of the window is chosen as a trade-off between the detection delay and stability of the detector output. Thus shorter detection delays typically go on account of detector instability.

A way to improve diagnostic stability is to use windowed residual sets. Various statistical tests may be applied, e.g. generalised likelihood ratio (GLR) test [10], which serve to reject/accept *null* hypothesis (fault/no-fault). Such approaches are successfully applied in situations in which the null hypothesis considers residuals in the fault-free case as stationary with known distribution. However, in our case we cannot assume process stationarity.

The idea we propose in this paper is to utilise entire information related to the residuals that is the associated pdfs. What we have to do is to take two ensembles of residuals

- $\Pi_n = \{\mathcal{P}_i, i = N_m, \dots, N_M\}$ where \mathcal{P}_i stands for distributions $\mathcal{N}(\mu(i), \sigma^2(i))$, obtained in the nominal condition,
- $\Pi_t = \{\mathcal{P}_i, i = t - N_c + 1, \dots, t\}$ calculated from the current operating condition (which can be affected by fault).

If there is no fault in the system the distributions in Π_t should be “similar” to the distributions in Π_n . In order to quantify similarity (or dissimilarity) among several pdfs, relative *entropy* or divergence is often employed. Here, we apply Jensen-Rényi (JR) divergence JR_α^w in order to quantify similarity of n pdfs denoted by \mathcal{P}_i :

$$JR_\alpha^w(\mathcal{P}_1, \dots, \mathcal{P}_n) = H_\alpha \left(\sum_{i=1}^n w_i \mathcal{P}_i \right) - \sum_{i=1}^n w_i H_\alpha(\mathcal{P}_i) \quad (8)$$

where $\sum_{i=1}^n w_i = 1$ and $H_\alpha(\cdot)$ denotes Rényi entropy:

$$H_\alpha(\mathcal{P}) = \frac{1}{1 - \alpha} \ln \sum_{x \in \mathcal{D}} p^\alpha(x). \quad (9)$$

In Eq. (9), $p(x)$ is corresponding pdf, and α is arbitrary parameter of Rényi entropy.

3.4 Threshold selection based on probability of false alarm

One of the most important features of the diagnostic algorithm is threshold selection, i.e. unambiguous decision rule that clearly indicates whether a change occurred or not. A common approach is to set a threshold on a given indicator, in our case divergence. If the divergence exceeds the threshold value, an alarm is triggered.

It was shown in [11] that probability of false alarm can be a powerful design parameter for threshold selection. When the idea is applied to our case, the solution turns to be very elegant owing to the fact that JR divergence is random variable with analytic distribution in the fault-free case. This means that that critical value of the distribution is directly calculated from the given probability of false alarm.

Under fault-free condition and no modeling mismatch, it can be shown that the residuals are zero-mean Gaussian distributions with corresponding variance σ^2 . Assuming $\alpha \rightarrow 1$, and $p(x) = \mathcal{N}(0, \sigma^2)$, Rényi (Shannon) entropy has a closed form:

$$H_1(\mathcal{N}(\mu, \sigma^2)) = \frac{1}{2} \ln(2\pi e\sigma^2). \quad (10)$$

In [12] it is shown that the Eq. (8) can be split in two parts: (i) entropy of a mixture distribution of n pdfs, and (ii) average entropy of these same n pdfs. The authors also showed the dependence of the divergence on the sample distribution of the variance σ^2 , which holds under assumptions above. Assuming identical assumptions and following similar steps as in [12], it can be shown that JR divergence in fault-free state is Gaussian distributed:

$$JR_\alpha^w \sim \mathcal{N}(\mu_{JRD}, \sigma_{JRD}^2), \quad (11)$$

where μ_{JRD} and σ_{JRD}^2 are parameters of normal distribution.

With known analytic form of JR divergence in fault-free condition (11), and data set \mathcal{D}_n obtained from the system in fault-free operation, the parameters μ_{JRD} and σ_{JRD}^2 can be estimated by means of maximum likelihood approach. The detection threshold can then easily be set at the critical value of the normal distribution defined by PFA. Note that the above derivation holds for certain assumptions presented in [12].

4 Application to the monitoring of solid oxide fuel cell

4.1 Process description

The potential of the proposed methodology is demonstrated on a simulated solid oxide fuel cell (SOFC) power generating unit. The system consists of 80-cell SOFC stack with total of 550 cm² of active area and balance of plant (BoP) module [13, 14].

The main objective of the BoP is to recover exhaust heat and supply it to the inlet gases, hence increasing overall efficiency of the system. Additionally, the pre-reformer serves an assisting reforming unit, where a portion of methane (cca 15%) is reformed. The pre-treated reactants are then fed to the stack where corresponding electro-chemical reactions take place thus generating electrical power.

In this preliminary study, a single subsystem is treated, the stack itself. Therefore, the selected outputs of the model is the output voltage y in range $[-1.5, 1.5]$ V around the operating point.

By analysing the flowsheet in SOFC system, it turns that there are five independent inputs that completely define the output. All together are put into the vector $\mathbf{u} = [\Phi_a \ \Phi_f \ \Phi_r \ I \ T_a]^T$ where Φ_a , Φ_f , Φ_r , I , T_a denote the air flow, fuel flow, recycle flow, current, and anode inlet temperature, respectively.

4.2 Model identification

To simulate the process we use a first principle nonlinear model in the form of a system of differential and algebraic equations [15]. The dynamic range, as well as the operating point, were selected in such a way that the main operating envelope of the plant was covered. As a nominal model we chose a reduced-order state-space model obtained by subspace identification from realisations of input and output data sampled every 1min. For the sake of persistent excitation a combination of filtered pseudorandom binary signal (PRBS) and low frequency white Gaussian noise was employed.

Prior to nominal model identification it was assumed that system is linear around operating point. Accordingly, local dynamics of the system is

described with a system of difference equations:

$$\begin{aligned}\Delta \mathbf{x}(k+1) &= \mathbf{A}\Delta \mathbf{x}(k) + \mathbf{B}\Delta \mathbf{u}(k) \\ \Delta \mathbf{y}(k) &= \mathbf{C}\Delta \mathbf{x}(k) + \mathbf{D}\Delta \mathbf{u}(k).\end{aligned}\tag{12}$$

where $\Delta \mathbf{u} \in \mathbb{R}^p$ is vector of inputs, $\Delta \mathbf{x} \in \mathbb{R}^n$ is state vector and $\Delta \mathbf{y} \in \mathbb{R}^q$ is vector of the outputs. $\mathbf{A}_{n \times n}$, $\mathbf{B}_{n \times p}$, $\mathbf{C}_{q \times n}$, and $\mathbf{D}_{q \times p}$ are system matrix, input, output and feed-through matrices, respectively. The order of system n indicates the number of considered linear differential equations, while p and q denote the number of inputs and outputs.

In Eq. (12), $\Delta \mathbf{u}$ and $\Delta \mathbf{y}$ denote deviation of the corresponding signal from its mean value. Accordingly, the operating point denoted by the mean value of inputs and outputs, was removed from the signals prior to model identification such that $\Delta u_i = u_i - \bar{u}_i$ and $\Delta y = y - \bar{y}$ where u_i denotes i^{th} input variable, y is voltage output, and \bar{u}_i and \bar{y} are corresponding means.

Although the model \mathcal{M}_0 fits with the stack voltage apparently quite accurately, there is still some mismatch between the two responses. In turn, the residual (6) is non-zero even in fault-free operation, clearly impeding fault detection.

4.3 Assessment of the proposed detection approach

We will present two simulated examples. The fault-free case and the parametric fault in the system, i.e. gas leakage between pre-reformer and stack. The system excitation signals was kept within the nominal operating envelope of the system. Accordingly, the input signals were low-pass filtered white Gaussian noise of appropriate amplitudes fluctuating around steady-state operating point. During the simulation, the power output of the stack varied approximately about 30%.

Fault-free case Figure 2(a) shows residual of the nominal model $z(k)$. Obviously it is non-zero even in fault-free case, hence hindering fault detection. Figure 2(b) shows the corrected residual employing the Gaussian process (GP) model. The GP model accurately captures the actual mean value of the residual $z(k)$ and significantly attenuates the impact of unmodelled dynamics.

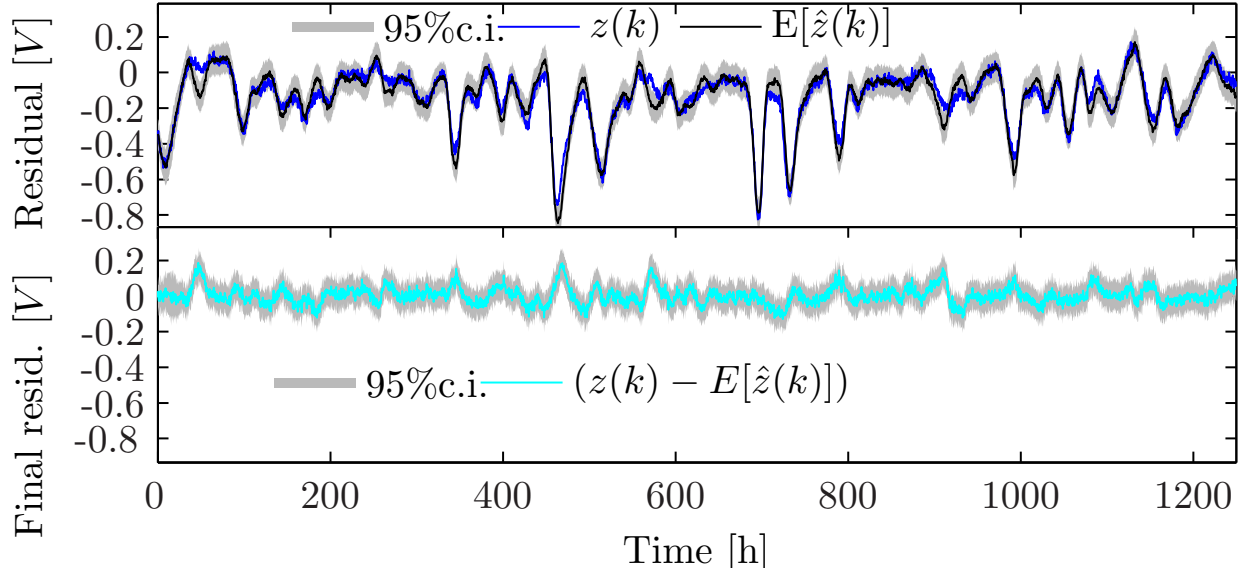


Figure 2: Fault-free residuals: (a - upper window) nominal model residual with its GP-NFIR estimate and (b - bottom window) GP-NFIR model final residual. The effect of non-modelled dynamics is significantly attenuated by the correction GP-NFIR model.

Parametric fault A pipe leak between pre-reformer and anode inlet is simulated. The fault magnitude is as high as 2% mass lost between these two components. In such a case insufficient reactants are fed to the stack, thus exposing stack to e.g. fuel starvation. This, in turn, leads to anode re-oxidation. The time of the fault was set at $t = 709h$. Figure 3 shows the final residual calculated from Eq. (7). JR divergence is employed to detect the change in the residual pdfs, calculated by Eq. (7). For the calculation of JR divergence from Eq. (11) we considered 300 reference pdfs and another 300 on-line pdfs. The JR divergence is shown in Figure 3(b). The detection threshold is set according to probability of false alarm (PFA) at 0.99 percentile of the corresponding cumulative density function (cdf).

From examples presented it can be seen that GP-NFIR model clearly contributes to the precision of the model and hence improved diagnostic sensitivity. JR divergence greatly improves the diagnostic stability since changes in JR divergence are much easier to detect than changes in the residuals.

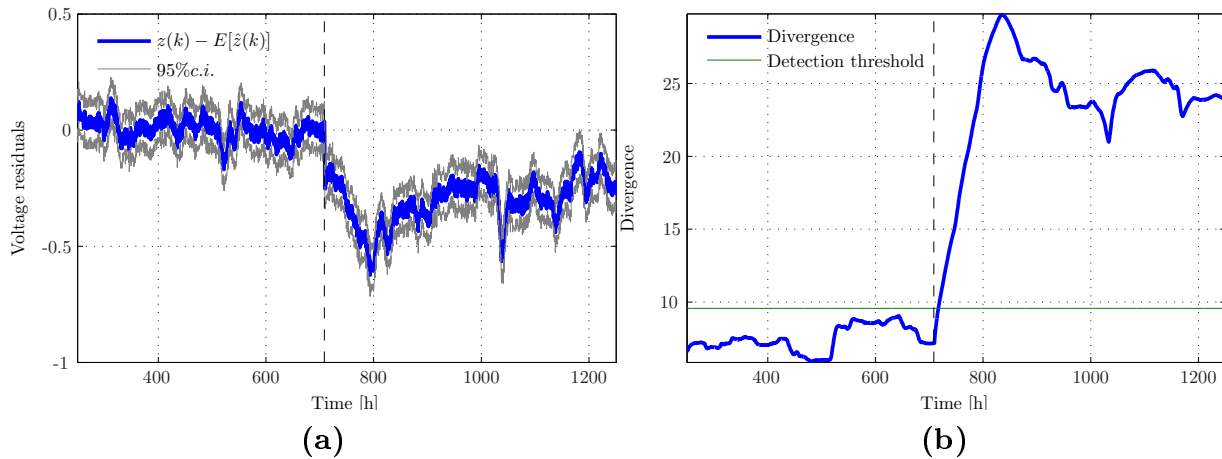


Figure 3: Residual (a) and JR divergence (b) for the case of leak simulation. The fault was introduced at $t = 709h$, as marked by dashed line. The residual pdfs are fluctuating around zero in the fault-free period and drift away when the fault is introduced to the simulation, hence divergence increases.

5 Conclusions

An approach to the characterisation of the model error in terms of a second order Gaussian stochastic process, which is function of process inputs, is proposed. The main contributions of the paper are twofold. First, the GP-NFIR model, serving as refinement of the nominal process model, is able to capture unmodelled nonlinear dynamic effects fairly easy. Simulations and some preliminary tests indicate that benefits can be substantial. As weak points one can consider (i) need for rich enough training data set and (ii) considerable computational load in the identification stage of the GP-NFIR. The latter is an exciting issue open to further research. Second notable contribution is the diagnostic procedure based on divergence measures between reference and on-line data sets. Strikingly simple selection of the diagnostic thresholds by only one design parameter and superb detection reliability indicate significant practical potentials of the approach. In the follow-up stress will be on more exhaustive laboratory assessments.

References

- [1] O. K. Kwon, G. C. Goodwin, and W. H. Kwon Robust fault detection method accounting for modelling errors in uncertain systems *Control Engineering Practice* 5:763–773, 1994.

- [2] D. Juricic and M. Zele Robust detection of sensor faults by means of a statistical test *Automatica* 38:737–742, 2002.
- [3] L. Ljung, G. C. Goodwin, and J. C. Aguero Stochastic Embedding revisited: A modern interpretation *Decision and Control (CDC), 2014 IEEE 53rd Annual Conference on* 3340 – 3345, 2014.
- [4] R. A. Delgado, G. C. Goodwin, R. Carvajal, et al. A novel approach to model error modelling using the expectation-maximization algorithm *Decision and Control (CDC), 2012 IEEE 51st Annual Conference on* 7327 – 7332, 2012.
- [5] M. Milanese, J. P. Norton, H. Piet-Lahanier, et al. *Bounding Approaches to System Identification* Plenum Press, 1996.
- [6] G. Klančar, D. Juricic, and R. Karba Robust fault detection based on compensation of the modelling error *International Journal of Systems Science* 33:97–105, 2002.
- [7] C. E. Rasmussen and C. K. I. Williams *Gaussian Processes for Machine Learning* MIT Press, 2006.
- [8] J. Q. Candela, C. E. Rasmussen, and C. K. Williams Approximation methods for gaussian process regression *Large-scale Kernel Machines* 203–224, 2007 subsection 3.4.
- [9] J. Kocijan *Modelling and Control of Dynamic Systems Using Gaussian Process Models* Springer International Publishing, 2016.
- [10] M. Basseville and I. V. Nikiforov *Detection of Abrupt Changes: Theory and Application* Prentice Hall, 1993.
- [11] B. Dolenc, Boskoski, and D. Juricic Change detection based on entropy indices with application to bearing faults. *9th SafeProcess 2015 IFAC* (1438-1443), 2015.
- [12] B. Dolenc, P. Boskoski, and D. Juricic Optimal threshold selection in fault diagnosis of mechanical drives based on information indices *Surveillance 8 : International Conference*, 2015.
- [13] A. Pohjoranta, M. Halinen, J. Pennanen, et al. Solid oxide fuel cell stack temperature estimation with data-based modeling - Designed experiments and parameter identification *Journal of Power Sources* 277:464–473, 2015.
- [14] M. Halinen, M. Rautanen, J. Saarinen, et al. Status of SOFC Demonstration Unit with 10 kW Stack *219th ECS Meeting*, 2011.
- [15] D. Marra *Development of Solid Oxide Fuel Cell stack models for monitoring, diagnosis and control applications* Ph.D. thesis University of Salerno, Italy, 2012.

For wider interest

Fault detection, isolation (FDI) is a subfield of control engineering which concerns itself with monitoring a system, identifying when a fault has occurred, and pinpointing the type of fault and its location. It is an important, but challenging problem in chemical, nuclear, aerospace, and automotive engineering. An interesting subfield is machine fault diagnosis, concerned with finding faults arising in machines. A particularly well developed part of it applies specifically to rotating machinery, one of the most common types encountered. To identify the most probable faults leading to failure, many methods are used for data collection, including vibration monitoring, thermal imaging, oil particle analysis, etc. Then these data are processed utilizing methods like spectral analysis, wavelet analysis, wavelet transform, short term Fourier transform, correlation method, and others.

Low-cost spectrum sensor for ultra-narrowband transmissions

Tomaž Šolc^{1,2}

¹Department of Communication Systems, Jožef Stefan Institute, Ljubljana, Slovenia

²Jožef Stefan International Postgraduate School, Ljubljana, Slovenia

tomaz.solc@ijs.si

Abstract. Growing interest in wireless sensors and actuators for the Internet of things has recently prompted development of wireless protocols employing ultra-narrowband transmissions at the physical layer. These transmissions present new challenges for spectrum sensing, both in the context of technology coexistence and in supporting dense ultra-narrowband networks through collision avoidance. In this paper we present a custom designed, low-cost spectrum sensor hardware designed from off-the-shelf integrated circuits and associated software implementing covariance based-detection. We also show results of a table-top experiment where we tested the sensor's detection performance with ultra-narrowband signals in the UHF frequency range.

Keywords: ultra-narrowband, spectrum sensing, covariance-based detection, hardware, internet of things

1 Introduction

Recently there has been growing interest in small autonomous interconnected sensors and actuators. Some predictions for the growth of the so-called Internet of things now tell of trillions of deployed wireless devices by 2020 in densities up to 100 devices per m² [1]. Existing, widely deployed wireless technologies, like LTE and IEEE 802.11 WLAN are ill-suited for such use: they have been optimized for low-latency, high-throughput applications typical for laptop computers and smartphones. Their low spectral efficiency and high preamble overhead become significant burdens when faced with high density of devices that only need to infrequently transfer a few bytes of data at a time, with very relaxed requirements regarding latency and bitrate.

A number of technologies and standards employing so-called ultra-narrowband transmissions have emerged recently specifically to address such use cases: Sigfox [2], Weightless [3], 3GPP Cooperative Ultra-Narrowband (C-UNB) [4]. These technologies employ very low bit-rate transmissions (on the order of 100 to 1000 bits/s) using binary phase-shift keying (BPSK) or Gaussian frequency-shift keying (GFSK) modulations with bandwidths on the order of 100 Hz to 1 kHz. Hence they exhibit high spectral efficiency and low preamble overhead with short payloads [5].

Narrow bandwidth allows for demodulation at low signal-to-noise ratios. Combined with use of sub-1 GHz bands with good propagation properties, these technologies enable long range with relatively low transmit powers, which makes them suitable for battery operated devices. 868 MHz European Short-range devices (SRD) band is most often used at the moment. Extension to TV whitespaces as well as dedicated spectrum in the 694 - 790 MHz range [6] is possible in the future.

Using a spectrum sensor for detecting whether a frequency channel is occupied by an ultra-narrowband transmitter has several applications. In general, reliable sensing of other users of radio spectrum is seen as an important component of future smart radios that will be able to intelligently optimize their operation. It is highly likely that currently emerging standards will be still in use when such radios will be commonplace. If ultra-narrowband devices will reach predicted deployment numbers and densities, other technologies sharing same frequency bands will have to rely on spectrum sensing to avoid interference with them.

Apart from coexistence concerns, spectrum sensing is also interesting for increasing the density of ultra-narrowband devices that can be supported in a cell. Currently, most devices choose transmission time and channel pseudo-randomly. Beyond a certain device density, such a scheme leads to high collision rate and requires a high number of packet retransmissions. Detecting channel occupancy opens the possibility of media-access protocols with collision avoidance.

Properties of ultra-narrowband that make it convenient for the described use cases also make it problematic for spectrum sensing. Large cell sizes and low signal-to-noise ratios mean that traditional energy detectors will not be able to reliably detect

many transmissions [7]. Hence, energy detection carrier sense, like for instance employed in IEEE 802.11 CS-MAC, becomes impractical. Detecting signals buried in noise typically requires advanced, computationally complex sensing methods and high-performance software-defined radio front-ends. This is in stark contrast to simple, low-cost transceivers employed on ultra-narrowband devices.

In this paper we present a simple spectrum sensing setup that we believe is well suited for ultra-narrowband applications – both from the standpoint of performance as well as required hardware and software complexity.

2 Hardware

VESNA SNE-ESHTER is a low-cost compact spectrum sensor. The device consists of two parts: the SNE-ESHTER analog front-end and the VESNA low-power sensor node core (SNC) [8]. A simplified block diagram is presented in Fig. 1. Device without an antenna measures approximately 70 x 50 x 20 mm.

The analog front-end performs the frequency down-conversion and signal conditioning before analog-to-digital conversion. The front-end is a custom designed single-conversion, low-intermediate frequency (IF) receiver based on the off-the-shelf NXP TDA18219HN integrated circuit. The specified input frequency range is between 42 MHz and 870 MHz. The local oscillator (LO) signal is generated by a FRAC-N phase-locked loop (PLL) from a 16 MHz crystal oscillator.

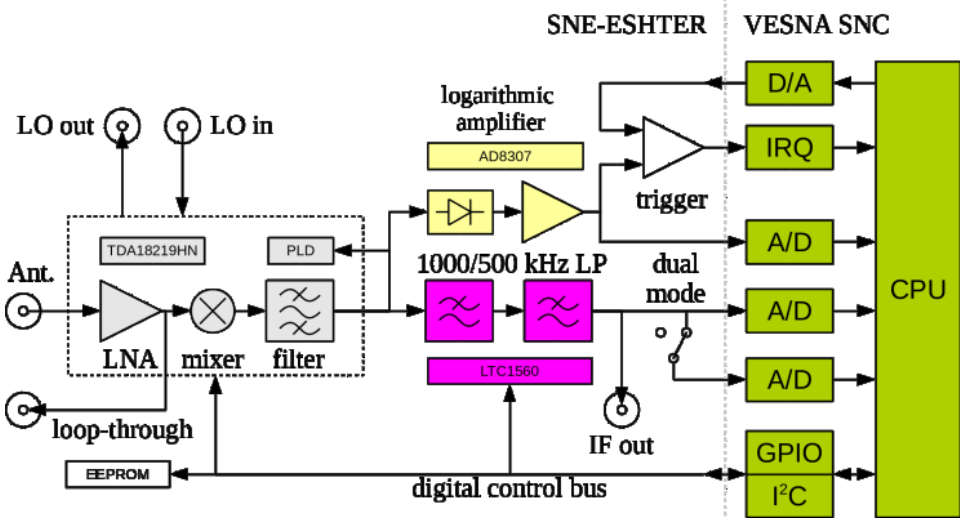


Figure 1: Block diagram of VESNA SNE-ESHTER

The radio-frequency (RF) signal from the antenna is amplified in a low-noise amplifier (LNA) and mixed with the LO in an image-rejection mixer to produce a signal at IF. Several stages of automatic gain control are used to minimize non-linear distortion and maximize signal-to-noise ratio of the signal. The signal passes through one tracking RF and two IF band-pass filters with software-selectable bandwidth. The final stage is a 10th order elliptic anti-aliasing filter with two settings: 500 kHz and 1000 kHz, corresponding to 1 Msample/s and 2 Msample/s sampling rates. After the anti-aliasing filter, the IF signal is routed to the SNC to be sampled by an analog-to-digital converter (ADC).

VESNA SNC contains three 12-bit successive approximation ADCs with up to 2 Msample/s sample rates. ADCs are driven by a DMA controller and store samples directly into a sample buffer in SRAM without any intervention from the CPU. The sample buffer has space for up to 25000 real samples (up to 12.5 ms of continuous reception at 2 Msample/s sample rate).

SNC is driven by an integrated microcontroller with an ARM Cortex M3 CPU core with a 56 MHz clock and 64 KB of SRAM. The microcontroller also contains an RS-232 interface with a 576 kbit/s maximum bitrate that can be used to connect the device to a PC. The software on the microcontroller controls the front-end through an I²C bus and several GPIO lines.

3 Software and sensing algorithm

Microcontroller on the SNC was programmed to calculate elements of the covariance matrix σ_l from the signal samples x_n in the ADC sample buffer using the following equation:

$$\sigma_l = \frac{1}{N_s} \sum_{n=0}^{N_s-1} x_n \cdot x_{n-l} \quad l \in [0, L - 1] \quad (1)$$

where N_s is the length of the ADC sample buffer and L is size of the covariance matrix \mathbf{R} .

$$\mathbf{R} = [r_{ij}] = \begin{bmatrix} \sigma_0 & \sigma_1 & \cdots & \sigma_{L-1} \\ \sigma_1 & \sigma_0 & \cdots & \sigma_{L-2} \\ \vdots & \vdots & \ddots & \vdots \\ \sigma_{L-1} & \sigma_{L-2} & \cdots & \sigma_0 \end{bmatrix} \quad (2)$$

The ARM Cortex M3 core does not support floating point arithmetic instructions. To achieve high performance and still retain sufficient resolution of covariance estimates, fixed point arithmetic was used instead of software floating point implementation or integer arithmetic. We found the ARM architecture especially convenient for the fixed point implementation because the barrel shifter allows correction of the scaling factor in multiplications without consuming additional CPU cycles. We used scaling factor 8 (3 bits), which allowed multiplication of two 12 bit ADC samples in Equation 1 to be performed in a single 32 bit CPU register.

In our experiment, the resulting L covariance values were sent over the RS-232 line to a laptop computer where a Python script implemented the rest of the signal detection. We chose to implement part of the detection outside of the device to simplify development and experimentation. Since the most computationally intensive task, the covariance estimation, was performed on the device itself, we believe our results are comparable to the case where the complete detector would be implemented on the device. Implementation of the remaining parts of the detectors on the SNC itself would be trivial.

We implemented three detector test statistics based on the estimated sample covariance matrix:

$$\gamma_{ED} = r_{11} \quad (3)$$

$$\gamma_{CAV} = \frac{\sum_{i=1}^L \sum_{j=1}^L |r_{ij}|}{\sum_{i=1}^L |r_{ii}|} \quad (4)$$

$$\gamma_{MAC} = \frac{\max_{i,j} |r_{ij}|}{|r_{11}|} \quad (4)$$

γ_{ED} is identical to the common energy detection test statistic. γ_{CAV} is the ‘‘covariance absolute value’’ statistic [9]. γ_{MAC} is the ‘‘maximum auto-correlation’’ statistic [10].

For each of these test statistics we determined a threshold γ_0 that resulted in the chosen constant false alarm rate (P_{fa}) according to the complementary cumulative distribution function method described in [11]. The detector performed a binary decision: if $\gamma > \gamma_0$ then the detector considered the channel occupied by a transmission. Otherwise, the channel was considered vacant.

4 Experiment setup

To generate the ultra-narrowband signal we used a Rohde & Schwarz SMBV100A vector signal generator. We used the arbitrary wave form generator function (ARB) to generate a BPSK signal at 160 bits/s. Sequence length was 324 bits. Bit values were pseudo-randomly generated. ARB sample rate was 1600 Hz. These settings correspond to a C-UNB packet with 12 bytes of payload. Central frequency was set to 700 MHz.

The generator was connected to 30 dB attenuator using 60 cm of LMR-195 coaxial cable. Before starting the experiment, all devices were left turned on for 2 hours to reach their temperature equilibriums. Total signal attenuation \mathcal{A} at the attenuator connector, including cable loss, was measured using the average channel power measurement mode on a Rohde & Schwarz FSV signal analyser. True input power P_{in} was calculated by subtracting \mathcal{A} from signal generator output power level.

$$\mathcal{A} = 33.2 \text{ dBm}$$

During the experiment, attenuator output was connected to the SNE-ESHTER antenna input connector. Receiver was tuned to 700 MHz. Receiver filter bandwidth was set to 1 MHz. Sampling rate was 2 Msamples/s. Detector was programmed to operate in a continuous loop: collect the full buffer of N_s signal samples, calculate L covariances and send them to the laptop computer over RS-232 for final processing.

For $N_s = 25000$ and $L = 20$, our implementation took approximately 280 ms to obtain one detector decision (including signal sampling, covariance estimation and test statistic calculation). Since this time was shorter than C-UNB packet transmission time (approximately 2 s), no special provisions were necessary to synchronize detection with the packet transmission. Hence ARB trigger on SMBVA100A was set to “automatic”.

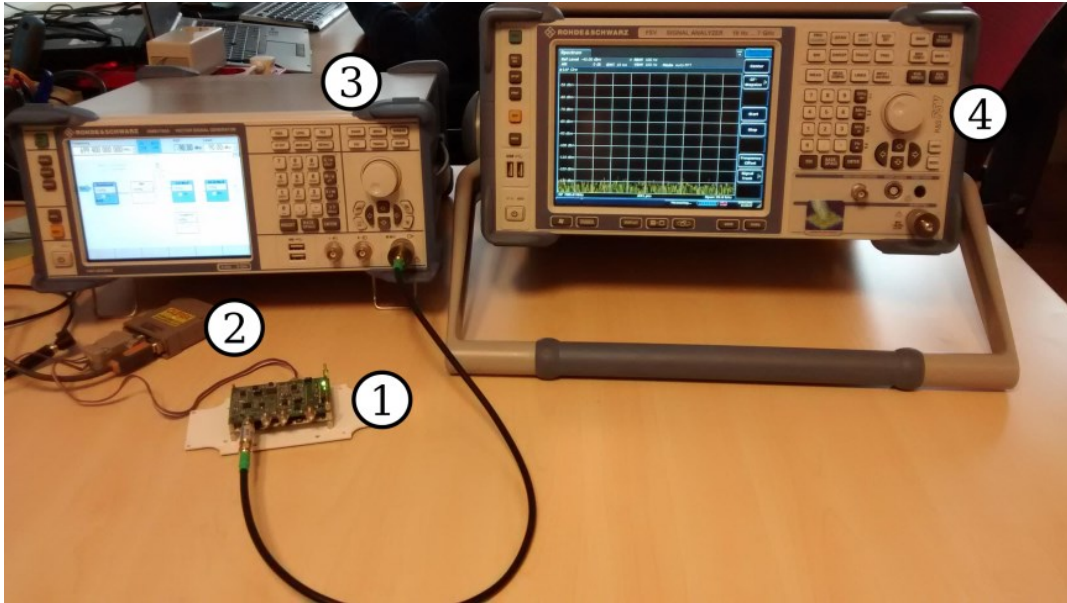


Figure 2: Experimental setup. (1) VESNA SNE-ESHTER sensor, (2) RS-232 interface, (3) vector signal generator, (4) signal analyser.

Detector thresholds were set for $P_{fa} = 0.05$. Two separate measurement campaigns were performed: To estimate the lowest detectable signal power, the generator output power was swept from -100 dBm to -75 dBm in increments of 1 dBm. For each generator setting, 500 binary decisions for each of detector were recorded. To estimate the frequency range of the detector, the generator central frequency was swept from 699.00 MHz to 700.60 MHz in increments of 0.05 MHz, while the receiver was kept tuned to 700 MHz. Generator output power was kept constant at -90 dBm. Again, 500 binary decisions for each detector were recorded.

5 Results

From the recorded binary decisions for each campaign, the probability of detection was estimated for each of the three detectors. Results of the two measurement campaigns are shown in Fig. 3. Lines show maximum likelihood estimate for P_d . Shaded areas show $1-10^{-5}$ confidence interval.

Minimum input power required to reach probability of detection $P_d = 0.99$ for energy detector was -119.2 dBm, for CAV (at $L = 20$) it was -123.4 dBm and for MAC (at $L = 5$) it was -122.4 dBm. Same minimum P_d was reached in a 392 kHz wide band for CAV and 107 kHz wide band for MAC at -123.2 dBm input power.

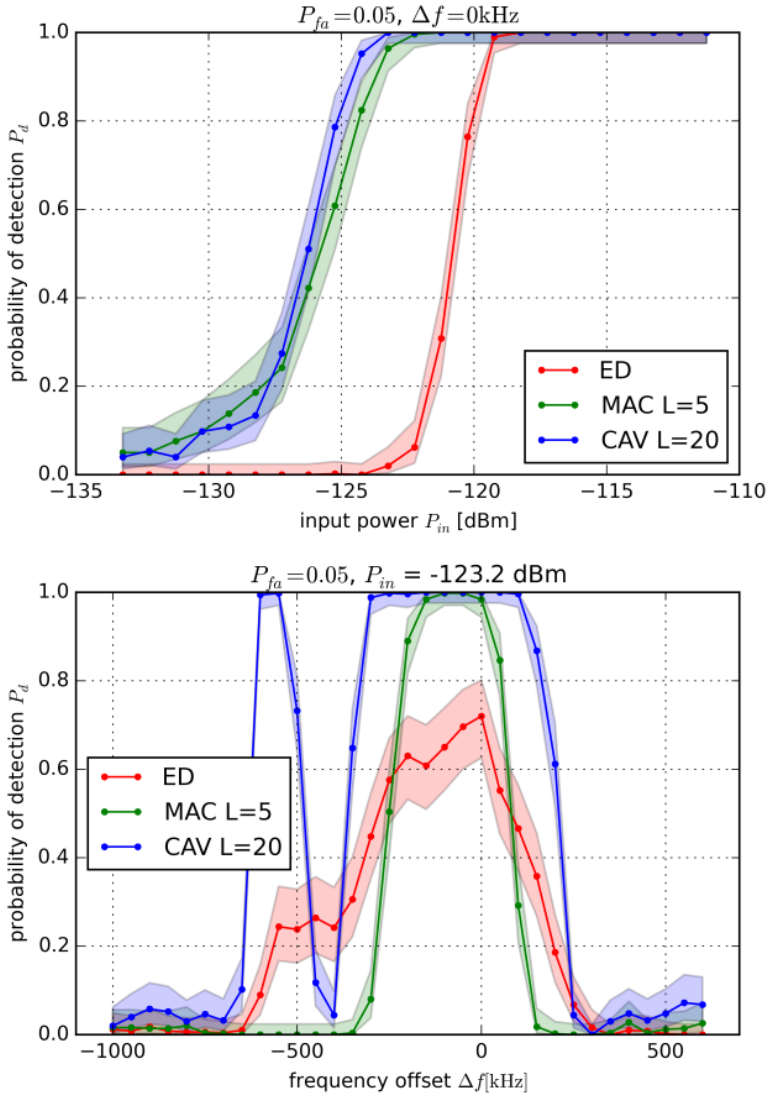


Figure 3: Probability of detection versus power (top) and frequency offset (bottom).

6 Discussion

Our results show that covariance-based detection can be successfully applied for sensing of ultra-narrowband transmissions. They achieve 99% probability of detection at 3 dB lower signal power than an energy detector. We can also see that the lowest detectable power of the MAC detector is only 1 dB worse than that of CAV detector, with significantly lower L . This is important since number of required multiplications in the detection algorithm scales linearly with L .

Another interesting property of these detectors is their frequency dependency. We can see that the width of the frequency band with reliable detection differs significantly between the three tested detectors. Even though MAC detector is sensitive to a significantly narrower range of frequencies than the width of the

receiver's 1 MHz channel, it would still be capable of detecting transmissions with 99% probability over approximately half of the C-UNB 200 kHz uplink band.

A limitation of our approach is the fact that the detector only produces a binary decision for the complete reception bandwidth. It does not provide information on the exact frequency of the transmission. This means that such a detector would be most useful for other users that wish to avoid interference with ultra-narrowband transmissions. On the other hand, inability to distinguish individual channels would make it less useful for use in an ultra-narrowband CS-MAC implementation.

Channel information could be obtained by implementing additional signal filtering in software before detection. However filtering would likely add significantly to processing time required to arrive at the binary decision. Considering inherent frequency selectivity of covariance methods itself, another interesting possibility would be exploring possible ways of adjusting frequency selectivity of the detector itself without the need for additional filtering.

Acknowledgements:

The research leading to these results has received funding from the European Horizon 2020 Programme project eWINE under grant agreement n°688116.

References:

- [1] The 5G Infrastructure Public Private Partnership (5GPPP). *5G empowering vertical industries*. https://5g-ppp.eu/wp-content/uploads/2016/02/BROCHURE_5PPP_BAT2_PL.pdf, 2016.
- [2] Sigfox. *Makers & Developers portal*. <http://makers.sigfox.com>, 2016.
- [3] Weightless SIG. *Weightless-N*. <http://www.weightless.org/about/weightlessn>, 2016.
- [4] 3GPP. *C-UNB technology for Cellular IoT – Physical Layer (GP-150057)*. Shanghai, China, 2015.
- [5] T. Lassen. *Long-range RF communication*. Texas Instruments, 2014.
- [6] European Commission. *Commission proposes to boost mobile internet services with high-quality radio frequencies*. http://europa.eu/rapid/press-release_IP-16-207_en.htm, 2016.
- [7] S. Anant, N. Hoven and R. Tandra. Some fundamental limits on cognitive radio. In *Allerton Conference on Communication, Control, and Computing*, 2004.
- [8] M. Smolnikar, et al. Wireless Sensor Network Testbed on Public Lighting Infrastructure. In *The Second International Workshop on Sensing Technologies in Agriculture, Forestry and Environment*, 2011.
- [9] Y. Zeng and Y. C. Liang. Spectrum-Sensing Algorithms for Cognitive Radio Based on Statistical Covariances. In *IEEE Transactions on Vehicular Technology*, 2009.
- [10] Y. Zeng and Y. C. Liang. Robust spectrum sensing in cognitive radio. In *IEEE International Symposium on Personal, Indoor and Mobile Radio Communications Workshops*, IEEE, 2010.
- [11] T. Šolc. *Spectrum sensing methods and implementations*. Jožef Stefan International Postgraduate School, 2014.

For wider interest

There is only a limited amount of useful radio frequencies that can be used for wireless communications. Rapid increase in demand for wireless technologies in recent years has made this limitation evident. Ultra-narrowband is a new technology that is optimized for sensors and other devices that only occasionally transmit small amounts of data. Compared to existing mobile networks or Wi-Fi it is capable of accommodating many more devices in the same amount of radio spectrum.

Spectrum sensing is a special method of radio reception where instead of extracting information being sent by a transmitter we are only interested in the fact that a transmission exists. The most basic and widely used method is detecting the energy emitted into the electromagnetic field. However physical laws impose limits on how weak a signal can be reliably detected with energy detection. More sophisticated methods, like those based on statistical covariances, can reliably detect transmitters even when their signals are many times weaker than noise.

Spectrum sensing can be used to provide real-time information on which radio frequencies in an area are in use and which are vacant, independent of the radio technology. This can help network planners in manually optimizing their wireless networks. More interestingly, it opens a possibility for intelligent devices that can autonomously and dynamically adapt to environment, avoiding interference from other devices. Early application of this technology can be seen for example in automatic channel selection in modern Wi-Fi routers.

Spectrum sensors were traditionally complex devices. Just as new radio technologies continuously decrease the cost of wireless devices, to the point where billions of are now predicted to be in use in the near future, so must spectrum sensors follow this trend if they are to be included on such devices. In this paper we present a custom designed spectrum sensor that was developed using off-the-shelf components intended for use in TV receivers. We show that advanced spectrum sensing algorithms can be implemented on low-cost hardware and that they are effective in detecting the kind of radio transmissions that will likely be widely used in the future by smart wireless sensors and other devices in the future Internet of things.

Nanoznanosti in nanotehnologije (Nanosciences and Nanotechnologies)

1 Introduction

The development of new methods for the construction of C-O and C-N bonds following the principles of green chemistry [1] is one of the most challenging tasks in organic synthesis. Transformation of organic molecules under high concentration reaction conditions (HCRC) or under solvent-free reaction conditions (SFRC) is receiving more and more attention and increased importance for the research and development in the field of organic chemistry due to their simplicity and cost efficiency.

Alkyl aryl ethers are important solvents and synthetic building blocks for the production of fragrances, cosmetics, pharmaceuticals, and dyestuffs [2], while nitrogen containing compounds are important in synthetic organic compounds because of their biological activities [3].

C-O bond formation by direct coupling of alcohols with other alkyl or benzyl alcohols could be very attractive strategy from practical, atom-efficient and environmentally point of view, producing water as only by-product of the reaction [4]. Because of their lower ability, hydroxyl moieties are rarely substituted under mild conditions and must often be activated before treatment with nucleophiles [5]. Numerous related methodologies have been developed using catalytic amount of NaAuCl_4 as simplest and least expensive gold catalyst for the etherification of benzylic and tertiary alcohols under mild conditions [6], rhenium (V)-oxo complex for the formation of C-O bond by the coupling of simple alcohols and propargyl alcohols [7]. The triphenyl phosphite-palladium complex was used as the catalyst for the substitution reactions of allylic alcohols via a direct C-O bond cleavage thus giving the corresponding allylic ethers and the related C-N bond-forming product [8]. It was shown C-N bond formation from allylic/propargylic and other alcohols with various *N*- nucleophiles, in the presence of iodine catalyst in MeCN, at room temperature [9].

The aforementioned methods suffer some disadvantages, including use of metals as a catalyst, the use of environmentally undesirable solvent and high temperature. Thus, the development of an efficient and environmentally benign catalytic methodology for C-O and C-N bond construction remains an attractive research subject. On the basis of our research group's continuing interest in developing greener methods, for comprehensive types of organic molecule transformation, we found it challenging to developed new efficient and selective methodology for the

direct C-O bond construction through the direct coupling of various types of alcohols (primary, secondary and tertiary benzyl alcohols and tertiary alkyl alcohol) with other alkyl, benzyl alcohols, TMSOEt, TMSOiPr or TMSCN as nucleophile sources and C-N bond construction in the presence of acetonitrile, anilines or TMSNCS as nucleophile sources catalysed by *N*-halo organic compounds as new type of metal-and acid-free catalysts under HCRC, SFRC or in solution, which offers a potential solution to environmental issues, producing only water as by-product of the reaction.

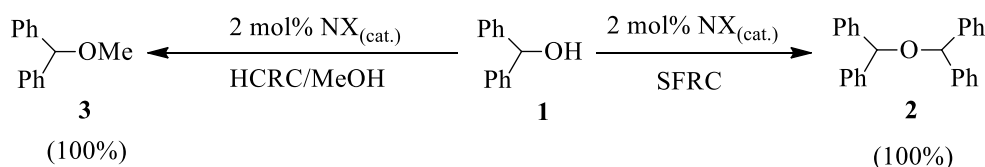
2 Materials and Methods

All alcohols substrates were purchased from commercial sources and were used without further purification. Analytical methods: column chromatography (CC) and flash chromatography (FC) were used for purification of products. Spectroscopic methods: mass spectroscopy (MS, electron spray ionization-ESI), nuclear magnetic resonance (300 NMR instrument, ¹H: 303.0 MHz, ¹³C: 76.2 MHz; using CDCl₃ as the solvent and SiMe₄ (TMS) as an internal reference), infrared spectroscopy (IR) and melting point (open capillary tube methodology; uncorrected) were used for identification and structure elucidation.

3 Results and discussion

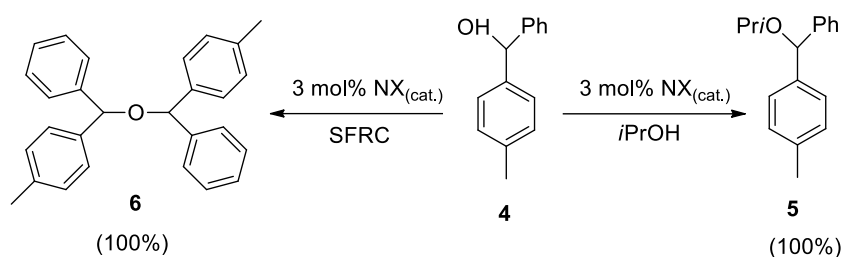
Initially, we chose diphenylmethanol (1) as the basic model substrate, to check the efficiency of *N*-halo organic compounds as catalysts and find the best reaction conditions for alcohol transformation. We showed that transformation of diphenylmethanol (1) catalysed by *N*-halo compound, in the presence of methyl alcohol under HCRC gave ether (3), while in the absence of MeOH, under SFRC, dimerization process took place, resulting in the formation of symmetric ether (2, Scheme 1).

Scheme 1. Transformation of diphenylmethanol (1) catalysed by *N*-halo compound under HCRC and SFRC.



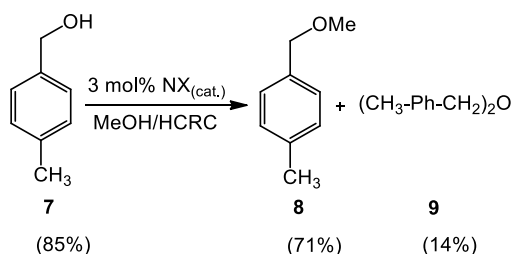
Furthermore, we performed the reaction of 4-methylbenzhydrol (**4**) catalysed by *N*-halo compound, in the presence of isopropyl alcohol (*i*PrOH) in solution, providing ether in quantitative yield (**5**), while in the absence of *i*PrOH, under SFRC, dimerization process took place, resulting in the formation of symmetric ether (**6**, Scheme 2).

Scheme 2. Transformation of 4-methylbenzhydrol (**4**) with *i*PrOH catalysed by *N*-halo compound under SFRC and in solution.



We further tested the role of *N*-halo organic compound as a catalyst by direct etherification of primary benzyl alcohol bearing electron-donating substituent on the aromatic ring, with MeOH under HCRC. We performed the reaction of 4-methyl benzyl alcohol (**7**) in the presence of *N*-halo compound as a catalyst under HCRC, we found out that the reaction resulted in the formation of ether in good yield (**8**), accompanied with small amount of dimeric ether (**9**, Scheme 3).

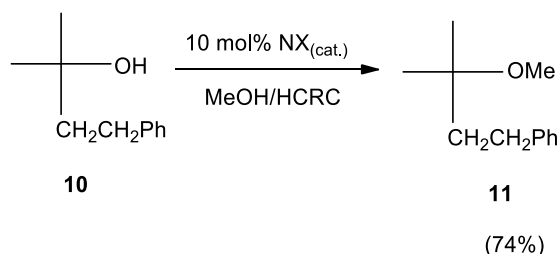
Scheme 3. Etherification of 4-methyl benzyl alcohol (**7**) with MeOH catalysed by *N*-halo compound under HCRC.



Moreover, this method was applied for tertiary alkyl alcohols with MeOH under HCRC. We performed the reaction of α,α -dimethylbenzenepropanol (**10**) in the

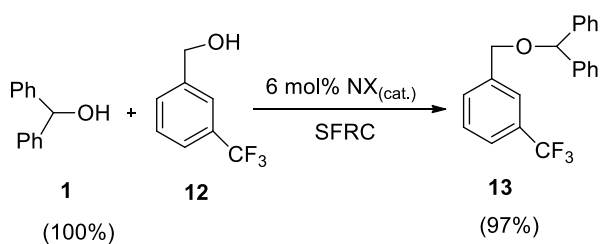
presence of *N*-halo compound as a catalyst under HCRC, we found out that the reaction resulted in the formation of ether in good yield (11, Scheme 4).

Scheme 4. *Etherification of α,α -dimethylbenzylpropanol (9) with MeOH, catalysed by *N*-halo compound under HCRC.*



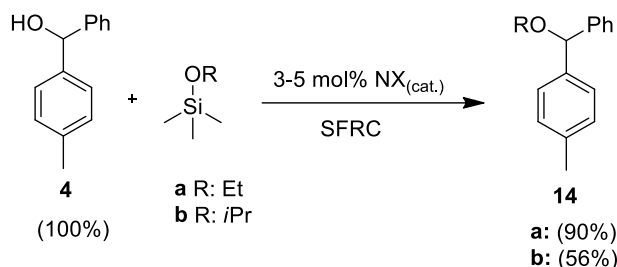
Inspired with these results, we further demonstrated the impact of *N*-halo compounds as catalysts by direct etherification of diphenylmethanol (1) with primary benzyl alcohols under solvent-free reaction conditions. Etherification of diphenylmethanol (1) with 3-trifluoromethyl benzyl alcohol (12) was carried out using *N*-halo compound as a catalyst under solvent-free reaction conditions which leads to the ether (13) in up to 97% yield, accompanied with a small amount of oxidized alcohol and dimeric ether as the side products (Scheme 5).

Scheme 5. *Etherification of diphenylmethanol (1) with primary benzyl alcohol (12) catalysed by *N*-halo compound under SFRC.*

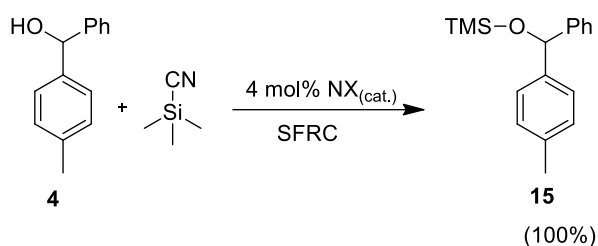


Additionally, we investigated reactions of 4-methylbenzhydrol (4) as the model compound in the presence of *N*-halo organic compound as a catalyst, using TMSOEt, TMSO*i*Pr, or TMSCN. In the case of TMSOEt or TMSO*i*Pr isopropoxy or ethoxy were introduced successfully into organic molecules (14a and 14b, Scheme 6). The courses of reactions were noticed to be quite different in the case of TMSCN and the formation of trimethylsilyl ethers (15, Scheme 7) as the sole product was observed.

Scheme 6. Etherification of 4-methylbenzhydrol (**4**) with TMSOEt or TMSOiPr catalysed by *N*-halo compound under SFRC.

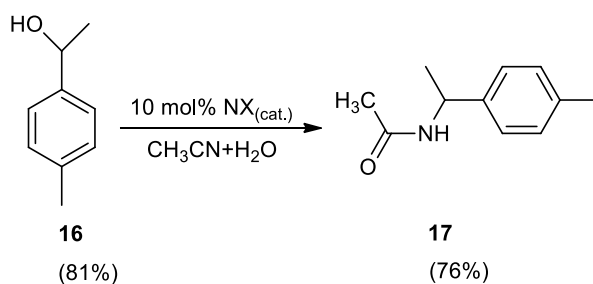


Scheme 7. Trimethylsilylation of 4-methylbenzhydrol (**4**) with TMSCN catalysed by *N*-halo compound under SFRC.



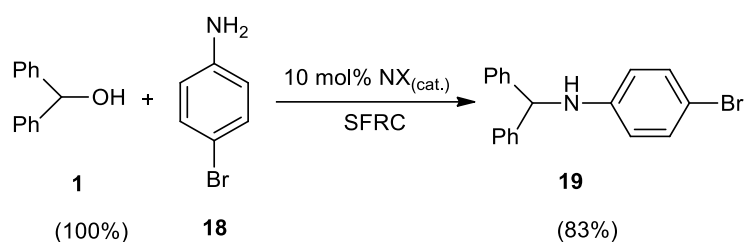
On the other hand, the role of *N*-halo compound as a catalyst was observed in reactions of alcohols with acetonitrile in solution, where products with new C-N bond formation could be obtained. The example of this possibility was demonstrated by the reaction of 1-(*p*-tolyl)ethan-1-ol (**16**), with acetonitrile, producing efficiently the corresponding *N*-alkylated compounds in good yield (**17**), accompanied with small amount of dimeric ether and oxidized alcohol (Scheme 8).

Scheme 8. Direct coupling of 1-(*p*-tolyl)ethan-1-ol (**16**) with acetonitrile catalysed by *N*-halo compound in solution.



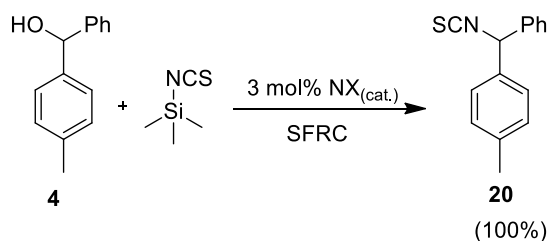
Additionally, the direct coupling of aniline, bearing an electro-withdrawing group on the aromatic ring (18), with diphenylmethanol (1), in the presence of *N*-halo compound as a catalyst, under SFRC, afforded the corresponding *N*-alkylated compound in good yield (19) accompanied with small amount of oxidized alcohol (Scheme 9).

Scheme 9. *Direct coupling of diphenylmethanol (1) with 4-bromoaniline (18) catalysed by N-halo compound under SFRC.*



Additionally, C-N bond could be achieved by the reaction of 4-methylbenzhydrol (4) with TMSNCS catalysed by *N*-halo compound under SFRC, where isothiocyanate was introduced successfully into organic molecules (20, Scheme 10).

Scheme 10. *Isothiocyanation of 4-methylbenzhydrol (4) with TMSNCS catalysed by N-halo compound under SFRC.*



4 Conclusions

In conclusion, we have demonstrated a novel, efficient and selective, metal- and acid-free method for C-O bond formation through the direct transformation of alcohols to dimeric ethers using *N*-halo compound as a catalyst under solvent-free reaction conditions, while under alkyl alcohol high concentration reaction conditions, alkyl aryl ethers were obtained. Additionally, we have demonstrated that

the etherification could also be achieved by cross coupling of two different benzyl alcohols catalysed by *N*-halo compounds under solvent-free reaction conditions. Furthermore, C-O bond could be constructed by nucleophilic substitution of hydroxyl group using ethoxytrimethylsilane, isopropoxytrimethylsilane or cyanotrimethylsilane as source of nucleophiles in the presence of *N*-halo compound as a catalyst under solvent-free reaction conditions.

On the other hand, we have developed convenient C-N bond formation reactions of alcohols with anilines or acetonitrile under solvent-free reaction conditions or in solution catalysed by *N*-halo compound with a good yield. Additionally, we have showed that C-N bond could also be formed using (trimethylsilyl)isothiocyanate where isothiocyanate was introduced efficiently and selectively into organic molecules. The presented methodology is the new highly efficient and easy to perform approach to the synthesis of comprehensive new type of derivatives starting from hydroxyl functional group targets and applying solvent-free reaction conditions as green chemical reaction protocol.

Acknowledgments

We are grateful to the Slovene Human Resources Development and Scholarship Fund (contract: 11011-9/2011), Slovenian Research Agency (contract: Programme P1-0134) for the financial support. National NMR Centre at the National Institute of Chemistry, Ljubljana, Slovenia, is acknowledged for the use of NMR instrumentation.

References:

- [1] P. T., Anastas, J. C. Warner. *Green Chemistry: Theory and Practice*, Oxford University Press: New York, 1998.
- [2] E. Fuhrmann, J. Talbiersky. Synthesis of Alkyl Aryl Ethers by Catalytic Williamson Ether Synthesis with Weak Alkylation Agents. *Organic Process Research & Development*, 9, 206, 2005
- [3] A. A. Katak, S. Potavathri, R. A. Barham, K. M. Romano, B. DeBoef. Metal-Free Intermolecular Oxidative C–N Bond Formation via Tandem C–H and N–H Bond Functionalization. *Journal of the American Chemical Society*, 133, 19960, 2011
- [4] B. M. Trost. On Inventing Reactions for Atom Economy. *Accounts of Chemical Research*, 35, 695, 2002
- [5] M. Yasuda, T. Saito, M. Ueba, A. Baba. Direct Substitution of the Hydroxy Group in Alcohols with Silyl Nucleophiles Catalyzed by Indium Trichloride. *Angewandte Chemie International Edition*, 43, 1414, 2004

- [6] A. B. Cuenca, G. Mancha, G. Asensio, M. Medio-Simón. Water Compatible Gold(III)-Catalysed Synthesis of Unsymmetrical Ethers from Alcohols. *Chemistry - A European Journal*, 14, 1518, 2008
- [7] B. D. Sherry, A. T. Radosevich, F. D. Toste. A Mild C–O Bond Formation Catalyzed by a Rhenium-Oxo Complex. *Journal of the American Chemical Society*, 125, 6076, 2003
- [8] Y. Kayaki, T. Koda, T. Ikariya. Halide-Free Dehydrative Allylation Using Allylic Alcohols Promoted by a Palladium–Triphenyl Phosphite Catalyst. *The Journal of Organic Chemistry*, 69, 2595, 2004
- [9] Z. Liu, D. Wang, Y. Chen. Mild and Efficient Iodine-Catalyzed Direct Substitution of Hydroxy Group of Alcohols with C- and N-Nucleophiles. *Letters in Organic Chemistry*, 8, 73, 2011

For wider interest

- New green chemical approach of the synthesis of aryl alkyl ethers and *N*-alkylated products could be of considerable interest to producer of these kinds of chemicals often used as active ingredients in fragrances, cosmetics, dyestuffs and pharmaceutical industry.
- In comparison with known related methods and processes, considerably improved green chemical profile of our original methodology offers a potential impact to environmental effect, in related production processes.

Building thick spinel iron oxide layer onto the hexaferrite core nanoparticles using multiple co-precipitation of iron ions

Blaž Belec^{1,2}, **Darko Makovec**^{1,2}

¹ Department of Material Synthesis, Jožef Stefan Institute, Ljubljana, Slovenia

² Jožef Stefan International Postgraduate School, Ljubljana, Slovenia

blaz.belec@ijs.si

Abstract: One of the possible approaches to tune the hysteresis loop of bi-magnetic core-shell (CS) composite nanoparticles is with varying the thickness of the shell. In the present work the synthesis procedure aiming to increase the thickness of the maghemite layer coated onto the hexaferrite core nanoparticles was investigated. The method for synthesizing the composite nanoparticles with thick maghemite layer based on the two-step co-precipitation process of the $\text{Fe}^{3+}/\text{Fe}^{2+}$ ions. The product of the co-precipitation heterogeneously nucleates on the hexaferrite core nanoparticles in their aqueous suspension. After the first coating step, the product contains only composite nanoparticles where hexaferrite core nanoparticle is positioned in-between two maghemite layers, forming a “sandwich” type structure. The maghemite layer was approximately 2 nm thick. The separate, homogeneous nucleated maghemite nanoparticles were never observed. After the first coating step, the composite nanoparticles were re-dispersed in water to increase thickness of the layer with by coating with maghemite in the second step. The main problem of the second step is agglomeration of the composite nanoparticles due to the magnetic interactions. The agglomeration decreases the surface area available for growth of the maghemite layer and could promote the formation of separate, homogeneously-nucleated maghemite nanoparticles. To minimize the agglomeration of the nanoparticles polyvinylpyrrolidone (PVP) was added. After the second coating, the thickness of the maghemite layer increased to approximately 3.5 nm. Although we minimize the agglomeration effect of the core nanoparticles with the addition of the PVP, product still contains some homogeneously-nucleated maghemite nanoparticles.

Keywords: composite nanoparticles, spinel ferrites, synthesis, co-precipitation, heterogeneous nucleation

1 Introduction

Composite nanoparticles are nanomaterials where different functional materials are combined in the single nano-unit. While the properties of single-phase materials depend on the intrinsic properties of the materials, their size and shape, the properties of the composite nanoparticles depend additionally on the interactions between the properties of the different functional materials they are made of. The coupling between the materials in the composite nanoparticles can result in new phenomena and novel functional properties that are unachievable with single component materials [1].

Bi-magnetic composite nanoparticles combining two different magnetic materials represent an important class of the composite nanoparticles. With coupling between properties of hard- and soft-magnetic materials in single composite nanoparticle, the shape of magnetic hysteresis can be tuned. The direct exchange coupling between the two magnetic materials can result in increased energy product ($|BH|_{\max}$). $|BH|_{\max}$ is a figure of merit for the quality of the magnets. It depends on the area of the magnetization curve, thus for large $|BH|_{\max}$, a material with high saturation magnetization (M_s) and high coercivity (H_C) is required [2, 3]. Therefore the bi-magnetic nanoparticles can be potentially used as building blocks for the permanent magnets with enhanced $|BH|_{\max}$. The coupling between two magnetically dissimilar materials can also be used to tune the shape and the temperature dependence of the nanoparticles' hysteresis loop for requirements of a specific application [4, 5]. For instance, by combining soft-magnetic MnFe_2O_4 and hard-magnetic CoFe_2O_4 in the bi-magnetic nanoparticles the shape of their hysteresis was tuned for improved conversion of the electromagnetic energy into heat required for mediators used in magnetic hyperthermia cancer treatment [4].

Bi-magnetic nanoparticles usually display core-shell (CS) structure, since it was found that the coupling between two different magnetic materials is stronger in the CS nanoparticles than in other composite structures, where the contact area between magnetic materials is smaller [6]. In the present paper bi-magnetic nanoparticles were synthesized by combining soft-magnetic maghemite shell with hard magnetic barium hexaferrite [5]. CS nanoparticles with spinel ferrite shell are usually synthesized with the thermal decomposition of organometallic precursors (metal acetoacetate, benzylacetate, metal-oleates) in high-boiling point solvents

(octadecene, benzyl ether, hexadecanediol) in a presence of the capping agent (olein amine, oleic acid) [4, 6-8].

Bi-magnetic composite nanoparticles can also be synthesized with a simple, low temperature co-precipitation method of iron ions in an aqueous suspension of the core nanoparticles [9]. The spinel iron oxide (maghemite) layer is deposited onto the core nanoparticles with co-precipitation of the $\text{Fe}^{3+}/\text{Fe}^{2+}$ ions in the colloidal aqueous suspension of the core nanoparticles. The maghemite is formed in a sequence of the chemical reactions and transformations. First, the Fe^{3+} precipitates at low pH of 2.8 as iron (III) hydroxide. Depending on the reaction conditions the hydroxide transform into iron-oxide hydroxide (FeOOH). If the FeOOH is in its γ - FeOOH modification (lepidocrocite) it will react with the Fe^{2+} ions precipitated at the pH above ≈ 5.5 to form the magnetic spinel iron oxide. Initially magnetite (Fe_3O_4) is formed, which oxidizes to maghemite (γ - Fe_2O_3) when it is exposed to ambient air. To enable exclusively heterogeneous nucleation of the initial product of the precipitation and growth of the spinel ferrite as layer at the core nanoparticles, supersaturation of the initial product has to be closely controlled. As the ionic chemical reactions in aqueous solutions are very fast, the supersaturation depends mainly on the concentration of the reactants, which is difficult to be controlled. Controlled release of the Fe^{3+} ions into the reaction suspension was enabled by thermal decomposition of a Fe^{3+} urea complex ($[\text{Fe}((\text{CO}(\text{NH}_2)_2)_6)(\text{NO}_3)_3]$). The hydroxyl ions needed for the precipitation were homogeneously released into the reaction mixture by using solid $\text{Mg}(\text{OH})_2$, which has limited solubility increasing with the temperature. The immobilization of Fe^{3+} into the complex also postpones the precipitation of Fe^{3+} ions to higher pH values close to 6, where Fe^{2+} ions are precipitate. The synthesized composite nanoparticles are composed of a hexaferrite core positioned in between the two layers of the maghemite. The maghemite layer is homogeneous and with uniform thickness up to approximately 2 nm [5].

One of possible mechanisms for tuning the shape of the hysteresis loop of bi-magnetic composite nanoparticles is with varying the thickness of the layer [4, 7]. The thickness of the layer can be increased by increasing reactant concentration while the amount of the core nanoparticles remains unchanged. In preliminary research it was found that the maximum thickness of the maghemite up to 2 nm could be obtained with the nominal ratio between the amount of the Fe^{3+} ions and

calculated surface area of the hexaferrite core nanoparticles ($n_{\text{Fe}^{3+}}:A_{\text{HF}}= 34.8$ mol/m²). If the ratio is increased over this value, the separate maghemite nanoparticles form in the solution, because the supersaturation level increases over the limit required for the heterogeneous nucleation, while thickness of the maghemite layer remains unchanged. Thus, the thickness of the maghemite layer can only be increased using multiple-step coating. In the present work the thickness of the layer was increased by coating of the maghemite in the two-step process. After the first step coating, the product - composite nanoparticles were re-dispersed and coated with the maghemite in the second step. The main problem represents strong remanence of the composite nanoparticles after the first coating which causes their magnetic agglomeration in the suspension during the second coating. The agglomeration was minimized by using polyvinylpyrrolidone (PVP).

2. Materials and methods

1.1 Materials

Iron (III) nitrate hepta hydrate ($\text{Fe}(\text{NO}_3)_3 \times 7\text{H}_2\text{O}$), iron (II) chloride (FeCl_2), magnesium hydroxide ($\text{Mg}(\text{OH})_2$), urea, barium nitrate ($\text{Ba}(\text{NO}_3)_2$), scandium nitrate ($\text{Sc}(\text{NO}_3)_3$), sodium hydroxide (NaOH), nitric acid (HNO_3), ammonia solution (NH_3 , 25%), polyvinylpyrrolidone (PVP). A nitrate complex of Fe^{3+} with urea ($[\text{Fe}((\text{CO}(\text{NH}_2)_2)_6)(\text{NO}_3)_3]$), referred to as Fe^{3+} -urea, was synthesized according to the procedure described in the literature [5]

1.2 Preparation of aqueous suspension of the hexaferrite core nanoparticles

Barium hexaferrite (HF) core nanoparticles were synthesized using hydrothermal method [10-12]. In short, Nitrates with the molar ratio $n_{\text{Ba}} : (n_{\text{Fe}} + n_{\text{Sc}}) = 1:5$ and $n_{\text{Ba}} : n_{\text{Sc}} = 2:1$ were dissolved in water and co-precipitated with NaOH . The slurry was hydrothermally treated at 240 °C. The product was washed with water and nitric acid. According to the ζ -potential measurements, suspension of the HF nanoparticles was adjusted to the $\text{pH} \approx 4.5$ with ammonia solution. At this pH value the nanoparticles exhibit large positive surface potential, enabling preparation of their stable suspension. The amount of the HF nanoparticles added into the reaction mixture was determined according to their overall surface area of 5.45m². The estimated area was calculated in a way, that the added concentration of Fe precursors would form a 3 nm thick shell [5].

1.3 Synthesis of the maghemite layer

The maghemite layer was synthesized using slightly modified procedure as it is reported in the literature [5, 9]. The optimized process was as follows: 80 mL of the stable aqueous suspension of the HF core nanoparticles was heated at 60 °C under argon flow. Then a Fe³⁺-urea complex (n=0,19 mmol) and FeCl₂ (n= 0.095 mmol) were dissolved into the suspension (pH = 2.2) and mixed. After the 10 minutes of thermal hydrolysis at 60 °C, the Mg(OH)₂ (0,46 mmol) was admixed into the reaction mixture, resulting in an increase of a pH to a pH ≈ 7.5. After 2 hours at the final pH the reaction mixture was cooled to room temperature and the product was washed several times with diluted HNO₃ at pH ≈ 4 to dissolve excess of Mg(OH)₂. After the coating, the initial composite nanoparticles were re-dispersed and coated with maghemite in the second step. The synthesis procedure of the second step coating was similar as in the first step. According to the ζ-potential, the suspension containing composite nanoparticles was adjusted to a pH ≈ 4.5. At this pH they exhibit the largest positive surface potential, thus enabling to prepare stable their stable suspension [13]. Additionally, for the better stability of the system, PVP was added (c_{PVP} = 2 g/L). We also decrease the concentration of the reactants, n(Fe³⁺-urea) = 0,12 mmol, n(Fe²⁺) = 0,06 mmol and n(Mg(OH)₂) = 0,24 mmol.

Characterization of the materials

The nanoparticles were characterized using transmission electron microscopy (TEM) in combination with energy-dispersive X-ray spectroscopy (EDXS). For TEM analysis, the nanoparticles were suspended in ethanol and deposited on a copper-grid-supporter perforated electron-transparent carbon foil.

2. Results and discussion

The process of coating the core nanoparticles with the maghemite layer can be divided into 3 stages. First, the stable aqueous suspension of the core nanoparticles with iron precursors (Fe³⁺-urea and Fe²⁺ ions) was maintained at the 60 °C for the incubation time needed for the thermal decomposition of the Fe³⁺-urea complex. At this stage, iron oxi-hydroxide γ-FeOOH (lepidocrocite) was formed at the surfaces of the core nanoparticles. After the incubation time, solid Mg(OH)₂ was admixed into the suspension. When the solid hydroxide was slowly dissolved, the hydroxyl ions were relatively homogeneously released into the reaction mixture, resulting in a gradual increase of the pH. When the pH reached the value of approximately 5.7, the Fe²⁺ ions start to precipitate, marking the beginning of the

second stage of the process. At this stage Fe^{2+} ions react with $\gamma\text{-FeOOH}$ forming the spinel iron oxide. The third stage of the process begins when the final pH is reached and the reaction mixture was maintained at this point for 1.5 h [9]. The synthesis resulted in formation of the “sandwich” type composite nanoparticles where HF core nanoparticles were positioned in-between the two maghemite layers.

The structure of the core and composite nanoparticles was observed by high resolution transmission electron microscopy (HR)TEM. To observe the structure of the nanoparticles, they have to be oriented edge-on, i.e., with its large surfaces parallel to the electron beam. **Figure 1** represents (HR)TEM image of the HF core nanoparticle oriented with its basal planes parallel to the electron beam. The dominant periodicity of the HREM pattern of 1.15 nm correspond to the $(0002)_{\text{HF}}$ planes of the hexaferrite magnetoplumbite structure .

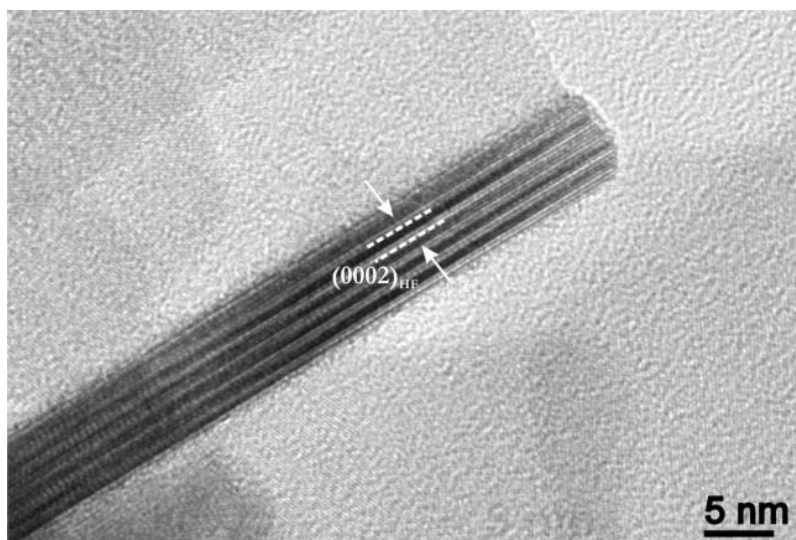


Figure 1: HRTEM image of the hexaferrite core nanoparticle oriented edge-on, with its large surface parallel to the electron beam.

The coating of the hexaferrite core nanoparticles with maghemite layer resulted in synthesis of the composite nanoparticles with “sandwich” type structure. The separate, homogeneously-nucleated nanoparticles of maghemite were never observed. The TEM image (**Figure 2a**) of the platelet composite nanoparticle oriented edge-on shows that the nanoparticle is composed of the HF core positioned in-between the two maghemite layers. The maghemite layers were uniformly deposited exclusively onto the basal-plane surfaces of the HF core nanoparticles. The thickness of the maghemite layer, which was measured on the several composite nanoparticles, was ≈ 2 nm. Both structures, magnetoplumbite structure of the HF core and the spinel structure of the deposited layer, are related. The magnetoplumbite structure can be represent as a hexagonal stacking of closely-

packed layer composed of larger oxygen and barium ions with smaller iron ions positioned in the interstition. The structure can be divided into two alternating blocks: the Ba-containing R block with hexagonal stacking and the S block with cubic stacking. The S block represent the (111) slice of the spinel structure [14]. The $\{111\}_S$ planes of the cubic spinel structure (marked in **Figure 2b**) are parallel to the HF basal $\{0001\}_{HF}$ planes . Thus, the spinel layer grows topotactically on the both sides of the core nanoparticles, forming a coherent $(0001)_{HF} || (111)_S$ interface with the HF core. The maghemite was never observed at the side surfaces of the core nanoparticles, where there is no matching between the two structures[5].

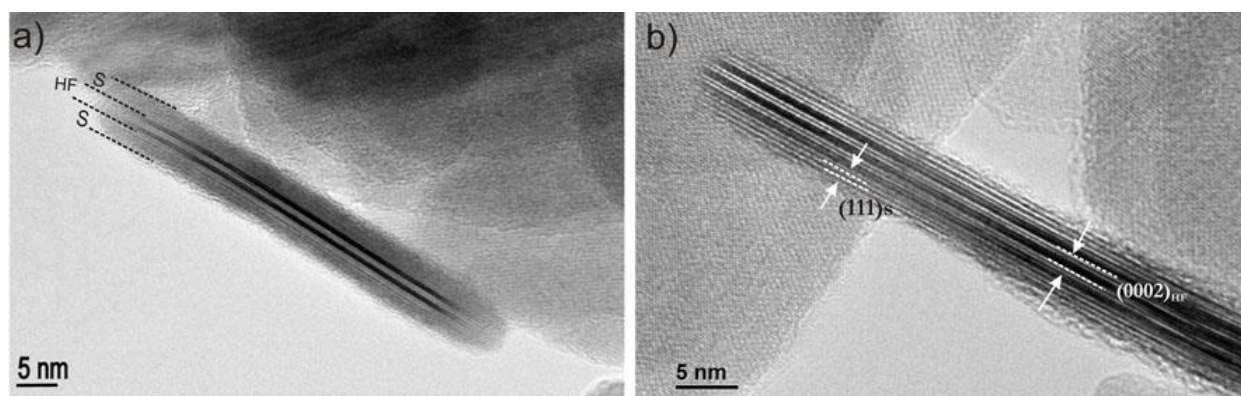


Figure 2: (a) TEM image of the platelet composite nanoparticle after the first coating oriented edge-on, with its large surface parallel to the electron beam (S ... spinel and HF... hexaferrite), (b) HRTEM image of the composite nanoparticle.

After the first coating, the composite nanoparticles were re-dispersed in water and again coated with maghemite in the second step. The main problem of the second step coating is stability of the suspension, containing the initial composite nanoparticles. The strong remanence of the composites causes their magnetic agglomeration in the suspension during the coating. Agglomeration of the nanoparticles results in a decrease of the surface area available for the nucleation and growth of the maghemite layer. The decreasing of the surface area can lead to formation of the homogeneously-nucleated maghemite nanoparticles. The agglomeration of the nanoparticles was minimized by using PVP, which sterically prevents their agglomeration. To avoid the homogeneous nucleation of the product, the low supersaturation of the product has to be maintained. To maintain the low supersaturation level in the second step, the concentration of the reactants was decreased compared to the first step coating ($n(\text{Fe}^{3+})=0.12$ mmol and $n(\text{Fe}^{2+})=0.06$ mmol).

The problem of the second coating is also the purification of the initial product, which contains un-reacted solid $\text{Mg}(\text{OH})_2$. The excess of the hydroxyl ions in the second step results in a rapid increase of the pH value which can lead to increased supersaturation of the products resulting in unwanted homogeneous nucleation [15]. To wash and neutralize excessive hydroxide which remains in the reaction mixture after the first stage, the initial product was washed several times with diluted HNO_3 (pH = 4).

Figure 3a represent TEM image of the product after the second coating. The image reveals that the product consists of two types of nanoparticles: typical “sandwich” type composite nanoparticles (A) and larger homogeneously-nucleated maghemite nanoparticles (B). The homogeneously-nucleated maghemite nanoparticles were probably formed due to the agglomeration of the initial composite nanoparticles during the second coating process, which decreases the surface available for heterogeneous nucleation. (HR)TEM image of the composite nanoparticles in **Figure 3b** reveals that the thickness of the maghemite layer was increased after second coating. The thickness of the maghemite layer was estimated to be ≈ 3.5 nm which is twice as thick as maghemite layer obtained after the first coating.

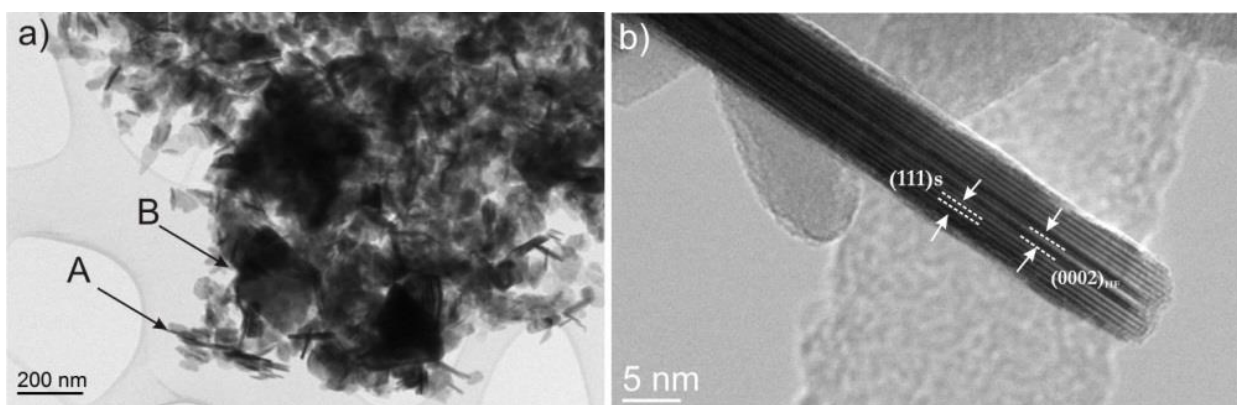


Figure 3: (a) Representative TEM image of the product after the second coating. The product contains classical composite nanoparticles (A) and large homogeneous nucleated nanoparticles (B), (b) (HR)TEM image of the composite nanoparticle after the second coating, oriented edge-on.

3. Conclusion

Composite nanoparticles, combining soft-magnetic maghemite layer coated onto the hard-magnetic HF core nanoparticles, can be synthesized using simple coprecipitation method of $\text{Fe}^{3+}/\text{Fe}^{2+}$ ions in a colloidal aqueous suspension of the core nanoparticles. The maghemite layer is formed with heterogeneous nucleation of the precipitating species on the surface of the core nanoparticles. For heterogeneous

nucleation of the maghemite layer, the low supersaturation of the precipitating species has to be maintained, which was enabled with slow thermal decomposition of the Fe^{3+} -urea complex.

Varying the thickness of the maghemite layer could influence on the magnetic properties of the composite nanoparticles. One of the possibilities approaches to tune the thickness of the layer is changing nominal the ratio between the amount of Fe^{3+} ions and estimated surface area of the core nanoparticles. However, with this method it is possible to synthesize the composite nanoparticles with maximum maghemite layer of 2 nm. With increasing the ration, the separate homogeneously-nucleated maghemite nanoparticles start to form.

In our work we try to increase the thickness of the maghemite layer with two-step coating method. After the first coating, the composite nanoparticles were re-dispersed in water and coated again with maghemite. The main problem of the second-step is the stability of the nanoparticles it suspension. Due to strong magnetic forces the composite nanoparticles tend to agglomerate. Agglomeration results in a decrease of the surface area available for the layer formation and could promote the formation of the separate, homogeneously-nucleated nanoparticles. The agglomeration was minimized with the addition of the PVP. Despite the minimization of the agglomeration, the product contains two types of nanoparticles: typical composite nanoparticles with maghemite layer deposited onto the surface of the HF core nanoparticle and homogeneously-nucleated maghemite nanoparticles. The thickness of the maghemite layer, after the second coating increased compared to the thickness of the layer obtained after the firs coating and it was estimated to be approximately 3.5 nm.

With the two-step approach it is possible to increase the thickness of the maghemite layer. However it is still needed to optimize for the second step coating to obtain the product containing only the typical composite nanoparticles.

Acknowledgments: The support of the Ministry of Higher Education, Science and Technology of the Republic Slovenia with National Research Program PR-05558 is gratefully acknowledged. The authors also acknowledge the use of equipment in the Centre of Excellence on Nanoscience and Nanotechnology – Nanocenter.

References:

- [1] Camarago, P.H.C., K.G. Satyanarayana, and F. Wypych; Nanocomposites: Synthesis, structure, properties and new application opportunities *Mater. Res.* **12**: p. 1-39 (2009).
- [2] Kneller, E.F. and R. Hawing; The exchange-spring magnet: A new material principle for permanent magnets. *IEEE Trans. Magn.* **27**: p. 3588-3600 (1991).
- [3] Sellmyer, D.J.; Strong magnets by self-assembly. *Nature.* **420**: p. 374-375 (2002).
- [4] Lee, J.-H., et al.; Exchange-coupled magnetic nanoparticles for efficient heat induction. *Nature Nanotech.* **6**: p. 418-422 (2011).
- [5] Primc, D. and D. Makovec; Composite nanoplatelets combining soft-magnetic iron oxide with hard-magnetic barium hexaferrite. *Nanoscale.* **7**: p. 2688-2697 (2015).
- [6] Nandwana, V., et al.; Bimagnetic nanoparticles with enhanced exchange coupling and energy products. *J. Appl. Phys.* **205**: p. 1-5 (2009).
- [7] Song, Q. and Z.J. Zhang; Controlled synthesis and magnetic properties of bimagnetic spinel ferrite CoFe_2O_4 and MnFe_2O_4 nanocrystals with core-shell architecture. *J. Am. Chem. Soc.* **134**: p. 10182-10190 (2012).
- [8] Meffre, A., et al.; A simple chemical route toward monodisperse iron carbide nanoparticles displaying tunable magnetic and unprecedented hyperthermia properties. *Nano Lett.* **12**: p. 4722-4728 (2012).
- [9] Primc, D., B. Belec, and D. Makovec; Synthesis of composite nanoparticles using coprecipitation of a magnetic iron-oxide shell onto core nanoparticles. *J. Nanopart. Res.* (18:64): p. 1-13 (2016).
- [10] Drogenik, M., et al.; The concept of a low-temperature synthesis for superparamagnetic $\text{BaFe}_{12}\text{O}_{19}$ particles. *J. Am. Chem. Soc.* **93**: p. 1602-1607 (2010).
- [11] Lisjak, D. and M. Drogenik; Chemical substitution - an alternative strategy for controlling the particle size of barium ferrite. *Cryst. Growth Des.* **12**: p. 5174-5179 (2012).
- [12] Lisjak, D., M. Bukovec, and K. Zupan; Suppression of the exaggerated growth of barium ferrite nanoparticles from solution using a partial substitution of Sc^{3+} for Fe^{3+} . *J. Nanopart. Res.* **18:44**: p. 1-22 (2016).
- [13] Primc, D., Heterogeneous nucleation of iron oxides ($\gamma\text{-Fe}_2\text{O}_3$) in colloidal systems, in "Jožef Stefan" Institute. 2013, "Jožef Stefan" Postgraduate School: Ljubljana.
- [14] Smit, J. and H.P.J. Wijn, *Ferrites: Physical properties of ferrimagnetic oxides in relation to their technical applications* (N.V. Philips, Eindhoven, 1959).
- [15] Jolivet, J.P., *Metal oxide chemistry and synthesis: From solutions to solid state* (John Wiley & Sons, Chichester, 1994).

For wider interest

Composite nanoparticles are composite materials, where one of their dimension is in nanometre range ($1 \text{ nm} = 10^{-9} \text{ m}$). Within the individual composite nanoparticle at least two different materials displaying different composition, crystal structures and properties are combined. Such nanoparticles have potential to exhibit novel physical and chemical properties.

Applications of magnetic materials are based on their response to a magnetic field. The response of the magnetic material to the external magnetic field can be described with hysteresis loop. According to the shape of the loop, the magnetic materials can be classified as magnetically hard or soft materials. The soft magnetic materials are those where relatively low external field is required for their saturation. Typically they exhibit strong saturation magnetization (M_S) and low coercive field (H_C). Contrary, the hard-magnetic materials display large H_C however low M_S . With coupling between properties of hard- and soft-magnetic materials in single composite nanoparticle, the shape of magnetic hysteresis can be tuned. The coupling means, that one property of the material can be tuned with influence on the other. The bi-magnetic nanoparticles usually exhibit core-shell (CS) structure, since it was found that coupling between different magnetic materials is stronger than in the other composite structures. The hysteresis loop of the bi-magnetic composite nanoparticles possessing CS structure, can also be tuned with the varying the thickness of the shell.

Generally for synthesis of CS nanoparticles, high temperature ($<200 \text{ }^\circ\text{C}$) and toxic, expansive chemicals are required. In our work used environmentally-friendly, inexpensive method based on the co-precipitation of the $\text{Fe}^{3+}/\text{Fe}^{2+}$ ions and heterogeneous nucleation of the soft-magnetic maghemite layer onto the hard-magnetic HF core nanoparticles in the aqueous suspension at $60 \text{ }^\circ\text{C}$.

The problem of the method is that we could synthesize the layer with maximum thickness of 2 nm. In our work we solve this with two-step coating method. Problem of the two step synthesis is preventing the agglomeration of the core nanoparticles which decrease of the surface area available for the layer formation.

With two-step coating it is possible to increase the thickness of the maghemite layer, although the synthesis has to be optimized, so that we could obtain the product containing only the composite nanoparticles.

The formation of silica coatings on barium hexaferrite nanoparticles and functionalization with 3-aminopropylsilane

Tanja Goršak^{1,2}, Slavko Kralj¹, Darko Makovec¹, Darja Lisjak¹

¹Department for Materials Synthesis, Jožef Stefan Institute, Ljubljana, Slovenia

²Jožef Stefan International Postgraduate School, Ljubljana, Slovenia

tanja.gorsak@ijs.si

Abstract. In our research we aim to tune the nanoparticles' surfaces for further conjugation with bio-molecules. Here we studied barium hexaferrite nanoparticles doped with Sc³⁺, which were synthesized using hydrothermal synthesis. The nanoparticles were coated with silica, using a modified Stöber process, with the addition of cetyl trimethylammonium bromide or citric acid, which were used to ensure stability of the suspension during the reaction. Silica coating provides reactive –Si-OH surface groups that can be used for further conjugation. We confirmed the reactivity of silanol groups by grafting the coated nanoparticles with 3-aminopropyltriethoxysilane.

Keywords: Hexaferrite, nanoparticles, citric acid, CTAB, silica, APS

1. Introduction

Magnetic nanoparticles have been widely studied because of their wide range of technological applications as: ferrofluids (in loud speakers), for magnetic recording media, in separation processes and catalysis[1]–[3]. Recently there has been an increasing interest for biomedical applications in therapy (targeted drug delivery and magnetic hyperthermia) and in diagnostics (in magnetic resonance imaging (MRI) and magnetic particle imaging (MPI))[4]–[7].

Barium ferrite, BaFe₁₂O₁₉, is a hexagonal ferrite (hexaferrite), which is distinguished from other ferrites by a large magnetocrystalline anisotropy, high intrinsic coercivity, relatively large magnetization, excellent chemical stability and corrosion resistivity [8]. For biomedical applications, the nanoparticles have to be conjugated with biomolecules. To enable conjugation of biomolecules, specific functional groups (amino, carboxyl, etc.) have to be introduced onto the nanoparticle surfaces. This

can be done with grafting organic molecules onto the surfaces in the process, usually referred to, as “functionalization”. The surface of barium hexaferrite nanoparticles is relatively inert. Surface reactivity of the particles is usually improved with a thin layer of amorphous silicon oxide – silica [9]. The rigid silica layer provides reactive silanol -Si-OH surface groups for strong covalent bonding of the molecules. Different alkoxy silane molecules, such as 3-aminopropyltriethoxysilane (APS) are usually used for functionalization of silica-coated nanoparticles [9], [10]. The layer of surface molecules should provide biocompatibility of the nanoparticles and their colloidal stability.

Different approaches can be used for coating nanoparticles with silica. The most frequently used procedure is a Stöber sol–gel process. The process is based on the hydrolysis and condensation of an alkoxy silane (tetraethyl orthosilicate - TEOS), in the presence of water and an appropriate catalyst [11].

During the whole coating process, the colloidal stability of nanoparticles in aqueous suspension has to be maintained to enable a homogeneous coating of a single particle. Stabilizing molecule can provide steric repulsive forces, electrostatic repulsive forces or both to aid the long-term stability. Different molecules have been used in water-based ferrofluids, including small molecules such as citric acid (CA), polymers including polyethyleneglycol (PEG), polysaccharides, such as dextran and its derivatives, and polypeptides, and surfactants, such as cetyl trimethylammonium bromide (CTAB) [12], [13]. CA has three carboxyl groups and one hydroxyl group. When adsorbed onto the nanoparticles surfaces it increases their surface charge and electrostatic repulsions in the suspension. On the other hand, CTAB is a surfactant, which provides electro-steric stabilization with its hydrocarbon tail and a polar head group [14].

In this research barium hexaferrite nanoparticles were coated with silica using a modified Stöber process. The addition of stabilizing agent CTAB or CA ensured stability of the aqueous suspension during the reaction. Homogeneously coated nanoparticles were subsequently grafted with APS.

2. Material and Methods

2.1 Materials

Barium, indium, scandium and iron nitrates, citric acid 99+%, tetra-ethylorthosilicate 99%, 3-aminopropyltriethoxysilane 99.5%, sodium hydroxide 98% and cetyl trimethylammonium bromide 98% were purchased from Alfa Aesar. Nitric acid 65 %, hydrochloric acid 37%, ethanol 99.5% and ammonium hydroxide 25% were purchased from Carlo Erba Reagents S.A.S. All the chemicals were used without any further purification. The precise metal concentration in the nitrates was determined using optical emission spectroscopy with inductively coupled plasma (Agilent 720).

2.2 Synthesis of barium hexaferrite nanoparticles

Barium hexaferrite nanoparticles doped with Sc^{3+} (BSc) were hydrothermally synthesized, as described previously [15], [16]. In short, nitrates with a molar ratio: Ba:Fe:Sc = 1:4.5:0.5, were dissolved in water and coprecipitated with NaOH. The slurry was transferred to an Inconel autoclave (Parr Instruments) and heated to 240 °C. The autoclave was then naturally cooled to room temperature. The as-synthesized particles were washed with HNO_3 , pH below 1 and water.

2.3 Coating of the nanoparticles with silica and grafting of APS

In a subsequent process, the as-synthesised nanoparticles were coated with a layer of silica. To maintain stable colloidal suspension during the coating procedure, CTAB or CA were used.

Coating of the nanoparticles stabilized with CTAB

Coating of barium hexaferrite nanoparticle in the presence of CTAB surfactant was performed in the following reaction mixture: 0.115 wt% BSc nanoparticles, 2.68 mM CTAB and 16.1 mM TEOS were dispersed in water/ethanol solution (volume ratio was 40/1). pH of the suspension was adjusted to 2.9 using 0.1 M HBr. After the addition of the TEOS, the pH value was increased twice. First, 1 h after the TEOS addition to pH 4.1, using 0.1 vol.% ammonia, and 3 h after the TEOS addition to pH 8.5, using 0.5 vol.% ammonia. The reaction mixture was then stirred overnight. Coated nanoparticles (BSc-CTAB-Si) were sedimented by centrifugation and redispersed in water. A fraction of BSc-CTAB-Si nanoparticles agglomerated during

the coating procedure and could not be re-dispersed to form a stable suspension, so only the stable part of the suspension was used for further grafting with APS.

0.1 wt% of BSc-CTAB-Si nanoparticles were dispersed in water/ethanol/ammonium hydroxide solution (volume ratio was 5/1/0.3) and 1.6 mM of APS (corresponding to approx. 20 mmol APS per m² of the nanoparticles surface) was added. The reaction mixture was then heated to 50 °C and stirred for 5 h. The nanoparticles grafted with APS (BSc-CTAB-APS) were washed with a diluted HCl solution at pH 4, to remove any unbound APS from the suspension.

Coating of the nanoparticles stabilized with CA

Coating of BSc nanoparticles, where CA was used as a stabilizing agent, was carried out using a modified procedure described before [9]. In short, to 80 ml of the dispersion of BSc, 0.5 wt%, an aqueous solution of 1.6 g of CA (0.5g/ml) was added. pH value was adjusted to pH 5.1 with 25% ammonium hydroxide. The suspension was then heated to 80 °C and vigorously stirred for 90 min and then cooled to room temperature, at that point the pH was increased to 10.1. The suspension was sedimented with a centrifugation to remove excess CA and redispersed in a diluted ammonia solution at pH 10.1. The as-prepared stable suspension of BSc-CA was used for the coating nanoparticles with silica. 0.05 wt% of the nanoparticles BSc-CA were dispersed in water/ethanol solution ((volume ratio was 1/4), and 7.46 mM TEOS was added. The coating reaction was catalysed by the addition of 1 vol.% of concentrated ammonium hydroxide. As in previous procedure the reaction mixture was stirred overnight. The produced silica coated nanoparticles (BSc-CA-Si) were sedimented and redispersed in water. Grafting with APS (BSc-CA-APS) was performed using the same procedure as described above. However, there was a different volume ratio of water/ethanol/ammonium hydroxide = 1/1/0.06 and 4.8 mM of APS (corresponding to approx. 60 mmol APS per m² of the nanoparticles surface) was used.

2.4 Characterization of the materials

The nanoparticles were characterized using transmission electron microscopy (TEM). For the analysis, the nanoparticles were deposited on a copper-grid-supported perforated electron-transparent carbon foil. The particle sizes were evaluated from the TEM images. The surfaces of the particles were determined with

Gatan Digital Micrograph Software, from surface their equivalent (circular) diameter was calculated. 150–200 particles per sample were accounted for statistics. The thicknesses of hexaferrite nanoparticles and of the silica coating was determined from the edge-on oriented nanoparticles, directly from the TEM images. The ζ -potential of the nanoparticles dispersed in water was monitored with electro-kinetic measurements (Brookhaven Instruments Corporation, ZetaPALS).

3. Results

3.1 Barium hexaferrite nanoparticles

Hydrothermally synthesised BSc consists of thin nanoplates (**Figure 1**). The average equivalent (circular) diameter of nanoplates, was 43 ± 15 nm. The thickness of nanoplates was between 4 and 8 nm.

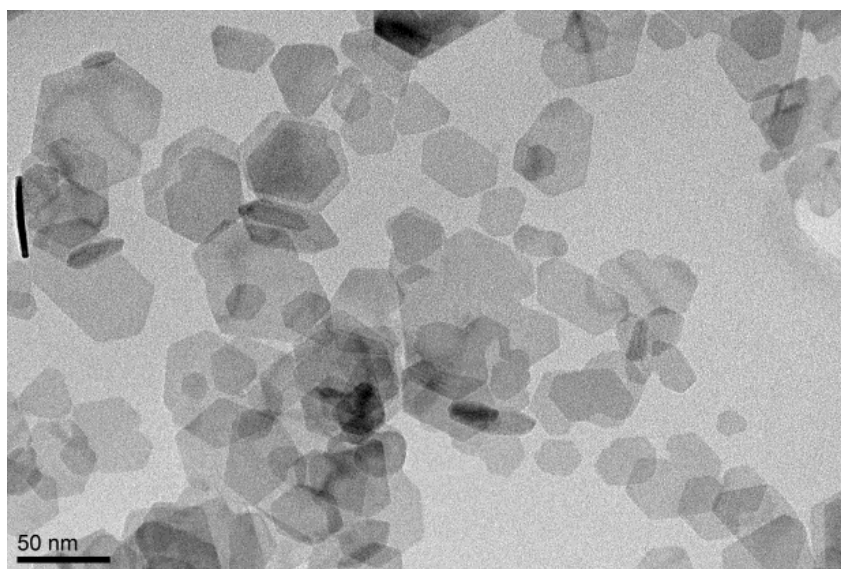


Figure 1: Representative TEM image of BSc nanoparticles

3.2 Coating of the nanoparticles stabilized with CTAB

For a successful coating of nanoparticles with silica the colloidal stability of the suspension has to be assured. As first, a surfactant CTAB was used. As mentioned above, a fraction of BSc-CTAB-Si nanoparticles agglomerated during the coating procedure and could not be re-dispersed to form a stable suspension. The fraction of BSc-CTAB-Si, that formed a stable suspension, and the aggregated fraction were analysed separately.

Figure 2a shows TEM image of BSc-CTAB-Si nanoparticles (that formed a stable suspension). The silica coating is 7-8 nm thick and rough. The aqueous suspension of BSc-CTAB-Si does not show any signs of a spontaneous sedimentation at a neutral pH for the duration of one month. TEM image of agglomerated BSc-CTAB-Si nanoparticles (**Figure 2b**) reveals a formation of self-assembled ring like structures. Nanoparticles within agglomerates are coated with a layer of silica. The reasons for such ring-like agglomeration can, in part, be explained from magnetic properties of BSc. Namely, these nanoparticles are ferrimagnetic and the magnetic interaction between them plays an important role, even in the absence of an external magnetic field. Due to the relatively large saturation magnetization ($32.1 \text{ Am}^2/\text{kg}$ [16]) and nanoparticles sizes a strong magnetic dipol-dipol attractions are present between nanoparticles. As a result, the particles in the suspensions magnetically interact with each other. The BSc plates tend to form agglomerates, with connected basal planes since their magnetic moments are perpendicular to the basal planes [17]. The formation of ring like agglomerates could be a result of the minimisation of magnetostatic energy. The lowest energy state for a magnetic ring is the so called vortex state that happens in zero magnetic field. In such a state magnetic moments chase one another in a circle, resulting in a zero magnetostatic energy [18][19]. However, no such agglomerates were ever observed in any other system [8], [15]–[17], [20]. Therefore, the origin of the formation of circular agglomerates (**Figure 2b**) must be a complex interplay of interparticle forces (magnetic and electro-steric), forces between CTAB and particles, between CTAB-CTAB on particles surfaces and CTAB-solvent forces.

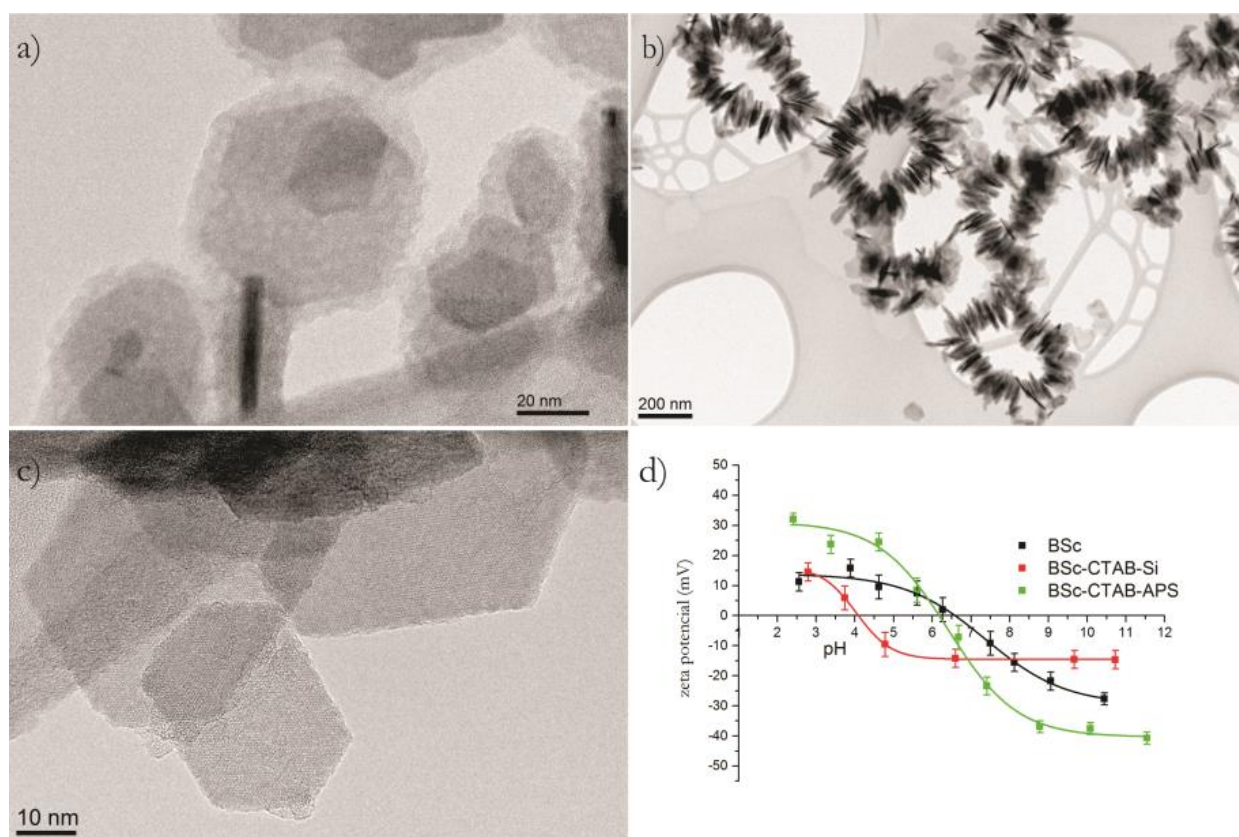


Figure 2: Representative TEM images of a) silica coated BSc (BSc-CTAB-Si), b) aggregated BSc-CTAB-Si, c) BSc-CTAB-Si after an attempt to graft them with APS (BSc-CTAB-APS) and d) ζ -potential behaviour of BSc nanoparticle in aqueous suspension

Figure 2c shows a TEM image of BSc particles after an attempt of grafting the silica-coated nanoparticles (BSc-CTAB-Si) with APS. It reveals that there is no silica layer on the surface of nanoparticles.

The effect, of silica coating and grafting with APS, on the ζ -potential charge of BSc particles was monitored with electro-kinetic measurements (**Figure 2d**). The graph shows a change of the ζ -potential of the as-synthesised BSc particles from positive (10 to 15 mV) values at acidic pH, to negative values (-20 to -30 mV) at alkaline pH, and with an iso-electric point (IEP) at a neutral pH. When the surface of the nanoparticles was coated with a layer of silica (BSc-CTAB-Si), their IEP shifted to a pH of around 4.1. The ζ -potential of BSc-CTAB-Si nanoparticles above neutral pH was around -15 mV. The pH of IEP is relatively high (around 4), considering that silica structure is terminated with negatively charged Si-OH groups. The relatively low absolute ζ -potential and high IEP can be explained by the presence of residual cationic surfactant CTAB that partially neutralises the surface charge.

The ζ -potential of BSc-CTAB-APS nanoparticles changes from positive values (20 to 30 mV) at acidic pH, to negative values (-35 to -40 mV) at alkaline pH, with an IEP at a neutral pH. The surface amino groups, introduced by grafting with APS should define ζ -potential of BSc-CTAB-APS and move the IEP to higher pH values than observed in **Figure 2d**. If we also consider the degradation of the silica coating (**Figure 2c**), it is reasonable that the ζ -potential behaviour is similar to as-synthesized nanoparticles BSc.

In the following explanation we suggest a possible mechanism of the formation of silica coating. The amount of added CTAB in the reaction was above the critical micelle concentration - CMC (CMC \sim 1 mM). At a given acidic pH, CTAB forms positively charged micelles with a diameter of around 3 nm [14]. The micelles repel the positively charged BSc nanoparticles and, with that, enhance the colloidal stability of the suspension. Negatively charged silanol groups of alkoxy-hydrolytes are attracted to the positively charged CTAB micelles. Therefore the added TEOS most likely condenses around micelles forming small silica nanoparticles [21].

With the precise adjustment of pH to slightly alkaline conditions the rate of the silica formation is slow. The low reaction rate promotes a deposition of small silica nanoparticles on the surface of BSc nanoparticles [22]. Such mechanism would explain the appearance of the rough silica layer (**Figure 2a**). The degradation of the silica layer from BSc-CTAB-APS (**Figure 2c**) could also be explained with the presence of CTAB, if it is assumed that CTAB was adsorbed on the surface of BSc and small silica nanoparticles. This should prevent direct bonding – condensation of silica nanoparticles with each other and BSc surface. Instead the attachment could be caused by adsorbed CTAB on neighbouring particles forming a bilayer. Since the bilayer is formed with hydrophobic tails of CTAB (hydrophobic bond) it is relatively stable. But the reaction conditions of APS grafting (long exposure to elevated temperature, ethanol and pH above 10) could destabilize the bilayer and with that would induce the degradation of the thin silica layer. However, to confirm or reject the proposed mechanism of the formation and degradation of silica, further research is needed.

3.3 Coating of the nanoparticles stabilized with CA

In the following experiments CTAB was replaced by CA. The effect, of the adsorption of CA, formation of silica coating and grafting with APS was monitored

with electro-kinetic measurements (**Figure 3a**). The ζ -potential behaviour of as-synthesized BSc nanoparticles varies from positive values at acidic pH, and decreasing to negative values at alkaline pH, and with an IEP at a neutral pH. The adsorption of CA on the nanoparticles (BSc-CA) shifts IEP to around 2.2. This is a consequence of the dissociation of CA carboxyl groups, which in turn induces electrostatic stabilization of the nanoparticles.

When the surface of the nanoparticles was coated with a layer of silica (BSn-CA-Si), the IEP increased slightly to a pH of around 3, because the Si-OH groups have smaller charge than carboxyl groups. The grafting of APS influenced the ζ -potential of the BSc-CA-APS nanoparticles, which varied from positive (20 to 30 mV) values at an acidic pH, to negative values (-35 to -40 mV) at an alkaline pH, having an IEP at a slightly alkaline pH. According to literature [10] the IEP was expected at higher pH values. It is possible that some of the negative silanol groups remain exposed at the surface and they lower the IEP of the BSc-CA-APS nanoparticles. This suggests that the grafting of APS was not optimal and that the reaction conditions have to be optimized.

Nevertheless, a TEM image of the BSc-CA-APS (**Figure 3b**) shows that silica layer remained attached to the particle after the grafting with APS, as oppose to the BSc-CTAB-APS. The layer of silica is 6-7 nm thick and remains unchanged after the grafting with APS.

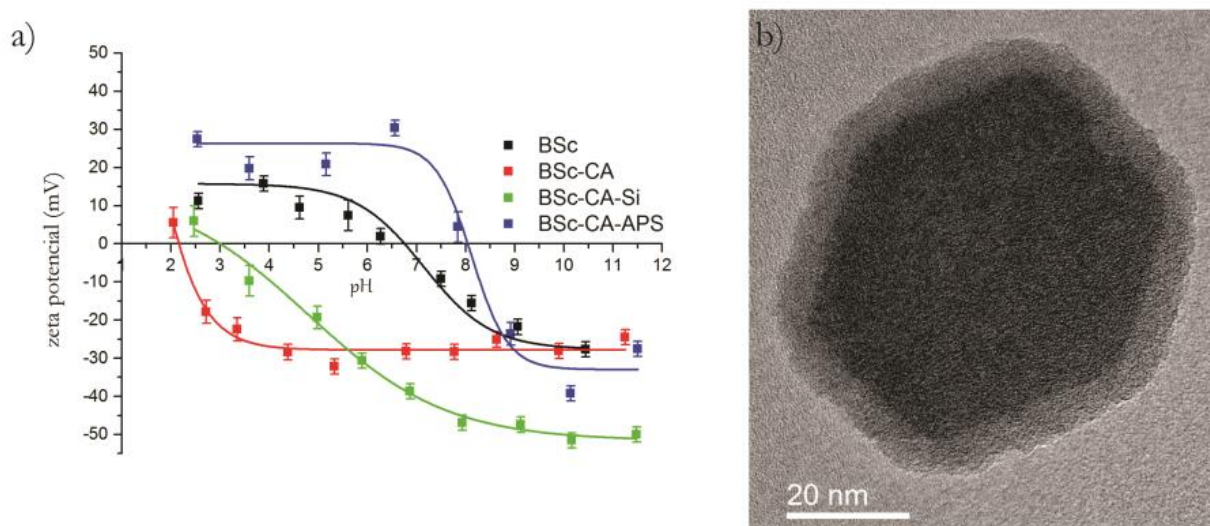


Figure 3: ζ -potential behaviour of the BSc nanoparticle in aqueous suspension, b) a TEM image of BSc nanoparticle after grafting with APS (BSc-CA-APS)

4. Conclusions

The coating of BSc nanoparticles with silica was performed with the use of two different stabilizing agent CTAB and CA. However, during the grafting with APS, the silica formed in the presence of CTAB degraded. We successfully coated BSc with a layer of silica, when CA was used as a stabilizing agent, and subsequently graphed with APS. However, the APS graphing will be optimized in the future to improve surface properties of the nanoparticles.

Acknowledgments

The support of the Ministry of Higher Education, Science and Technology of the Republic of Slovenia within the National Research Program is gratefully acknowledged.

References:

- [1] A. Akbarzadeh, M. Samiei, and S. Davaran, "Magnetic nanoparticles: preparation, physical properties, and applications in biomedicine.," *Nanoscale Res Lett*, vol. 7, no. 1, p. 144, 2012.
- [2] S. Hasany, A. Rehman, R. Jose, and I. Ahmed, "Iron oxide magnetic nanoparticles: A short review," in *International Conference on Nanotechnology - Research and Commercialization 2011:(ICONT 2011)*, vol. 1502, no. 1, pp. 298–321, 2012.
- [3] E. Blums, A. Cebers, and M. M. Maiorov, *Magnetic fluids*. Walter de Gruyter, Berlin, New York, pp 1-10, 1997.
- [4] W. Andrä, U. Häfeli, R. Hergt, and R. Misri, "Application of magnetic particles in medicine and biology," *Handbook of Magnetism and Advanced Magnetic Materials*, Wiley, Published on line, 2007.
- [5] Q. A. Pankhurst, J. Connolly, S. Jones, and J. Dobson, "Applications of magnetic nanoparticles in biomedicine," *Journal of physics D: Applied physics*, vol. 36, no. 13, p. 167, 2003.
- [6] C. W. Jung, "Surface properties of superparamagnetic iron oxide MR contrast agents: ferumoxides, ferumoxtran, ferumoxsil," *Magn Reson Imaging*, vol. 13, no. 5, pp. 675–691, 1995.
- [7] A. K. Gupta and M. Gupta, "Synthesis and surface engineering of iron oxide nanoparticles for biomedical applications," *Biomaterials*, vol. 26, no. 18, pp. 3995–4021, 2005.
- [8] M. Drogenik, I. Ban, D. Makovec, A. Žnidaršič, Z. Jagličič, D. Hanžel, and D. Lisjak, "The hydrothermal synthesis of super-paramagnetic barium hexaferrite particles," *Materials Chemistry and Physics*, vol. 127, no. 3, pp. 415–419, 2011.
- [9] S. Kralj, D. Makovec, S. Čampelj, and M. Drogenik, "Producing ultra-thin silica coatings on iron-oxide nanoparticles to improve their surface reactivity," *Journal of Magnetism and Magnetic Materials*, vol. 322, no. 13, pp. 1847–1853, 2010.
- [10] S. Čampelj, D. Makovec, and M. Drogenik, "Functionalization of magnetic nanoparticles with 3-aminopropyl silane," *Journal of Magnetism and Magnetic Materials*, vol. 321, no. 10, pp. 1346–1350, 2009.

- [11] W. Stöber, A. Fink, and E. Bohn, "Controlled growth of monodisperse silica spheres in the micron size range," *Journal of colloid and interface science*, vol. 26, no. 1, pp. 62–69, 1968.
- [12] D. Makovec, S. Gyergyek, D. Primc, and I. Plantan, "The formation of magnetic carboxymethyl-dextrane-coated iron-oxide nanoparticles using precipitation from an aqueous solution," *Materials Chemistry and Physics*, vol. 153, pp. 376–383, 2015.
- [13] S. Campelj, D. Makovec, and M. Drogenik, "Preparation and properties of water-based magnetic fluids," *Journal of Physics: Condensed Matter*, vol. 20, no. 20, p. 204101, 2008.
- [14] V. Patel, N. Dharaiya, D. Ray, V. K. Aswal, and P. Bahadur, "pH controlled size/shape in CTAB micelles with solubilized polar additives: a viscometry, scattering and spectral evaluation," *Colloids and Surfaces A: Physicochemical and Engineering Aspects*, vol. 455, pp. 67–75, 2014.
- [15] M. Drogenik, M. Kristl, A. Znidarsic, D. Hanzel, D. Lisjak, and others, "Hydrothermal synthesis of Ba-hexaferrite nanoparticles," *Journal of the American Ceramic Society*, vol. 90, no. 7, pp. 2057–2061, 2007.
- [16] D. Lisjak and M. Drogenik, "Chemical Substitution - An Alternative Strategy for Controlling the Particle Size of Barium Ferrite," *Crystal Growth & Design*, vol. 12, no. 11, pp. 5174–5179, 2012.
- [17] S. Ovtar, D. Lisjak, and M. Drogenik, "Barium hexaferrite suspensions for electrophoretic deposition.," *J Colloid Interface Sci*, vol. 337, no. 2, pp. 456–463, 2009.
- [18] C. Pappas, "Magnetic Properties of Rings of Magnetic Dots," 2007.
- [19] C. A. Vaz, T. Hayward, J. Llandro, F. Schackert, D. Morecroft, J. A. C. Bland, M. Kläui, M. Laufenberg, D. Backes, U. Rüdiger, "Ferromagnetic nanorings," *Journal of Physics: Condensed Matter*, vol. 19, no. 25, p. 255207, 2007.
- [20] K. Ma, U. Werner-Zwanziger, J. Zwanziger, and U. Wiesner, "Controlling growth of ultrasmall sub-10 nm fluorescent mesoporous silica nanoparticles," *Chemistry of Materials*, vol. 25, no. 5, pp. 677–691, 2013.
- [21] R. K. Iler, "The chemistry of silica: solubility, polymerization, colloid and surface properties, and biochemistry," Wiley, 1979.

For wider interest

Magnetic nanoparticles (MNP) have been widely studied because of their wide range of applications: magnetic liquids – ferrofluids (e.g., in car brakes and speakers as vibration dampers), MNP are being used in computer science for storage and recording media. MNP have a potential in (environmental) cleaning and separation processes, for example, in ocean oil spillage MNP with modified surface can be dispersed in oil and then used to remove oil from ocean surface magnetically. Recently there has been an increasing interest for biomedical applications of MNP: in therapy for targeted drug delivery and hyperthermia and in diagnostics for magnetic resonance imaging (MRI) and magnetic particle imaging (MPI).

Our work is focused on the functionalization of MNP for biomedical applications. For such application materials have to express specific surface and magnetic properties, suitable size distribution of nanoparticles, and biocompatibility.

The magnetic properties are controlled by the choice of material. Barium hexaferrites is distinguished from other ferrites by high intrinsic coercivity and good chemical stability. Size distribution can be controlled by appropriate synthesis route such as hydrothermal synthesis, a reaction in hot water under high pressure.

The surface properties of nanoparticles are tuned with organic/inorganic coatings (e.g., thin layer of amorphous silica). The coating prevents the agglomeration of nanoparticles and further enables easier preparation of their dispersion in various liquids. For biomedical applications, biomolecules (e.g., polysaccharides like dextran) have to be attached - conjugated on the nanoparticles. To enable conjugation of biomolecules, first specific functional groups (amino, carboxyl, etc.) have to be introduced onto the nanoparticle surfaces. This can be done with grafting organic molecules (such as 3-aminopropyltriethoxysilane) onto the nanoparticles surfaces in the process usually referred to as “functionalization”. In our work the surface of barium hexaferrites nanoparticles was modified by coating with silica. Silica introduced reactive silanol groups, -Si-OH on the surface which were then be used in functionalisation reaction with 3-aminopropyltriethoxysilane, so that amino groups are now on the surface of the nanoparticles. In the future amino groups will be conjugated with biomolecules.

Influence of concentration and size of Al₂O₃ particles on their distribution in reinforced austenitic stainless steel.

Ana Kračun^{1,2}, Franc Tehovnik¹, Fevzi Kafexhiu¹, Bojan Podgornik¹

¹ Institute of Metals and Technology, Ljubljana, Slovenia

² Jožef Stefan International Postgraduate School, Ljubljana, Slovenia

ana.kracun@imt.si

Abstract. The purpose of this investigation was to study the influence of Al₂O₃ particles concentration and size on their distribution in reinforced austenite stainless steel. In the frame of this work steels dispersed with Al₂O₃ particles were produced by conventional casting method and their microstructure investigated with light microscopy (LM), scanning electron microscopy (SEM) and auger electron spectroscopy (AES) techniques. Microstructural analysis shows that the distribution of Al₂O₃ particles is non-uniform and has a high degree of agglomeration. Particle distribution shows that when mass fraction of Al₂O₃ is 0,5 or 1,0 wt% the distribution of particles is homogenous in all three sampling areas of the cast ingot. However, when the mass fraction of Al₂O₃ increases to 2,5 wt% the distribution of particles becomes less homogenous, especially for larger particles size.

Keywords: particle distribution, microscopic characterization, steel matrix

1 Introduction

Insertion of ceramic reinforcements into metal matrices to produce composite materials with improved properties has been a subject of intensive research during the past three decades [1-3]. Ceramic particulates such as borides, carbides, oxides and nitrides are added to metal matrix composites (MMCs) to improve their elastic modulus, wear resistance, creep and strength [4-5].

The ductility of the MMCs however, deteriorates at high ceramic particle concentrations [5]. The metal matrix nanocomposites (MMnCs) are a type of nanocomposite in which nanoparticles, such as ceramic nanoparticles, are added to a

metal matrix [6]. These nanoparticle reinforcements can significantly increase the mechanical strength of the metal matrix, as they promote particle hardening more effectively than micro particles. Moreover, MMnCs improve performance significantly at elevated temperatures because the ceramic nanoparticles can maintain their properties at high temperatures [6].

Steel matrix composites commonly have a combination of hard ceramic (e.g. TiC, TiB₂, WC and Al₂O₃) reinforcements and ductile metallic matrix, which makes them promising candidates for high strength and wear resistance applications. There are several methods for fabricating particulate reinforced steel matrix composites, such as powder metallurgy, conventional melting and casting, reactive sintering and self-propagating high-temperature synthesis (SHS). The casting process is simple and more economical than the other available routes for integrating nanoparticles into the microstructure of steel. However, it is extremely difficult to obtain a uniform dispersion of ceramic nanoparticles in liquid metals due to the poor wettability and to the difference in specific gravity between the ceramic particles and metal matrix [7].

The microstructure of metals is generally characterized by advanced microscopic techniques (e.g. LM, SEM and TEM) which probe and map the surface and sub-surface structure of a material. These techniques can use photons, electrons, ions or physical cantilever probes to gather data about a sample's structure on a wide range of length scales [8]. Auger electron spectroscopy (AES) also provides quantitative elemental and chemical state information from surfaces of solid materials [9].

The current work aims at contributing to the knowledge and understanding of the conventional casting route for particle inoculation in a steel matrix. This production route seems to show potential and offers more cost efficiency in achieving the dispersion of second phase particles compared to the powder and metallurgical techniques used until now. The aim of the work was therefore to study the influence of Al₂O₃ particles on the microstructure of a steel matrix using a conventional casting method. The additional aim is to determine the influence of Al₂O₃ particles concentration and size on the distribution of Al₂O₃ particles in reinforced austenite stainless steel.

2 Material and Methods

2.1. Material

Austenitic stainless steel has been used for the work, mainly due to distinctive two phase microstructure of austenite and ferrite. The chemical composition of this alloy was measured and is given in Table 1. These steels are the most used group of stainless steels. The steels are paramagnetic, have a face-centred cubic lattice and excel with a good combination of hot and cold workability, mechanical properties and corrosion resistance.

Table 1: Chemical composition of austenitic stainless steel in mass fractions (wt.%).

Alloying element	C	Mn	Cr	Ni	Cu	Mo	V	Si
wt %	0,02	1,24	17,4	10,1	0,36	1,29	0,08	0,33

As reinforcement particles commercial ultrafine Al_2O_3 powder with a mean particle size of 500 nm and 50 nm has been used, respectively. The Al_2O_3 particles were selected due to their high chemical stability to Fe and high-specific gravity, respectively. Particularly, it was reported that the wetting angle Θ between Al_2O_3 and molten iron alloy is less than 50° even at high temperatures and in many different types of atmospheres [10].

2.2. Specimens preparation

A weighted quantity (14 kg) of austenitic stainless steel was melted in the induction furnace. We prepared six different experiments in which we used two different particle sizes (500 nm and 50 nm) and three different concentrations (0,5 wt%, 1,0 wt% and 2,5 wt%) of Al_2O_3 . Al_2O_3 particles were wrapped into the aluminium foil and put into the mould and the molten metal was poured over it into the same mould. The aluminium foil melts and dissolves in the metal.

2.3. Characterization

The microstructural changes and the dispersion of the ceramic particles in the steel matrix were observed and analysed by light microscopy (LM), scanning electron microscopy (SEM) and auger electron spectroscopy (AES) techniques. Samples for

microstructure analysis were taken from the bottom, middle and top portion of the cast piece, as shown in Figure 1. Metallographic samples were prepared by grinding, polishing, followed by ionic etching and analysed to reveal the particles distribution. Samples for Auger electron spectroscopy were prepared by grinding and polishing the surface. Prepared samples were attached to the bracket, placed in an experimental container-airlock, pumped to UHV and transferred into analytical container. The surface of the sample was ion etched and analysed to determine the elemental composition in the surface region of a sample.

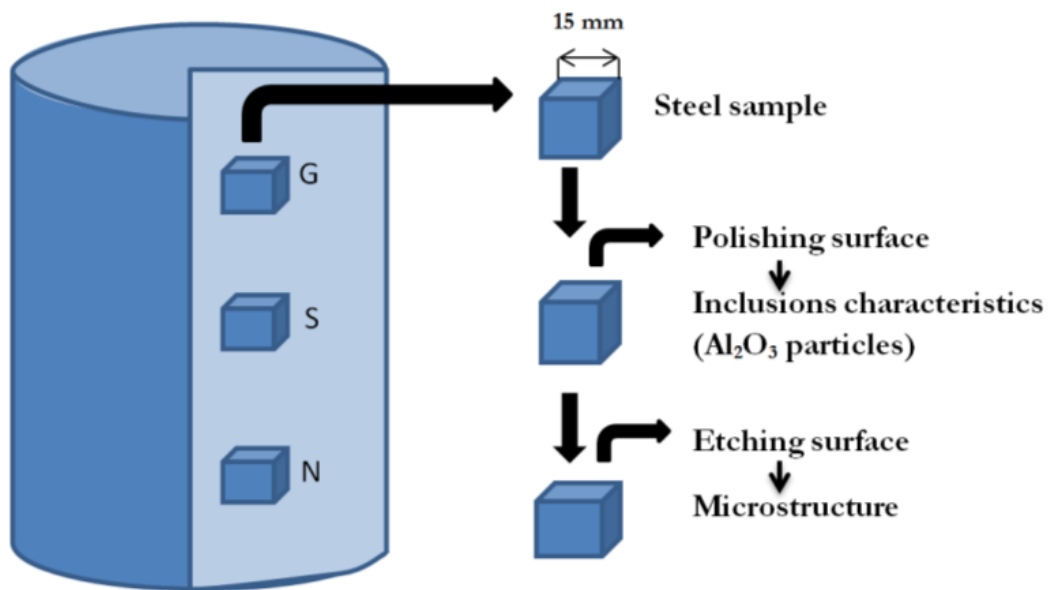


Figure 1: Schematic diagram of subtraction and preparation of metallographic steel samples.

To analyze the particles distribution, we took several photos of samples taken from the bottom (N), middle (S) and top (G) portion of the cast piece with scanning electron microscope. Then ImageJ commercial software was used to calculate and determine the particles distribution.

3 Results

Figure 2 shows a LM micrograph of the microstructure of pure austenitic stainless steel with a distinctive two-phase microstructure of austenite and δ -ferrites obtained. LM micrograph of the microstructure and particles distribution of the sample produced by casting process of the austenitic stainless steel poured over the Al₂O₃ ultrafine particles (500 nm, 0,1% wt) is shown in Figure 3.

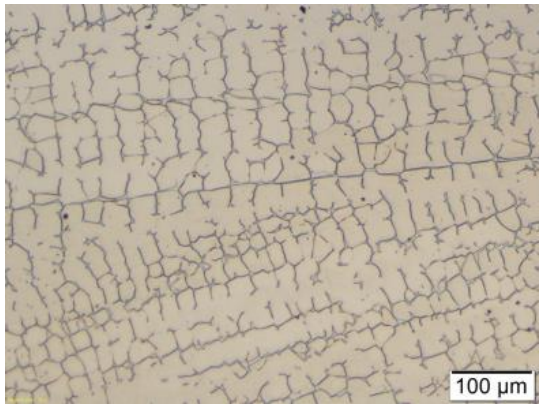


Figure 2: Cast microstructure of austenitic stainless steel with 6% of δ -ferrite.

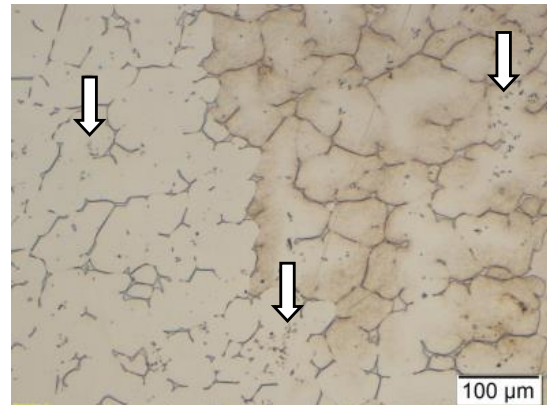


Figure 3: Cast microstructure of austenitic stainless steel with 6% of δ -ferrite and Al_2O_3 ultrafine particles (white arrows).

As shown in Figure 3, microstructure of austenitic stainless steel is modified after the addition of Al_2O_3 particles, being incorporated in the metal matrix. However, distribution of Al_2O_3 particles (white arrows in Figure 3) is non-homogeneous and concentrated to certain area.

From the SEM elemental analysis, shown in the Figure 4 it was confirmed that the bright, small spot-like features represent the Al_2O_3 particles that are non-uniformly distributed in the steel matrix.

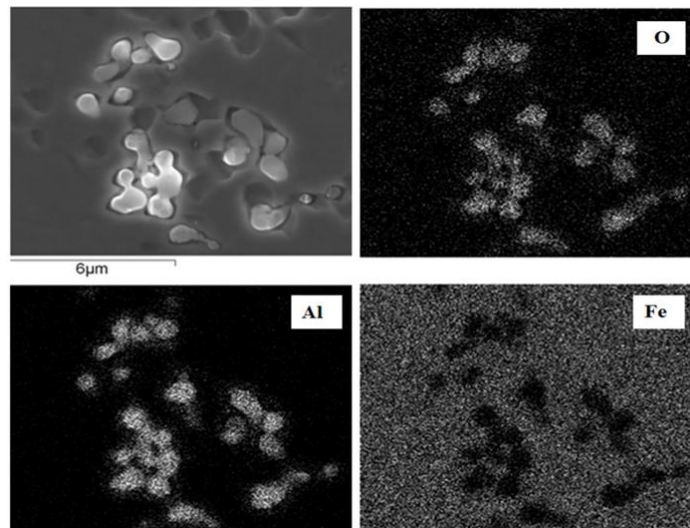


Figure 4: SEM elemental analysis of Al_2O_3 particles in the cast microstructure of austenitic stainless steel.

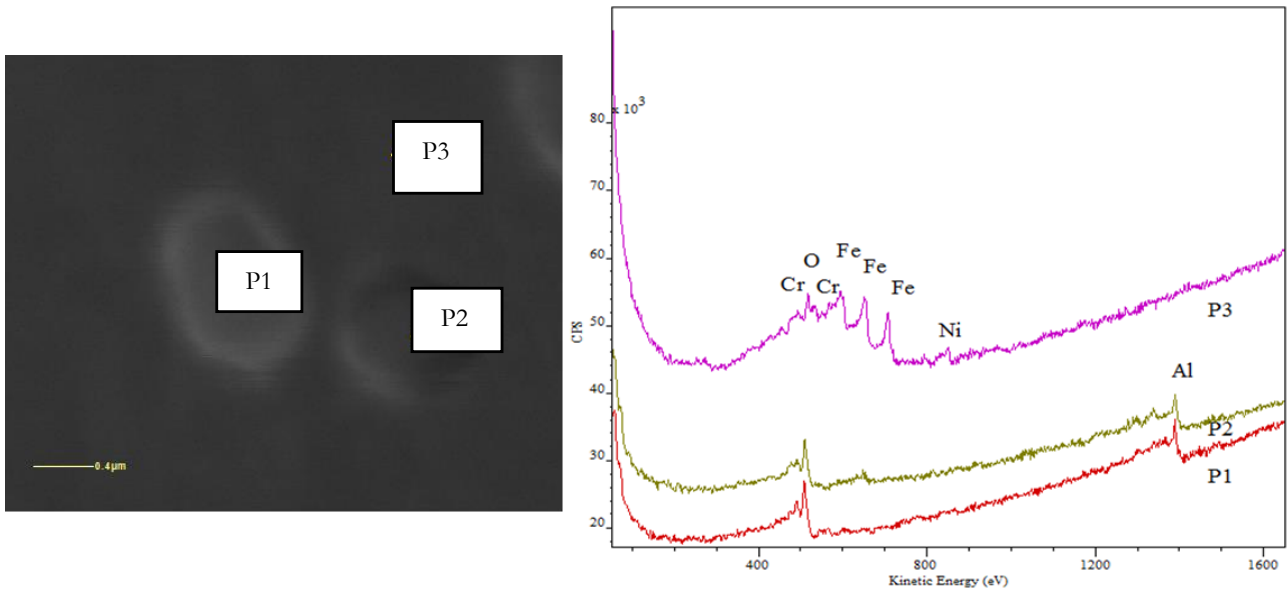


Figure 5: AES spectrum of Al_2O_3 particles in the cast microstructure of austenitic stainless steel.

In the Figure 5 the AES spectrum of the Al_2O_3 particles in the cast microstructure of austenitic stainless steel is shown. Spectres of particles (P1 and P2) showing only O and Al peaks confirm successful introduction of Al_2O_3 particles in the steel matrix (P3) without any intermetallic reaction taking place, which is true for all Al_2O_3 particles size and concentration used.

In the Figure 6, 7, 8 the statistical analysis of particles distribution data from the ImageJ program is shown. The particle distribution of Al_2O_3 particles with a mean particle size of 500 nm is shown in the Figure 6. It can be seen that when mass fraction of Al_2O_3 particles is 0,5 or 1,0 wt% the distribution of particles is homogenous in all three sampling areas of the cast piece; from the top to the bottom of the cast ingot. When the mass fraction of Al_2O_3 increases to 2,5 wt% the distribution of particles becomes less homogenous, with their concentration reducing toward the bottom of the ingot.

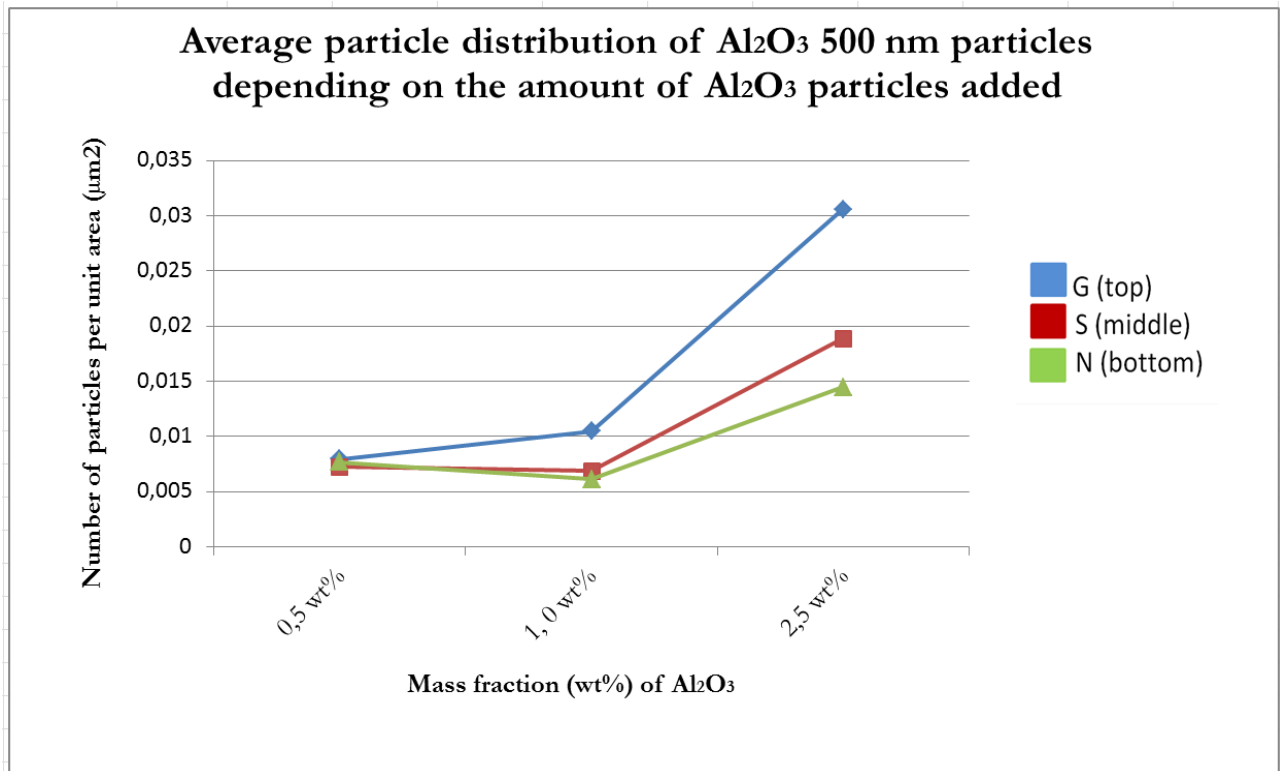


Figure 6: Average particle distribution of Al₂O₃ 500 nm particles depending on the amount of Al₂O₃ particles added.

Figure 7 shows the particle distribution of Al₂O₃ particles with a mean particle size of 50 nm. Similarly to 500nm particles size, the particles distribution is homogenous in all three sampling areas of the cast piece when Al₂O₃ particles mass fraction is 0,5 or 1,0 wt%. However, when a mass fraction of particles has increased to 2,5 wt% the distribution of particles becomes less homogenous, but without any definite distribution orientation, as shown in Figure 7.

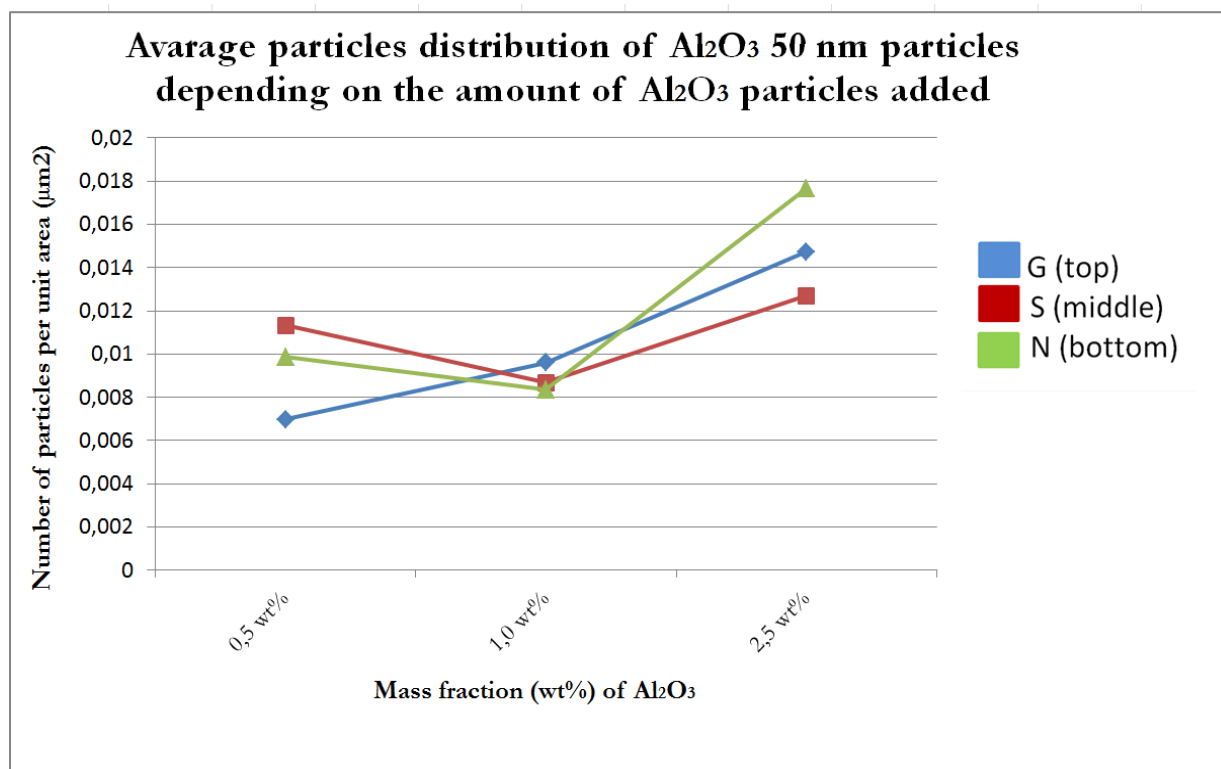


Figure 7: Average particle distribution of Al₂O₃ 50 nm particles depending on the amount of Al₂O₃ particles added.

The overall influence of different concentrations and sizes of Al₂O₃ particles on distribution is shown in the Figure 8. The particle distribution diagram in Figure 8 shows that mass fraction 0,5 to 1,0 wt% of Al₂O₃ with a mean particle size of 500 nm or 50 nm, results in relatively homogeneous distribution of Al₂O₃ particles. However, as the mass fraction has increased to 2,5 wt% the particle concentration ratio starts to decrease toward the bottom of the cast ingot. Furthermore, for low particle concentrations of 0,5 and 1,0 wt% distribution of Al₂O₃ particles in the cast ingot was found more or less independent on the position, concentration and size of particles, resulting in about 0,01 particle/µm². As the particle mass fraction has increased to 2,5 wt%, their concentration in cast ingot increased for up to 3 times, with the size of particles starting to play a role. Larger the particles more particles are found in the cast ingot.

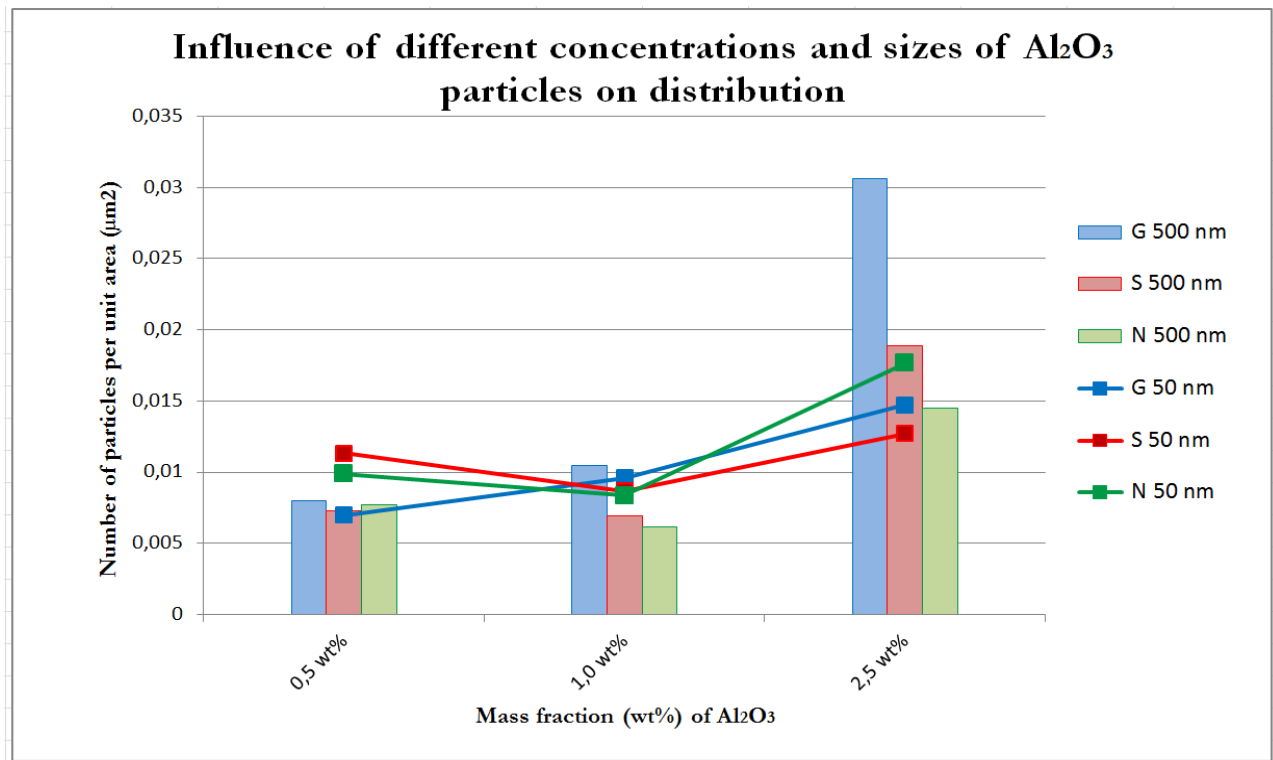


Figure 8: Influence of different concentrations and size of Al₂O₃ particles on their distribution in the cast ingot.

4 Conclusions

The steel matrix composite with non-uniformly dispersed Al₂O₃ particles were produced by conventional melting and casting method. The purpose of this investigation was to study the influence of Al₂O₃ particles, their size and concentration on the microstructure of a steel matrix using a conventional casting method.

Based on the experimental results the dispersion of the Al₂O₃ particles in the steel matrix is non-homogeneous and concentrated in certain areas. With the EDS and AES analysis it was confirmed that the bright, small spot-like features represent the Al₂O₃ particles, without any clear indication of intermetallic reactions between the particles and the steel matrix. The results of the particle distribution analysis show that at the mass fraction 0,5 to 1,0 wt% of Al₂O₃ with a mean particle size of 500 nm and 50 nm, the distribution of particles is relatively homogeneous throughout the cast ingot with a very small deviations. However, when the mass fraction has increased to 2,5 wt% the concentration ratio of particles distribution decreases toward the bottom of the cast ingot. In this case also the size of particles starts to play a role, leading to an increased degree of incorporating particles in the steel matrix.

References:

- [1] Y.Q. Liu, H.T. Cong, W. Wang, C.H. Sun, H.M. Cheng. AlN nanoparticle-reinforced nanocrystalline Al matrix composites: Fabrication and mechanical properties. *Met.Sic.Eng.A*, 505: 151-156, 2009.
- [2] C.S. Goh, J. Wei, L.C. Lee, M. Gupta. Ductility improvement and fatigue studies in Mg-CNT nanocomposites. *Compos. Sci. Tech.*68: 1432-1439, 2008.
- [3] Z. Razavi Hesabi, A. Simchi, S.M. Seyed Reihani. Structural evolution during mechanical milling of nanometric and micrometric Al₂O₃ reinforced Al matrix composites. *Mater. Sci. Eng. A*, 428: 159-168, 2006.
- [4] J.Llorca. Fatigue of particle-and whisker reinforced metal-matrix composites. *Prog Mater Sci.* , 47: 283-353, 2002.
- [5] BN.Chawla, Y. Shen. Mechanical Behavior of Particle Reinforced Metal Matrix Composites **. *Adv Eng Mater.*, 3(6):357-370, 2001.
- [6] R. Casati , M. Vedani. Metal Matrix Composites Reinforced by Nano-Particles—A Review. *Metals (Basel)*, 4(1):65-83, 2014.
- [7] S.H. Lee, J.J. Park, S.M. Hong, B.S. Han, M.K. Lee, C.K. Rhee. Fabrication of cast carbon steel with ultrafine TiC particles. *Trans Nonferrous Met Soc China (English Ed.)*, 21:54-57, 2011.
- [8] R. Konwar, A.B. Ahmed. Nanoparticle: an Overview of Preparation, Characterization and Application. *Int Res J Pharm.*, 4(4):47-57, 2013.
- [9] C. Linsmeier. Auger electron spectroscopy. *Vacuum*, 45(6-7):673-690, 1994.
- [10] S-Y.Cho, J-H. Lee. Anisotropy of wetting of molten Fe on Al₂O₃ single crystal. *Korean J Mater Res.*, 18(1):18-21, 2008.

For wider interest

It is well established that the steel matrix composites commonly have a good combination of hard ceramic reinforcement particles (e.g. TiC, TiB₂, WC and Al₂O₃) and ductile metallic matrix, which make them a promising candidate in wear resistance applications. Generally, there are several methods for fabricating the particulate reinforced steel matrix composites, such as powder metallurgy, conventional melting and casting, reactive sintering and self-propagating high-temperature synthesis. The casting process is more economical than the other available routes for integration of nanoparticles into microstructure of steel. However, it is extremely difficult to obtain uniform dispersion of ceramic nanoparticles in liquid metals due to the poor wettability and the specific gravity difference between the ceramic particles and metal matrix. Furthermore, low concentrations and only few nanometers size limit the possibility of identifying presence, distribution and effect of ceramic nanoparticles in the steel matrix.

The aim of the present work is to identify the distribution of particles in the steel matrix introduced through conventional melting and casting method, and above all to determine the influence of different concentrations and sizes of Al₂O₃ particles on the distribution of Al₂O₃ in reinforced austenite stainless steel. In the frame of this work the steels dispersed with Al₂O₃ particles were produced by conventional casting method and their microstructure investigated by light microscopy (LM), scanning electron microscopy (SEM) and auger electron spectroscopy (AES) techniques. To calculate and determine the particle distribution we used ImageJ. Based on the experimental results the dispersion of the Al₂O₃ particles in the steel matrix is non-homogeneous and concentrated in certain areas. With the EDS and AES analysis it was confirmed that the bright, small spot-like features represent the Al₂O₃ particles without any intermetallic reactions observed between the particles and the steel matrix. The results of the particle distribution show that at the mass fraction 0,5 to 1,0 wt% of Al₂O₃ with a mean particle size of 500 nm and 50 nm, the distribution of Al₂O₃ particles is relatively homogeneous with only a small deviation. However, when the mass fraction increases to 2,5 wt% the concentration ratio of particles deviates throughout the cast ingot, with the concentration decreasing toward the bottom of the cast ingot.

An infrared study of Concanavaline A aggregation at pH 5 and 9

Urban Novak^{1,2} and Jože Grdadolnik¹

¹ National Institute of Chemistry, Ljubljana, Slovenia

² Jožef Stefan International Postgraduate School, Ljubljana, Slovenia

urban.novak@ki.si

Abstract. We presented the application of infrared spectroscopy to study protein aggregation. The aggregation of Concanavaline A was induced by heating the protein solution at two different pH values. We showed that properly processed infrared spectra provide valuable information about the protein structure and structural changes during the process of aggregation. It is shown, that infrared spectroscopy offers an opportunity to distinguish between two similar and related processes; aggregation and fibrillation. Moreover, difference spectra provide details about hydrogen bonding.

Keywords: Concanavaline A, aggregation, fibrillation, infrared spectroscopy, difference spectroscopy, Amide I, Amide III

1 Introduction

The importance of protein aggregation in a wide variety of situation, including protein-deposition diseases, protein-folding studies and the stability of protein drugs, is widely recognized. Understanding the early events during amyloid aggregation is crucial to identify the involved mechanisms and for designing the strategies to prevent and reverse amyloidogenic disorders. However, little is understood about the structural changes underlying those processes. Fourier transform infrared (FTIR) spectroscopy is one of the few techniques that can be applied to determine the structure of proteins in early stages of aggregation. Especially applicable is the Attenuated Total Reflectance (ATR) spectroscopy [1] in which the sample is probed on the surface of a high reflective material (ZnSe, Ge, diamond). The application of single reflection ATR experiment permits the sampling of the protein solutions in water or in buffers with low concentration of the solute and prevents saturation distortions of the most intense solvents bands [2]. Thus the solvents spectra can be efficiently subtracted; the analyses of the structural sensitive protein bands such as Amide A, Amide I, Amide II, and Amide III are free of the interference with the solvent bands.

Concanavaline A (Con A), used in the presented research, belongs to the legume lectin family. It is “all β ” protein, which quaternary structure is governed by dimer-tetramer equilibrium depending on pH and temperature. At physiological pH values, the protein is essentially a tetramer, while at pH values lower than 6 it exists as dimer. The tetramer consists of two identical dimers, which are perpendicularly joined through the central part of their back-sheets [3]. Each monomer has three specific binding sites for carbohydrate and two ions (Ca^{2+} and Mg^{2+}). At basic pH (away from the pI) well defined long and thin amyloid-like fibrils are formed and in parallel the native structure changes involving the formation of intermolecular β -sheets [4]. At pH values closer to the pI of the protein (i.e. pH=5.1) amorphous aggregates are formed [5]. These evidences suggest that the average charge per molecule affects the aggregation pathway and specific morphology. In the acidic pH range, Mg^{2+} and Ca^{2+} are bound to Con A that may provide stabilization of protein structure [6].

Con A has several important characteristics. Its structure is remarkably similar to the structure of human serum amyloid P component, a protein which is constituent of almost all amyloid deposits. It has been reported that Con A is able to induce programmed cell deaths on cortical neurons by cross-linking of specific membrane receptors. The mechanism is similar to programmed cell deaths induced by amyloid β -peptide [7]. Moreover, the study of aggregation processes in “all β ” proteins is interesting also in a view of the observation that amyloid core structure mainly consists of β -sheets and that many short peptides with high β propensity display a strong tendency to form amyloid fibrils [8]. Here we report an infrared study of Con A aggregation monitored at pH 5 and 9. The changes in secondary structure triggered by temperature were probed by FTIR and difference spectroscopy [9].

2 Materials and Methods

Lyophilised powder of Con A (MW = 25692 Da), insulated from *Canavalia ensiformis*, was purchased from Sigma-Aldrich and used without further purification. The samples were freshly dissolved in 0.1 M phosphate buffer to a final concentration of 20 mg/ml. The pH of 0.1 M phosphate buffer was adjusted to appropriate pH values by using appropriate amounts of 0.1 M KH_2PO_4 and 0.1 M K_2HPO_4 buffer solutions. The pH was monitored by Mettler Toledo SevenEasy pH meter coupled with Mettler Toledo InLab Micro Pro pH electrode. The system was calibrated using Mettler Toledo certified pH solutions (pH 7,00, pH 4,01 and pH 9,21). Before measurements the sample was filtrated through 0.2 μm filter to remove any

aggregates formed during the sample preparation. Filtrated samples were kept on ice to prevent initiation of aggregation before actual measurements.

The FTIR spectra were measured using the Bruker Vertex 80 FTIR spectrometer. We employed Specac's Golden gate ATR cell with diamond crystal and heated top plate. Spectra were recorded in the range between 4000 and 500 cm^{-1} . Final spectrum was averaged from 64 interferograms. Before any spectral analysis the spectrum of pure buffer/water was subtracted. ATR absorbance spectra were used as recorded without post-processing due to reflection contributions to the overall absorbance spectra. Spectra were simplified by applying difference spectroscopy, a spectroscopic method, sensitive to band-shape changes [9]. Alterations in band-shapes due to external perturbations are in general due to huge overlapping of the internal vibrational modes very difficult to evaluate. However, the subtraction of two consecutive spectra with different temperature or recorded at different time, eliminates all undisturbed spectral feature, leaves visible only altered band shapes. Simplification of the difference spectrum versus recorded one permits accurate analyses. The subtraction factor was determined by eliminating the bands that corresponds to the sidechain CH, CH_2 , and CH_3 stretching vibrations (2800–3000 cm^{-1}) that are not affected by external perturbation. The band overlapped regions were additionally analysed using the Grams band fitting procedure by modelling the sum of the bands with the mixed Lorentzian and Gaussian band shapes. The solution spectra of Con A at various values of pH were measured in a temperature range from 15 °C to 75 °C. To reduce the strong bands due to the absorption of diamond, backgrounds were collected at each recorded temperature. The assignment of the structural sensitive bands in Amide I, II and III regions is based on previous results on blocked dipeptides [10] and vibrational spectra of proteins in solution with known structure [11, 12].

3 Results and discussion

The infrared spectra of proteins possess in fingerprint region several characteristic bands. The first and the most intense one is known as Amide I band. The Amide I mode is predominately C=O stretching with small contributions to the potential energy distribution by CN stretching, C_αCN deformation and NH in plane bending [13]. This composite nature of the Amide I band results in the sensitivity of the mode with respect to the type of secondary structure. Besides the complex potential energy distribution of Amide I mode, a C=O group act as a proton acceptor and hence is also sensitive to formation of hydrogen bonds. To assign a complex band

structure we applied the frequency structure correlation of Amide I band proposed by Mirtič and Grdadolnik [12]. These correlations were evaluated on the basis of the structural study of poly-L-lysine peptide and are shown in the Table 1.

Following the Figure 1 and Table 1, the second most intense peak belongs to Amide II mode. The Amide II mode is dominated by NH in plane bending and CN stretching. Significant contributions to this mode are also $C_{\alpha}C$ stretching, $C=O$ in plane bending and $N_{\alpha}C$ stretching [13]. Since the most important contribution to this mode is the NH in plane bending, the Amide II band is sensitive to formation of the hydrogen bond, where NH proton acts as a proton donor. However, strong overlapping prevents their use in the secondary structure determination.

Table 1. The assignment of the model bands from the Amide I, II and III region [12].

conformation	Frequency (cm ⁻¹)		
	Amide I	Amide II	Amide III
turn	1664–1674	1563–1572	1257–1260
P _{II}	1648–1654	1543–1546	1308–1311
P _{II} -conformation	1634–1640	1560–1550	1308–1311
α	1643–1645	1550–1552	1290–1295
α -conformation	1648–1654	1560–1550	1290–1295
β -conformation	1648–1654	1560–1550	1270–1280
β -strand	1625–1630	/	1240–1243
β -sheet	1685, 1630–1640	/	1230
aggregated β -sheets	1692, 1618	1530	1219–1222

Next to Amide II bands sidechain region appears. In the spectrum of Con A two groups of bands are visible, the first one is culminated around 1450 cm⁻¹ and the second one around 1400 cm⁻¹. Various modes from the side chains can be found from deformation modes of CH₂ and CH₃ groups to symmetric stretching of the ionized COO⁻ groups located near 1400 cm⁻¹ [14]. The Amide III region finishes the infrared spectrum presented in the Figure 1. It appears as moderate intensive band between 1320 cm⁻¹ and 1220 cm⁻¹. This vibration arises mainly due to the NH in plain bending coupled to some other peptide modes (CN stretching, CC stretching, and CO in plain bending) [13, 15]. The sensitivity of the Amide III components for

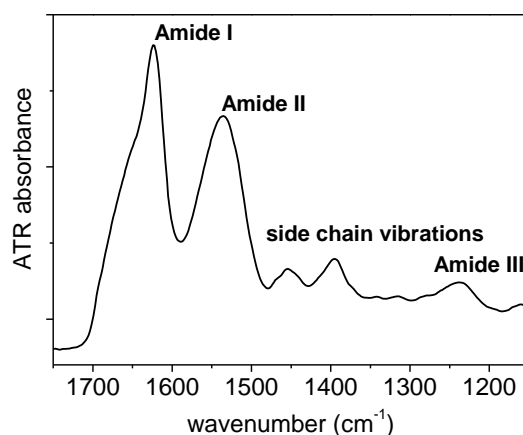


Figure 1. The spectrum of Con A in the fingerprint region recorded at 15 °C and pH 9.

particular conformation has been tested by numerous experimental and theoretical studies [13]. These studies show that the frequency of the Amide III depends on both dihedral angles. This opens a possibility that this vibrational parameter can be used to distinguish the conformations which are in generally not accessible by application of the decomposition of the Amide I band (see Table 1).

First we tested the applicability of infrared spectroscopy to monitor the aggregation of protein as a function of time. The pH value of the protein solution was adjusted to 9. Following the assignment of the band components of Amide I band found in the Table 1 low frequency components are due to protein aggregation. The band values of Amide I of aggregated protein are substantial lower even comparing with the Amide I components characteristic for β -sheet formation. Aggregation gains the low frequency component as presented in Figure 2.

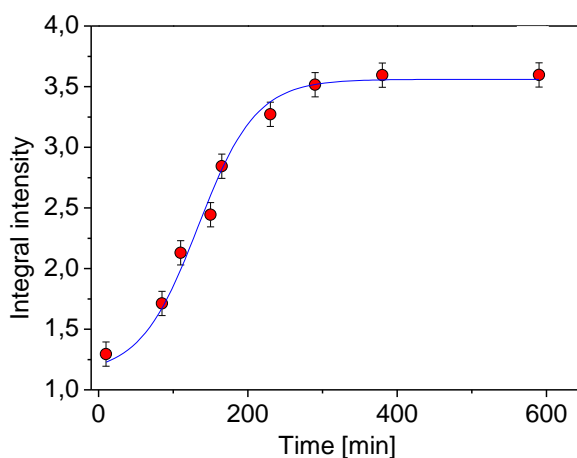


Figure 2. The variation of the integral intensity of the Amide I band in the region between 1627 cm^{-1} and 1600 cm^{-1} as a function of time. The spectra were recorded at 42 °C.

Although a method of band decomposition presented in the Figure 3 has many weaknesses it is the only way how to quantitatively evaluate conformational changes due to aggregation triggered by the increase of the temperature. The initial band parameters (number, position and relative intensity) were derived from the deconvolved spectra and second derivative spectroscopy (data not shown).

It is evident that aggregation at both probed pH values significantly alters the secondary structure of the protein. The band at 1230 cm^{-1} (β -sheet) loses the intensity while at the same time the band at lower wavenumbers (1627 cm^{-1} aggregated β -sheet and 1620 cm^{-1} , cross β -structure) gains the intensity. These conformational changes are also confirmed by the intensity variations of the Amide III band components at 1230 cm^{-1} and 1220 cm^{-1} , respectively. It is worth to note, that partially aggregated proteins exist already at $15\text{ }^{\circ}\text{C}$ at both pH values. The population is small (16 % at pH 5 and 13 % at pH 9) but noticeable (Table 1).

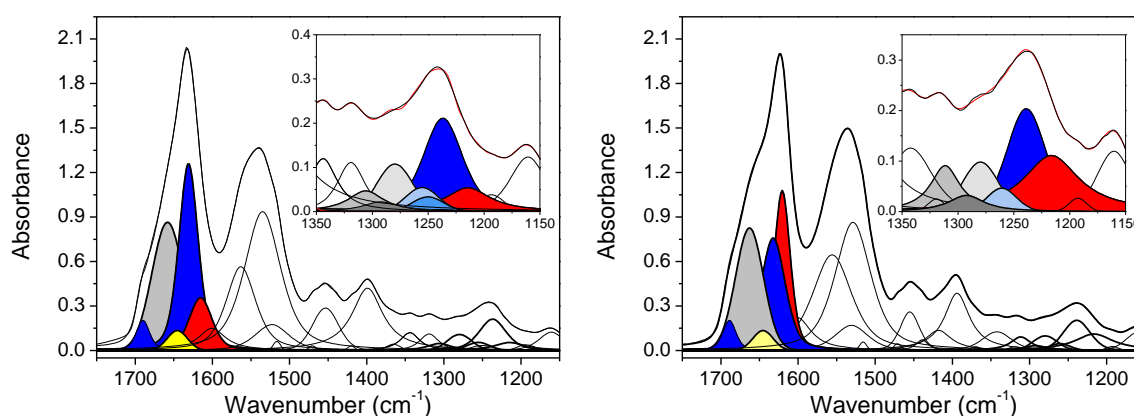


Figure 3. Decomposition of the Amide I, II, and III region of Con A (pH=9) at $T=15\text{ }^{\circ}\text{C}$ (left) and $T=75\text{ }^{\circ}\text{C}$ (right).

Table 2. The summary of the conformational changes observed by analysis of the Amide I and Amide III region applying band fitting algorithm.

mode	Aggregation pH=5			assignment	Fibrillation pH=9		
	(cm ⁻¹)	T=15 °C (%)	T=75 °C (%)		(cm ⁻¹)	T=15 °C (%)	T=75 °C (%)
Amide I	1690	5	5	β -sheet	1690	5	5
	1664	36	30	turns, loops	1660	40	34
	1632	44	35	β -sheet	1630	41	31
	1626	15	30	β -sheet agg.	1620	13	30
Amide III	1310	3	7	P _{II}	1310	10	15
	1290	4	5	α	1290	5	6
	1280	15	15	β_{120}	1280	17	13
	1260	13	3	β_{150}	1260	8	5
	1250	4	0	β -strand	1248	5	0
	1236	45	39	β -sheet	1230	42	31
	1220	16	30	β -sheet agg.	1220	13	30

The decomposition of Amide I and II reveals that both types of aggregations affect the protein structure similarly. Besides the already mentioned differences in protein structure, the rise up of the temperature slightly changes the populations of α , β , and P_{II} conformers. More radical is the reduction of the model band at 1260 cm⁻¹. The assignment of this band does not belong to any characteristic conformations found in Table 1. The band position is close to bands found in the blocked di-alanine and tri-alanine peptides, where intense bands at 1257 cm⁻¹ were attributed to the more opened β conformation (β_{150}). For detailed structural changes of particular conformation see the Table 2.

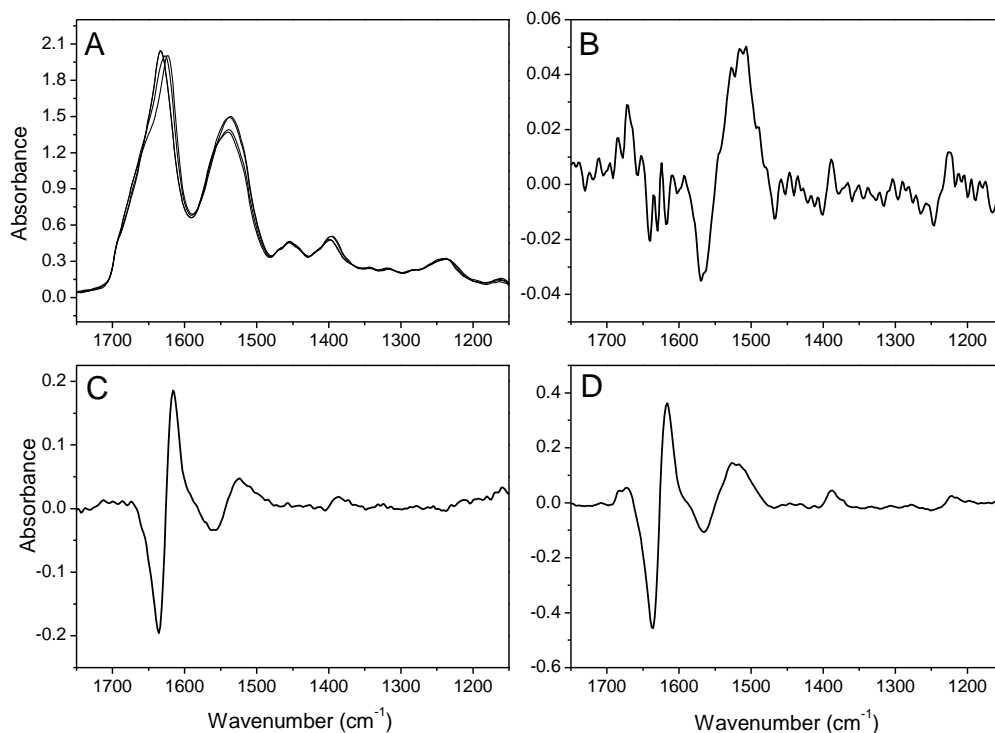


Figure 4. The application of the difference spectroscopy. (A) Protein solution as recorded at different temperatures. Solvent subtracted. (B) 35 °C - 15 °C, (C) 75 °C - 60 °C, and (D) 75 °C - 15 °C.

The changes of protein bands in fingerprint region of protein spectrum upon heating were monitored also by difference spectroscopy. In the Figures 4B, C, and D, typical difference spectra are shown. The first one is calculated at the beginning of the heating process. From the spectrum recorded at 35 °C, the spectrum recorded at 15 °C was subtracted. The initial difference spectrum is quite different with respect to other two, recorded at higher temperatures. While in other two (Figures 4C and D) the main feature is observed, as expected, in the amide I region, the change in the Amide II region is the most intense one. The negative band located at higher frequency moves upon heating to lower frequency. Since the NH deformation is the main constituent Amide II mode, the origin of frequency shift is weakening of the hydrogen bonds where NH groups from the backbone act as a proton donor. The changes in the Amide I and III region are less intensive. However, the low frequency component of Amide III band is already noticeable and its appearance indicates structural changes due to protein aggregation. Structural changes already described by band fitting algorithm are more visible in the last two difference spectra. The formation of the fibrils is approved by the intense positive

band at lower frequency in Amide I region. The Figure 5 presents enlarged spectral regions. The first region belongs to the mode of COO^- group from the side chains. This antisymmetric stretching band moves to lower frequencies governed by the same mechanism as found in Amide II. The rise up of the temperature weakens the established hydrogen bonds. The second one belongs to Amide III mode, where similar changes in bands intensities found by spectral resolution enhancement technique were observed. A complex features confirm the structural changes summarized in the Table 2.

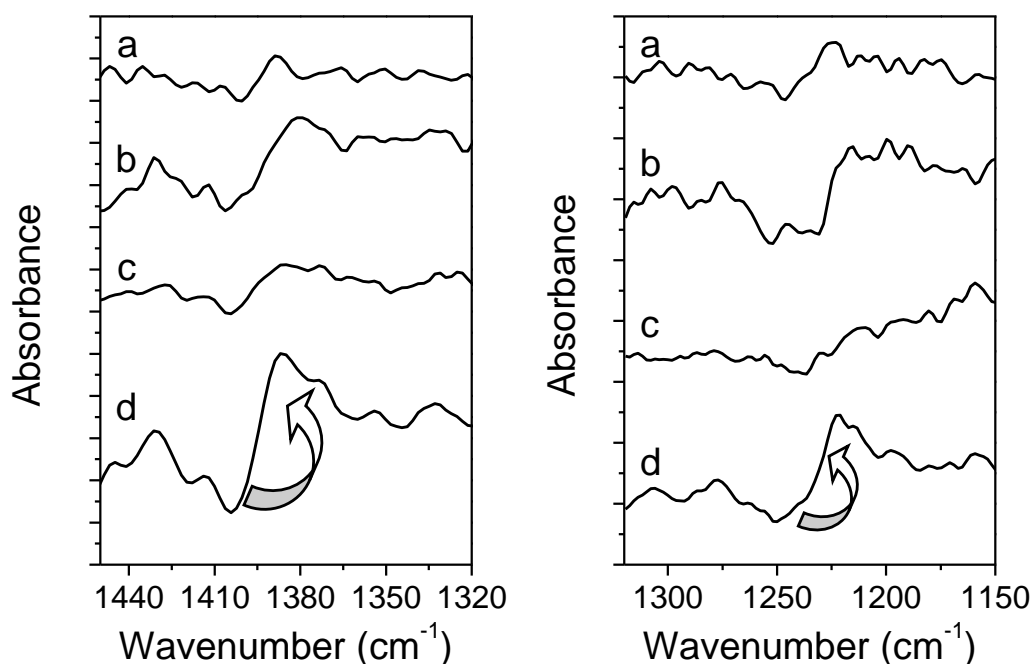


Figure 5. Left plot: difference spectra in the $\nu_s \text{COO}^-$ region: (a) 35 °C - 15 °C, (b) 60 °C - 35 °C, (c) 75 °C - 60 °C, and (d) 75 °C - 15 °C. Right plot: difference spectra in Amide III region: (a) 35 °C - 15 °C, (b) 60 °C - 35 °C, (c) 75 °C - 60 °C, and (d) 75 °C - 15 °C.

4 Conclusions

The presented study shows that we are able to distinguish between the protein aggregation and fibrillation. The appearance of the Amide I component at 1620 cm^{-1} indicates the presence of fibrils. Difference spectra present a useful method for following spectral changes. Moreover, together with the analysis of the Amide III region reveals the structural changes of the protein during aggregation.

References

- [1] J. Grdadolnik. ATR-FTIR spectroscopy: Its Advantages and limitations. *Acta Chim. Slovenica*, 49: 631-642, 2002.
- [2] J. Grdadolnik. Saturation Effects in FTIR Spectroscopy: Investigation of Amide I and Amide II Bands in Protein Spectra. *Acta Chim. Slovenica*, 50: 777-788, 2003.
- [3] J. W. Becker, G. N. Reeke, Jr., J. L. Wang, B. A. Cunningham, G. M. Edelman. The Covalent and Three-Dimensional Structure of Concanavalin A. III. Structure of the Monomer and its Interactions with Metals and Saccharides. *J Biol Chem*, 250: 1513-1524, 1975.
- [4] R. Carrota *et al.* Amyloid Fibrils Formation of Concanavaline A at basic pH. *J. Chem. Phys. B*, 115: 2691-2698, 2011.
- [5] V. Vetri *et al.* Amyloid Fibrils Formation and Amorphous Aggregation in Concanavaline A. *Biophys. Chem.*, 125: 184-190, 2007.
- [6] C. A. Stark, A. D. Sherry. Metal Ion Induced Conformational Changes in Concanavaline A: Evidence for Saccharide Binding to One Metal Free Structure. *Biochem. Biophys. Res. Comm.*, 87: 598-604, 1979.
- [7] K. Andersson, A. Olofsson, E. H. Nielsen, E. Svegah, E. Lundgren. Only Amyloidogenic Intermediates of Thransthyretin Induce Apoptosis. *Biochem. Biophys. Res. Commun.*, 294: 309-314, 2002.
- [8] A. L. Fink. Protein Aggregation: Folding Aggregates, Inclusion Bodies, and Amyloid. *Fold. Des.*, 3: 9-23, 1998.
- [9] J. Grdadolnik. Infrared Difference Spectroscopy: Part I. Interpretation of the Difference Spectrum. *Vibrat. Spectr.*, 31: 289-294, 2003.
- [10] J. Grdadolnik, V. Mohacek-Grosev, R. L. Baldwin, F. Avbelj. Populations of the Three Major Backbone Conformations in 19 Amino Acid Dipeptides. *Proc. Natl. Acad. Sci. USA*, 108: 1794-1798, 2011.
- [11] J. Grdadolnik, Y. Maréchal. Bovine Serum Albumin Observed by Infrared Spectroscopy. I. Methodology, Structural Investigation and Water Uptake. *Biopolymers (Biospectroscopy)*, 62: 40-53, 2001.
- [12] A. Mirtic, J. Grdadolnik. The Structure of Poly-L-Lyzine in Different Solvents. *Biophys. Chem.*, 175-176: 47-53, 2013.
- [13] S. Krimm, in *Infrared Analysis of Peptides and Proteins* B. R. Singh, Ed. Oxford University Press, Washington, 2000, pp. 38-53.
- [14] A. Barth. The Infrared Absorption of Amino Acid Side Chains. *Prog. Biophys. Mol. Biol.*, 74: 141-173, 2000.
- [15] J. Grdadolnik, S. Golič Grdadolnik, F. Avbelj. Determination of Conformational Preferences of Dipeptides Using Vibrational Spectroscopy. *J. Phys. Chem. B*, 112: 2712-2718, 2008.

For wider interest

Protein aggregation is a very important process associated with conformational diseases such as Alzheimer or Parkinson Disease or stability of protein drugs. The protein aggregation is a very complex process characterized by a remarkable polymorphism, where soluble amyloid oligomers, amyloid fibrils and amorphous aggregates are found as final product. This polymorphism is further related with the existence of multiple independent and competing assembly pathways leading to aggregation. Some of those oligomers are considered to be major initiators of the neurodegenerative cascades of corresponding diseases. However, not all oligomers are equally harmful, and several amyloidogenic proteins have been shown to form nontoxic oligomers, some of which were efficient fibrillation inhibitors.

In order to find a method, which can accurately spectroscopically determine the formation of fibrils, we systematically utilise infrared spectroscopy on the structural study of thermal aggregation of model protein (Concanavaline A). We have shown that proper application of the vibrational spectroscopy (ATR experiment) and accurate processing of recorded spectra (band fitting algorithm, deconvolution, second derivatives, and difference spectroscopy) provide a deeper insight into formation of the protein aggregates and fibrils. We found the markers in Amide I region, which uniquely expresses the presence of fibrils during the aggregation. Moreover, analysis of Amide I and Amide III regions by modelling of the intrinsic bands gives us an opportunity to monitor structural changes upon protein-protein interaction. The developed methodology presented in this manuscript will be applied in aggregation studies of proteins connected with neurodegenerative diseases.

Since FTIR spectroscopy allows fast and easy determination of protein secondary structure and in particular a very sensitive detection of conformational changes, it has important application values. The methods of FTIR spectroscopy described in this paper can be used in pre-formulation and formulation studies, forced degradation studies, quality control and binding studies to name a few.

Chemical speciation of third-row elements via valence-to-core x-ray emission spectroscopy

Marko Petric^{1,2}, Klemen Bučar¹, Matjaž Žitnik^{1,3}, and Matjaž Kavčič¹

¹ Department of Low and Medium Energy Physics, Jožef Stefan Institute, Ljubljana, Slovenia

² Jožef Stefan International Postgraduate School, Ljubljana, Slovenia

³ Faculty of Mathematics and Physics, University of Ljubljana, Slovenia

m.petric@ijs.si & matjaz.kavcic@ijs.si

Abstract. An experimental and theoretical study of electronic structure of the third-row elements based on high resolution x-ray emission spectroscopy was performed. The measured spectra are compared to the results of first-principle calculations based on the density functional theory (DFT). The agreement between the measured and calculated $K\beta$ emission spectra permits to discuss valence orbitals in terms of molecular orbital (MO) theory. The $K\beta$ spectral shape of the XO_4^{n-} ions ($X=P, S, \text{ or } Cl$) is explained in detail. Finally, the possibility of valence-to-core x-ray emission spectroscopy to address polysulfide formation within the cathode of the Li-S battery during the battery cycle is discussed.

Keywords: high resolution x-ray emission spectroscopy (XES), chemical speciation of phosphorus, sulfur and chlorine

1 Introduction

The knowledge of electronic structure is of fundamental importance in various research fields. X-ray inner shell spectroscopic methods are elemental and bulk sensitive and provide the most direct information on the local chemical environment of the central atom within different complex systems. In case of x-ray absorption spectroscopy (XAS) transition of the core electrons into the unoccupied state above the Fermi level are probed, while in high-resolution x-ray emission spectroscopy (XES) we are studying the relaxation of the core-ionized atom by a radiative transition from the occupied electron states below the Fermi level. They provide

complementary information on the electronic structure, but there is one conceptual difference between these two techniques. While XAS relies on the use of a monochromatic tunable x-ray beam provided by the synchrotron, XES can be performed also with the laboratory excitation sources as it is based on a second order relaxation process independent from the excitation mode [1]. In order to extract chemical information from a XES a dedicated crystal spectrometers is required, which provides energy resolution in emission channel comparable to the resolution of the synchrotron beamline monochromator. In the conventional x-ray spectroscopy nomenclature of isolated atoms $K\beta$ emission line refers to electron dipole transition from 3p to 1s atomic orbital. In case of phosphorus (P), sulfur (S), and chlorine (Cl) the 3p electrons are involved in the chemical bonding and the $K\beta$ spectrum corresponds to electronic transitions from the occupied valence molecular orbitals. Consequently, this valence-to-core x-ray emission spectrum should reflect the chemical environment of the central atom.

In this paper we study the capability of XES spectroscopy to study the electronic structure of P, S, and Cl atoms within molecules with T_d local symmetry. High energy resolution $K\beta$ emission spectra were recorded employing an in-vacuum x-ray emission spectrometer and experimental data are compared to ab-initio quantum chemical calculations based on the density functional theory (DFT). At the end, we have calculated the sulfur $K\beta$ spectral shape of different Li polysulfides and discussed the possibility of valence-to-core XES to study sulfur reduction within the cathode of a Li-S battery during the working cycle. Li-S batteries are considered as one of the most promising candidates for future batteries in applications where high energy density is required. So far, XAS has been predominantly used to study sulfur electrochemistry within the cathode of a Li-S battery [2]. With ab-initio quantum chemical calculation of the sulfur K-edge [3], many features of spectra are well interpreted, but the full discharge mechanism in Li-S batteries is still not fully known so additional experimental approaches should be considered.

2 Experimental section

Measurement of P $K\beta$ emission spectra were carried out at ID26 beamline of the European Synchrotron Radiation Facility (ESFR). Measurements of S and Cl $K\beta$ emission spectra were performed at 2 MV tandem accelerator of the Jožef Stefan

Institute (IJS) in Ljubljana. In all experiments the Johansson-type crystal spectrometer for high energy resolution XES in the tender x-ray range was used [4]. At ESRF the incident photon beam was tuned to 3keV and in case of proton induced x-ray emission (PIXE) measurements at IJS the proton energy was set to 2 MeV. The emission spectrometer operates in slightly modified Johansson focusing geometry where the target holder is positioned inside the Rowland focal circle. In this case broad excitation beam can be used without any significant loss of the energy resolution and the dispersive mode of operation is achieved enabling simultaneous collection of the full spectrum at fixed Bragg angle. In case of P compounds the induced x-ray photons were reflected in the first order by (1010) planes of SiO₂ crystal ($2d=8.510\text{\AA}$), while in case of S and Cl samples the first order reflection on a Si(111) crystal ($2d=6.271\text{\AA}$) was used. The diffracted photons were detected by a charged coupled device (CCD) detector. The position spectra recorded by the CCD detector were converted into energy scale relative to the position of $K\beta_{1,3}$ line of the K₃PO₄, Na₂SO₄ and NaCl compound target which served as references, with corresponding reference emission energies of 2138 [5], 2467.15 [6] and 2815.11 [7] eV, respectively. The energy bandwidths covered by the CCD size at a fixed detector position were 56, 39, and 71 eV for P, S, and Cl respectively. The energy resolution of the spectrometer was between 0.50 and 0.60 eV, depending on the Bragg angle corresponding to each of three measured elements. The experimental uncertainty was determined as a standard deviation of absolute emission energies of few independent measurements yielding final value <0.03 eV [8].

3 Theoretical framework

In order to calculate the electronic structure of third-row elements in different molecules the StoBe-deMon molecular cluster code [9] was used. The StoBe-deMon program is based on the density functional theory (DFT) [10], where the electron density completely determines properties of the system. After geometry optimization of the molecule, yielding the ground state of each molecule, the Mulliken population analysis [11] and Bader analysis of electron density [12] were performed. In order to calculate the $K\beta$ emission spectra, both initial core-hole state and final valence-hole state were represented by Kohn-Sham orbitals of the ground state [13] and the dipole transition moments were calculated as an explicit one-electron transitions.

The same TZVP (73111/6111/1) orbital basis set was used for P, S and Cl atoms. The exchange functional of Becke, Be88 [14] and correlation functional of Perdew PD91[15], were applied. More details about the calculations can be found in [16].

4 Results and discussion

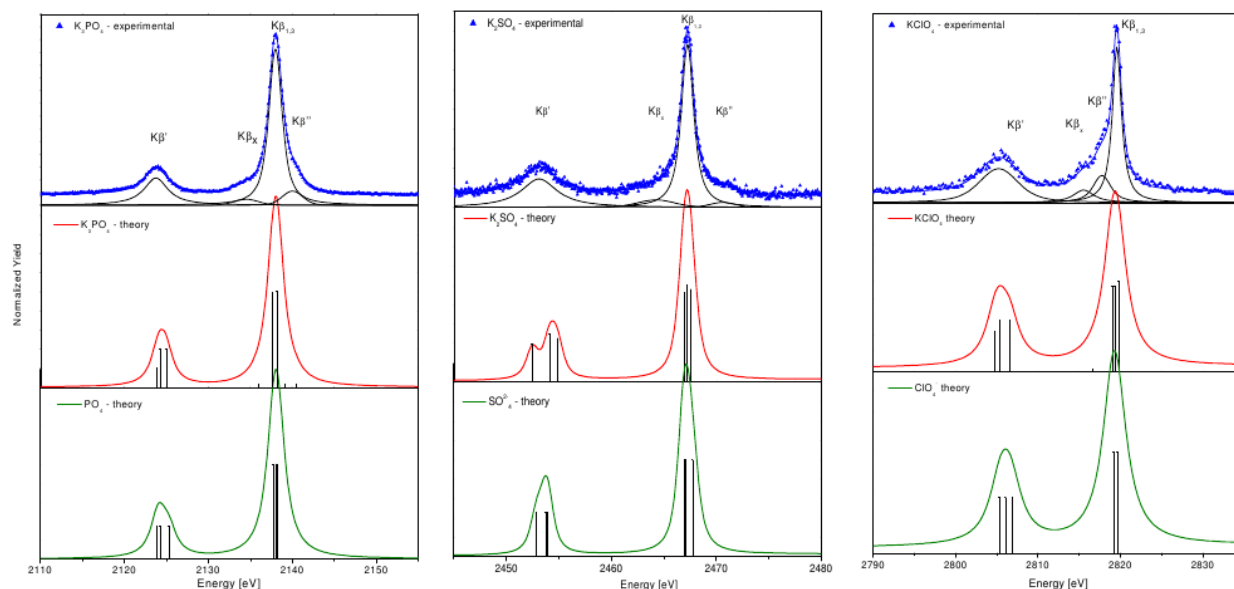


Figure 1: The experimental and the theoretical $K\beta$ emission spectra of phosphorus (left), sulfur (centre) and chlorine (right) in T_d local symmetry [16].

The P, S, and Cl $K\beta$ x-ray emission spectra measured from K_3PO_4 , K_2SO_4 and $KClO_4$ compounds are presented in the top part of Figure 1. The two characteristic peaks, commonly label as $K\beta_{1,3}$ and $K\beta'$, appear in spectra of all three compounds. In order to correlate the measured spectral shape with electronic structure, the DFT calculations of the electronic transitions corresponding to the $K\beta$ emission spectra were performed. We take into consideration two models, a full neutral molecule and the XO_4^{n-} ($X= P, S$ or Cl) ion containing only the first coordination sphere around the centre atom. As seen from Figure 1, there are no significant difference between the theoretical model spectra of the isolated XO_4^{n-} ion and the neutral molecule. The reason is in ionic bond between the cation and the XO_4^{n-} ion, where the valence electron from cation is transferred to the ion without significantly perturbing the electronic structure of the ion. Therefore, the main characteristics of the $K\beta$ emission spectrum can be successfully modelled only with the first coordination sphere around the centre atom. The structure of the valence MO reflects the

tetrahedral molecular geometry of the XO_4^{n-} ions and valence MO are labelled according to the irreducible representations of the T_d point group: $4a_1$, $3t_2$, $5a_1$, $4t_2$, $1e$, $5t_2$, and $1t_1$. According to the dipole selection rule, electron transitions to the $1s$ state are allowed only from the orbitals of t_2 symmetry. In our case, the $K\beta'$ emission line corresponds to transition from the $3t_2$ and $K\beta_{1,3}$ from the $4t_2$ MO. The Mulliken population analysis was performed for SO_4^{2-} ion and the results are presented in Table 1. Similar results are obtained also for other two ions [16].

Table 1: Ground state electronic configuration of SO_4^{2-} ion performed by Mulliken population analysis [16].

MO	S 3s	S 3p	S 3d	O 2s	O 2p
4a1	26	0	0	60	13
3t2	0	11	2	81	5
5a1	24	0	0	46	29
4t2	0	27	0	16	56
1e	0	0	5	0	95
5t2	0	8	5	0	87
1t1	0	0	0	0	100

Besides Mulliken population analysis we have also constructed the molecular orbital diagram and plotted schematically the corresponding $3t_2$ and $4t_2$ orbitals. Mulliken population analysis reveals that the O 2s atomic orbitals contribute to both $3t_2$ and $4t_2$ MO so that four O 2s atomic orbitals can be arranged in T_d symmetry in two types of orbitals, one in-phase with a_1 symmetry and three out-phase with t_2 symmetry. Only orbitals with the same symmetry can build the MO, so the O 2s in-phase together with X 3s build $4a_1$ and $5a_1$ MO. On the other hand, O 2s out-phase orbitals together with the X 3p orbitals, which have the same t_2 symmetry, build the $3t_2$ and $4t_2$ MO. The arrangement of atomic orbitals in $3t_2$ MO is presented in Figure 2, and since electron transitions from the $3t_2$ orbital contribute to the $K\beta'$ spectral line, this peak directly reflects O 2s and X 3p bonding. In a similar way, Mulliken population analysis show that mixing of O 2s and 2p orbitals needs to be included in the construction of the $4t_2$ MO. This mixing process changes significantly the ratio of O 2s and 2p orbitals so that the $4t_2$ MO is mostly built from O 2p and X 3p atomic orbitals. The $4t_2$ MO is schematically presented in Figure 2.

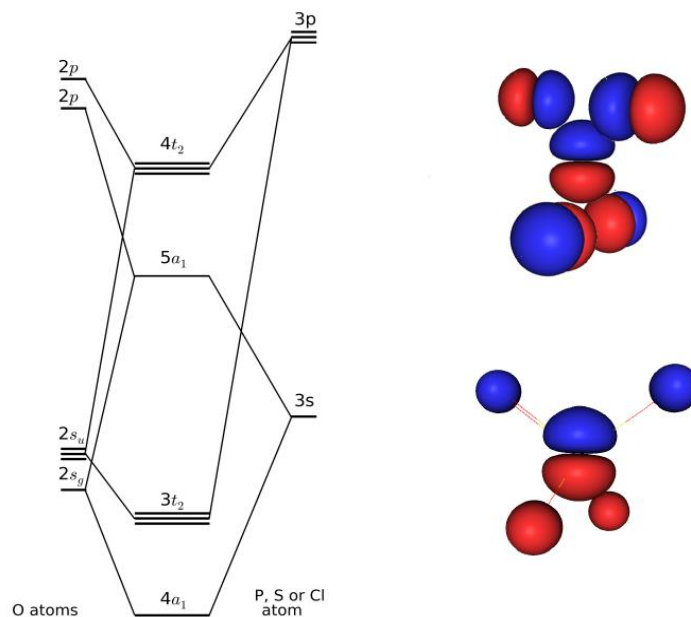


Figure 2: (left) Qualitative molecular diagram for the XO_4^{n-} ions. (right) Schematic presentation of the $4t_2$ and $3t_2$ molecular orbitals, top and bottom, respectively [16].

After we have successfully explained the $\text{K}\beta$ emission spectrum of compounds with T_d local symmetry, we can study also the effects of covalent bonding to the XO_4^{n-} ion. In Figure 3 the experimental $\text{K}\beta$ emission spectra of four different phosphate compounds are showed, where except the cations also hydrogen is bonded to the phosphate ion. The characteristic structure is still composed of two main $\text{K}\beta_{1,3}$ and $\text{K}\beta'$ peaks for all samples, however, the intensity of the $\text{K}\beta_x$ and $\text{K}\beta''$ side peaks increases with additional hydrogen atoms bond to the PO_4^{3-} ion. In order to explain these side peaks and its dependence on the number of hydrogen atoms, the theoretical model was expanded to the next coordination shell, Figure 4. The theoretical spectra were built from the calculated stick spectrum using Voigt profiles with fixed width. An overall shift of the absolute emission energy scale of less than - 5 eV was applied to theoretical spectra to match experimental energies. As mentioned before, the first coordination shell yields two main peak and this model is sufficient for compounds with ionic bond between the cation and the PO_4^{3-} ion. With additional hydrogen atoms bond to phosphate ion the original tetrahedral symmetry is broken leading to different mixing of the atomic orbitals and changing the dipole transition matrix elements that contribute to the spectrum. By adding additional protons the theoretical spectrum starts to develop both side peaks which also grow in intensity with increasing number of hydrogens in agreement with experimental observation.

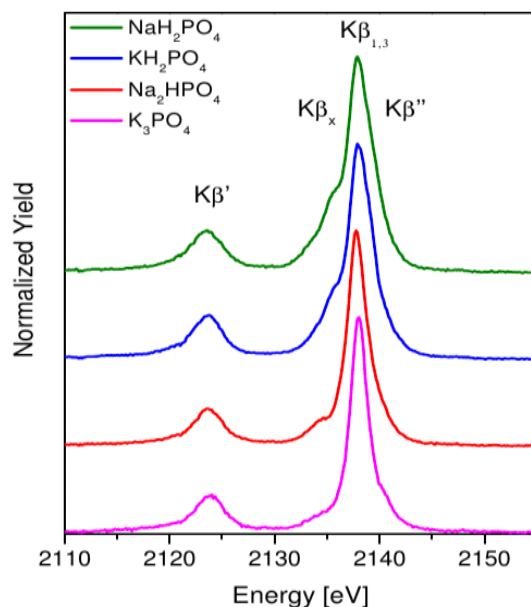


Figure 3: The experimental $K\beta$ emission spectra of phosphate ions.

For example, the electron transition from the $5a_1$ MO to P $1s$ orbital in PO_4^{3-} ion is forbidden by selection rule and cannot contribute to the spectrum. Adding hydrogen atom to the PO_4^{3-} ion, the $5a_1$ change its atomic character yielding significant amount of P $3p$ orbital and start to build the $K\beta_x$ peak on the low-energy tail of the main $K\beta_{1,3}$ peak. The development of the $5a_1$ orbital building the $K\beta'$ peak is presented on the right side of Figure 4. In a similar way, electron transitions from $1e$ MO build the $K\beta''$ peak. So, our calculations qualitatively explain also the spectral features of these compounds.

XES technique can be applied to different system in chemistry, biology, geology, and others. In case of third row elements studied here, very interesting and important system represent the Li-S batteries, which are considered as one of the most promising candidates for future batteries. The cathode in the Li-S battery is elemental sulfur which is during the battery cycle reduced to lithium sulfide (Li_2S). The reaction is not straightforward, the process go through a series of stepwise redox reaction forming various lithium polysulfide (Li_2S_x ; $x=2-8$). The migration of these polysulfides away from the cathode during the battery cycle result in irreversible process [3]. The knowledge of the electronic structure and precise information about the mechanism of polysulfide formation and the interaction of

sulfur and polysulfides with the host matrix and electrolyte is crucial to improve the design of the batteries and provide the industrial production.

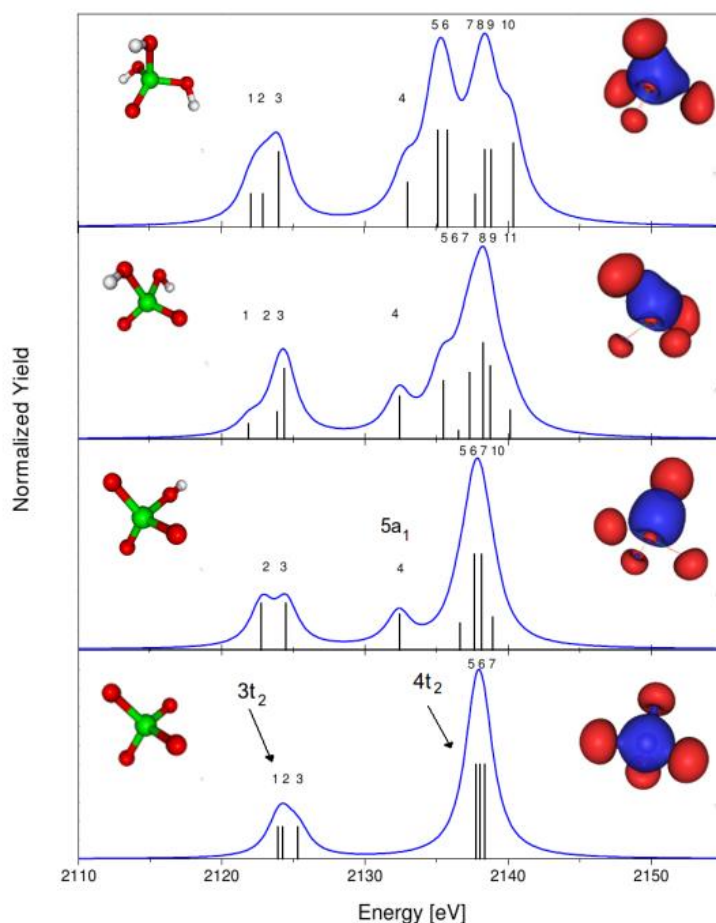


Figure 4: The theoretical $K\beta$ emission spectra of (from bottom to top) PO_4^{3-} , HPO_4^{2-} , $H_2PO_4^-$, H_3PO_4 . [1]

In order to analyse sulfur electronic structure within lithium polysulfide, we have first constructed the theoretical model for the elemental S which was compared with the measured spectrum (Figure 5). In this model eight S atoms were considered. After geometry optimization they are arranged in a crystalline α -S₈ structure, forming the ring. In geometry optimization for all S atoms the same (73111/6111/1) basis set was used. To avoid linear combination of core-orbitals from neighbouring atoms the seven atoms were described by means of an effective core potential. For the atomic nucleus and electrons from K and L atomic shell electrostatic potential was used, while for the valence electrons (311/211/1) basis set was used.

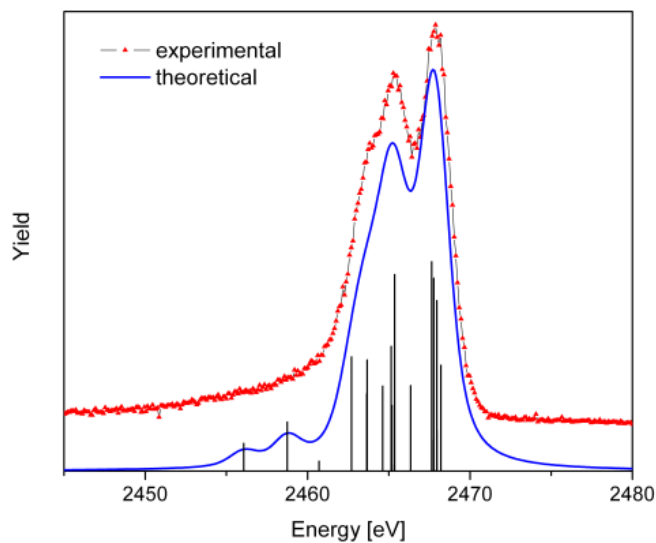


Figure 5: Experimental and theoretical $K\beta$ emission spectrum of elemental sulfur.

The theoretical spectrum was built from the calculated stick spectrum using Voigt profiles. The width of the Voigt profiles was adjusted in order to fit experimentally observed lineshape, yielding the final width of 0.57 eV and 0.61 eV for Gaussian and Lorentzian component, respectively. An overall shift of the absolute energy scale of 75.42 eV was applied to the theoretical spectrum in order to match experimental energies.

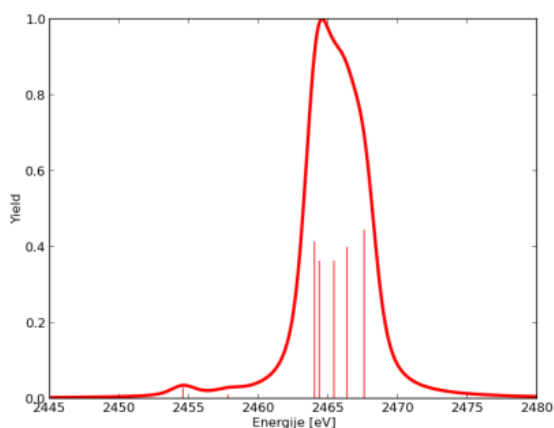


Figure 6: The theoretical S $K\beta$ emission spectrum of the Li_2S_2 .

The experimental $K\beta$ emission line of the elemental S has two characteristic close-sharp peaks which are well reproduced by the theoretical model. The same theoretical framework can be now applied also to Li_2S_x molecular systems. Also in this case the model spectra were built from the calculated stick spectra, the overall shift and width of the Voigt profiles were the same as the ones used in the model

spectrum of elemental S. The obtained theoretical spectra for molecules Li_2S_x ($x=2, 3, 4,$ and 5) are presented in Figures 6-7.

In case of the Li_2S_2 molecule both S atoms are directly bond to Li atoms. In first approximation, we can assume covalent S bond like in diatomic molecule and each Li atom gives one electron to the S_2 molecule. This is confirmed with Bader analysis in Table 2., where the S atoms have charge -0.943 . The S $\text{K}\beta$ spectra shape is the same for both atoms in Li_2S_2 molecule, where in case of Li_2S_3 , Li_2S_4 , and Li_2S_5 we need to separately calculate the emission spectrum for each S atom. The S atoms can be grouped in internal atoms and terminal atoms which are directly bond to two Li atoms.

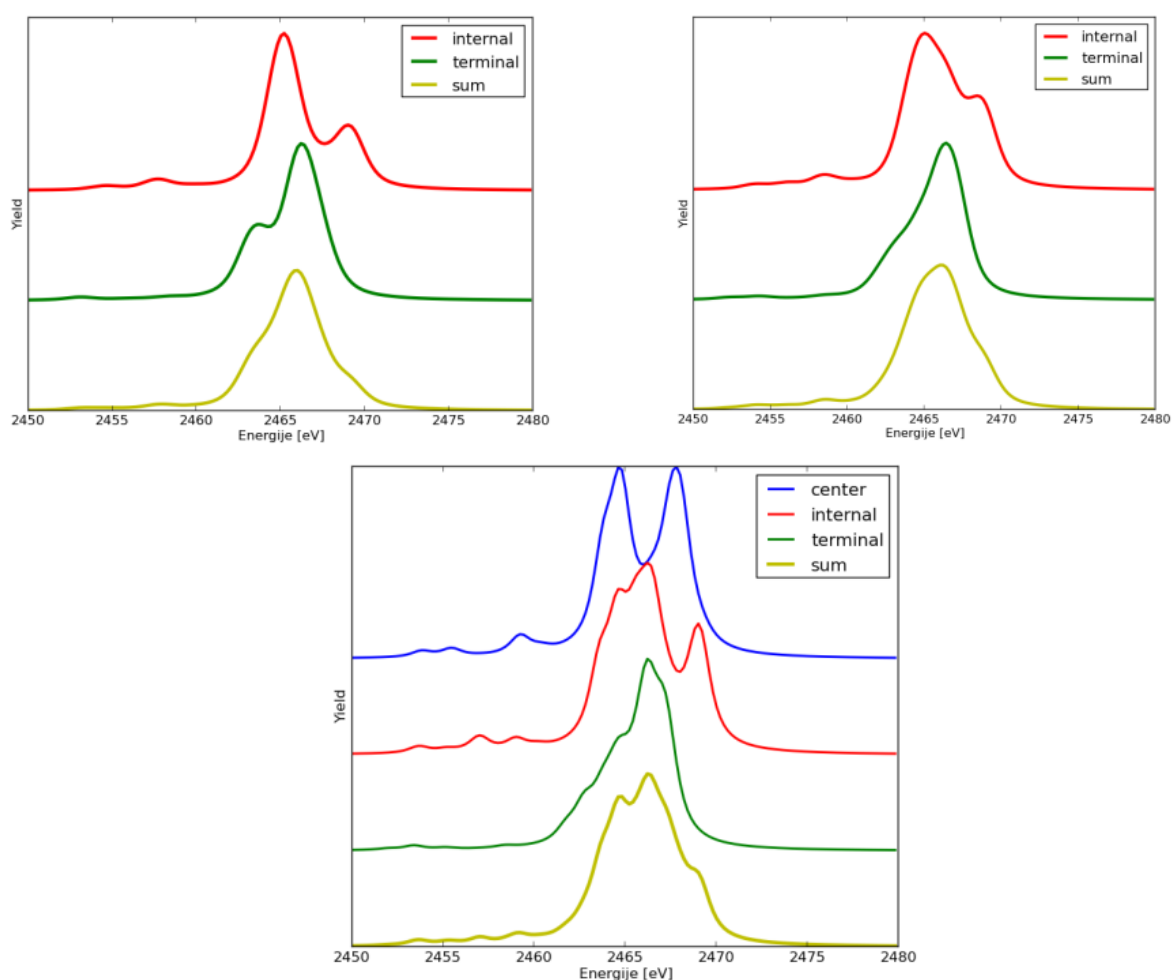


Figure 7: The theoretical S $\text{K}\beta$ spectra of the (*top-left*) Li_2S_3 , (*top-right*) Li_2S_4 , and (*botton*) Li_2S_5 .

The electron density on each S atom can be characterized by using Bader analysis. Results of the Bader analysis for our system for each group of atoms are given in Table 2. in good agreement with the results of more elaborated theoretical analysis [3]. In order to interpret the electronic structure in terms of atomic orbitals Mulliken population analysis was performed for both group of S atom and results are presented in Table 3. The Mulliken population analysis can be performed separately for each MO and interpreted in term of linear combination of atomic orbitals (LCAO), so the full description of electronic structure is done. Our calculations demonstrate capabilities of sulfur valence-to-core emission spectroscopy to characterize sulfur within Li-S battery and study the mechanism of polysulfide formation within the battery. One problem is that these polysulfides are only produced electrochemically during the battery cycle and reference standard samples are not available in order to compare directly calculations with the measured data. Full characterization can be only performed using *in-operando* XES measurements on battery itself.

Table 3: Mulliken population analysis of Li_2S_x system.

Li_2S_x	Terminal[3s - 3p - 3d]	Internal[3s - 3p - 3d]
2	5.931 - 10.335 - 0.022	-
3	5.951 - 10.271 - 0.028	5.972 - 9.903 - 0.065
4	5.950 - 10.254 - 0.031	5.951 - 9.935 - 0.070
5	5.956 - 10.256 - 0.031	5.948 - 9.950 - 0.070

5 Conclusion

High energy resolution valence-to-core emission spectroscopy can be used as a sensitive probe of a local electronic environment of third-row elements. The interpretation of the experimental data is provided by the DFT calculations, which explain the measured spectral shape in terms of atomic orbitals. This is presented in more details for the P, S, and Cl $\text{K}\beta$ emission spectra in compounds with Td local symmetry. We have demonstrated that the $\text{K}\beta$ emission spectra provides information about bonding, ligand type, and symmetry. Finally, the spectra of the lithium polysulfides (Li_2S_x ; $x=2-5$) were also calculated providing a basis for the sulfur characterization within the Li-S battery.

Acknowledgements:

This work has been supported by Marie Curie Actions – Initial Training Networks (ITN) as an Integrating Activity Supporting Postgraduate Research with Internships in Industry and Training Excellence (SPRITE) under EC contract no. 317169. The authors acknowledge the support of the Slovenian Research Program P1-0112 and an excellent assistance of the ID26 beam line staff in preparation of synchrotron experiment.

References:

- [1] M. Petric, R. Bohinc, K. Bučar, M. Žitnik, J. Szlachetko, M. Kavčič. Chemical State Analysis of Phosphorus by X-ray Emission Spectroscopy. *Anal. Chem.* **87**: 5632-5639, 2015.
- [2] R. Dominko and al. Analytical Detection of Polysulfides in the Presence of Adsorption Additives by Operando X-ray Absorption Spectroscopy. *J. Phys. Chem. C*, **119**(33): 19001-19010, 2015.
- [3] T. A. Pascal and al. X-ray Absorption Spectra of Dissolved Polysulfides in Lithium-Sulfur Batteries from First-Principles. *J. Phys. Chem. Lett.*, **5**: 1547-1551, 2014.
- [4] M. Kavčič, M. Budnar, A. Mühleisen, F Gasser, M. Žitnik, K Bučar, R Bohinc. Design and performance of a versatile curved-crystal spectrometer for high-resolution spectroscopy in the tender x-ray range. *Rev. Sci. Instrum.* **83**: 033113, 2012.
- [5] C. Sugiura, H. Yorikawa, S. Muramatsu. K β x-ray emission spectra and chemical environments of phosphorus in some selected compounds. *J. Phys. Soc. Jpn.*, **65**: 2940-2945, 1996.
- [6] C. Sugiura, Y. Gohshi, I Suzuki. Sulfur K β x-ray emission spectra and electronic structures of some metal sulphides. *Phys. Rev. B*, **10**: 338-343, 1974.
- [7] C. Sugiura. K β X-ray Emission X-Ray Absorption of Cl in NaCl. *Phys. Rev. B*, **6**: 338-343, 1972.
- [8] M. Petric and M. Kavčič. Chemical speciation via X-ray emission spectroscopy in the tender X-ray range. *J. Anal. At. Spectrom.* **31**: 450-457, 2016.
- [9] K. Hermann and al. StoBe-deMon, version 3.1., 2011. [http:// www.fhi-berlin.mpg.de/KHsoftware/StoBe/index.html](http://www.fhi-berlin.mpg.de/KHsoftware/StoBe/index.html).
- [10] W. Kohn. Nobel Lecture: Electronic Structure of Matter; Wave Function and Density Functionals. *Rev. Mod. Phys.* **71**: 1253-1266, 1999.
- [11] R.S. Mulliken. Electronic Population Analysis on LCAO-MO Molecular Wave Functions III. *J. Chem. Phys.* **23**: 2338, 1955
- [12] R.F.W. Bader, *Chem. Rev.*, **91**: 893, 1991.
- [13] A. Nilsson, L.G. Pettersson. Chemical bonding on surfaces probed by X-ray emission spectroscopy and density functional theory. *Surf. Sci. Rep.* **55**: 49-167, 2004.
- [14] A. Becke. Density-functional exchange-energy approximation with correct asymptotic behaviour. *Phys. Rev. A* **38**: 3098-3100, 1988.
- [15] J. Perdew, J. Chevary, S. Vosko, K. Jackson, M. Pederson, D. Singh, C. Fiolhais. Atoms, molecules, solids, and surfaces: Applications of the generalized gradient approximation for exchange and correlation. *Phys. Rev. B*, **46**: 6671-6687, 1992
- [16] M. Petric, R. Bohinc, K. Bučar, S.H. Nowak, M. Žitnik, and M. Kavčič. Electronic Structure of Third-Row Elements in Different Local Symmetries Studied by Valence-to-Core X-ray Emission Spectroscopy. *Inorg. Chem.* DOI: 10.1021/acs.inorgchem.6b00237

For wider interest

The particle induced x-ray emission (PIXE) is well established non-destructive analytical technique for rapid multielemental detection. The technique is based on the detection of characteristic x-ray emission following inner shell ionization induced in collision with MeV protons. Solid state detectors with energy resolution of ~ 150 eV are commonly applied in such analysis, which is enough to separate characteristic x-ray lines from different elements. However, if we push the energy resolution on the level of the natural linewidth, the valence-to-core x-ray emission spectra reflects the chemical environment of the x-ray emitting atom.

In present work, valence-to-core x-ray emission spectra of phosphorus, sulphur, and chlorine are studied experimentally and theoretically. In order to record $K\beta$ spectra with high energy resolution an in-vacuum curved-crystal spectrometer was employed. Theoretical model spectra were built using calculations based on the density functional theory (DFT) and the main spectral features were explained in a molecular orbital picture. In particular, detailed analysis of P, S, and Cl in compounds with T_d local symmetry is presented, demonstrating that valence-to-core XES is a sensitive probe of electronic structure, symmetry of the molecule and ligand bonding. Finally, the first-principle DFT calculation of the S $K\beta$ spectra of lithium polysulfide (Li_2S_x) compounds were performed, which can be used to study Li-S batteries in operando conditions.

The effect of benzene ring and mercapto group in imidazoles on the corrosion inhibition of copper alloy with 10% zinc

Monika Žnidaršič^{1,2}, Črtomir Podlipnik¹ and Ingrid Milošev^{2,3}

¹ University of Ljubljana, Faculty of Chemistry and Chemical Technology, Večna pot 113, 1000 Ljubljana

² Jožef Stefan Institute, Department of Physical and Organic Chemistry, Jamova c. 9, 1000 Ljubljana

³ Jožef Stefan International Postgraduate School, Jamova c. 39, 1000 Ljubljana
znidarsic.monika@gmail.com

Introduction

Corrosion has an important role in diverse fields of industry and everyday life [1]. The main goal of research is to find methods for the minimization and prevention of corrosion. Corrosion protection directly affects the costs related to maintenance of e.g. metallic constructions and other engineering objects, i.e. corrosion protection is important due to saving of high economic costs. Corrosion inhibitors are one of the most common methods for preventing the corrosion of copper and its alloys. Hitherto the most effective inhibitor of copper corrosion was benzotriazole [2], which has been used for decades. In order to find less toxic compounds with similar inhibition efficiency the research is focused on alternative corrosion inhibitors for copper and its alloys. In our experiments we focused on copper alloy with 10 wt.% of zinc, i.e. Cu90Zn10 alloy, which is stronger and harder than copper. This alloy is easily molded into various shapes and forms, it has good thermal conductivity and very good corrosion resistance in salt water [3].

In our previous study the effect of structural variation of target imidazole molecule by mercapto and methyl group functionalization or by fusion with a benzene ring on the corrosion inhibition of copper was studied [4]. In the present study comparative measurements were performed on Cu90Zn10 brass alloy.

Materials and methods

Corrosion protection of Cu90Zn10 (90 wt.% Cu and 10 wt.% Zn, Wieland Werke, Germany) was determined through electrochemical measurements performed in a

three-electrode corrosion cell at 25°C with an Autolab potentiostat/galvanostat PGSTAT-302N operated by NOVA software. Ag/AgCl electrode was used as a reference electrode and stainless steel rods as the counter-electrode. Brass samples, in the shape of discs of 15 mm diameter, served as working electrodes. Samples were successively ground at a circulating device under a stream of water using SiC papers of gradations 500, 800, 1000, 1200, 2400 and, 4000, and then rinsed and dried. Aqueous solution of 0.1 M NaCl was used as electrolyte. Measurements were performed in electrolyte with and without additions of following inhibitors (Figure 1): imidazole (ImiH), 1-methyl-1*H*-benzo[d]imidazole-2-thiol (SH-BimiMe) or 2-mercapto-1-methylimidazole(SH-ImiMe) added at the concentration of 0.1 mM.

Prior electrochemical measurement the samples were stabilized for 1 hour at open circuit potential (OCP) where the potential was measured as a function of time. Polarization resistance, R_p , was then measured. The R_p reflects the resistance of a metal in a certain solution to general corrosion, i.e. larger the R_p , the more resistant the metal. Curves of current density vs. potential were measured within ± 10 mV vs. OCP using a potential scan rate of 0.1 mV/s. The R_p was determined as a slope of the j vs. E curve. Measurements were carried out in triplicate and the representative results were given. Based on the R_p values the inhibition efficiency was calculated according to the equation (1):

$$IE = \frac{R_p^* - R_p}{R_p^*} \times 100 \quad (1)$$

Following the R_p measurements, potentiodynamic polarization curves were measured in a broader potential region ± 250 mV using a potential scan rate of 1 mV/s.

Results and discussion

The values of R_p increased from 32506 k Ω cm² in NaCl solution to 33389 k Ω cm² and 101800 k Ω cm² in the presence of 0.1 mM ImiH and SH-BimiMe thus giving

the IE values of 2.6% and 68%, respectively. The addition of SH-ImiMe resulted in the decrease in R_p indicating that this inhibitor acts as an corrosion activator. Measurements of potentiodynamic polarization curves (Figure 2) in the broad potential region enabled the determination of the following electrochemical parameters: corrosion potential, E_{corr} , corrosion current density, j_{corr} . The E_{corr} values ranged between -0.183 V and -0.042 V. The value of j_{corr} reflects the degree of corrosion process and is expected to decrease in inhibited solution. Again, for the SH-ImiMe the j_{corr} is larger than in NaCl solution confirming that its presence activates the dissolution reaction. For the ImiH and SH-BimiMe the values are similar or smaller than in NaCl solution indicating inhibition. Polarization curves recorded in 0.1 M NaCl solution with and without addition of organic inhibitors serve as a basis for studying of mechanism of electrochemical inhibition.

Conclusions

The mercapto group beneficially affects the inhibition efficiency of imidazoles as corrosion inhibitors of Cu90Zn10 alloy in chloride solution but only in combination with benzene ring present in the target molecule. When combined with methyl group it acts as a corrosion activator. Compared to the benzotriazole as best effective corrosion inhibitor for copper-based alloy, however, the results achieved by SM-BimiMe are still less effective. Namely, in 0.5 M NaCl solution the benzotriazole at the concentration of 0.1 mM achieved almost two orders of magnitude smaller corrosion current density [5]. Nonetheless, environmentally more acceptable imidazole-based inhibitors should be studied further and future experiments will be devoted to a more systematic approach of studying the effect of different functional groups to the inhibition mechanism.

References:

- [1] M. M. Antonijević and M. B. Petrović. Copper Corrosion Inhibitors. A Review. *Int. J. Electrochem.* 3: 1-28, 2008
- [2] M. Finšgar and I. Milošev. Inhibition of copper corrosion by 1,2,3-benzotriazole. *Corros. Sci.* 52(9): 2737-2749, 2010.
- [3] <http://www.madehow.com/Volume-6/Brass.html>
- [4] I. Milošev, N. Kovačević and A. Kokalj. The roles of mercapto, benzene and methyl groups in the corrosion inhibition of imidazoles on copper: I Experimental characterization. *Corrosion Science.* 98: 107-118, 2015
- [5] T. Kosec, I. Milošev, B. Pihlar. Benzotriazole as an inhibitor of brass corrosion in chloride solution. *Applied Surface Science.* 253(22): 8863-8873, 2007

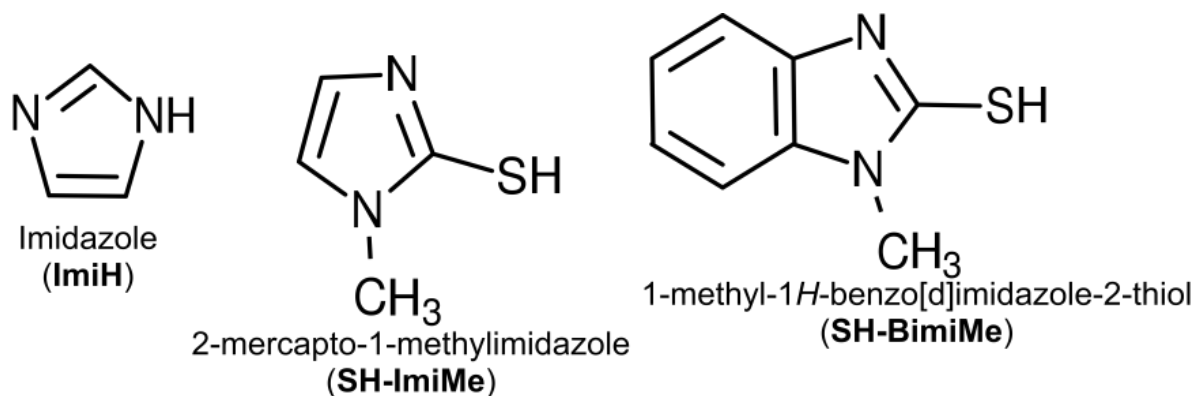


Figure 1: Organic inhibitors used in the study.

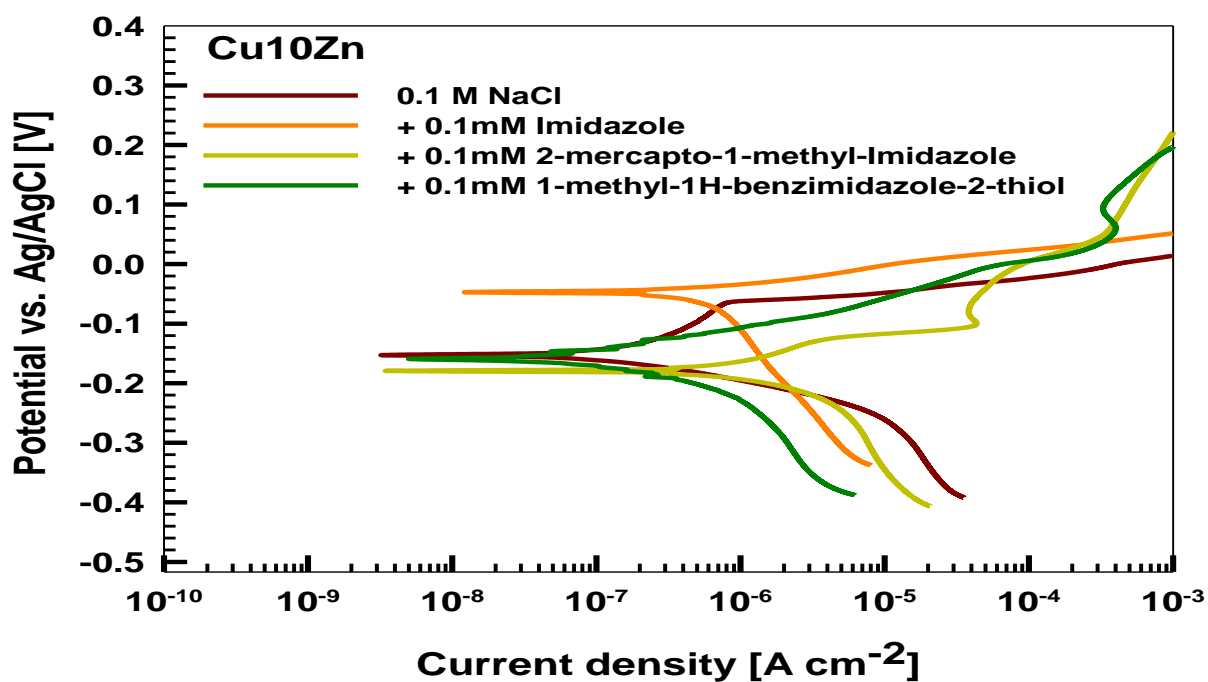


Figure 2: Potentiodynamic curves recorded for Cu90Zn10 in 0,1M NaCl solution, without and with addition of inhibitors. $dE/dt=1\ mV/s$.

For wider interest

Corrosion has an important role in diverse fields of industry and everyday life. Loss due to corrosion are estimated between 2 to 5 % of the world's gross national products. The main goal of research is to search for new methods for the minimization and prevention of corrosion. The aim of the to find a cheap, non-toxic and efficient inhibitor which prevents corrosion. That was the main reason why we studied the inhibition efficiency of different types of imidazoles as corrosion inhibitors of copper alloy which is widely used material in many applications. The mercapto group beneficially affects the inhibition efficiency of imidazoles as corrosion inhibitors of Cu₉₀Zn₁₀ alloy in chloride solution but only in combination with benzene ring. On the other hand, imidazole combined with methyl group acts as a corrosion activator.

Kazalo Avtorjev (List of Authors)

- Ajvazi, N. **206**
Kobal, A. B. **46**
Babič, J. **140**
Belec, B. **216**
Bertoncelj, B. **3**
Bregar, K. **130**
Bučar, K. **261**
Cvetković, B. **154**
Debeljak, M. **165**
Debevec, T. **140**
Dežman, M. **140**
Dolenc, B. **180**
Draganski, B. **175**
Drinčič, A. **20**
Džeroski, S. **165, 175**
Eftimov, T. **149**
Fajon, V. **122**
Falnoga, I. **106**
Ferlan, M. **56**
Gams, A. **140**
Gams, M. **154**
Gačnik, L. **31**
Germ, M. **52, 65**
Gjoreski, H. **154**
Gjoreski, M. **154**
Gornik, T. **39**
Goršak, T. **227**
Grdadolnik, J. **250**
Heath, E. **39**
Horvat, M. **46, 91, 106, 122**
Horvat, M. **13**
Hrovat, A. **130**
Iskra, J. **39, 69**
Jagodica, M. **46, 106**
Janko, V. **154**
Jačimović, R. **31, 91**
Jerabek, K. **39**
Jerše, A. **52, 65**
Juričič, Đ. **180**
Kacjan-Maršič, N. **52, 65**
Kafexhiu, F. **239**
Kavčič, M. **261**
Kocev, D. **175**
Koler, A. **39**
Kononenko, L. **46, 106**
Koroušič-Seljak, B. **149**
Korošec, P. **149**
Kosec, G. **81**
Kosjek, T. **39**
Kotnik, J. **122**
Krajnc, A. **39**
Krajnc, B. **56**
Krajnc, P. **39**
Kralj, S. **227**
Kračun, A. **239**
Kroflič, A. **52, 65**
Krsnik, M. **46, 106**
Kuzmanovski, V. **165**
Lisjak, D. **227**
Luštrek, M. **154**
Makovec, D. **216, 227**
Malič, B. **3**
Mazej, D. **46, 106**
Milačič, R. **20, 76, 113**
Mileski, V. **175**
Milošev, I. **274**
Mladenovič, A. **113**
Mohorčič, M. **130**
Možina, Š. **69**
Nečemer, M. **96**
Nikolič, I. **20**
Novak, P. **76**
Novak, U. **250**
Ogrinc, N. **56, 96**
Oprčkal, P. **113**
Pahor, J. **81**
Pavlin, M. **46, 91**
Petkovič, H. **81**
Petric, M. **261**
Podgornik, B. **239**
Podgoršek, A. **81**
Podlipnik, Č. **274**
Popović, A. **91**
Potočnik, D. **96**
Rihtaršič, J. **3**
Snoj, J. **46, 106**
Stajnkó, A. **46, 106**
Stavber, S. **13, 69, 81, 206**
Stepančič, M. **180**
Stibilj, V. **52, 65**

Tehovnik, F. **239**

Trajanov, A. **165**

Trefalt, G. **3**

Turnšek, M. **39**

Vidmar, J. **113**

Vojisavljević, K. **3**

Zuliani, T. **20, 76**

Čebular, K. **13**

Čusak, A. **81**

Šircelj, H. **52, 65**

Šolc, T. **193**

Šolić, M. **122**

Ščančar, J. **20, 76, 113**

Žitnik, M. **261**

Živković, I. **122**

Žnidaršič, M. **274**

Sodelujoča podjetja "Od ideje do uspeha":



Sodelujoča podjetja in organizacije:





**MEDNARODNA
PODIPLOMSKA ŠOLA
JOŽEFA STEFANA**

**JOŽEF STEFAN
INTERNATIONAL POSTGRADUATE SCHOOL**

Jamova 39, SI-1000 Ljubljana

T +386 (0)1 477 31 00

F +386 (0)1 477 31 10

E info@mps.si

www.mps.si

31.5 - 1.6. 2016, Ljubljana